Optimisation of silicon content in Fe-Si alloys processed via Laser Powder Bed Fusion for an additively manufactured soft magnetic core

by

Leonidas Gargalis, MEng, MSc

Doctoral Thesis

Thesis submitted to the University of Nottingham for the degree

of Doctor of Philosophy (PhD)

Centre for Additive Manufacturing (CfAM), 2021

Contents

Abstract

Additive Manufacturing (AM) of electric motors, specifically, Laser Powder Bed Fusion (LPBF), for rotating soft magnetic cores is of research interest because of its potential benefits in industry sectors such as energy, aerospace and automotive. AM, also commonly known as 3D printing (3DP), offers unrivalled design freedom and the capability to produce components with complex geometries from metal alloys that cannot be processed with conventional manufacturing methods (casting, injection moulding etc.). However, before AM becomes the norm in the production of novel electric drives and power generators, it is necessary to understand how the selection of materials in the motor affects the performance of the 3D printed active components (rotor, stator, windings). This thesis aims at enabling the AM of more compact, lightweight, reliable and efficient electric machines through the development of a comprehensive understanding of the metallurgy and material properties of the additively manufactured components of an electric drive. It focuses on two materials: a soft ferromagnetic alloy, namely silicon steel, for the soft magnetic core and high purity copper for the windings of the electric motor. The study investigated the mechanical, thermal and magnetic properties of high silicon steel (from Fe-3.5%wt Si up to Fe-6.9%wt Si) by adjusting – for the first time – the alloys' chemistry in order to improve ductility and avoid the risk of in-process cracking; this is achieved by mixing pre-alloyed Fe-6.9%wt Si powder with high-purity Fe powder. Another material investigated, which has lately received increased interest both for electrical applications and heat exchangers, was pure copper. Although high purity copper is challenging to process with LPBF due to its high reflectivity, oxidation and high thermal conductivity, it was included in the study due the potential to further increase a motor's performance by optimising the design of the windings in a 3DP electric motor. The absorptivity of pure

copper powder and bulk material and the electrical conductivity of copper parts were experimentally measured.

All the materials under investigation were subjected to heat treatments. Annealing of the soft magnetic parts produced by LPBF changed their microstructure by increasing the grain size and increased their permeability. Experiments were also performed to investigate how the performance of a Switched Reluctance Motor (SRM) could be improved by manufacturing the soft magnetic rotor core using LPBF. A prototype SRM soft magnetic core was additively manufactured from 5%w.t. silicon steel and tested. We compared the efficiency of the motor with the 3D-printed rotor core to a motor with an identical but traditionally laminated rotor.

This investigation has therefore, developed an understanding of the various aspects of the LPBF process for the successful manufacturing of a prototype functional electric motor. The results from this work can be used to advance the implementation of AM in the production of lightweight high-performance electrical machines and revolutionise the way electrical motors are designed and manufactured. We suggest that future research should focus on the design of novel topologies of motors based on AM design principles in order to maximise the advantages of LPBF. Further research into soft and hard magnetic materials is required as well as into copper and copper alloys, to expand the list of materials available for manufacturing soft magnetic cores for a variety of applications.

Acknowledgements

I would like to express my gratitude to all the people who believed in me and supported me all these years to pursue my dreams and reach my goals. First and foremost, I would like to thank my life partner Mariana who has been able to withstand my temper and capricious character all these years. You have been by my side since we first met, and you have made me realize that my PhD is just another beautiful journey and a unique learning experience. You are the love of my life.

I would also like to thank my family especially my mother Styliani, my father Achilles and my sister Xenia for their invaluable moral and financial support. Mother you have always supported my life choices and you helped me become the man I am today. Father, you have always keep pushing me towards my goals without ever doubting my abilities. My beloved sister you have been my inspiration to follow my dreams and I have always looked up to you.

I cannot express in words my gratitude to my supervisors Prof. Ian Ashcroft and Prof. Richard Hague for their continuous understanding and support. I appreciate the long discussions during our meetings over the years and the knowledge that you have passed on to me. You have supported this project and me personally without ever running out of patience. Thank you for all the opportunities that you have given me and for encouraging me to achieve the extraordinary through this PhD. Most importantly, thank you for helping me develop as a person and a researcher. I would also like to thank Prof. Phill Dickens for his kind comments and constructive advice and for agreeing to examine my work during the first years of my research. I also want to express my gratitude to Dr. Manyalibo Matthews and his research team at Lawrence Livermore National Lab, for

making me feel like home during my stay in the USA and for helping me expand my horizons. You all contributed to an amazing internship experience.

I am also deeply grateful to Mark East and Mark Hardy who were patient with me and spent more working hours than I can count to teach me how to operate all the different types of 3D printing machines and software. You have both been true friends and mentors.

In addition, I would like to thank my friends and colleagues Dr. Michele Garibaldi for his guidance at the beginning of my PhD, Dr. Cassidy Silbernagel for the many interesting discussions and our successful collaboration, Dr. Marco Simonelli aka "metallurgy guru", Mr. Joe White who has been my Personal Design Trainer, Dr. Nesma Aboulkhair for her continuous inputs, Dr. Ian Maskery, Mr. Richard Selo for the exchange of ideas and Dr. Luke Parry. I gratefully acknowledge the help of Dr. Nigel Neate, Ms. Hannah Constantine and Mr. Jason Greeves in various sample preparations and testing.

Finally, I would like to acknowledge the support from Marie Skłodowska-Curie Actions Innovative Training Network (ITN), the Institute for Aerospace Technology and the University of Nottingham-Faculty of Engineering, because without their financial support the realisation of this thesis would not have been possible.

List of Publications and Conferences

Journal Papers

Published:

Leonidas Gargalis, Vincenzo Madonna, Paolo Giangrande, Roberto Rocca, Mark Hardy, Ian Ashcroft, Michael Galea, Richard Hague, "Additive Manufacturing and Testing of a Soft Magnetic Rotor for a Switched Reluctance Motor", IEEE Access, Vol.8, 2020

Cassidy Silbernagel, **Leonidas Gargalis**, Ian Ashcroft, Richard Hague, Michael Galea, Phill Dickens, "Electrical resistivity of pure copper processed by medium-powered laser powder bed fusion additive manufacturing for use in electromagnetic applications", Additive Manufacturing, 29, (2019) https://doi.org/10.1016/j.addma.2019.100831

Leonidas Gargalis, Jianchao Ye, Maria Strantza, Alexander Rubenchik, James W. Murray, Adam T. Clare, Ian Ashcroft, Richard Hague, Manyalibo J. Matthews "Determining processing behaviour of pure Cu in laser powder bed fusion using direct micro-calorimetry", Journal of Materials Processing Technology 294 (2021) 117130, https://doi.org/10.1016/j.jmatprotec.2021.117130

Under Review:

Leonidas Gargalis, Ian Maskery, Martin Lees, Ian Ashcroft, Richard Hague, "Effect of Silicon content on microstructure, micro-hardness and magnetic properties of Fe-Si alloys processed by Laser Powder Bed Fusion", Additive Manufacturing Journal

Conference Papers and Talks

Leonidas Gargalis, Vincenzo Madonna, Paolo Giangrande, Mark Hardy, Ian Ashcroft, Michael Galea and Richard Hague, "3D Printing as a Technology Enabler for Electrical Machines: Manufacturing and Testing of a Salient Pole Rotor for SRM", ICEM International Conference on Electrical Machines, August 2020, Sweden (online)

Leonidas Gargalis, Vincenzo Madonna, Paolo Giangrande, Roberto Rocca, Ian Ashcroft, Richard Hague and Michael Galea, Development and Testing of Soft Magnetic Rotor for a Switched Reluctance Motor Built through Additive Manufacturing Technology", ICEMS, Japan, 2020 (online), ***Best paper award of ICEMS 2020***

Manyalibo Matthews, Jianchao Ye, **Leonidas Gargalis**, Gabe Guss, Saad Khairallah, Alexander Rubenchik, "Absorptivity and energy scaling associated with laser powder bed fusion additive manufacturing", Conference of Lasers and Electro-Optics 2019, San Jose, California, USA.

Leonidas Gargalis, Marco Simonelli, Ian Ashcroft, Richard Hague, Michael Galea, "Additive Manufacturing of Soft Magnetic Silicon steel parts: Metallurgy and Magnetic Characterisation of the printed material", 147th Annual Meeting of The Minerals, Metals & Materials Society 2018 (TMS 2018), Phoenix, Arizona, USA.

Leonidas Gargalis, Marco Simonelli, Ian Ashcroft, Richard Hague, Michael Galea, "A study on the Production of oriented high silicon steel by Laser Powder Bed Additive Manufacturing", 147th Annual Meeting of The Minerals, Metals & Materials Society 2018 (TMS 2018), Phoenix, Arizona, USA.

Leonidas Gargalis, Cassidy Silbernagel, Ian Ashcroft, Richard Hague, Michael Galea, "Electrical resistivity of pure copper processed by medium-powered laser powder bed fusion additive manufacturing for use in electromagnetic applications", 148th Annual Meeting of The Minerals, Metals & Materials Society 2019 (TMS 2019), San Antonio, Texas, USA.

List of Abbreviations

AC: Alternating Current

AM : Additive Manufacturing

ASTM : American Society for Testing and Materials

BLDC: Brushless DC Motor

CfAM: Centre for Additive Manufacturing

CAD : Computer Aided Design

DC: Direct Current

DMLS : Direct Metal Laser Sintering

DOE: Design of Experiment

EBSD: Electron Backscatter Diffraction

EDX: Energy Dispersive X-Ray

EV: Electric Vehicle

FDM : Fused Deposition Modelling

HAZ: Heat Affected Zone

HIP : Hot Isostatic Pressing

IACS: International Annealed Copper Standard

IEC: International Electro-technical Commission

IEEE: Institute of Electrical and Electronics Engineers

LENS : Laser Engineered Net Shaping

LPBF : Laser Powder Bed Fusion

LoF: lack of fusion

MEA: More Electric Aircraft

MMC : Metal Matrix Composite

PM : Powder Metallurgy

PMSM : Permanent Magnet Synchronous Motor

PF: Pole Figure

RP: Rapid Prototyping

IM: Induction Motor

IPF : Inverse Pole Figure

PD: Point Distance

SEM : Scanning Electron Microscopy

SLM : Selective Laser Melting

SLS: Selective Laser Sintering

SRM: Switched Reluctance Motor

SS: Scan Speed

SynRM: Synchronous Reluctance Motor

STL : Standard Tessellation Language (Stereolithography file format)

TO : Topology Optimization

TPMS : Triply Periodic Minimal Surface

UK: United Kingdom

USA: United States of America

w.t.: weight

XRD: X-Ray Diffraction

3DP: 3-D Printing

List of Figures

List of Tables

Nomenclature

Unit of measure	Unit type	Unit of measure	Unit type
Degrees (Angle)	^{o}	Volts (Voltage)	V
Degrees Celsius (Temperature)	^{o}C	Revolutions per minute (Rotational speed)	rpm
Amps (current)	A	Watts (Power)	W
Grams per cubic centimetre (Density)	g/cm^3	Flux density	B
Hours (Time)	h	Diameter	D
Hertz (Frequency)	Hz	Angular velocity	ω
Kelvin per second (Cooling rate)	K/s	Electrical conductivity	σ
Grams (Mass)	g	Electrical resistivity	ρ
Metres (Length)	m	Number of turns of poles	N
Litres (Volume)	L	Power	P
Millimetres per second (Speed)	mm/s	Resistance	R
Square millimetres (Area)	mm^2	Normalised enthalpy	β
Cubic millimetres (Volume)	cm^3	Normalised thermal diffusion length	L*
Newtons (Force)	N	Torque	T
Seconds (Time)	s		

1. Chapter 1: Introduction

1.1 Introduction

Additive Manufacturing (AM) has emerged across a wide range of industrial sectors including automotive aerospace and medical for the creation of functional lightweight metallic parts. AM, also commonly known as 3D printing (3DP), is comprised of several different technologies that build components by adding material, layer by layer, based on a sliced 3D CAD (Computer Aided Design) model. The most common metallic based AM processes include Laser Powder Bed Fusion (LPBF)/Selective Laser Melting (SLM), Direct Metal Laser Sintering (DMLS) and Electron Beam Melting (EBM) [1]. Although AM has been used for over 30 years, only recently has it started evolving into a mainstream manufacturing process, with the development of more refined technologies and materials, including new metal alloys. The production of metallic parts with AM has gained popularity due to the many advantages of this technology; such as a high degree of design freedom that enables the manufacture of geometrically complex parts and the customisation of parts on demand. In some cases, it is even possible to manufacture parts of complex geometry using AM that cannot be produced using any conventional manufacturing techniques [2,3]. Another important benefit that AM has to offer is the reduction of waste material compared to traditional subtractive manufacturing. For the aerospace industry, less material waste for expensive materials such as titanium and nickel super-alloys translates to a drastic reduction in costs. Rather than subtracting material from a large billet, AM offers the possibility of manufacturing near net shape parts in a single-step process, with little or no post-processing required [4]. The raw material (metallic powder) can be recycled and reused, contributing to a reduction in costs and simultaneously, reducing the environmental impact of the

manufacturing process. Because of the simplicity of the AM process, it is more straightforward to make design changes or produce different products with the same equipment, simply by changing the input of the 3D CAD model. For the aerospace industry where mass production and lead time are crucial, AM can improve the manufacturing and assembly process by simplifying the design and reducing the number of parts required in a component.

However, before AM becomes implementable and widely adopted, directly competing against conventional manufacturing technologies, there are many challenges to overcome [5]. Though it is a great enabler for design freedoms, there is much work to be undertaken into developing materials specific for the process, as well as making the systems more reliable. For example, because of the inherent nature of the process, precise monitoring of the powder bed and/or the melt pool is required to ensure the quality of the end-use metallic parts [6][7]. Additionally, as a high-power laser beam is used to irradiate material in powder form, there exists a series of complex physical phenomena. The formation of defects such as porosity, surface finish, residual stresses, crack formation and propagation depend on material properties as well as on the processing parameters. To ensure reliability and the required quality of the end parts in high-demanding industry sectors, further research and standardisation processes are necessary.

There are three main types of metallic AM systems, categorised based on the system employed to supply the material. These are: powder-bed systems, powder-feed systems, and wire-feed systems. Besides the material feeding mechanism, the heat source used to process the material might also be used to categorise different processes, with the most popular heat sources for melting metal powders being electron and laser beams. The

technology of interest in the current study is LPBF (Laser Powder Bed Fusion), which is a powder-bed process with a laser beam as the heat source.

Despite the use of LPBF for the production of structural parts using metals such as steel alloys, aluminium, Ti6AlV4 and Nickel super-alloys, there has been limited work to date focusing on more functional materials, such as soft magnetic metallic alloys and copper. The lack of literature on ferromagnetic materials suitable for the fabrication of electric machines indicates a gap in the knowledge, thus, additional research to expand the materials list available for LPBF is required.

1.2 Motivation and Aim of this study

The interest in LPBF of electric motors is motivated by the increasing demand for automotive and aerospace vehicle electrification and by the aim of producing more lightweight highly efficient electric drives and generators that will be easier to operate and maintain [8]. Although a handful of attempts at producing 3D printed soft and hard electromagnetic components for electric motors have been published, there is a lack of sufficient data available with regards to the performance of the additively manufactured parts. Furthermore, high purity copper, which is a common material for electrical applications, has been very difficult to process via LPBF due to its high reflectivity and high thermal conductivity. Several researchers have attempted to process copper but failed to provide any electrical or thermal properties such as resistivity and conductivity.

The superior design capabilities of AM can be fully exploited in electrical power generation applications by designing a completely new machine topologies. However, this can prove a very difficult and complicated task. In order to focus on the challenges related to material processing and to the specific manufacturing technology, an existing

design from a commercial electric motor was used in this study as a prototype. For this purpose, and in order to provide an initial proof of concept, a Switched Reluctance Machine (SRM) s chosen as a case study. Its soft magnetic rotor core was investigated by additively manufacturing it via LPBF of Fe-5%Si. The performance of the 3DP rotor was then compared to that of an identical commercial motor featuring a laminated rotor core, via in-depth experimental tests.

Although numerous AM technologies are capable of producing a wide range of materials from plastics to metals, only LPBF features a high technology readiness that can deliver the 3D printed parts needed for this research. Some of the examples that AM can offer in the production of electric motors include continuous skewed rotors, innovative flux barrier designs, control of magnetic properties and complex cooling systems with internal cooling channels embedded in 3DP parts. Innovative AM methods and new materials will inevitably replace conventional manufacturing techniques of electrical machines in high performance applications as AM technology matures. One of the main reasons hindering the adoption of LPBF for the production of electric motors currently, however, is the lack of suitable materials, gas atomised ferromagnetic materials, which this study addressed. The overall aim was to investigate a range of Fe-Si alloys with varying silicon content and optimise it for LPBF using a SRM soft magnetic core as a feasibility study. The main objectives are listed below:

- Investigate the possibility of processing high silicon steel alloys and determine the optimum amount of silicon content for the fabrication of soft magnetic cores by LPBF.

- Investigate the possibility of processing high purity copper for the fabrication of windings for an electric motor with a 200W LPBF machine

- Manufacturing and testing of the SRM rotor prototype to evaluate the performance and proof of concept
- Comparison of AM core with laminated commercially available rotor core

1.3 Methodology

The methodology of this study will provide a comprehensive understanding of the LPBF process in terms of the role of the process parameters in manufacturing near fully dense parts. The resultant microstructure mechanical and magnetic properties as well as electrical resistivity will validate the performance of the materials under investigation. In order to select the best combination of process parameters a progressive study looking into several parameters that can influence the quality of the final parts is conducted. Such parameters include powder characteristics, laser power, scan speed, hatch distance scan strategy and more. With the aim of determining the impact of silicon content in Fe-Si alloys several compositions were created and the microstructure was analysed. The mechanical properties were assessed by means of microhardness and tensile tests. Moreover, AC and DC magnetic measurements shed light on the magnetic properties and electrical resistivity values are measured. Finally, with all the above-mentioned data at hand, the performance of the soft magnetic rotor core is assessed and compared to a conventional laminated rotor core.

1.4 Thesis Structure

This research is structured in such a manner as to show that AM can produce a fully functional highly efficient electric motor with the use of LPBF technology. This first Chapter provides an introduction and overview of the areas that this research will cover. It presents the aim and motivation for this study and the structure of this thesis is shown

in Figure 1-1. Chapter 2 is a literature review where the state of the art in AM of electric motors is presented. The aim and objectives are identified, and the novelty of this study is outlined based on the gaps of knowledge ascertained from the literature. Chapter 3 analyses the materials and methods used in this research. Several compositions of high silicon steel alloy were investigated with the main focus being on the fabrication of a soft magnetic core. In addition, pure copper was examined with the potential of being employed for the production of windings by LPBF. The equipment used for various experiments is presented as well as the methodology of the tests. Chapter 4 focuses on the windings of the electric motor. High purity copper was processed and in-situ absorptivity values are reported for the first time. Moreover, electrical resistivity values are also presented together with prototype coils.

Chapter 5 is a parametric study of the effect of various process parameters in the LPBF of Fe-Si and focuses on producing near-fully dense parts. The results of the metallurgical and microstructural characterisation of the LPBF Fe-Si alloys are presented. Chapter 6 focuses on the mechanical, electrical and magnetic characterisation of the LPBF Fe-Si parts. In particular the effect of Si content is investigated with the aim of determining the maximum Si content that still enables crack free parts with good structural integrity to be manufactured.

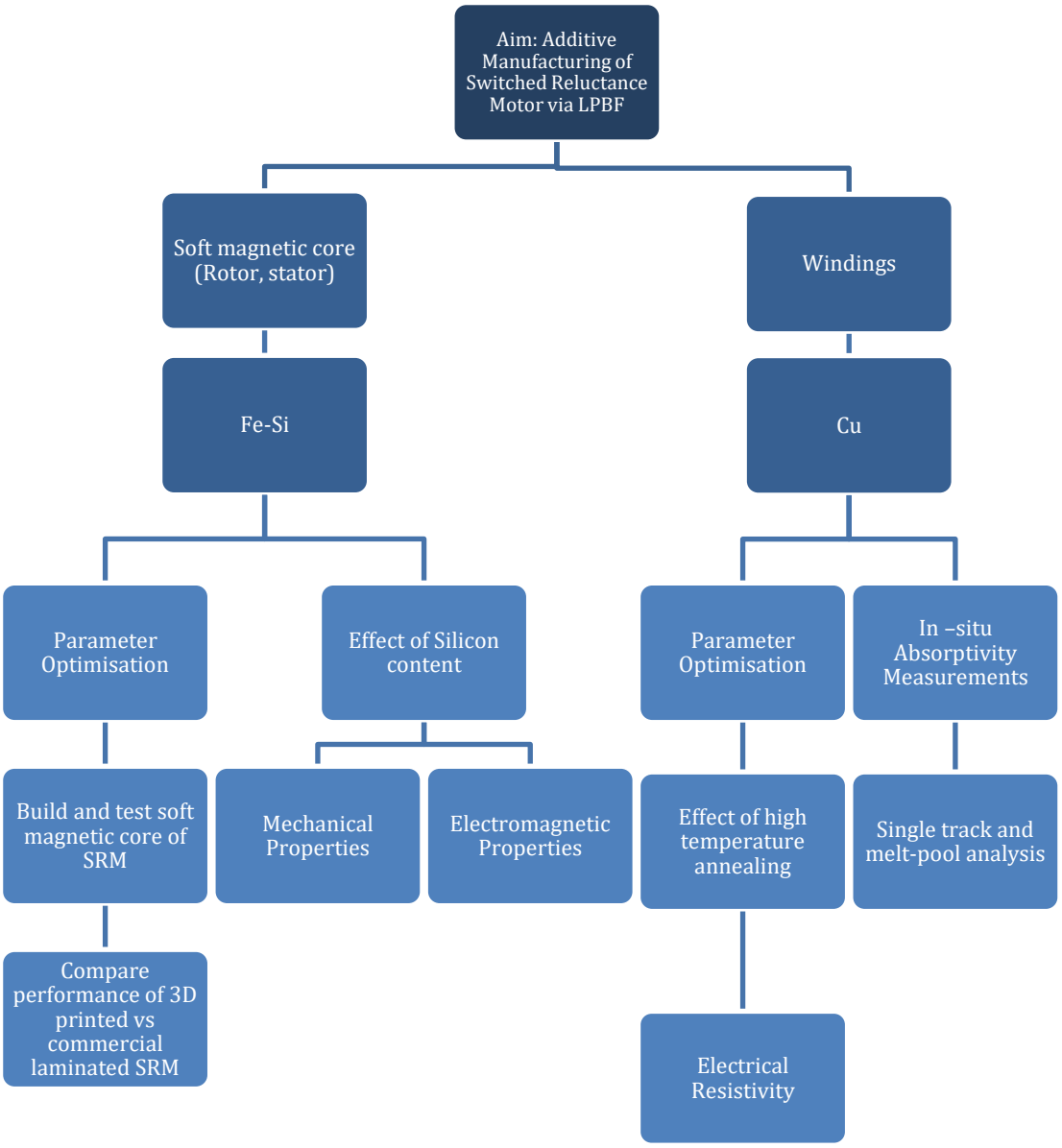

Figure 1-1: Thesis Outline – Structure of study based on components and materials

In addition, it presents the effect of annealing heat treatment on the material's microstructure. Chapter 7 presents the experimental details and performance of a SRM rotor prototype with an AM rotor. The performance of the motor was measured experimentally and compared to a conventionally manufactured motor (with a Fe-3%w.t. Si laminated rotor). Finally, Chapter 8 presents conclusions and recommendations for future work.

2. Chapter 2: Literature Review

2.1 Introduction

The aim of this Chapter is to provide a critical state of the art review of the published literature pertinent to the thesis. Firstly, the LPBF process is reviewed, with discussion of the effect of process parameters and scan strategies. The electric motor topologies are reviewed and the active parts of a rotating electrical machine, such as soft magnetic cores and windings, are discussed with special focus on the materials used to manufacture these components with a view to providing context for their potential replacement with AM parts. An overview of the AM technologies that have previously been used in the production of electric motor components is presented. The main materials in this study, namely silicon steel and copper are then discussed in more detail. The potential and challenges of LPBF in manufacturing of an electric motor as well as the gaps in the literature are identified. A comparison between materials and motor topologies is conducted in order to conclude that high silicon steels are the best candidate for manufacturing an SRM soft magnetic core via LPBF.

2.2 Laser Powder Bed Fusion

Laser powder bed fusion is an additive manufacturing process in which metal components are fabricated from loose powder spread flat on a powder bed. The energy for laser processing is provided by a high laser power concentrated beam typically between 100 W-1000 W. The LPBF process, starts with a thin layer of metal powder spread over a build platform, which is selectively irradiated by a laser beam that melts the powder. The build platform is then lowered, and a new layer of powder is spread. The process is repeated until the part is complete (Figure 2-1).

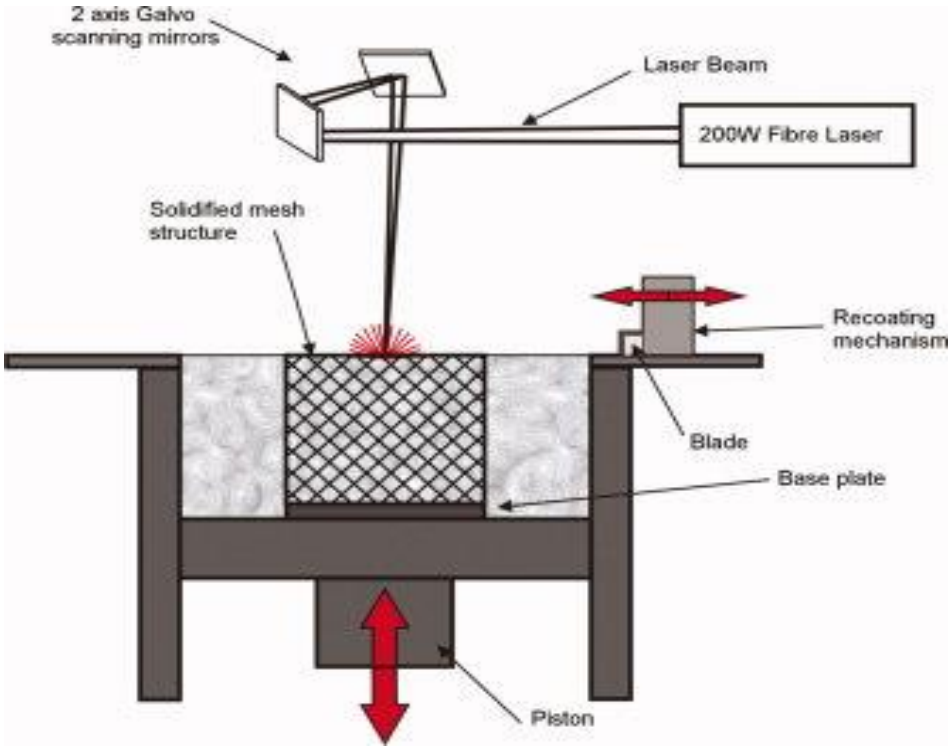

Figure 2-1: LPBF set up and operation from [219]

Due to the reactive nature of some powdered metal alloys, the build chamber is usually purged with Argon gas to provide oxidation protection and a more stable welding process. During the LPBF build process, the build platform is normally heated to at least 100ºC to raise the temperature of the powder. This lowers the amount of energy required to melt the powder by the laser and reduces the stresses resulting from the steep thermal gradients induced by the localised rapid heating/cooling and solidification of molten metal [9]. For that reason, there is usually a need to design support structures that will help conduct heat towards the build platform and will prevent part distortion and in-process metal cracking. When the build is complete, the parts are removed from the base plate (substrate) by breaking or cutting the support structures. One of the most common processes used in this stage is Electrical Discharge Machining (EDM). After the part has been removed, several finishing procedures are usually needed either to improve the

surface finish, such as milling or/and polishing, or heat treatments, such as stress relief, annealing etc. to achieve a desired microstructure. AM parts become functional when the post processes are complete.

LPBF is a generic term and this process is also known as Selective Laser Melting (SLM), Direct Metal Laser Sintering (DMLS) [10], Direct Metal Printing (3D Systems Corporation), Laser Beam Melting (LBM) [11], Laser CUSING (Concept Laser GmbH) [10], Laser Metal Fusion (TRUMPF Laser Technology), Micro Laser Melting or Micro Laser Sintering (MLM-MLS) [12][13]. In this thesis, the term LPBF will be used for simplicity.

2.2.1 Parameter Optimisation

The LPBF process is controlled by more than 130 parameters [14], however, only few of them are considered of main importance. The main set of parameters controlling LPBF is illustrated in Table 2-1. The major parameters involved in the process are: the scan speed of the laser beam (defined by the point distance and the exposure time), the hatch spacing (the distance between each two adjacent laser scans), the laser power, the layer thickness, and the properties of the laser beam in terms of laser power and spot size. These parameters are selected to adjust and control the building process. They can also affect the microstructure, mechanical properties, surface finish and overall quality. The geometrical features, such as point distance/sequence, hatch distance/geometry, border geometry, and layer thickness have been extensively investigated in numerous studies to enhance part density. Another parameter that offers a large degree of freedom to the LPBF process is the scan strategy. The scan strategy is defined by the scan pattern and scan orientation. The most common scan patterns are the unidirectional scan, the meander scan, and the checkerboard scan. The scan orientation describes the rotation in

degrees of the scan pattern from one layer to another and the number of scans per layer should be defined if each layer is to be scanned more than once.

Table 2-1: LPBF main process parameters adapted from [38]

Process Parameter			
Laser-related	**Powder-related**	**Scan-related**	**Temperature-related**
• Laser power	• Particle size	• Scan Speed	• Powder bed temperature
• Spot Size	• Particle shape & distribution	• Scan Spacing	• Powder feed temperature
• Pulse Duration	• Powder bed density	• Scan Pattern	• Temperature uniformity
• Pulse frequency	• Layer Thickness		
	• Material properties		

2.2.2 Scan Strategies

Residual stresses and deformations induced during LPBF manufacturing impose a serious limitation in the widespread adoption of this technology for processing brittle high silicon steel. Various scan strategies have been used in LPBF to reduce thermal stresses during fabrication aiming either to decrease or distribute stress more evenly inside the parts and minimise defects such as part distortion and delamination. The main reason for the induction of stresses in the part is the material expansion and contraction from rapid heating of the material by the laser to beyond its melting point, followed by a relatively high cooling rate in the build chamber [15]. Some of the most common scan patterns were presented in [16] where the authors showed that island scan strategies limit the thermal gradients in the part. In [17] L. Parry used a thermo-mechanical model and presented that short scan vectors reduce the residual stress during the LPBF process of Ti-6Al-4V. A spiral/helix scan strategy was investigated in [18][19], and a fractal scan paths were used in [20], aiming to stabilize thermal gradients and reduce residual stress in nickel superalloys. Except from the reduction of residual stresses, scan strategies can also influence the microstructure and crystallographic texture. Several studies on

different materials concluded that the direction of grain growth and the crystallographic texture is affected by the scan pattern during LPBF processing. Thijs et al. studied the influence of different scanning strategies on the microstructure and texture of LPBF printed AlSi10Mg [21] and Ti6Al4V [22] and found that using an optimum scanning strategy, an isotropic microstructure was achievable. The same author showed that a strong fibre texture obtained by scanning every layer using unidirectional vectors, could be changed into a weak cube texture when scan vectors rotated by 90˚between layers were employed. In [23] the authors processed Ni-Mo alloy with various scan strategies and presented the effect on texture. Single crystalline-like texture was produced via bidirectional scanning along one axis and bidirectional scanning with a 90o rotation between layers. However, a fibre texture was observed when bidirectional scanning with a 67o rotation was employed. All authors reported that the scan strategy affects both the direction of growth of the grains and their crystallographic texture, which is controlled by the preferential growth directions of columnar cells and the subsequent epitaxial growth. Scanning strategies are often overlooked, with the focus being on optimising process parameters. However, it has been shown that varying the scanning strategy results in different defects and anisotropy of mechanical properties. Scan strategies have also been used as a method to increase the density of LPBF parts. Aboulkhair et al. [24] showed that an alternate scanning strategy along with optimised process parameters could remove porosities and obtain about 99.8% dense AlSi10Mg parts. Moreover, Kruth et al.[9][25] presented the strong relevance of scanning strategy on densification

and mechanical properties of iron-based powders. The main scanning strategies used in LPBF are shown in Figure 2-2.

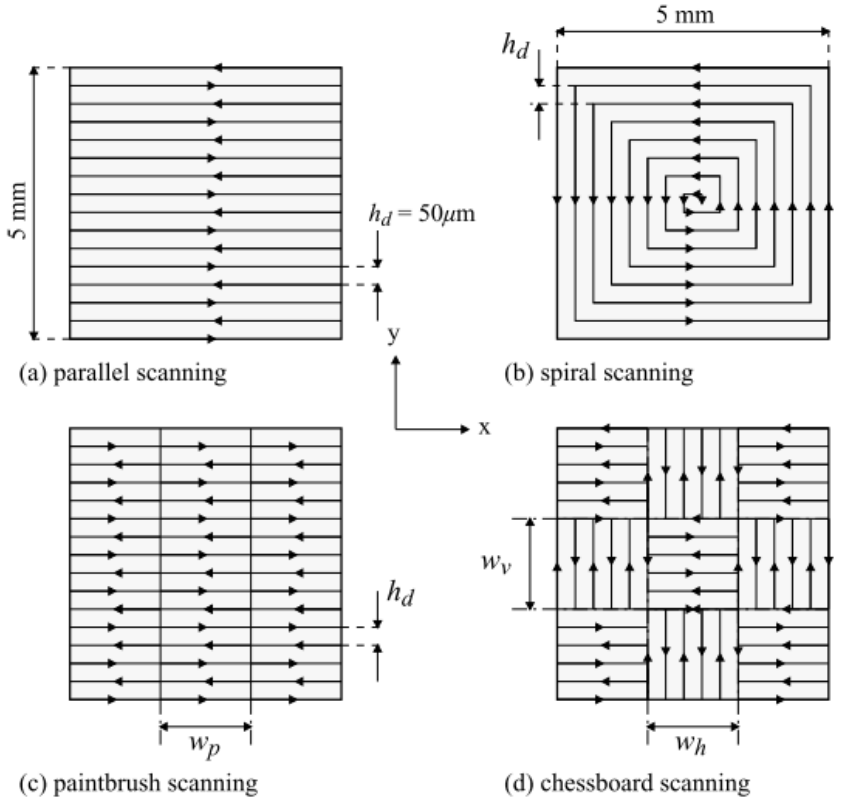

Figure 2-2: Main scan strategies commonly used in LPBF [18]

2.3 Electric Motors

An electric motor is a device that converts electrical power into mechanical power whereas a drive/generator is the electronic device that harnesses and controls the electrical energy sent to the motor. There are many different types of motors, however, at a fundamental level every motor has 3 main parts. A rotating part called the rotor, a static non-moving part called the stator and a part that generates a magnetic field [26]. In Figure 2-3 a view of an (induction) and permanent magnet electric motor shows the active components of a traditional electrical machine. In the static part, or stator, a rotating magnetic field is generated through an array of electromagnets. The magnetic field produced in the stator interacts with the rotating part, namely the rotor, resulting in

the production of a mechanical torque. Both the stator and the rotor consist of soft magnetic materials, whose function is to amplify and guide the magnetic field. Copper field coils are wound around the stator to produce an array of field-generating electromagnets. The interaction between the stator's magnetic field and the rotor determines the topology of the motor.

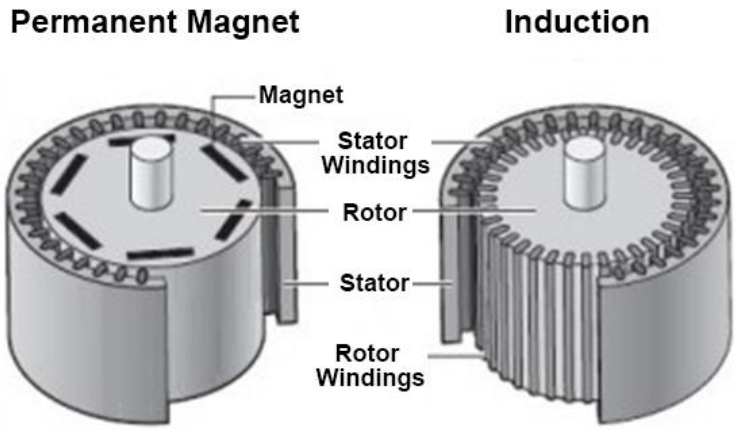

Figure 2-3: Stator and Rotor comparison between a permanent magnet and an induction machine [26]

2.3.1 Types of electric motors

There are two main categories of electric motors: DC and AC. As the name suggests they are categorised based on the type of current that runs through them and they can be sub-divided into four main classes. The first type is the DC electric motor, which was first developed in the beginning of the 19th century and is the oldest type of motor driven by DC current. The second type is the AC induction motor (also known as squirrel-cage

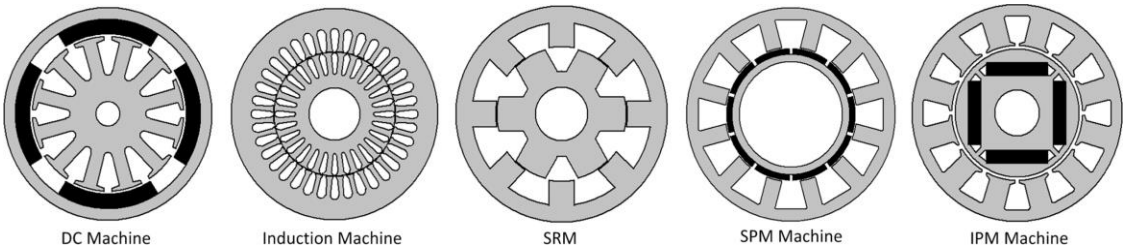

Figure 2-4: Topologies of Electric motors, DC, Induction Machine (IM), Switched Reluctance Machine (SRM), Synchronous Permanent Magnet machine (SPM) and Induction Permanent Magnet Machine (IPM) [220]

induction motor) and the third type is the AC synchronous motor (also called brushless AC motor or PM motor). The fourth and last type is the reluctance motor. The characteristics related to the different topologies of electric motors determine their respective field of application. Electric motors are also categorised based on the relative rotation speed of the rotor in relation to the magnetic field produced by the stator. When the rotor and the magnetic field rotate at the same speed the machine is called synchronous. On the contrary, when the rotor and the stator's magnetic field rotate at different speeds the motor is called asynchronous. The main types of electric motors are shown in Figure 2-4.

The advantages and disadvantages of each machine type make them suitable in different applications were different requirements such as power range, speed, torque and operational/maintenance conditions are critical. In hybrid/all-electric aerospace and automotive transportation, the primary requirements are high power density, high efficiency and lightweight motors with increased reliability [27]. The highest potential by taking into account these requirements is given by the brushless Permanent Magnet (PM) machine, the Switched/Synchronous Reluctance machine (SRM, SynRM, respectively) and the Induction Machine (IM) [27][28]. While the first two machine types are examples of synchronous machines, the IM is the most popular representative of the asynchronous category. In order to determine the most suitable electrical machine (EM) topology for manufacturing via AM and more specifically through LPBF, we need to assess their respective advantages and disadvantages and take into consideration design and manufacturing constraints. The selection of the motor suitable for fabrication through AM is an important step in this study and multiple criteria must be taken under consideration such as efficiency, reliability, power density, controllability operating

advantages and disadvantages for the various motors. The main advantages and disadvantages of the various types of EM are shown in Table 2-2.

Table 2-2: Comparison of electrical machine types with their respective advantages and disadvantages

Type of Electric Motor	Advantages	Disadvantages
DC Motor	Easy control	Frequent need of maintenance
	Desirable torque-speed characteristics	Low efficiency and reliability
		Low Speed range
Induction Motor	High speed range	Large size and low power density
	Highly reliably	Low efficiency
	Low cost	Thermal problems at higher speeds
	Robust in hostile environment of operation	
Permanent Magnet Synchronous Motor (PMSM)	High power density and small size	Limited speed range
	High efficiency	High Cost
		High stator core loss at high speed
Switched Reluctance Motor (SRM)	Desirable torque-speed characteristics	High torque ripple and noise
	High reliability	Low power density
	Low cost	Low efficiency
	Robust in hostile environment of operation	

During the comparison, several manufacturing and testing constraints were also taken into consideration i.e., material selection, manufacturing process, prototype design and motor testing (Figure 2-5).

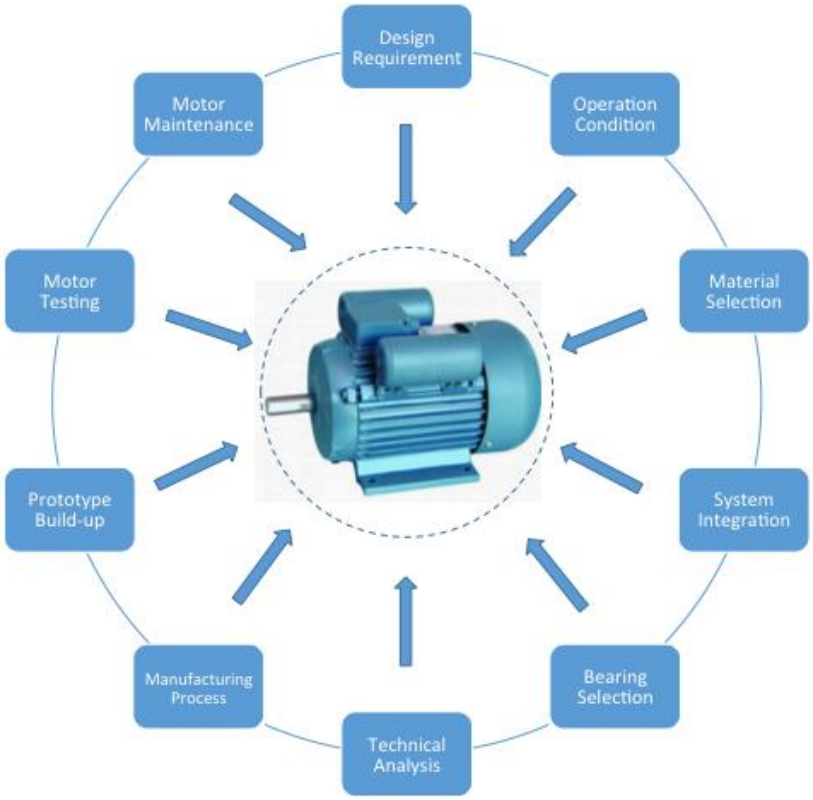

Figure 2-5: Motor manufacturing and testing considerations

2.3.2 Switched Reluctance Motor (SRM)

SRM has windings on the stator, but no permanent magnets or windings on the rotor, which allows it to operate at high temperatures. This property also leads to a lower manufacturing cost, simple and rugged structure, allowing it to be designed with reduced dimensions. The SRMs need an advanced control technology in their drive systems in comparison with other AC and DC motor drives. However, the SRM has some drawbacks that include vibration, noise, and use of a position sensor that makes the drive system more complex and less reliable. The advantages of SRMs in comparison with other electric motors are attributed to their simple structure, flexibility of control, high efficiency and lower cost. The rotor is conventionally made of laminated soft magnetic material and it does not have any windings or permanent magnets which enhances reliability along with fault tolerance making the SRM suitable for very high speed drive applications [29]. The most common SRM topology are shown in Figure 2-6. Recently

the interest in SRMs has increased because of the high cost of rare-earth materials required in permanent magnetic machines. SRM motors can be classified based on movement pattern (rotary or linear), flux path and type of excitation. SRMs have been designed mainly for the applications in high-power, high-efficiency, variable speed drives, enabling them to deliver a wide range of torque. This type of motor requires closed-loop position control. Therefore, due to the simplicity of the rotor design and lack of windings, the motor that best suits the aim of this study and seems to be the most suitable for laser powder bed fusion additive manufacturing is an AC reluctance motor and more specifically the SRM.

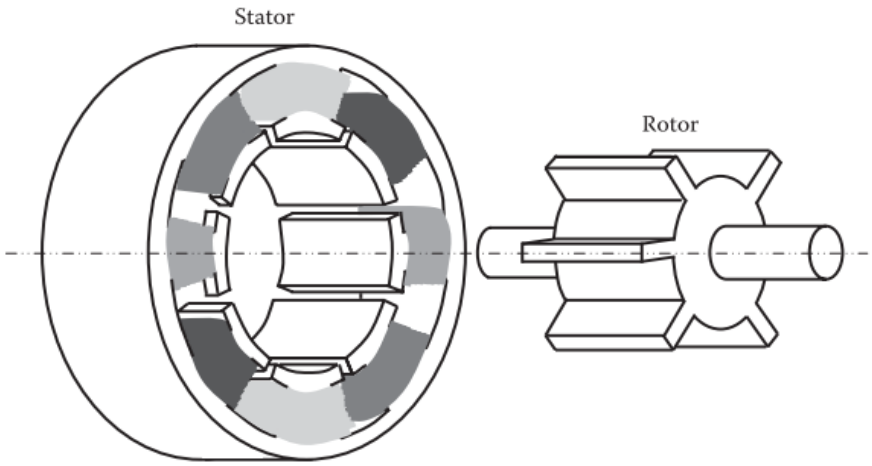

Figure 2-6: The salient rotor in an SRM [221]

Another parameter of importance, which led to the selection of an SRM motor for this study, is their availability within the predetermined size limitations imposed by the LPBF machines. Although SRM soft magnetic cores are conventionally produced by lamination stacks, in this study the rotor core will be fabricated as a solid component for a feasibility study though this might result to higher eddy current losses. Eddy current losses and their impact on the performance of a soft magnetic core will be presented in detail.

2.4 Soft Magnetic Materials

Since their development, electrical machines have used simple iron cores. However, that caused problems due to increased eddy current losses until 1880 when the first laminated core was produced [26]. Traditionally lamination sheets were punched by stamping machines and stacked together to form a rotor core. To this day, the use of laminated sheets is the most common method for manufacturing cores for electrical machines from Non-Oriented silicon steel. Intensive research is on-going aiming to improve the magnetic characteristics of materials and effectively the performance of electric motors. For example, various ferromagnetic alloys have been investigated such as silicon steel (Fe-Si) and nickel-iron (Fe-Ni) [30–32], as well as amorphous and nano-crystalline materials. More recently soft magnetic composites (SMCs) were processed for electric motor applications [33,34].

The typical material parameters that determine the material's, and thus subsequently the motor's, performance that must be taken under consideration during the machine design and manufacturing process are:

- Magnetic saturation
- Coercivity
- Permeability
- Iron losses (magnetic losses)
- Magnetostriction (noise)
- Delivery (forms, fully processed, semi-processed)
- Market availability (supply)
- Price

Further details of the magnetic properties of ferromagnetic materials are discussed in [35] by Bozorth. Conventional soft and hard magnetic materials are presented in [36] and the work in [37] covers amorphous and nano-crystalline materials. A general introduction to magnetic properties of materials can also be found in [38] whereas [39] covers analytically novel materials of technological and scientific interest, including advanced soft magnetic materials for power applications. As a summary: the magnetic saturation of the selected material usually determines the potential power density of an electrical machine. To achieve larger magnetic saturation values, less material is required to guide the magnetic flux inside the magnetic core. Coercivity determines the material hysteresis and thus the required magnetic field strength for the creation of the desired magnetic flux inside the machine. Magnetostriction is the property of ferromagnetic materials that causes them to change their shape or dimensions during the process of magnetisation and is related to its magneto-crystalline anisotropy. It is highly dependent on the chemical composition of the material and it can be controlled by changing or adding different alloying elements. In general, materials with low saturation magnetisation tend to also have lower magnetostriction (e.g., cobalt based amorphous alloys and 80% Fe-Ni). Magnetostriction can create vibrations and noise in the machine core therefore alloys with large magnetostriction characteristics can have a negative impact when used in motor applications. Over the years it has been established that high motor torque and power output can be achieved with magnetic core materials characterised by low core loss, high magnetic saturation and low coercivity.

An overview of the magnetic characteristics in terms of the magnetic field strength and coercivity of the most common soft magnetic materials used in electrical machines is presented in Figure 2-7.

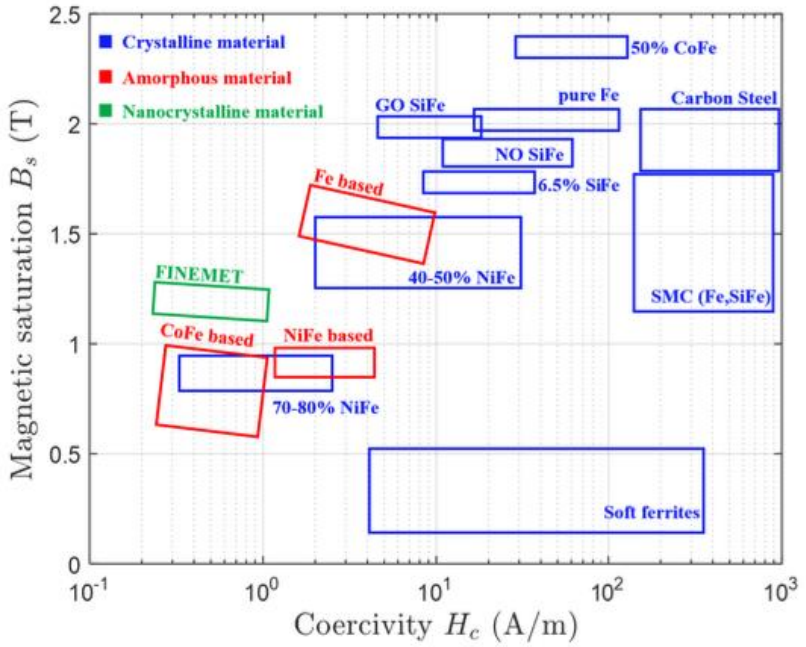

Figure 2-7: Magnetic saturation flux density vs magnetic coercivity for typical soft magnetic materials [222]

Soft magnets are ferromagnetic materials that can be easily magnetised and demagnetised. In other words, they are characterised by a narrow induction-applied field loop and they are typically employed to enhance or channel the flux produced by an electric current in a large variety of devices, including transformers, generators and motors. An example of a soft magnetic material magnetisation curve is shown in Figure 2-8, where the main points are indicated. A hysteresis loop or also known as B-H loop shows the relationship between the induced magnetic flux density (B) and the magnetising force (H) as it is successively magnetised to its saturation point (point a), then demagnetised (point b), magnetised in the reverse polar direction (point d) and then finally re-magnetised. The loop is generated by measuring the magnetic flux of a ferromagnetic material while the magnetising force is changed.

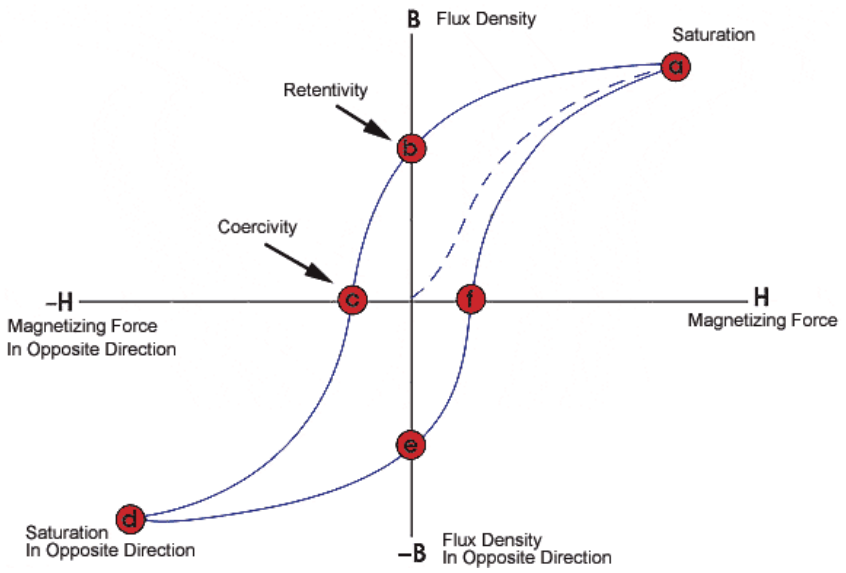

Figure 2-8: Hysteresis curve (B-H loop) showing the relationship between the induced magnetic flux density (B) and the magnetising force (H) [223].

Soft magnetic materials are an important industrial product and an overview of the market with the relative contribution of each material is shown in Figure 2-9 [39]. A major share of the market is covered by the grain oriented (GO) and non-oriented (NO) electrical steel. More commonly known as “silicon steel”, electrical steel is without doubt the most common soft magnetic material with a worldwide production of approximately twelve million tons annually, accounting for 80% of the total soft magnetic material market. Ferrites, powder, amorphous, Fe-Ni, and Fe-Co together reach an annual global value of approximately 17%. A high global demand for efficient electrical power generation drives the development of steels with lower magnetic losses and higher permeability [40].

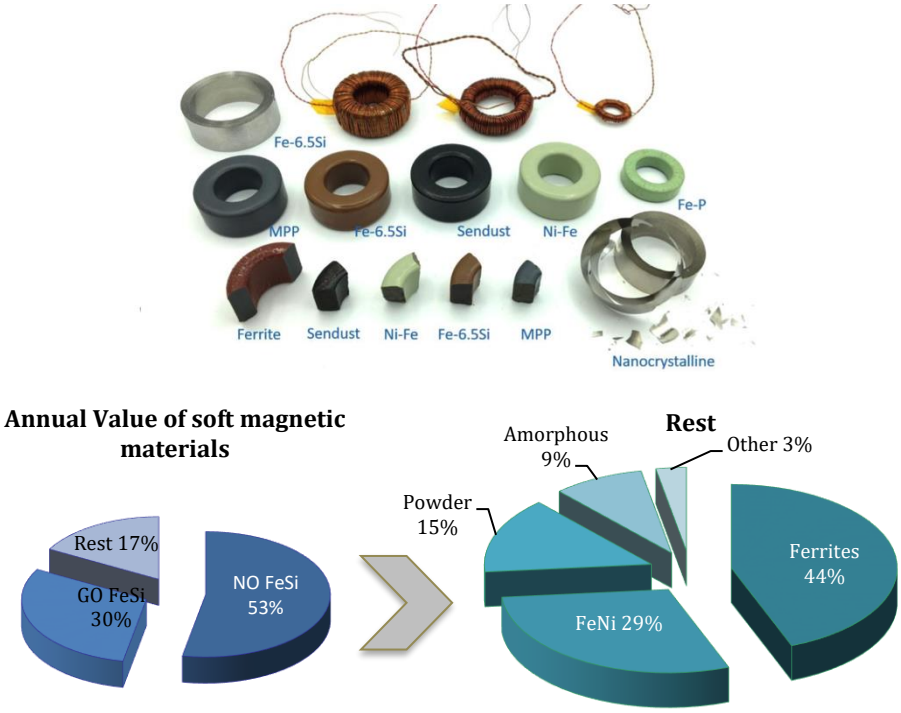

Figure 2-9: a) Commercially available soft magnetic materials in toroid form of different sizes adapted from [224] and b) Annual value of world production of soft magnetic materials adapted from [225]

Therefore, due to the excellent magnetic properties of Fe-Si, its low price and market availability, it has become the material of choice for laminated rotors, where typically rotating electric motors are constructed of Fe-Si laminations with thicknesses of 0.2 to 1 mm [41,42] where iron is the major element in the material composition and silicon, aluminium, nickel, cobalt, vanadium and other metals are the alloying elements that allow for adjustments to the magnetic and mechanical characteristics. For this reason, in this study, Fe-Si soft magnetic alloy with varying silicon content is proposed as the material to be processed via LPBF for the fabrication of a soft magnetic rotor core and is discussed in more detail below.

2.4.1 Silicon Iron alloys (Fe-Si)

The material of choice when it comes to electrical machine applications is silicon-iron (Fe-Si), also known as silicon steel. Alloying iron with silicon content between 1-6.5%wt makes the steel harder and significantly decreases eddy current losses by increasing the resistivity of the material [35]. The carbon content in all silicon-steels is low, approximately 0.003%, which makes rolling and other fabrication processes easier. To further minimise hysteresis losses, impurities such as oxides, nitrides, and sulphides in silicon steel must also be tightly controlled and kept to a minimum. During traditional manufacturing processes such as cold rolling, body centered cubic crystals are stretched and flattened (oriented along the rolling direction of the strip Figure 2-10) [43]. Fe-Si exhibits minimum coercivity and maximum permeability when magnetized along one of the <001> axes and the resulting silicon steel alloy is called Grain-Oriented (GO). The material is anisotropic and it is characterised by different permeability values in different directions. Non-Oriented (NO) silicon steel has isotropic magnetic properties in all directions after being subjected to an annealing heat treatment, which eliminates the grain structure in the material [44]. Most rotating electrical machines use NO Fe-Si because the flux direction constantly changes as it rotates in the stator yoke and stator tooth tips. NO Fe-Si are cold rolled carbon steels with silicon contents of between 1.5%-3%wt . GO silicon steel usually contains more silicon than non-oriented steel, approximately 3.0%–3.5% [45].

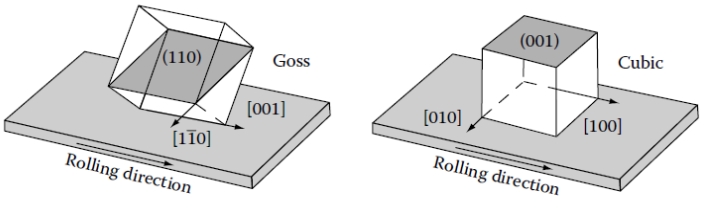

Figure 2-10: Goss (110)[001] and cubic (001)[100] texture, [43]

Currently, the maximum silicon content reached for laminations is 3.5% since any further increase in silicon makes the alloy more brittle and harder, hence, very difficult and expensive to process. In addition, higher silicon content may lead to an unwanted reduction of maximum flux density and permeability. The golden spot when it comes to magnetic efficiency is Fe-6.5%wt Si but there is a trade-off between minimising eddy current losses and maximising processability. To achieve such high silicon content there are two methods available. First, JFE Steel has developed a two-step industrial process where a Fe-3%wt Si is produced by typical cold rolling and then is doped in a chemical vapor deposition (CVD) process to further increase the silicon content [46]. The process is illustrated in Figure 2-11, however, this manufacturing process is energy intensive and increases the cost dramatically [47]. The second method to increase Si content in NO steels is diffusion annealing where the Fe-3%w.t.Si cold rolled steels are immersed in a molten Al-Si bath. This process modifies the alloying structure of the steel with an increase in Si and Al and changes the microstructure of the material while affecting its magnetic and mechanical properties [48].

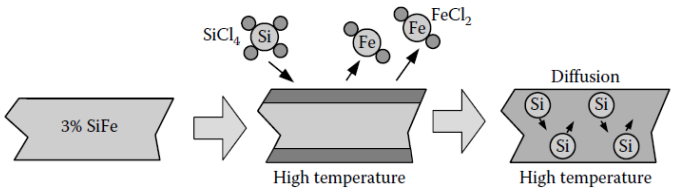

Figure 2-11: Simplified schematic of CVD technology for the production of 6.5%FeSi [43]

Several grades and thicknesses of silicon steel laminations are commercially available suited for a variety of applications and different types of electric motors. According to IEC 60404-8-8 [49], and ASTM A1086-13 [50], silicon steel is defined by thickness, grade and by total specific core loss.

2.4.2 Ordering-Disordering transformation in high silicon-steel alloys

At silicon concentrations above 2wt% electrical steel features an A2 body-centered cubic (bcc) structure. When the silicon concentration is increased to about 5.3 wt.%, B2 ordering starts to occur below 500°C according to the phase diagram shown in Figure 2.12 (a) [51]. D03 ordering starts to appear when the silicon content is increased beyond 6 wt.%. The terms A2, B2, and D03 are symbols that specify the crystal structure. The ordering of Fe-Si can be best described using the superlattice structure consisting of four interpenetrating face-centered cube (fcc) cells having a lattice parameter twice that of a single bcc cell [51], as depicted in Figure 2-12 (c). For high silicon contents around 6.5wt% Si electrical steel is ferritic (bcc) at all temperatures. A property of interest is that Fe-Si undergoes two ordering phase transitions during cooling [52], as it is depicted in the Fe-Si phase diagram in Figure 2-12 (b). For Fe-6.9wt% Si, the first disorder-order transformation occurs at approximately 820°C, where disordered ferritic solid solution, commonly referred to as A2, transforms into a short range ordered B2 phase. In this B2 phase, the previously randomly distributed Si atoms take the place of the centre atom of the bcc cell, while the Fe atoms occupy the corner positions at the cell [53]. Fe- 6.9wt% Si can be partially B2 ordered, since this phase has a stoichiometry of 1:1 Fe to Si atoms. When the alloy is cooled and the temperature drops further, a magnetic transition follows around 680°C and the material becomes ferromagnetic [54]. A last transformation takes place below 650°C, a further ordering reaction proceeds: B2 and residual A2 become B2+D03. D03 is an even more ordered structure, exhibiting also a long-range order [53]. In this structure, the centre atom of every second bcc cell is occupied by a Si atom, due to a stoichiometry of 1:3, ordering can attain a much higher extent than by the formation

of B2 phase. Advanced techniques are necessary to study the ordering effect in Fe-Si alloys processed by LPBF.

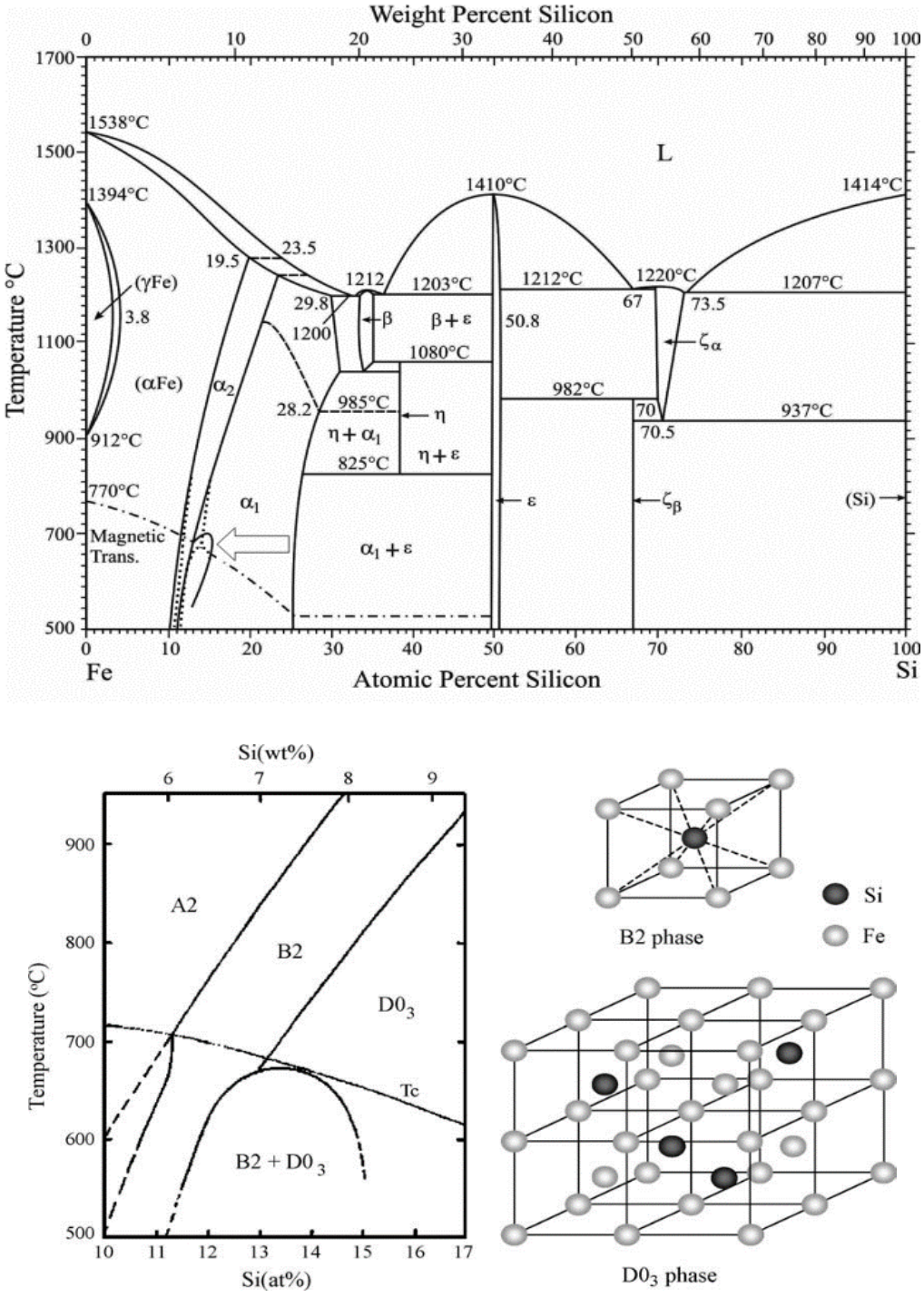

Figure 2-12: a) Fe-Si phase diagram over the full composition range [52], b) magnified extract of the region of interest (6wt%)where order disorder transformation takes place. c) Atomic structures of B2 and D03 phases [51]

Ordering has been investigated by TEM [55], XRD [56][57], Mössbauer spectroscopy [58] and neutron diffraction [59]. Lemke et al. used Differential Scanning Calorimetry (DSC) to analyse ordering-disordering transformations in a Fe-6.9wt% Si alloy. The authors correlated the calorimetric results with microhardness and heat treatments [60].

A superlattice structure can also be viewed as consisting of 8 bcc lattices stacked as a cube. A2 is in the disordered state, with random distribution of iron and silicon atoms in the superlattice. The atom pairing of the nearest-neighboring atoms results in B2 ordering, where silicon atoms preferably occupy the sublattice sites. Further ordering between the next-nearest-neighboring atoms results in D03 ordering, where only silicon atoms preferably occupy half of the sublattice sites with the longest separation. It should be noted that the full B2 structure requires all sublattice sites (bcc sites) to be occupied, corresponding to the stoichiometric compound Fe-Si. Fe-6.5wt%Si has insufficient silicon to form the stoichiometric compound. The B2 phase in Fe-6.5wt%Si adopts the structure, wherein silicon atoms occupy some of the sublattice sites (bcc sites) and iron atoms fill the rest of the sites. Similarly, the full D03 configuration requires 4 silicon atoms and 12 iron atoms, which correspond to the stoichiometric compound Fe3Si. The D03 structure in Fe-6.5wt%Si represents the structure in which silicon and iron tend to occupy the sites in the same manner as they do in Fe3Si D03.

The ordering interacts with dislocations resulting in a strengthening effect and a super-dislocation slip deformation mechanism as proposed for B2 and D03 lattices in [61] deteriorates the mechanical properties. B2 and D03 ordering leads to improved magnetic properties, where B2 growth is responsible for higher specific magnetization, and D03 growth is responsible for low magnetostriction, high maximum permeability, and low coercive force [62].

2.5 Effect of Silicon content

2.5.1 Magnetic properties

Bozorth studied the effect of Si content on various magnetic properties of Fe such as the magnetisation at saturation (Figure 2-13 (a)), total losses at a frequency of 60Hz (Figure 2-13 (b)) and maximum permeability, coercivity and hysteresis loss (Figure 2-13 (c)) [35]. The results show that the saturation magnetisation decreases with increasing Si content, whereas all the other magnetic properties (permeability, coercivity and total losses) are improved by the addition of Si to Fe. Specifically, Fe-Si alloy containing about 6.5%-Si features the lowest total losses at 1T magnetic induction and 60Hz frequency [35], thus, making it an ideal candidate for electric motors. The magnetocrystalline anisotropy also decreases with silicon addition, which results in higher relative permeability for high silicon steel [35][37]. The relative permeability was shown to increase slowly below 3%wt silicon, then increase rapidly reaching a maximum of 29,000 at around 6.5%wt silicon content before it drops [35]. The magnetostriction decreases rapidly along the <100> axes with increasing silicon content, while it increases slowly along the <111> axes, resulting in nearly zero combined magnetostriction for 6.5wt% silicon steel [48][63]. The saturation magnetization, however, decreases with increasing silicon content, reaching ~1.8 T at 6.5wt% silicon [35][37].

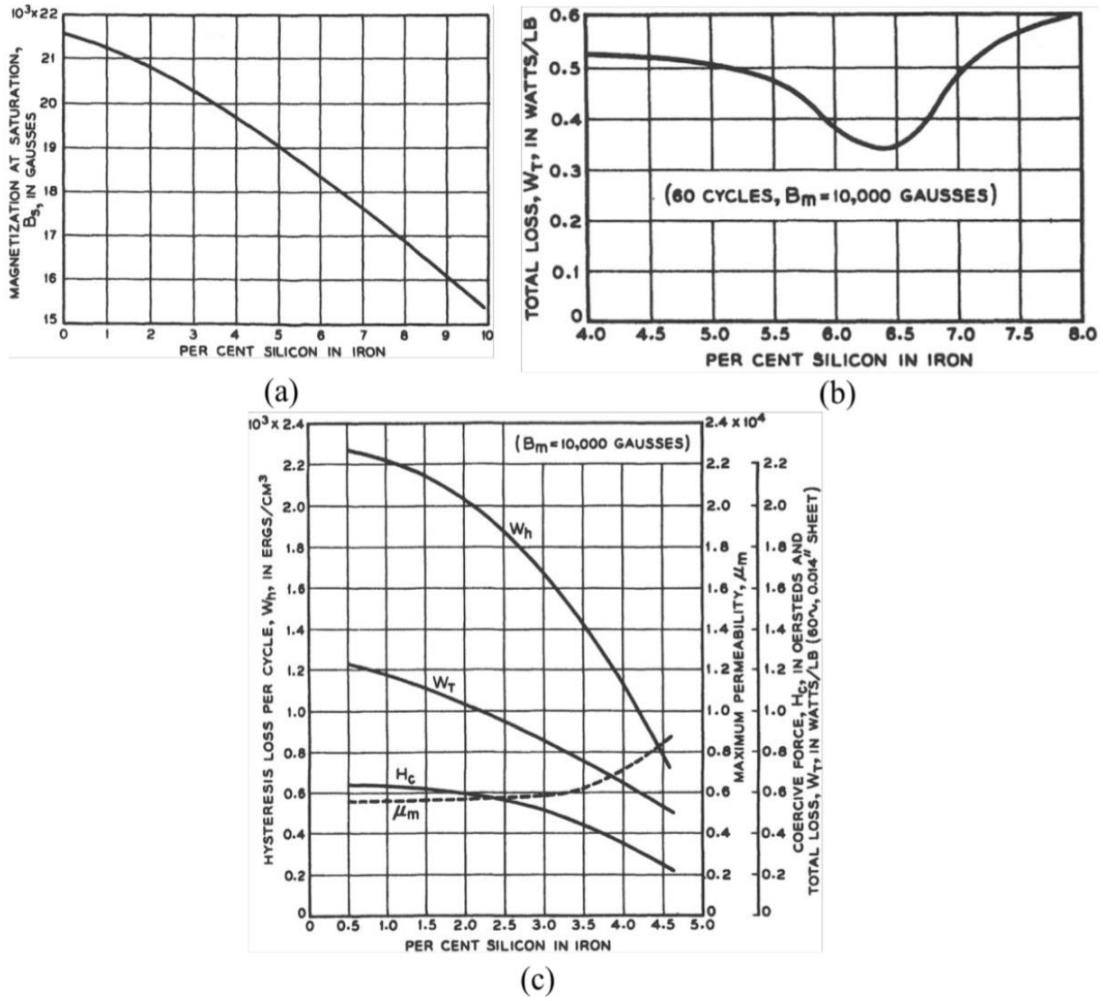

Figure 2-13: Effect of silicon content on several magnetic properties as presented by Bozorth [35], a) saturation magnetisation, b) total losses at 60Hz, c) permeability (μ_m), coercivity (Hc) and hysteresis loss (W_H)

2.5.2 Mechanical Properties

Steel becomes more brittle with increasing silicon content due to the formation of ordered phases. Bozorth in his work [35], also presented the impact of silicon content on the mechanical properties of Fe-Si alloys . Based on his findings, yield and tensile strength increase until 4.5wt% Si and above that, they decrease rapidly (Figure 2-14). Importantly, ductility tends to 0 in the vicinity of 5% Si. Because of the brittle nature of high-Si steels, processing this material (e.g., by rolling and punching) becomes extremely challenging. Therefore, practically all-commercial Fe-Si cores contain

around 3.5%w.t. Si. Tensile tests presented in [64] on annealed Fe-6.5%w.t. Si steel produced by melt spinning, suggested that the appearance of a D03 superlattice structure is responsible for the loss of ductility. The authors in this study also showed that the ductile as-quenched samples could be converted into brittle materials by air cooling or annealing, and brittle ribbons can be converted back into ductile ribbons by annealing above the B2-D03 temperature followed by quenching; this further supports the argument that D03 ordering renders the Fe-6.5%w.t. Si steel brittle.

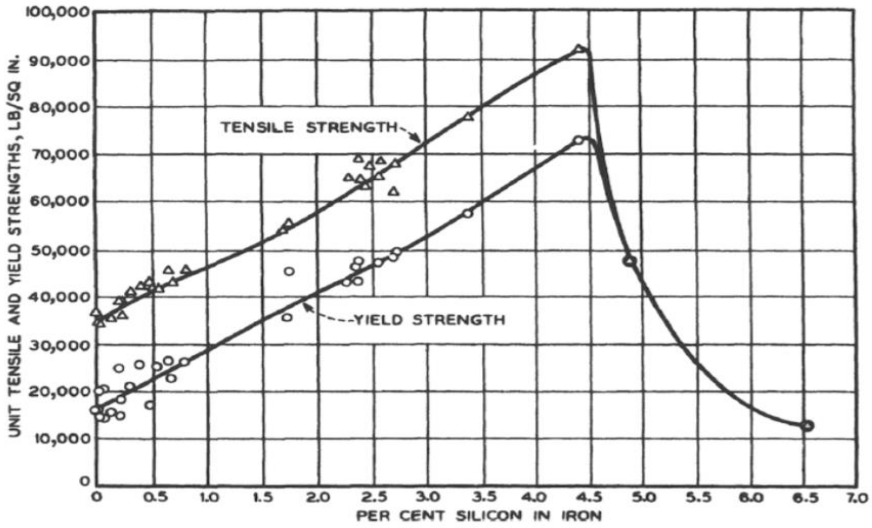

Figure 2-14: Effect of Si content on the mechanical properties (tensile and yield strength of Fe-Si alloys with increasing silicon content[35]

2.5.3 Micro-hardness

By increasing Si content in steel, the hardness and brittleness also increase and the processing of thin sheets below 0.5 mm by cold rolling becomes almost impossible for Si-content of over 3.5wt%. J. Shin et. al in [55], studied the hardness of silicon content between 5-6.5wt% by micro/nano-indentation tests with respect to composition and heat treatment conditions (Figure 2-15 (a)). They found that Vickers hardness varied linearly with silicon content and it was not influenced by heat treatment conditions. Two

empirical equations were established; for high silicon steel (more than 6%a.t.) equation 2.1 was used and for low (less than 6%at) silicon steel, equation 2.2 was validated.

$$HV = -112 + 41.1 \text{ at\% Si} \qquad (2.1)$$

$$HV = -59.9 + 24.3(\text{at\% Si})^{2/3} \qquad (2.2)$$

Moreover, in the high Si content range, the short-range order in A2 disordered phase caused a comparable hardness to that of the B2 ordered phase. Therefore, the micro-hardness should remain roughly the same irrespectively of the amount of ordered or disordered phases in the alloys. Garibaldi et. al. [65], presented the evolution of Vickers micro-hardness (HV) with increasing laser energy input for Fe-6.9%wt Si soft magnets, processed via LPBF, before and after stress-relief at 700 C for 5 hours (Figure 2-15(b)) [65]. Although the HV was not affected by the processing parameters, the stress-relief process caused a significant increase of HV in the high silicon steel samples. The observed increase of approximately 15% in HV following the stress-relief treatment, was attributed to the redistribution of the Si-rich micro-segregates as there was no direct evidence of phase ordering.

F. Faudot et. al. in [66], presented the effect of annealing temperature on micro-hardness (Figure 2-15 (c)). A noticeable difference in HV was found with an increase in hardness when the ordered structure DO3 was present in the alloy.

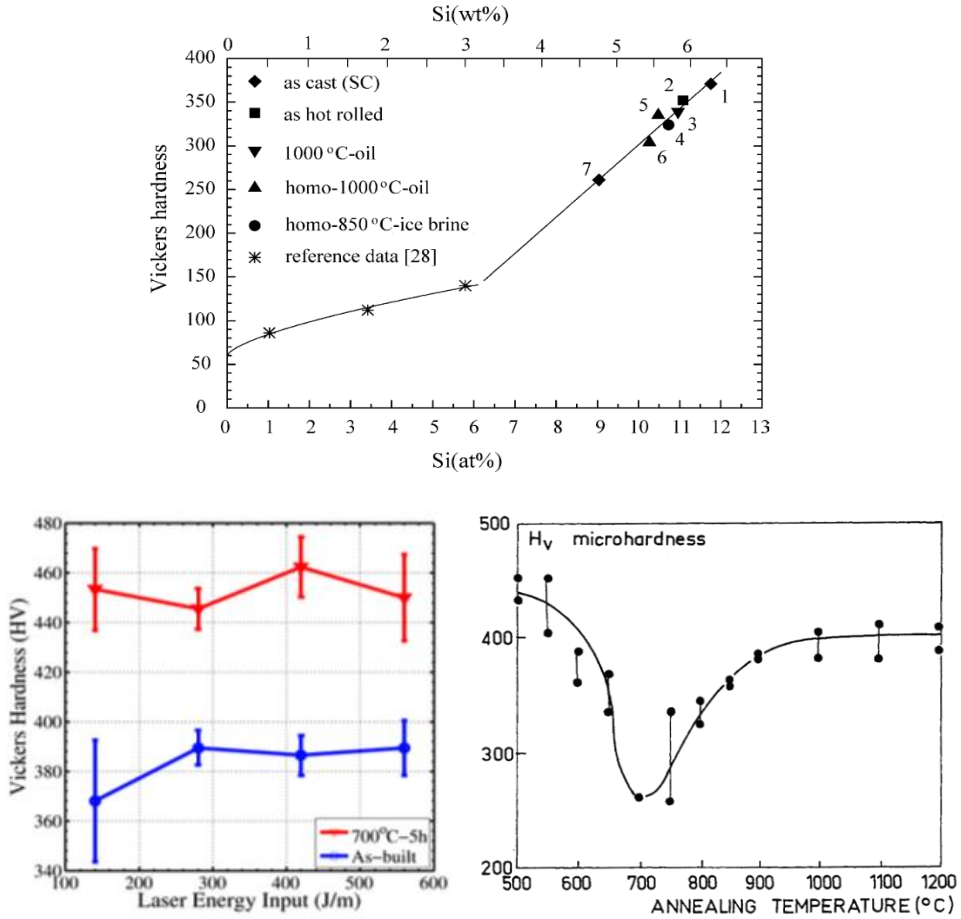

Figure 2-15: a) Effect of Si content on Vickers Hardness of high-silicon steels with various heat treatment conditions [55], b) hardness evolution with increasing laser energy density for as built and stress relief Fe-6.9wt%Si [65] and c) effect of annealing temperature on microhardness silicon content on Vickers Hardness [66]

A change in the slope of the curve shown in Figure 2-15 a), occurs at around 5%wt of silicon that corresponds to ordering (Figure 2-16). For pure iron the density is higher than 7.85 g/cm^3 and a linear decrease is observed with silicon addition up to 5wt% Si and a density of 7.55 g/cm^3. Fe-6.5wt% Si has a density of 7.48 g/cm^3 [35]. It must be noted that the density decreases less rapidly when the silicon content exceeds 5wt% and a break in the line is noticed at 5wt% where the ordering-disordering transformation occurs.

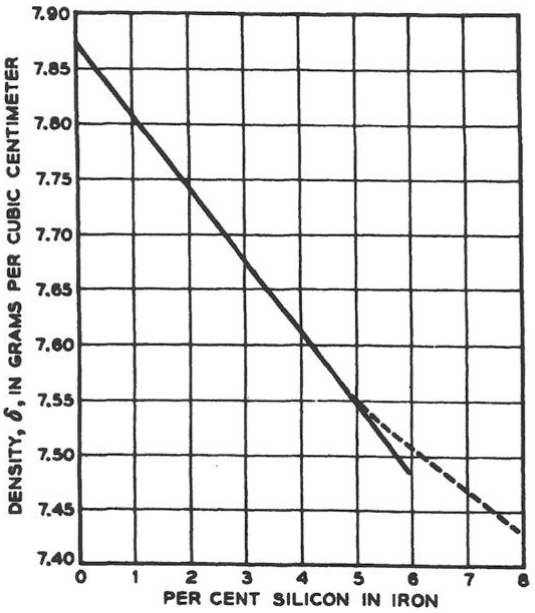

Figure 2-16: Effect of Si content on the density of Fe-Si alloys the break between the solid and dashed line corresponds to order-disorder transformation [35]

2.5.4 Electrical Resistivity

The addition of silicon in steel rapidly increases the electrical resistivity of silicon steel that results in lower eddy current loss and higher efficiency [35]. The electrical resistivity of 6.5wt% Si steel is 82 μΩ-cm, while that of pure iron is 10 μΩ-cm [32][35]. In [67][68] the authors found that Si addition increases the electrical resistivity linearly with a coefficient between 11.62-12.785 μΩ-cm per w.t.% for silicon between 0.15–2.2 w.t.% silicon steel. The increase in resistivity is less rapid beyond 5% silicon, when atomic ordering begins to occur, and as ordering increases the resistivity reaches a maximum at 11-12% silicon and then falls rapidly to its minimum value (Figure 2-17).

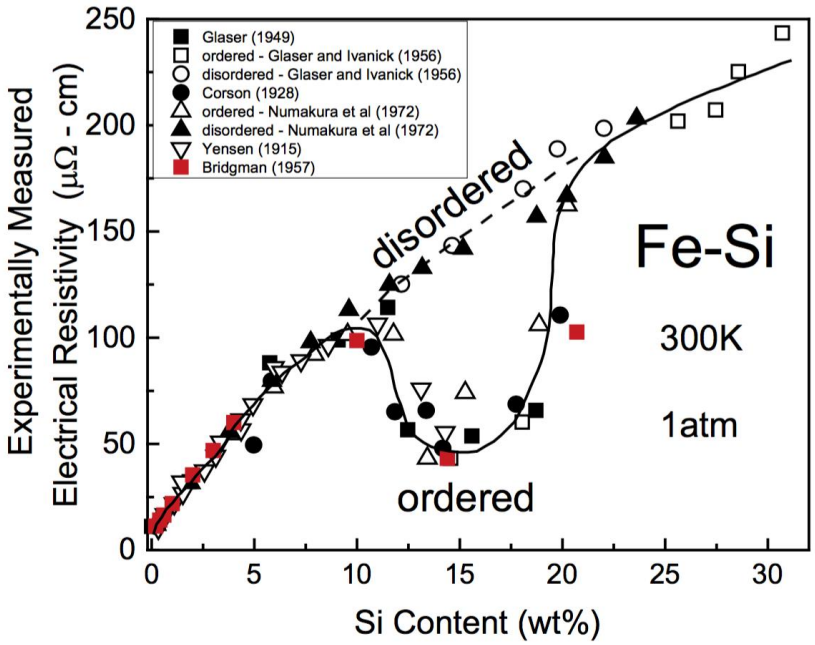

Figure 2-17: Evolution of electrical resistivity with silicon content experimentally measured from various sources also illustrating ordered and disordered phases [226]

The difference in the two trends is attributed to the order-disorder transformation in this system, which is related to the rate of cooling during sample preparation in various studies [69][70][71][72][73][74]. These studies showed that samples with 5–20wt% Si prepared by slow cooling have increased of ordering and lower resistivity than quenched samples, which have decreased ordering and higher resistivity. The change in electrical resistivity with respect to annealing temperature varies according to the order–disorder phase transitions. The magnetic properties change at three different stages with annealing temperature. The permeability reaches its maximum value and the coercivity is minimum after annealing at 850 C. The soft magnetic properties of the Fe–6.5wt% Si are improved upon annealing owing to the transformation of A2 to B2 whereby B2 domains are dispersed in the disordered A2 matrix.

2.6 Effect of post processing heat treatments

Residual stresses can have a detrimental effect on the mechanical and magnetic properties of soft magnetic alloys leading to the formation of defects. The introduction of stress will increase electrical losses in Fe-Si and several researchers investigated the relationship of deformation (in the form of both stress and strain) on the properties of electrical steel [58][75]. To minimise the impact of LPBF induced residual stresses in Fe-Si produced parts, post processing heat treatments are necessary. There are three primary effects that occur with annealing of electrical steel, namely stress and strain relief, additional grain growth, and decarburization. The magnetic properties of silicon steel consist of the complex interaction of several effects: grain size, defect number, defect size and distribution, anisotropy, ordered/disordered microstructure and residual stresses. This indicates that a compromise needs to be made when selecting heat treatment profiles for soft magnetic materials fabricated by LPBF because it is not possible to optimise all the parameters simultaneously. For example, heat treatments that could be beneficial for stress release and grain growth would also induce ordering and could eliminate favorable anisotropy. The impact of various traditional heat treatments on rolled silicon steel has been extensively studied and presented in the literature[66][76][77][78][79][80]. However, the only example of heat treatment previously reported in the literature for Fe-Si processed via LPBF is found in the work of Garibaldi et. al. [81].

As discussed earlier, when the silicon content is higher than 2%w.t. in the binary alloy, silicon suppresses the high temperature γ phase of Fe (austenite fcc phase), thus the alloy is ferritic (α or bcc phase) at all temperatures enabling higher annealing temperatures from 1000 to 1200^{o}C. To remove residual stress, temperatures between 700-800 C were

employed in [82] and temperatures between 1100-1200 C for annealing in [83]. S. Nakashima et. al, found that increasing the Si-content from 3 to 3.7% in commercial electrical steels can retard recrystallisation and grain growth [84]. In high-Si steels, grain-growth retardation has also been observed and was attributed to the onset of ordering by Faudot et. al [66]. The ordering reaction during various thermal treatments was investigated and it was concluded that the ordering effect for rapidly quenched Fe-6.5wt% Si alloys is insignificant with regard to grain size. Garibaldi et. al. in [81], after processing Fe-6.9wt%Si by LPBF, found that heat-treating samples for 5 hours at 700 ^{o}C is the required dwell time period and temperature necessary for the removal of residual stresses. The same authors also investigated the effect of the annealing temperature on the microstructural evolution and magnetic properties of high-silicon steel processed via LPBF. For an annealing treatment of 1100 C for 1 hour a recrystallized isotropic microstructure was obtained with grain sizes up to 300 μm and a maximum relative permeability of 24000 and coercivity of 16 A/m, as shown in Figure 2-18. The same authors compared the magnetic properties and losses of Fe-6.9wt% Si processed by LPBF to commercial grade of 0.1mm thick lamination (namely JNEX by JFE steel). They concluded that the eddy current loss component does not increase significantly with grain growth and that annealing does not alter significantly the <001> texture induced by LPBF along the build direction.

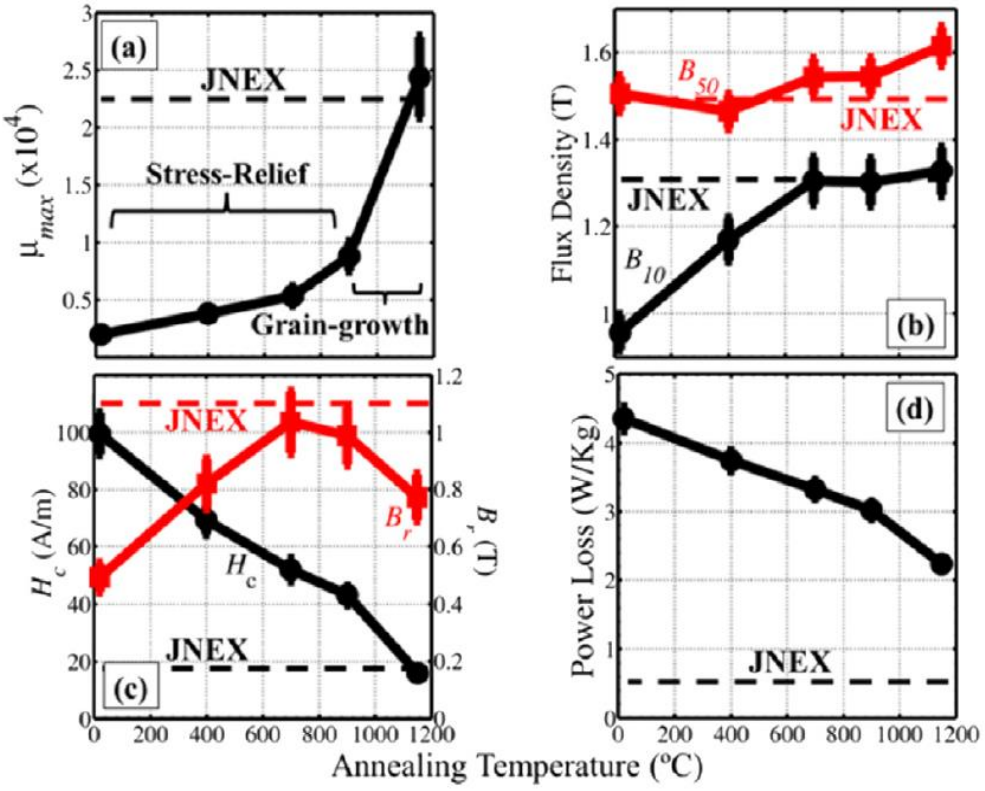

Figure 2-18: Annealing effect on magnetic properties and losses of Fe-6.9wt% Si processed by LPBF in comparison to commercial grade of 0.1mm thick lamination namely JNEX by JFE steel. a) Maximum permeability for an applied field of 1000 A/m (B_{10}), b) flux density, c) coercivity where the red line represents the remanence and d) power losses evolution with annealing temperature. [81]

Z. Zhang et. al. in [85] investigated the cooling process of electrical steel with the use of three quench media to suppress ordering transformations. The cooling rates of oil, water, and salt water (10% NaCl) were found to be 74, 304, and 375 C/s respectively. A remarkable decrease of the precipitated phase with increasing cooling rate and plasticity was found for an oil-quenched sample The faster cooling rates resulted in a reduction of the ordered region, but it is important to note that very high cooling rates resulted in larger residual tensile stress, which in effect, counteracts the ductility gained by lowering the degree of ordering.

The impact of the annealing atmosphere on the magnetic properties of Fe-Si was shown by S. C. Paolinelli [86]. The interaction of the steel surface with the annealing

atmosphere caused nitridation and/or oxidation of the metal. According to the findings by C. Bolfarini et. al.[87], grain size appears to be the key factor controlling the magnetic properties of Fe-6.5%w.t. Si sprayed formed alloy. However, there are optimum grain sizes for each frequency that give a minimum core loss the different effects of the grain size on the hysteresis losses and the classical eddy current losses, which are the primary component in total losses, must be taken under consideration. The heat treatment applied to Fe-Si alloys must be application specific and there are optimum grain sizes that will result in minimum core loss for each frequency [77,88]. Higher heat treatment temperatures would lead to larger crystal grain size and hysteresis loss decrease that would effectively increase eddy current losses [89].

Besides residual stress, ordering in Fe-Si alloys can have detrimental effects and several fast-quenching methods have been investigated in the literature as an attempt to suppress the ordering transformation. Ordering – disordering transformations of rapidly solidified Fe-6.5wt%Si were investigated in [90] and a strong dependence of ordering on the cooling rate was presented. The effect of cooling rate on Fe-6.5wt%Si-0.05wt%B alloy was presented by H.D. Fu et. al. [61]. Rapid oil quenching reduced the growth of boron-rich precipitates that are harmful to the mechanical properties. It appears that rapid cooling can suppress the formation of D03 and reduce the size of B2, but cannot completely suppress the B2 ordering. A summary of the relationship between known cooling rate and the resulting ordering is shown in Figure 2-19.

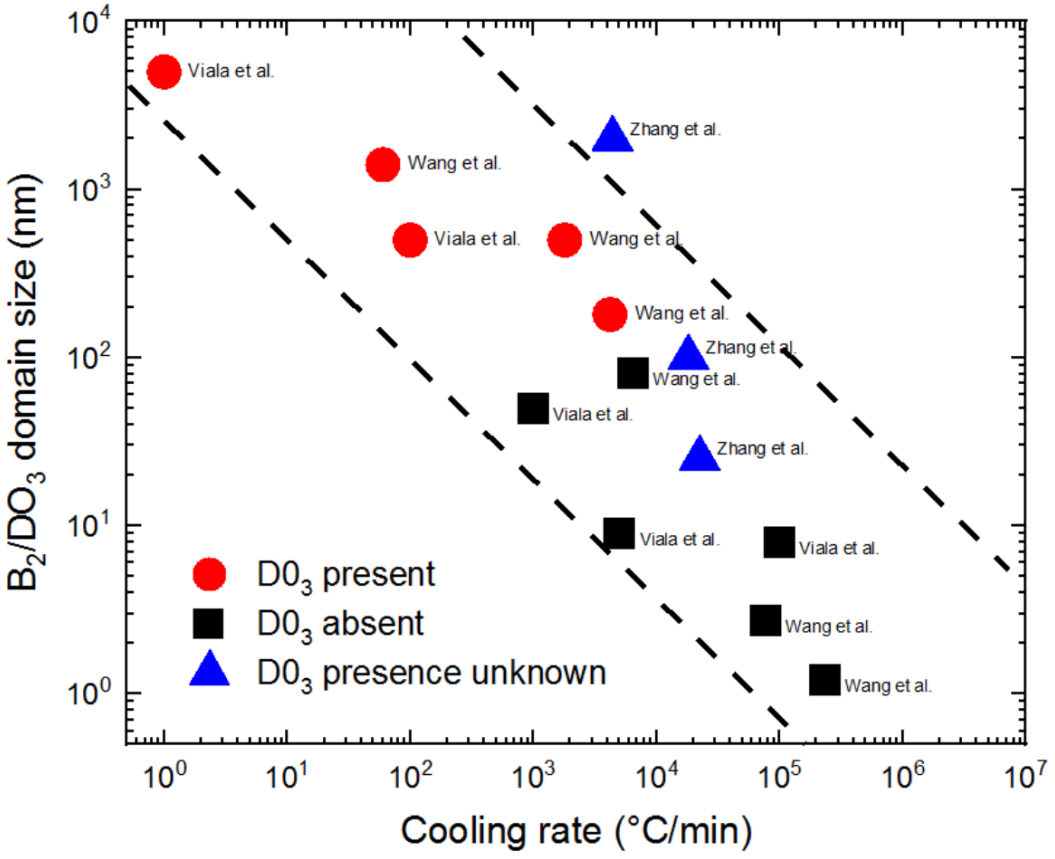

Figure 2-19: B2/D03 ordering as a function of cooling rate. Red circles indicate the presence of D03 phase, and black squares indicate the absence of D03 phase. The presence of D03 is unknown in the case of blue triangles [85][91][92]

2.7 Soft Magnetic Core Losses - Iron Losses

In addition to the magnetic values, the "iron losses" of soft magnetic materials are another key factor for electrical machine manufacturing, material screening and operation. All electric motors experience rotational losses during the conversion of electrical to mechanical power. These losses are generally categorised as magnetic losses or also known as core/iron losses, copper losses from the windings, brush losses and stray losses. Lower iron losses can be beneficial for machine efficiency while reducing thermal cooling requirements of the motor. Iron losses are comprised of the hysteresis loss due to the change in magnetisation and the eddy current loss from induced voltages

in the electrically conducting magnetic material. Losses in an electric motor can be classified as shown in Figure 2-20.

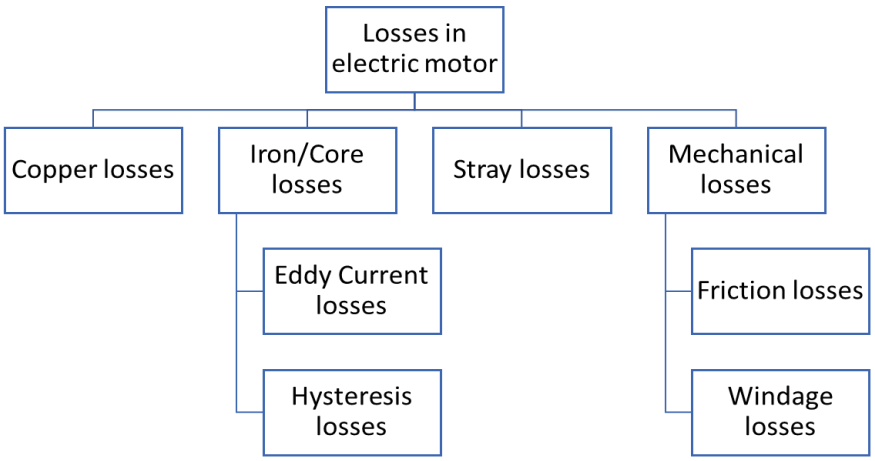

Figure 2-20: Classification of the various types of losses in an electric motor

Hysteresis loss is caused by the magnetisation and demagnetisation of the core as current flows in alternating directions. As the magnetising force increases, the magnetic flux increases. But when the magnetising force (current) is decreased, the magnetic flux decreases less gradually causing, a hysteresis. Therefore, when the magnetising force reaches zero the flux density still has a positive value. In order for the flux density to reach zero the magnetising force must be applied in the negative direction. The area of the hysteresis loop shows the energy required to complete a full cycle of magnetising demagnetising and the area of the loop represents the energy lost during this process. The loss, i.e., wasted energy, is mainly dissipated in the form of heat and determines the various grades and prices of silicon steel. Considerable research and development resources have been consequently applied to electrical steels, which are used to build soft magnetic cores, towards lower core losses, because even small improvement contributes to significant economic and environmental benefits [40]. Core losses in silicon steel have seen significant decrease over the last century. The loss has been

reduced very close to the theoretical value of 0.4 W/kg from the initial 15 W/kg at 1.5 T under 50 Hz AC magnetization [43]. The power loss can be expressed as the sum of three parts in the following:

$$P_{total} = P_h + P_e + P_a \qquad (2.3)$$

where, P_h is the hysteresis loss; P_e is the classical eddy current loss; P_a is the anomalous loss. The first part hysteresis loss P_h is proportional to the area of the static hysteresis loop and the frequency. Hence, P_h is a material characteristic and a function of the peak flux density. The well-known Steinmetz hysteresis loss empirical formula was first proposed in 1892 [93], and calculated by (2.4):

$$P_h = f k_h B_{pk}^n \qquad (2.4)$$

where f is the AC magnetisation frequency, k_h is the constant for the material, n is called the Steinmetz exponent and it was originally taken as a constant 1.6 by Steinmetz. In 1926, C. Webb found that exponent n varies a lot with the flux density [94]. The second part P_e (classical eddy current loss) is related to the loss caused by eddy currents induced by the main flux B. The classical eddy current loss for a constant permeability can be calculated from (2.5):

$$P_e = \frac{\pi^2}{6\rho} d^2 f^2 B_{pk}^2 \qquad (2.5)$$

where ρ is steel lamination resistivity and d is the thickness of the lamination. Building the core from a stack of thin laminations with high resistivity restricts the flow of eddy currents and reduces P_e. The third part, P_a is the anomalous loss (or excess loss), because it was found that there is always a difference between the measured specific power loss and the sum of theoretical calculated hysteresis loss and classical eddy current loss. This

anomalous loss was not explained well until the domain wall model (Figure 2-21) was proposed by Pry and Bean in 1958 [95]. Pa is thought to be proportional to the domain wall spacing 2L and inversely proportional to the sheet thickness d.

Figure 2-21: Diagram of domain walls for anomalous eddy current loss as presented by Pry and Bean

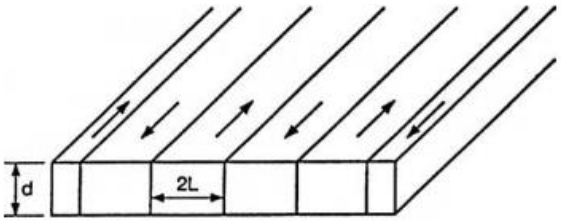

Further extension of the anomalous loss study following Pry and Bean were presented in [96][97], which can be simplified using (2.6), where ka is the material constant

$$P_a = k_a f^{1.5} B_{pk}^{1.5} \qquad (2.6)$$

The three components of the total core loss can thus be separated if the total specific core power loss curves at various frequencies are measured. The separated power losses will benefit the prediction of the specific power loss and the transformer core loss modelling for the future studies using the finite element method. The current popular power loss separation algorithms, based on the four equations (2.3), (2.4), (2.5), and (2.6), were not tested on the latest commercial GO steels, and particularly there was little measurement data at high flux densities [98].

In [99] the effect of silicon content on the iron loss of grain oriented electrical steel sheet was studied. With the addition of silicon up to 6.5 mass%, it was shown that the iron loss is decreased (Figure 2-22 (a)).

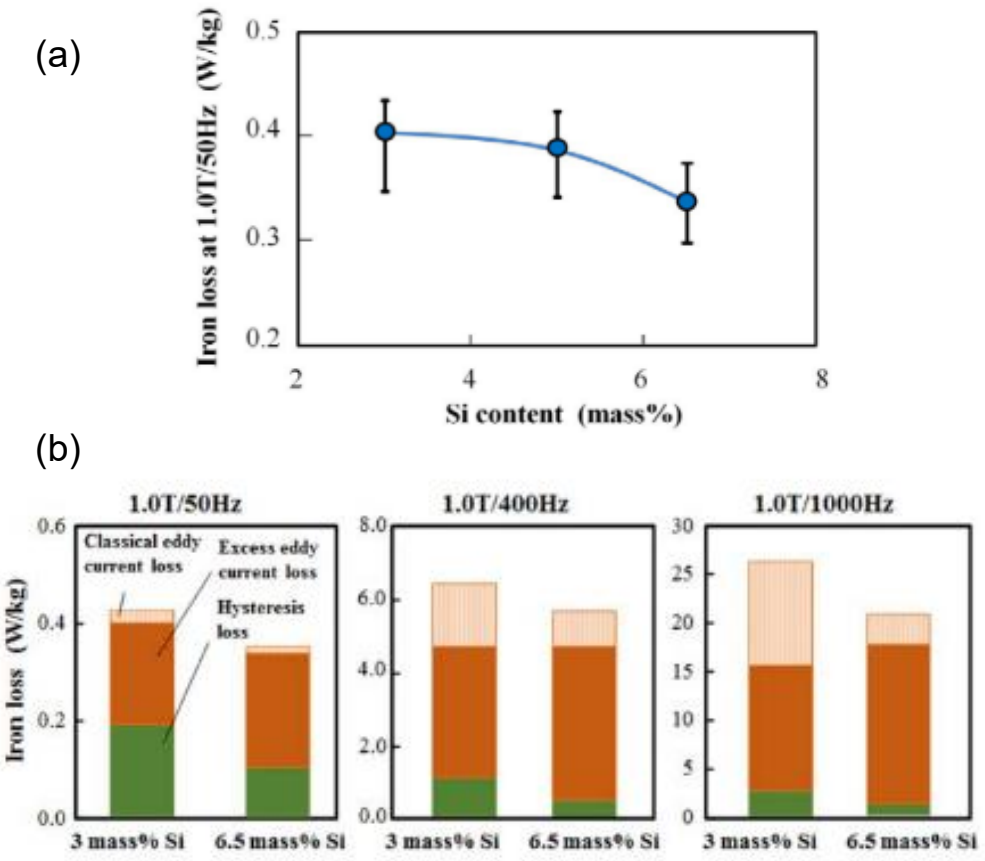

Figure 2-22: Effect of silicon content on a) iron loss, b) hysteresis and eddy current loss for 3% and 6.5% silicon steel [99]

At the same time, the hysteresis loss decreased drastically to almost half of that at 3 mass %, but the eddy current loss, measured at 50 Hz, increased slightly (Figure 2-22 (b)). This small increase in eddy current loss was attributed to the increase of the magnetic domain width for 6.5wt% silicon content in the alloy. Eddy current losses are resulting from Faraday's law, which states that any change in the environment of a coil of wire will cause a voltage to be induced in the coil regardless of how the magnetic change is produced. Thus, when a motor core is rotated in a magnetic field a voltage or

electromotive force (EMF) is induced in the coils. This induced EMF causes circulating currents to flow and these are referred to as eddy currents. The power loss associated to these currents is known as eddy current loss. The motor's soft magnetic cores use many thin pieces of iron referred to as laminations with insulation coating in between, with the resistance of individual pieces stacked together being higher than the resistance of a single solid piece. This higher resistance reduces eddy current losses and the insulation prevents eddy currents transferring from one lamination to another. The difference in Eddy currents between a solid and a laminated core is shown in Figure 2-23.

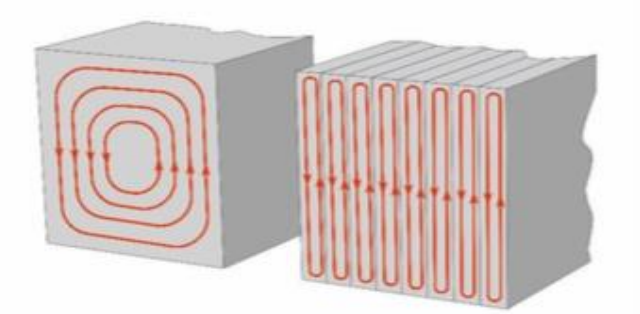

Figure 2-23: Schematic illustration of eddy currents in soft magnetic laminated core in comparison to bulk solid core.

2.7.1 Reduction of losses in soft magnetic cores via LPBF

The reduction of eddy current losses in soft magnetic cores is one of the main challenges in the production of high-performance electric motors and generators. In [100] several concepts that could result in a reduction of eddy-current losses and good magnetic performance were presented. Instead of the electrical insulation traditionally used between soft magnetic metallic sheets, additive manufacturing can offer alternative options such as separation by air gaps (slits). The authors presented complex topological structures with slits (Figure 2-24(a)) that caused disruptions of the electrical current paths and effectively reduction of eddy currents. They confirmed the results with finite element analysis (Figure 2-24 (b)).

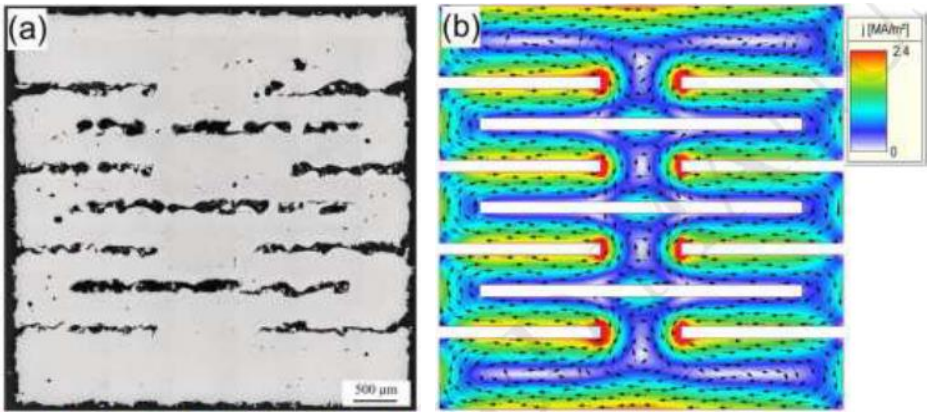

Figure 2-24: a) Cross section of a ring composed of four slits at the internal and external side of the ring and additional three slits in the volume of the ring, b) Finite element simulation of eddy currents.

In a concept similar to stacks of laminations, where electrical insulation is used between the soft magnetic strips, a multi-material approach was proposed by D. Goll et. al. [100]. In this concept, layers of Fe-6.9wt% Si with large saturation polarization were alternated with layers of soft magnetic FeAl16 featuring a higher specific electrical resistivity to limit eddy current losses to single layers (Figure 2-25).

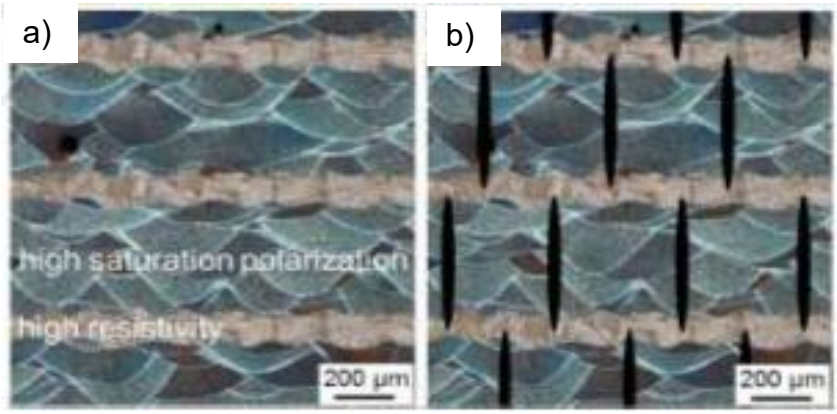

Figure 2-25: Concepts for the reduction of eddy current losses of soft magnetic cores by LPBF [100], a) multi-material layered structures to design and control electrical path length and magnetic flux, d) combination of microstructurally induced slits (air-gaps) with multi-material approach

The multi-material approach to solve the increased eddy current losses in solid bulk soft magnetic cores seems very promising but is currently limited, due to technological constraints, which impose single material usage in commercial LPBF systems. However,

LPBF offers the flexibility of tailored processing parameters, according to each material, allowing for a customizable microstructure, for example columnar grain orientation along the direction of the magnetic flux. LPBF can mimic the traditional stacking approach of Fe-Si laminations, while offering superior mechanical robustness in comparison to punched laminations.

In a similar study by A. Plotkowski et. al. [101], novel 3D geometries were produced via LPBF to reduce eddy current losses. The geometries comprised of parallel plates with increasing number of thin plates, a mesh structure and a Hilbert space-filling curve (Figure 2-26). A decrease in the spacing between thin walls was used to increase the stacking factor of the cross-section. However, smaller spacings resulted in unwanted electrical shorting between walls and an increase in the eddy current losses. Compared to simple parallel plate construction and a mesh structure, the cross-section design based on a Hilbert space-filling curve was found to produce the lowest power losses.

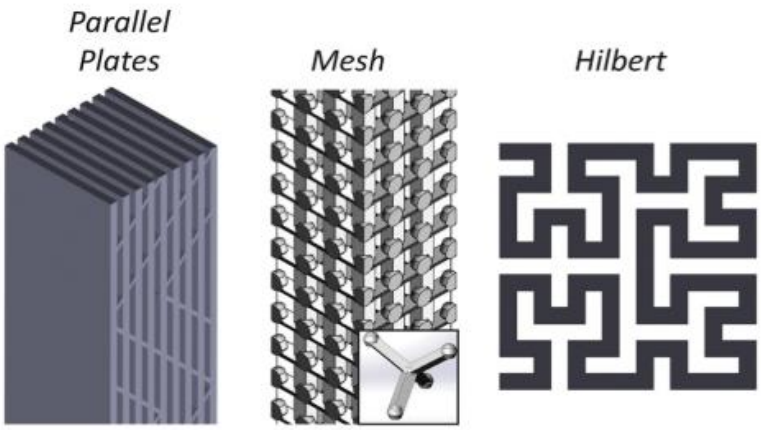

Figure 2-26: a) Schematics of novel 3D geometries for the reduction of eddy currents [101].

2.7.2 Additive Manufacturing of Soft Magnetic Cores

AM of soft magnetic materials is a relatively new research area that has attracted a lot of interest over the past few years, with efforts mainly focusing on producing near fully dense magnetic parts with magnetic and mechanical performance similar to those of conventionally manufactured magnetic materials. In other words, researchers try to develop materials that combine high magnetisation whilst minimising the hysteresis loop area that correspond to the magnetic losses of a material/component through the reduction of the intrinsic coercivity Hc. Table 2-3 lists typical magnetic properties of different types of soft magnetic materials.

Table 2-3: Comparison of properties for main Soft Magnetic Materials

Parameter	3% SiFe GO	FeSiB Metglas	Ni80Fe20 Permalloy	Co50Fe50 Permendur	MnZn Ferrite
B_s (T)	2.03	1.56	0.82	2.46	0.2–0.5
H_c (A/m)	4–15	0.5–2	0.4–2	160	20–80
P1.5T/50Hz (W/kg)	0.83	0.27		1	
P1T/1kHz (W/kg)	20	5	10	20	
$\mu_{max} \times 1000$	20–80	100–500	100–1,000	2–6	3–6
Frequency range (kHz)	3	250	20	up to 1kHz	2,000 NiZn—100,000

One of the first soft magnetic alloys that was additively manufactured by laser-based techniques such as LBPF and LENS is Fe-Ni. The specific alloy has been widely used in applications where magnetic shielding or high permeabilities are required. Custom powder blends consisting of Fe and Ni (spherical) powders as raw material were used in[106][107], where the authors produced soft magnetic parts via LPBF. They demonstrated that the processing parameters are closely related to the microstructural features and magnetic performance of Fe-30wt%Ni. Moreover, they showed that the scanning speed and the chemical composition can influence the shape and size of grains in the final AM part. Another study on Fe-Ni-based alloys (Ni-Fe-V and Ni-Fe-Mo) processed by LENS [104], concluded that both alloys feature saturation magnetisation

and coercivity higher compared to traditionally processed compositions. A Fe-Ni alloy was also processed via LENS in [105] and it was found that columnar grains with fcc crystalline structure are formed for slower scan speeds and a bcc phase was observed for faster scan speeds. Furthermore, it was shown that LENS results in higher coercivity by at least one order of magnitude in comparison to that observed for Fe-Ni processed by LPBF.

Fe-Co-V alloys are well known for possessing the highest saturation magnetisation among all magnetic materials, making them suitable for a range of applications. In [106–108] Fe-Co and Fe-Co-V was processed by LPBF and parts with a density up to 99.9% were reported. The authors did not mention the processing parameters, however mechanical properties and resistivity values were presented that were comparable to conventionally produced Fe-Co parts. For the same alloy, the authors in [109] employed LENS to fabricate parts of Fe-Co-1.5V. A pre-alloyed powder was processed under various parameter sets and the authors compared the magnetic properties of as-built versus annealed samples. A significant improvement of the coercivity and magnetic permeability was observed for the annealed samples as a consequence of eliminating residual stresses. Although there were microstructural differences between the as built and annealed samples, the crystallographic texture remained the same.

Among all soft magnetic alloys, Fe-Si has the most prominent position in the electronics industry due to its unique magnetic properties, relatively simple processability and affordable cost which makes it applicable in transformers (use of the grain-oriented FeSi), industrial motors and generators (use of non-grain oriented electrical steel). Garibaldi et al., processed high silicon steel (Fe-6.9wt%Si) by LPBF and reported several findings in numerous studies [56], [77] and[110]. The authors provided a

comprehensive understanding of the metallurgy of additively manufactured Fe-Si and they investigated relationships among laser energy input, microstructures and magnetic properties. Near fully dense parts (99.5%) were fabricated after identifying an optimum parameter set, however cracks were observed for the majority of Fe-6.9wt%Si samples. All printed samples were comprised of a single ferritic phase without phase ordering and a crystallographic <001> fibre texture. Through the introduction of post heat treatment, the authors modified the texture from fibre to cubic, which was identified through pole Figures, and they established porosity and texture as the main impact factors on the magnetic performance.

Another soft magnetic alloy of interest is Fe-Ni-Si that combines the benefits of Fe-Ni based alloys, such as magnetic permeability with low losses and higher saturation magnetisation in comparison to FeSi alloys. In [111] the authors processed Ni coated Fe-Si powders with the use of LPBF. Similarly to additively manufactured Fe-Si, alterations in the laser energy input can contribute in the elimination of porosity, however, due to the limited ductility of Fe-Ni-Si alloy, cracks were observed for higher values of energy density.

Another area of research that has attracted a lot interest, is the deposition of soft magnetic composites and characterisation of their fundamental material properties, such as permeability, losses etc. An example of this approach can be found in [112]. The authors produced complex shape soft magnets by combining polymer and magnetic powder instead of directly processing magnetic powder with lasers. ABS was mixed with stainless-steel filler that improved the magnetic properties of the printed parts but at the same time it deteriorated the mechanical properties. Additional examples of magnetic composites processed with diverse AM methods can be found in [112] and [113]

including development and characterisation of polymer formulations based on magnetic nanoparticles as well as magnetic composites produced by FDM. Combining polymers with magnetic powders degrades the magnetic performance of the resulting material, however, it paves the way for further development of soft magnets for a wide range of applications.

There have been only a handful of attempts to explore the capabilities of AM in electrical motor fabrication. In some cases, researchers have used Topology Optimisation and Finite Element Analysis simulations to investigate new prototype designs of electric motors [114][115]. Despite the fact that several claims have been made for a fully functional 3DP electric motor, there is still no evidence of an additively manufactured motor due to lack of performance from the materials available, risks associated with high acceleration, costs and limitations in manufacturing capabilities. This research is aiming to fill this gap in literature by presenting the experimental results of a 3D printed SRM rotor tested under different conditions.

In [116] the authors used LPBF to process H13 steel powder in order to produce a lightweight rotor prototype for a permanent magnet machine. The rotor in this study successfully demonstrated the ability of AM to produce the active parts of a motor with decreased weight (Figure 2-27 (a)), however, the steel alloy did not display soft magnetic behavior and its permeability was lower than expected. In [117], high silicon steel was processed via LPBF and topology optimisation was used to create an innovative design for a rotor intended for a PMM (Figure 2-27 (b)). The authors investigated in depth the metallurgical effect of the processing parameters on the microstructure and magnetic properties of 6.9%w.t. FeSi.

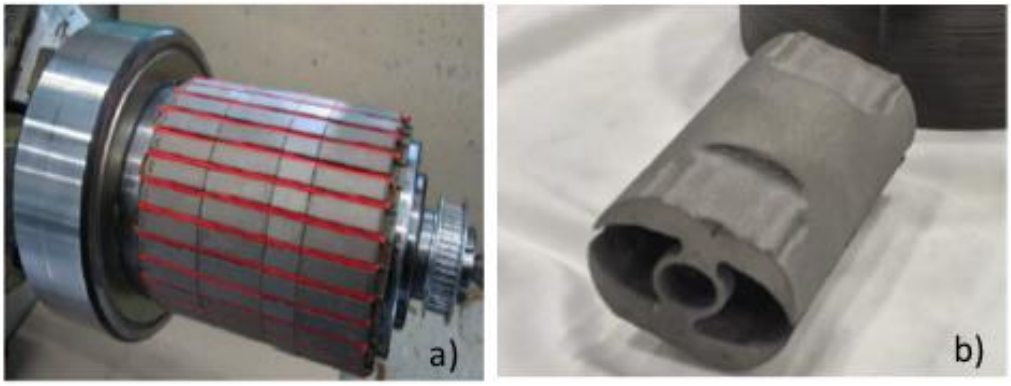

Figure 2-27: PMM rotors manufactured via LBPF a) soft magnetic rotor [227] and b) topology optimised rotor manufactured from Fe-6.9wt% Si [117].

In a study published by the VVT Technical Research Centre of Finland [118][119], an optimised SRM rotor was made from a custom Fe-Co-V powder blend. This soft magnetic alloy was processed to a maximum density of 99.9% and a magnetic saturation flux density value of 2.3T was achieved. This is the only example of an AM technology using Fe-Co for the production of a rotor as shown in Figure 2-28 a). In the same context, the authors in [120] produced a rotor for an SRM via LPBF using a maraging steel alloy as raw material. The elemental composition of the powder in this study included roughly 18% nickel, 9% cobalt and 5% molybdenum in w.t. %. As seen in Figure 2-28 b) the design of the rotor incorporates complex features such as 5% continuous skew and a rib feature which contributes in the reduction of torque ripple and windage loss. In [8] the potential of additively manufactured electrical machines used for more electric aircraft (MEA) was discussed. In terms of application, AM motors might be implemented in the aerospace sector due to the need for electrified aircraft and reduction of emissions.

Figure 2-28: Two rotor prototypes produced through LPBF a) Prototype rotor for low torque ripple of 6/4 SRM manufactured from a custom Fe-Co-V powder blend [119], (b) Asymmetric skew rotor made of maraging steel alloy with rib structure and pole slots for reduction of torque ripple [120]

The increased demand in terms of lightweight machines with increased performance can potentially be addressed by AM that has seen relative maturity to produce several aerospace and automotive structural parts.

2.8 Additive Manufacturing of Copper Coils/Windings

Copper and copper alloys are extensively used as functional materials in electronic devices and heat exchangers owing to the excellent thermal and electrical properties of the material [121][122]. The increasing demand to produce functional circuits, electronics, heat sinks and high performance devices with superior electrical and thermal properties has led to major breakthroughs in the ability to manufacture copper and copper alloy parts with several AM processes such as LPBF and Electron Beam Melting (EBM) [123–125].

However, there are some critical challenges facing the manufacturing of high-density copper parts with LPBF [126], including oxidation, need for very high power lasers (up to 1kW) due to high thermal losses [127] [128] and low laser radiation absorption [129] as well as the formation of an unstable melt pool [130]. Due to its high thermal

conductivity, copper can cause rapid heat transport away from the melt pool resulting in partial melting and insufficient interlayer adhesion. Samples produced with conventional LPBF machines (200 W laser power) typically have an average density of 83-88% depending on the laser power employed [131]. The poor densification is directly related to the low laser absorption of infrared radiation during LPBF of copper due to the wavelength dependency of the absorption coefficient [132][133].

In reality, a copper powder bed has very low absorptivity especially at infrared (IR) wavelengths (~1070 nm) commonly used in LPBF, absorbing only up to 5% of the incoming thermal energy when in flat solid form and up to 15% of the laser energy when it is in powder form depending on the temperature [134][135]. In such conditions, the powder bed reflects most of the radiation and a low amount of energy is absorbed by the powder and then transformed into thermal energy. When the laser wavelength is reduced (blue/green), copper absorptivity increases significantly and at wavelengths below 532 nm (green spectrum) it can reach values close to 40% [136] as shown in Figure 2-29.

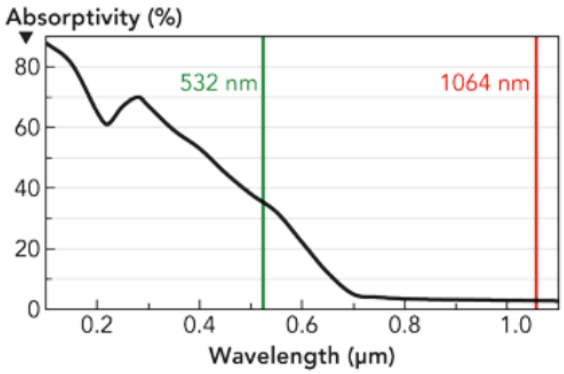

Figure 2-29: Absorptivity of IR and green wavelength laser by copper

The use of blue/green lasers has seen significant research interest [137–142] because they are much more effectively absorbed by copper. It has been shown that it is possible to increase the absorption by copper through the adoption of combined green and

infrared lasers systems, with 515 nm and 1030 nm wavelength respectively [143] . A green laser was used to pre-heat and pre-melt the material, improving the absorptivity to infrared radiation and favoring the subsequent melting by the infrared laser. The stability of copper weld tracks has also been greatly improved by using CW modulated green and IR laser beams [138]. The weld penetration depth was increased, the melt ejections were reduced, and a homogenous weld surface was achieved. Overall, an increase in absorption comes with shorter wavelengths, as the coefficient of absorption increases. In several studies, researchers used high power lasers up to 1 kW to fabricate near fully dense copper parts via LPBF [144–147].

An alternative approach to improve the ability to process copper with a laser beam is through alloying, however, elemental modification to pure copper has a negative influence on its thermal and electrical conductivity and impurities can reduce the conductivity dramatically as shown in Figure 2-30. For example, Carbon Nano-Tubes (CNTs) have been added to copper powder and an improvement in the optical absorption and powder flowability was observed [148]. The Cu-CNT blend facilitated the LPBF process and as a result, reduced laser energy density led to the production of near fully dense parts (98%). However, the printed samples featured relatively poor mechanical and electrical properties. Several examples in the literature exist where alloying has resulted in specialized alloys with excellent thermo-mechanical properties that can be processed by LPBF such as the copper-base GRCOP-84 developed by NASA [122][149][150].

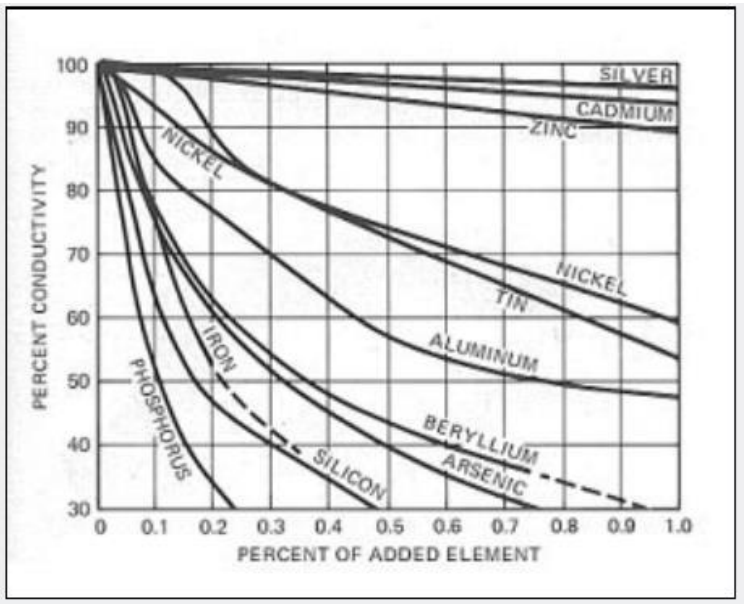

Figure 2-30: Effect of residual elements on the conductivity of pure copper [228]

Absorptivity of metallic powders is dependent on numerous parameters, including powder layer thickness, particle size and particle distribution in the powder bed, but is also affected by the temperature of the substrate and by laser scanning parameters such as laser power and scan speed [151][152]. Measuring absorptivity in LPBF is complex because the material undergoes continuous dynamic surface morphology fluctuations. In addition, several physical effects take place during laser-matter interaction, for example, multiple light reflections, energy loss by material evaporation and ablation, absorption and refraction of light by the vapor jet formed, etc. [153–155].

In most studies, absorptivity has been measured under only certain conditions, which may not be suitable for practical applications, such as large area low-laser power, or with integrating sphere reflectometers for higher temperatures [132][133][156]. For this reason, there is a need to measure the effective absorptivity of pure copper under conditions similar to the LPBF process focusing only on the energy absorbed by the substrate. An experimental method to directly measure the absorptivity using a micro-

calorimetric setup that was developed, validated and used previously in [157]. The results were in good agreement with an improved finite element simulation developed at LLNL for LPBF which depicts laser beam interaction with the melt pool through ray tracing analysis [158][159].

An area of research interest in the production of fully 3D printed electric motors is the manufacturing of highly conductive and functional coils through LPBF. Several AM methods with a varied level of technological maturity have been used to successfully process materials suitable for the fabrication of windings [160]. However only a limited number of studies have reported experimental findings on the electrical properties of the additively manufactured materials.

In this context, numerous examples can be found in the literature with the most representative example found in the literature is the work by C. Silbernagel [161][162] on copper and aluminium windings processed via LPBF. The electrical conductivity of copper is measured based on the International Annealed Copper Standard (IACS), which is an empirically derived standard value for the electrical conductivity of commercially available copper. In [162], the electrical resistivity of Cu was measured at 50.3% IACS which was better than AlSi10Mg at 30.4% IACS [161] and copper-tin alloys at 43.2% [163]. This research demonstrated the advantages of using AM for custom shaped coils for the reduction of losses. In a feasibility study [164], N. Simpson et. al. employed LPBF to fabricate a coil with the individual coil turns having a different profile as presented in Figure 2-31 This design aimed to reduce losses by balancing both DC and AC winding loss components. However, the electrical conductivity of the AM coil was found to be 51% IACS, which is significantly lower than the equivalent copper commonly used in fabricating coils. In [165], C. Wallis et. al. conducted further work

with CuCrZr and they accomplished a noteworthy improvement in the electrical conductivity of the coil material after heat treatment (75% IACS).

Figure 2-31: “Variable” profile copper coil for concentrated windings, Source: [164]

Despite the fact that casting has been used traditionally to create highly conductive coils, AM coils can offer several advantages such as freedom of geometry, increased fill factor, variable cross-sectional profiles, better surface accuracy and an improved surface finish. Usually coils produced via AM require post-processing where a coating of insulating material is applied [164]. AM of windings/coils is highly desirable because it could allow potential reduction or even elimination of various processes used in the conventional manufacturing of electrical machines.

2.9 Research Scope and Novelty

Although AM processes are being adopted by numerous industrial sectors, there is still a limited number of magnetic materials that can be successfully processed by LPBF. This is due to the different physical properties of the materials and their interaction with the laser beam. Since the main goal in this study is to produce a working, industrial-type, electric motor, ferromagnetic materials for the soft magnetic core and pure copper for the windings of the motor are the main materials of interest. In this research, the

possibility of manufacturing components via LPBF from high silicon steel alloys (Fe-5%w.t. Si, Fe-6%w.t. Si, Fe-6.9%w.t. Si) will be investigated. The only study available so far on Fe-Si [110], report parts to suffer from high degrees of in-process cracking.

To successfully manufacture a functional soft magnetic core and windings for a functional SRM using LPBF, the challenges related to processing high silicon steel and Cu must be resolved. High-silicon steel, i.e., Fe-Si alloy with Si content around 6.9%, is selected as the base feedstock material of choice, owing to its high electrical resistivity, which helps to reduce eddy currents and total losses. However, the crucial problem with high silicon FeSi LPBF parts is the type and total number of defects, mainly porosity and cracks, caused by the higher silicon content. This study evaluates how the amount of silicon content affects the ability to process the material by tailoring the chemical composition of the alloy. The effect of silicon content on the mechanical and magnetic properties of parts is assessed and the results of Fe-Si with varying silicon content are presented and compared.

Moreover, the poor workability of the alloy in conventional manufacturing techniques makes it suitable for investigating the advantages of AM over traditional manufacturing methods. As a case study, the rotor core of a switched reluctance machine (SRM) is selected as the most suitable topology because of the possibility to produce its rotor as a solid component, rather than as a lamination stack, owing to the near-static nature of the magnetic flux inside it. It is argued that the increased resistivity of the high-silicon steel selected for this research also helps counteract the eddy currents propagating across the solid component. In addition, prototype windings for the SRM are produced and their electrical and thermal performance is evaluated.

3. Chapter 3: Materials and Methods

3.1 Introduction

This Chapter presents the materials and experimental methods used with this work for the fabrication and characterisation of Fe-Si alloys with varying silicon composition and pure copper processed by LPBF. Initially, the feedstock powders and powder blends are characterised in terms of shape, size, elemental composition and flowability. The overall methodology covers the investigation of processing the materials of interest via LPBF and analysing functional properties such as electrical resistivity and magnetic properties. At first the ability to process the materials is evaluated and an extensive parameter optimisation study is presented in the respective Chapters. Mechanical tests and microhardness tests were conducted in order to ensure that the final Fe-Si parts used in the EM are robust enough to be functional and measure their performance. In order to compare the magnetic performance of Fe-Si alloys processed by LPBF to hot-cold rolled silicon steel manufactured conventionally, magnetic tests were performed and the magnetic properties were analysed. The impact of silicon content on the electrical resistivity was also measured to determine its effect on material performance and rotor efficiency. Thus, a description of the AM equipment, the various samples and methods of testing is carried out. Finally, the experimental equipment and methodologies used for in-situ absorptivity measurements, electrical, and magnetic.

3.2 Material Characterisation

3.2.1 Cu Powder

Samples of gas atomised copper powder were obtained from ECKA Granules GmbH (Germany). A number of other suppliers were contacted, however only ECKA met all

the requirements for high copper purity (99.5%+), availability and reasonable price. A gas atomised powder named 'ECKA Copper AN' was purchased which had a phosphorus content <0.05%.

3.2.2 Fe-Si powder blends

In this study Fe-Si powder blends with varying silicon content were used as feedstock material. A gas atomised pre-alloyed Fe-Si powder with approximately 6.9%wt Si was supplied from LPW Technology Ltd., Runcorn UK. The selected powder presents a Si content that is slightly higher than the ideal 6.5% for electromechanical applications as shown in Chapter 2. While the additional Si content is expected to cause a decrease in both magnetisation at saturation and ductility, it also causes an increase in electrical resistivity, which should minimise dynamic losses. This is deemed necessary in light of the final goal of the present research, which is to build an electrical machine rotor core as a solid component rather than in laminated form. However, based on the findings from [108], it was shown that it is possible to successfully process Fe-Si with such a high silicon content and produce small, nearly fully dense crack-free samples and demonstrated the influence of processing parameters and heat treatment on microstructure development. However, when the same pre-alloyed Fe-6.9%w.t. Si powder was used to fabricate parts that were larger than 10x10x10mm it was very hard to fabricate parts without cracks. Different laser scan strategies were used and various support structures including custom made supports were applied to slightly larger parts. All the above-mentioned solutions combined with maximum substrate temperature (170^{o}C) were employed in order to minimise residual stresses. Despite the efforts and the repeated attempts to build high Fe-6.9%w.t. Si it was impossible to build crack free parts.

For this research, the chemical composition of the soft magnetic alloy was changed to reduce the silicon content to increase ductility and reduce the risk of ordered phases. Therefore, the pre-alloyed high silicon steel powder was mixed in a tumbling mixer with a gas atomised high purity Fe (99.9%) supplied from Sigma-Aldrich. The Fe powder was chosen for its high purity and particle size. Three blends of Fe-Si alloy were produced with Si in concentration of 3.5%wt, 5.0%wt and 6.0%wt respectively. Prior to powder mixing, particle size distribution, apparent density and flowability of the powders were determined. Each measurement was repeated three times to ensure accuracy of the results. The mixing method and the particle size distribution can affect the flowability and can have a large impact on the quality of the powder layer deposition and melting behaviour [166]. In [167,168] R.M. German reported the beneficial effects of bimodal distributions of powders and in [169] A.B. Spierings it was showed that the flowability and packing density of powder layers can be improved with the use of bimodal powders. The main properties of bimodal powders include improved surface finish by having the small grains fill the voids among the large grains and increased packing density for the same reason. The powders were mixed for 10 minutes to achieve homogeneity. According to [170] the accuracy of the degree of mixing powder blends can be decreased if the mixing time is over 10 minutes due to particulate agglomeration and segregation. Good packing density can be restrained, thus decreasing the thermal conductivity in the powder bed and consequently decreasing density of the final parts. The average size of the particles and their distribution was determined using a Mastersizer 3000 (Malvern, UK) that uses laser diffraction to measure the intensity of light scattered as the laser beam passes through a dispersed particulate sample. The scattering pattern produced is then analysed to calculate the size of the particles [171]. To evaluate powder morphology and the microstructure of the as built samples a

scanning electron microscope (SEM) with a 20kV accelerating voltage was used (XL30, Philips, Netherlands). With regard to the chemical composition analysis, an energy dispersive X-ray (EDX) detector, which is mounted to the SEM, was used to provide analytical results of the chemical composition of the powders.

The average density of the powders was measured using a gas displacement pycnometry system (Accupyc II, Micromeritics, USA) at room temperature, running standard analysis software (Accupyc 1330, Micromeritics, USA). The pycnometer was calibrated with 10 purges of helium gas before testing the powders. The flowability of powders in LPBF process determines if the layers' thickness is consistent, thus setting the baseline for a uniform laser energy absorption in the processing area. In order to minimise the effect of moisture/humidity on the flowability, all powders were heated within a sample oven for 60 minutes at 70^{o}C before testing. The Hall flow meter test method uses gravity as a driving force to measure the time which 50gr of powder takes to flow out of the funnel. The flow-rate of the metal powder running through the outlet of the Hall funnel was measured according to [172,173].

3.3 Additive Manufacturing - LPBF Equipment

Both Fe-Si and Cu in this study were processed using a LPBF machine (AM125, Renishaw, UK) (Figure 3-1) equipped with a 200W laser (D-Series redPOWER ytterbium fibre CW, SPI Laser, UK) with a wavelength of 1070mm (±10nm) and a spot size of 20 μm (±15μm). This resulted in an average energy density of 22.1MW/cm^2 (±6.19MW/cm^2). It had a build volume of 125mm^3 with a base plate heater set to 170^{o}C, which was maintained at this temperature throughout the build process. A vacuum and argon purge were used in the build chamber in order to maintain an inert environment and keep oxygen content below a maximum of 500 parts per million (ppm). Mild steel

substrates were used for all the materials as it was found to be the most suitable material to build Fe-Si and Cu parts upon. The AM equipment selected was appropriate for processing copper due to its high laser power density resulting from a small laser spot size. To put this into perspective, a machine with a 70μm laser spot diameter (two times the size of Renishaw AM125) would need to operate at 800W laser power to achieve the same energy density.

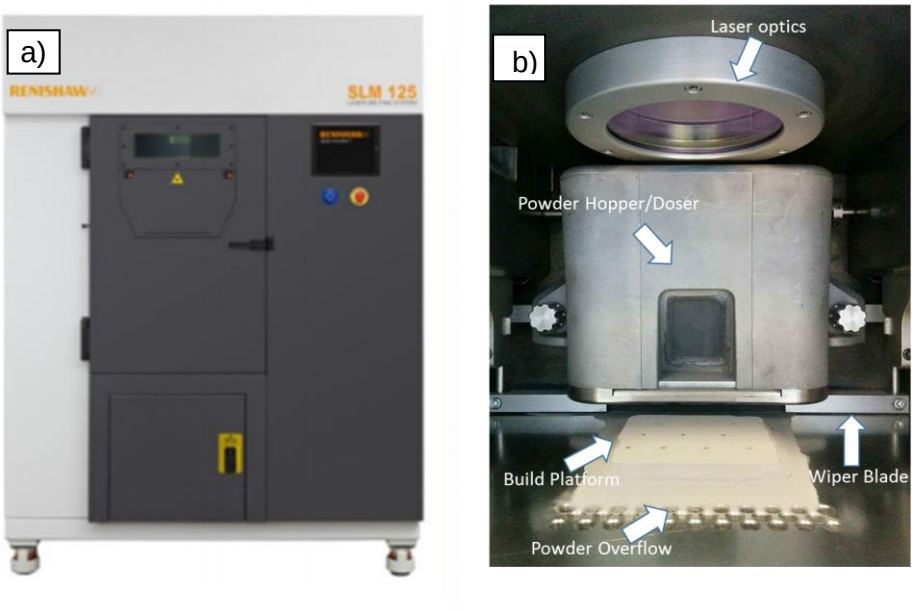

Figure 3-1: Renishaw LPBF125 machine a) exterior view, b) build chamber configuration

3.4 LPBF Process parameters

High silicon Steel and pure copper were processed in the Renishaw LPBF 125 machine and a processing parameter set was investigated for each material to optimise the density of the as-built parts. A set of parameters was reported in [108] where a Realizer SLM50 machine with a maximum laser power of 100W and a laser beam focus of 13.1 mm was employed. The process window used in one machine cannot be directly replicated by another machine that is characterised by different technical

specifications. Therefore, a new process window was defined for the Renishaw LPBF-125 machine with a maximum laser power of 200 W and a nominal spot size of 35 μm.

Table 3-1: Variables investigated to determine optimal processing conditions for silicon steel alloys and pure copper

Parameter	Value or Range
Laser power (W)	200 (maximum available)
Laser spot diameter (μm)	35 (minimum)
Powder bed temperature (°C)	170 (maximum allowable)
Laser scan speed (mm/s)	50 to 1250
Layer thickness (μm)	30, 45, 60
Laser beam focus position (mm)	-10 to 10
Hatch spacing (μm)	50 to 175
Scan strategies	Stripes, Islands, Rotation, Pre-sinter, Re-melt, Multiple Scan, Offset Hatch, Nested Contours

Pure copper has not received the same amount of attention in the past and there was a lack of process parameters for copper processed by a medium laser power machine within the range of 100-400W. An investigation into the printing parameters that would achieve the highest possible density for silicon steel and copper was necessary. The parameters that were investigated for this study are shown in Table 3-1.

Laser power is one of the parameters defining the energy density that will interact with the top surface layer of the powder. The maximum laser power of 200W was used as a starting point for all the materials in this study to ensure good wettability to the substrate and that the previously deposited layers of powder are fully melted. Laser spot diameter also influences the laser power density and was a variable that was fixed within the LPBF equipment.

Powder bed temperature was set to the maximum allowable value in order to preheat the powder and lower the energy required to melt the powder. Laser scan-speed and laser point-distance influence the length of time in which the laser interacts with the top surface of the powder. The laser scan speed in the Renishaw AM125 LPBF-machine was calculated by dividing the point distance over the laser exposure time (in μs). When a specific laser scan speed was tested, a number of point distances were also investigated. Then the laser exposure time was calculated with the use of a build preparation software (QuantAM, Renishaw, UK) to define the speed. For example, for a laser speed of 200mm/s and point distances of 50 and 100μm the exposure times would be 250 and 500μs respectively.

Layer thickness defines the amount of material that the laser needs to fully melt as well as how well the powder spreads on the powder bed. Thick layers spread well but make it difficult for a laser to fully melt, whereas thin layers are easier to fully melt but may be difficult to spread homogenously at the powder bed. Spreading very thin layers of powder evenly may be challenging due to powder particles that are larger than the desired layer thickness. Laser beam focus position adjusts the location of the focus and changes the spot diameter as well as the energy profile of the laser spot (edges of the laser become less defined). Hatch spacing influences the amount of overlap a laser weld track has with previous tracks in the same layer. An overlap occurs when the hatch distance is less than the weld track width and is desirable to ensure the fusion of adjacent tracks.

3.4.1 Scan Strategies

At the initial stages of this research study, only stripe scan strategies were used namely unidirectional and bidirectional as shown in Figure 3-2 a) and b) respectively. An extensive number of scan strategies were later tested in this study to assess their impact on density and texture as illustrated in Figure 3-2 c).

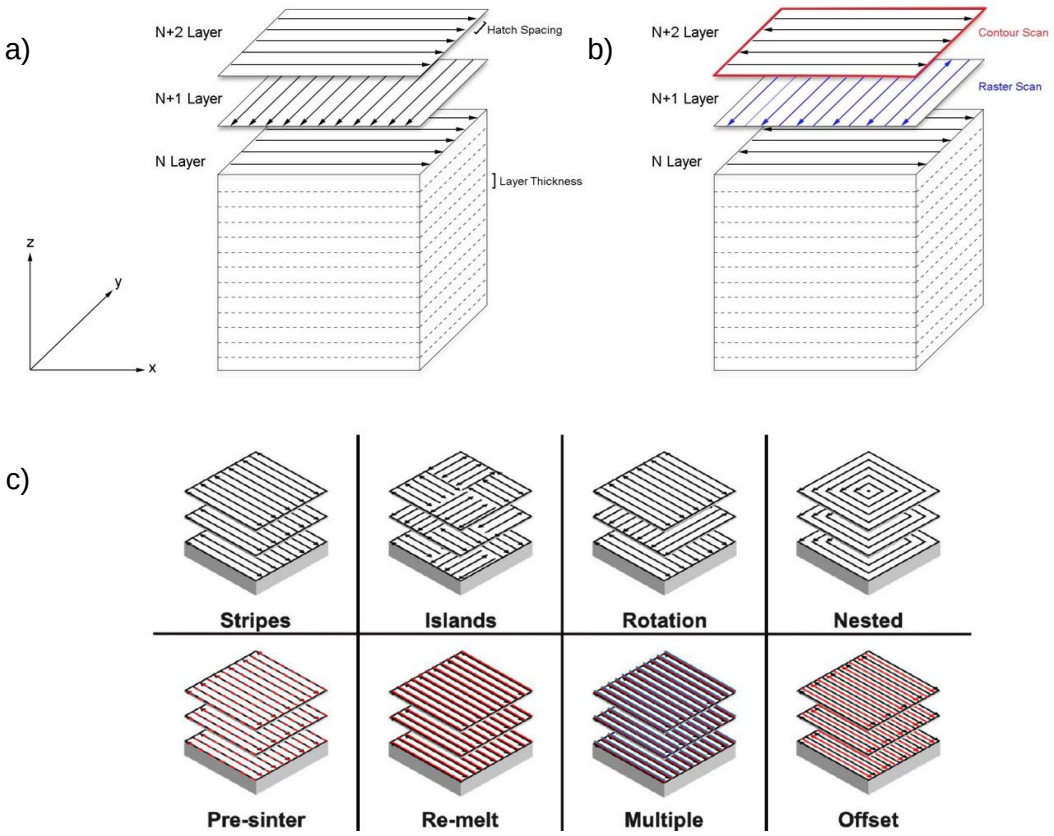

Figure 3-2: Stripes scan strategy (a) Unidirectional, (b) bidirectional scan strategy with the scan vectors scanning each layer by rotating 90o in X-Y direction and c) various single scan strategies on the top half and multiple scan strategies at the bottom half.

The various scan strategies can be divided into single scans per layer (stripes, islands, rotation, nested) and multiple scans per layer (pre-sinter with lower power first, re-melt by repeating the scan, multiple scans, and an offset scan between tracks). Rotation of the scan pattern either by 0^{o}, 67^{o}, or 90^{o} were tested with both island and rotation scan strategies. The stripes scan pattern allows long continuous tracks to be made whereas

the island pattern creates shorter clustered tracks. However, with islands being used as scan pattern the heat is more concentrated within the islands. Rotated scan patterns help even out defects from layer to layer. Nested scans attempt to maintain long tracks while also scanning close to previous scans to help reduce thermal gradients. Multiple scans per layer attempt to increase density by melting more material than a single scan can achieve. Pre-sinter and re-melting scans use laser powers less than the main scan power in an attempt to sinter the material and aid in increasing the density, as this has been shown to work with other materials such as AlSi10Mg and Ti6Al4V[21,24,174,175]. Re-melting scan strategies attempt to melt any un-melted powder particles, which may exist in areas of discontinuities or irregularities by using the same laser power and scan pattern. Similarly, the multiple scan pattern uses more than two scans per layer in addition to different laser powers per scan. Finally, the offset scan pattern focuses on attempting to melt and fuse the areas between the original scan tracks and melt any partially fused powder in this region.

3.4.2 Parameter Optimisation

The method for parameter optimisation was as follows for the two materials under investigation. First single scan tracks were fabricated to define laser power and scan speed. Next, thin walls were fabricated to evaluate the intra-layer bonding with a layer thickness being varied in the range 30-60μm at intervals of 10μm for Fe-Si and intervals of 15μm for copper. Thin walls were also used to evaluate the effect of focus position and hence spot size, on the quality of copper samples. Cubes with dimensions 5x5x5mm were then fabricated to assess hatch distance, rotation and scan strategy with respect to density and interlayer bonding. In addition, various scan strategies were used for both materials in an attempt to minimise defects and increase the density of as-built parts.

Furthermore, the scan strategies were used in order to evaluate the effect of different laser paths on the residual stresses and texture of Fe-Si. An optimum processing parameter set along with experimental results that support the findings will be presented for each material in Chapter 4 and Chapter 5 respectively.

3.5 Manufacture and preparation of Fe-Si and Cu samples

In order to investigate porosity, crack formation and micro-structural features, the manufactured cubic samples were cut along two perpendicular planes, parallel to the cube faces, horizontal (XY) and vertical along the build direction XZ (Figure 3-3). The test specimens were cross-sectioned, mounted, and polished. Metallographic preparation of the specimens was performed according to the procedure for Fe alloys and pure copper suggested by Struers (Struers AS, Denmark). Details on the grinding and polishing steps for silicon steel alloys can be found in Appendix 1. For the studies requiring the visualisation of the melt-pool boundaries and solidification structures, after the last polishing step the Fe-Si sample surfaces were chemically etched by exposing them to a solution of 2% Nital (2% nitric acid and 98% ethanol by volume) for 30s-60s. For copper samples, grain boundaries were identified using a macro-etch solution of 50mL water with a submersion into the solution for 2 seconds followed by a water rinse.

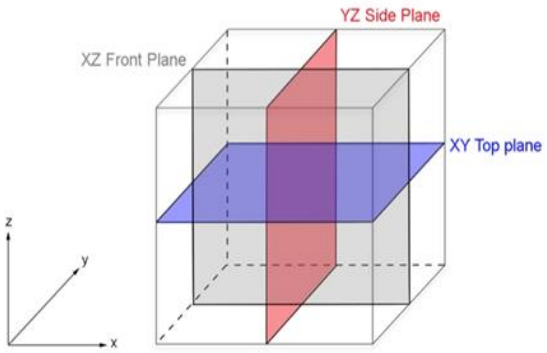

Figure 3-3: Schematic of the 3 cross sectioning planes XY, XZ and YZ for the evaluation of sample porosity

Test cube samples were ground using standard grit papers to remove scratches from the surface of the samples, polish and reveal the section of interest (Appendix 1). It was found that due to the soft nature of copper intermediate grit papers were not needed. Specimens were ground flat and polished according to Struers guide for pure copper. The steps of the grinding and polishing steps for each material can be found in Appendix 1. After initial optical imaging, grain boundaries were identified using a macro-etch solution of 50mL Nitric Acid (1.40pH) and 50mL water with a submersion into the solution for 2 seconds followed by a water rinse.

Test cubes were also imaged and analysed using an FEI XL-30 field emission scanning electron microscope (SEM) with backscattered electron detection. Images were taken using an acceleration voltage of 20kV along with an EDX spectrometer for elemental composition analysis, which was performed using an Oxford Instruments ISIS system. Density measurements, were made using the Archimedes method and the gas pycnometer. It was calibrated using a sphere with a known volume of 318.5510 mm^3. The maximum sample size that could be tested in this machine was a cylinder 17 mm in diameter and 35 mm long.

3.6 Tensile Samples

Tensile specimens were built only for silicon-steel alloys, as the high porosity in copper samples inhibited mechanical tests of copper. At first cylindrical dog-bones were manufactured according to the Test methods for Tension Testing of Metallic Materials with designation ASTME8/E8M [176]. Cylindrical specimens were selected over flat specimens in an effort to avoid residual stresses and resulting cracks at the edges of the samples. More details are and results can be found in Chapter 6.

3.7 Magnetic samples Test Rigs and Methodology

The magnetic properties of the binary Fe-Si alloy, with varying Si composition (Fe-5.0%w.t. Si, Fe-6.0%w.t. Si and Fe-6.9%w.t. Si), processed by LPBF were measured in collaboration with The Superconductivity and Magnetism Group, Department of Physics, University of Warwick. A Vibrating Sample Magnetometer (VSM) with a 12-tesla superconducting solenoid was employed for DC magneto-static measurements (MagLab, Oxford Instruments, UK). The as-built dimensions of the cylindrical samples manufactured for magnetic tests were height $h=5\ mm$ and diameter $d=4\ mm$. The samples were cut in half and ground to their final dimensions according to the restrictions imposed by the use of the VSM for the measurement of the DC magnetic properties. For example, the mass of the final magnetic sample had to be less than 1 gram. The VSM could operate between 1.5 and 300 ^{o}K using a standard Variable Temperature Insert (VTI). The operating principle of the VSM is based on Faraday's law which states that an electromagnetic force is generated in a coil when there is a change in flux through the coil. In the measurement setup a magnetic sample is moving in the proximity of two pickup coils as indicated in (Figure 3-4). M vs H loops were obtained and each loop was 6 quadrants from 0 to +0.5 T, then to -0.5 T, then back to +0.5 T and last back to zero field. The field sweep rate was set at 0.05 T/min. The voltage from the PSD was converted by a calibration to give the magnetisation. The VSM was calibrated prior to the experiments to a minimum error of 3%. On the field axis the trapped field in the coil is of the order of ±2 mT. Some noise was detected around zero - zero and it was attributed to the very quick signal change causing the PSD to auto-range. The coercive field and remanent magnetisation were extracted from the acquired data sets and remanence values are presented in Chapter 6.

In order to assess the effect of post-heat treatment on the magnetic properties of Fe-Si, prior to magnetic tests, the samples were subjected to a heat treatment at 1150 ^{o}C for 90 minutes. The measured magnetisation curve and corresponding permeability and coercivity are presented in Chapter 5.

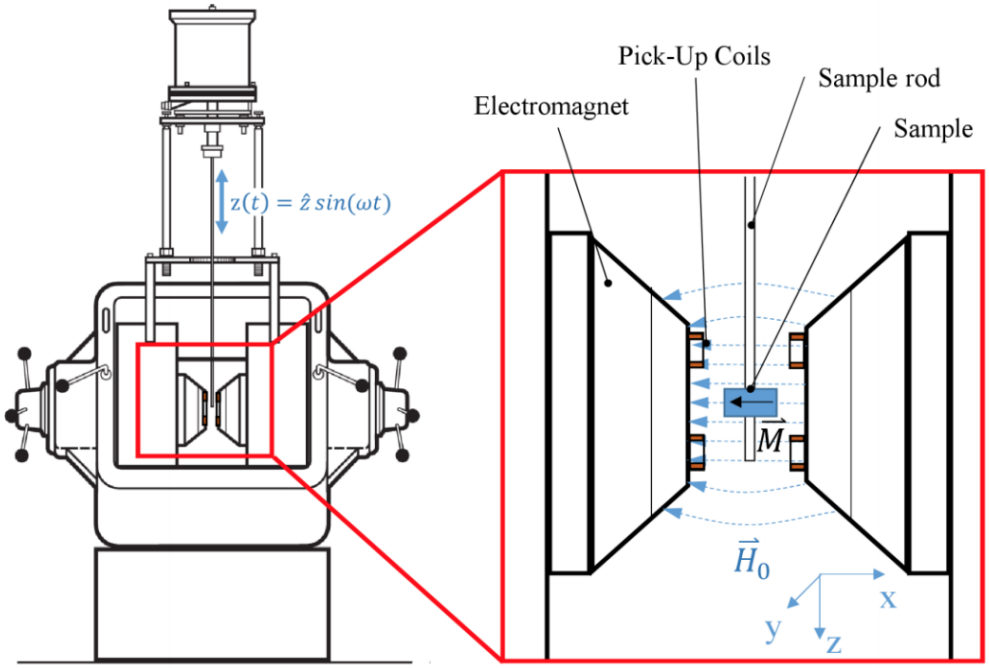

Figure 3-4: Diagram showing Vibrating Sample Magnetometer and measuring components

In addition to the DC magneto-static measurements, AC experiments were performed in a Quantum Design Physical Property Measurement System (QD – PPMS) using the AC Measurement System (ACMS) option. Each sample was mounted in a straw with the axis of the cylinder parallel to the AC and DC applied fields. The sample was centered in the coil set. Each point is a 5-point scan, which ensured that the calibration was correct. The test equipment was operated in the frequency range 20 to 10000 Hz and where H_{AC} < 100 Oe. The same samples used in DC magnetometry were also used for the characterisation of the AC magnetic properties of Fe-Si alloys.

3.8 Electrical Resistivity

In addition to density and microstructure, electrical test specimens were designed and manufactured. The resistance of a specimen can be directly measured by an ohmmeter but can also be calculated by the standard formula in equation 3.1:

$$R = \rho L / A \qquad (3.1)$$

Electrical resistance (R) is the product of the electrical resistivity (ρ) measured in μΩ-cm and the length of the specimen (L) in cm, divided by the cross-sectional area (A) of the specimen in cm^2. To calculate the resistivity of the material to a high degree of accuracy, the resistance, length and cross-sectional area need to be also known. However, LPBF can result in a rough surface finish that can cause deviations in the dimensions of the final samples. Therefore, it is critical to remove this roughness in order to accurately measure these dimensions. Surface grinding was applied to all resistivity samples as a standard post processing operation to ensure dimensional accuracy. All tests were undertaken at room temperature.

Silicon steel rectangular bars for electrical resistivity measurements from silicon steel alloys were printed at 10 x 10 x 50 mm and copper bars were and printed with dimensions of 2 x 2 x 25 mm. The optimum processing parameters for Fe-Si and Cu samples were selected from the set that resulted in the highest density for each material. Three samples in three build orientations with respect to the build direction (horizontal 0^o, diagonal 45^o and vertical 90^o) were produced for each material. The direction of the longest edge of the bar defined the name of the orientation. With regards to Fe-Si, test cases include samples with 5%, 6% and 6.9% silicon content as build and post heat-

treated at 1150 ºC for 90 minutes. The Cu test cases include: as build, two post-heat treatment temperatures (800 ºC and 1000 ºC) and three post heat treatment dwell times (30 minutes, 1hour, 4 hours). Overall, this resulted in the creation of 63 test samples. The build plate with the total number bar samples and two prototype coils is shown in Chapter 4. Specimens were individually measured along all dimensions in a minimum of four places using Mitutoyo digital callipers, which had a resolution of ±0.02mm. The values were averaged out to determine as accurately as possible the cross-sectional area and the length of each specimen.

Electrical DC resistance tests were performed using a Valhalla Scientific Inc. (USA) 4300B digital micro-ohmmeter. This DC four-wire Kelvin resistance measurement meter was calibrated internally to within 5% accuracy through tests using precision low-resistivity resistors and current shunts. It was capable of generating a current between 0.1 mA to 10 A, and was able to measure the voltage from 20 mV to 2 V with a minimum sensitivity of 1 μV. Each specimen was tested a total of five times. This was in accordance to ASTM B193-02 “Standard Test Method for Resistivity of Electrical Conductor Materials” [177].

3.9 In-situ absorptivity of Cu

Knowledge of the metal powder absorptivity is of significance not only in the optimisation of additive manufacturing but also in the evaluation of LPBF, cladding and alloying. For the purposes of this study, in-situ absorptivity measurements of high purity copper were conducted at Lawrence Livermore National Laboratory, California, USA. Absorptivity measurements of the effective laser absorptivity of bare copper plates and copper plates coated with copper powder are presented by performing single-track experiments.

The calorimetric setup consisted of a custom sample holder and two type K thermocouples. Each of the thermocouples was spot welded to the rear side of the substrates and the distance between the two thermocouples was kept at 3 mm (±0.1 mm) for all the measurements. The LPBF process took place in a custom build chamber that included a set of in-situ monitoring tools. A more detailed description of the experimental setup can be found in [157,158] and it is shown in Figure 3-5.

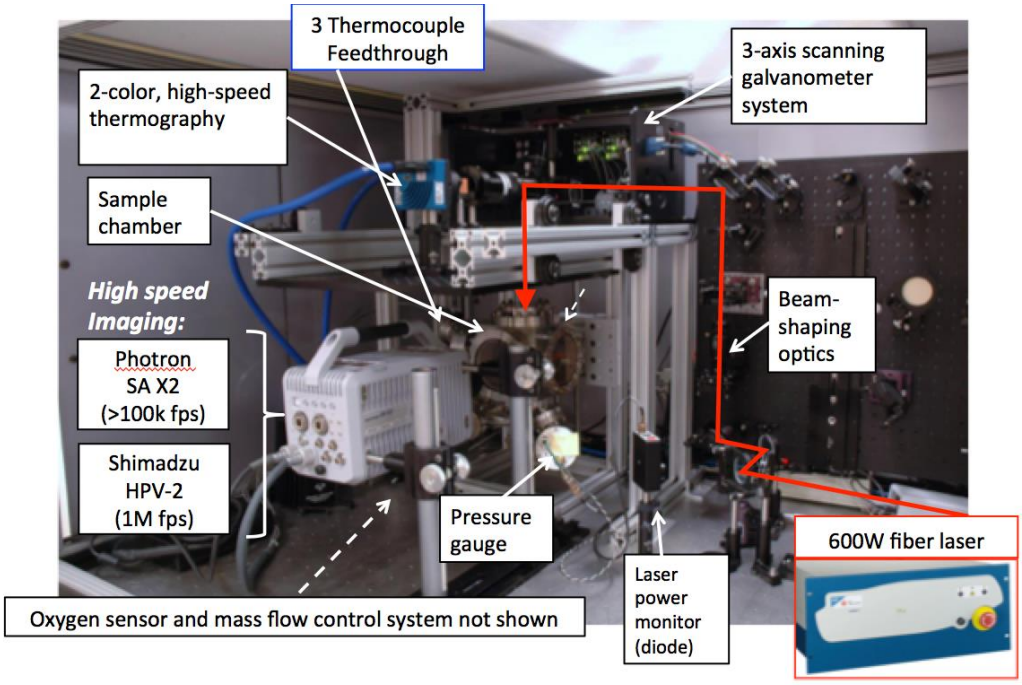

Figure 3-5: Experimental setup used for single scan tracks and absorptivity experiments of pure copper

The chamber was flooded with argon gas to create a controlled atmosphere and minimise the oxidation of the copper (oxygen content below 500ppm). A 600W Yb-fiber laser with an optical system resembling that of a commercial LPBF machine was employed. The laser beam was focused to a laser spot size of 50μm with the use of a convex-concave lens pair integrated into the scanner system (3XB, THORLABS, USA). The laser scans produced single tracks on the discs or powder surfaces. The temperature time curve was measured for a total time of 60s with a measurement frequency of 14Hz

using thermocouples. Each set of parameters was measured three times. The reported absorptivity is the mean value of the three measurements from the two thermocouples.

3.10 Micro-Hardness Measurements

In order to assess the effect of the processing parameters and heat-treatment on the mechanical properties of Fe-Si alloys, micro-hardness was measured using a Vickers indenter. For each sample, ten indentations were performed to cover a large surface area and minimise deviations in the measurements. An indentation force of 500g was employed to create the indents.

3.11 X-Ray Diffraction

X-ray diffraction (XRD) was used in this research for solid phase determination and lattice parameter measurement. Tests were carried out with the use of a Bruker D8 Advance diffractometer (Siemens, Munich, Germany) equipped with nine-position sample holder. A Cu anode was used, which produces a $K\alpha$ x-ray radiation characterised by a wavelength λ=1.54 Å. The radiation produced by the X-ray tube is not perfectly monochromatic, since standard monochromators are not able to separate the two $K\alpha$ components (known as $K\alpha 1$ and $K\alpha 2$). Therefore, background noise removal and $K\alpha 2$ radiation stripping was performed using Diffrac, EVA software (Bruker, Billerica, Massachusetts). Diffraction peaks in the range 2θ = [25°, 100°] were considered for determining solid phase composition. The study was performed in one vertical plane of powder samples and 3DP cubic samples (front view plane). The acquisition conditions were step size $\Delta\theta$ = 0.05° and step time t = 8s.

3.12 Electron Back Scattering Diffraction

In the present research work a Nova 600 Nanolab Dualbeam FIB/FEG-SEM system (FEI, Hillsboro, Oregon, USA) was employed for EBSD investigation. Grains were defined by a misorientation angle larger than 5^{o} and the scanning step size was 2 μm. The average confidence index of the EBSD imaging was approximately 0.90 for phase verification. The results from the EBSD scans are presented in Chapter 5 of this study with the use of pole figures (PF), inverse pole figures (IPFs) and orientation maps. EBSD maps for various scanning strategies are also presented and discussed. The final EBSD images were obtained using microstructural data analysis software (Aztec, Oxford Instruments, UK) by combining the orientation maps with the corresponding image quality maps.

4. Chapter 4: Processing of pure copper with LPBF

4.1 Introduction

Although there have been many studies on the LPBF of copper, none of these to date have resulted in good conductivity data. The motivation for this study was to produce copper windings for the EM and evaluate their density and conductivity. This Chapter explores the suitability of using an average powered (200W) LPBF system with a small laser spot size capable of delivering higher energy density which could be suitable to process copper to the maximum density achievable. This machine was selected as the best available option in the laboratory for processing copper. Electrical testing using direct four-wire Kelvin measurements was undertaken with respect to initial build orientation. Post heat treatments were carried out to measure their effect on electrical resistivity. In addition, in-situ absorptivity measurements were carried out in collaboration with Lawrence Livermore National Laboratory to determine a process window for laser powers below 600W. This was achieved with the use of custom designed and produced LPBF system and the experiments enabled a correlation of melt pool geometry, with absorptivity and track quality. For more details regarding the LPBF machines used for the absorptivity tests and the experimental apparatus refer to section 3.9. The thermal conductivity of the as-built copper samples and lattices was also experimentally measured. All the results are discussed and summarised in this Chapter.

4.2 Cu powder characterisation

The nitrogen atomised Copper AN was a spherical powder as shown in Figure 4-1 with a minimum 99.99%w.t. purity. It had an apparent density of 4.80g/cm3 (ISO3923/1) with 90% of the particles below 65.3μm. The size distribution is also presented in Figure

4.1 with an average D50 value of 38.0µm. It was confirmed through EDX analysis that the phosphorus content of Copper AN was below 0.02%w.t.

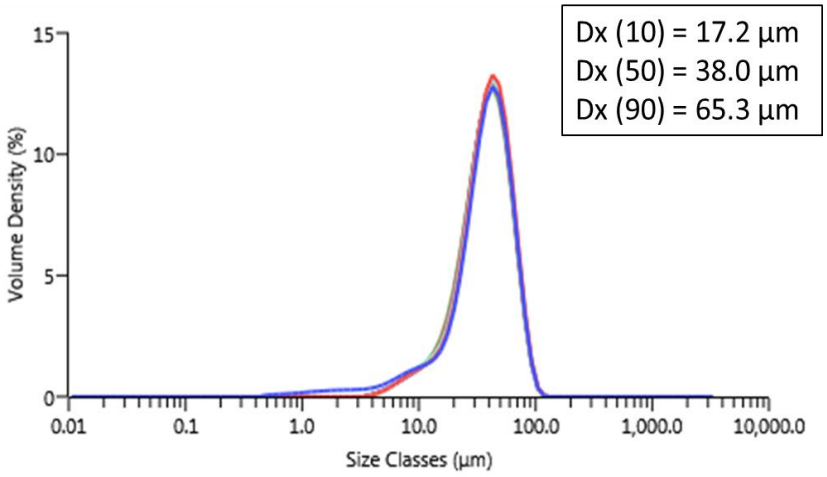

Element	Weight%
P	0.02
Cu	99.98
Totals	100

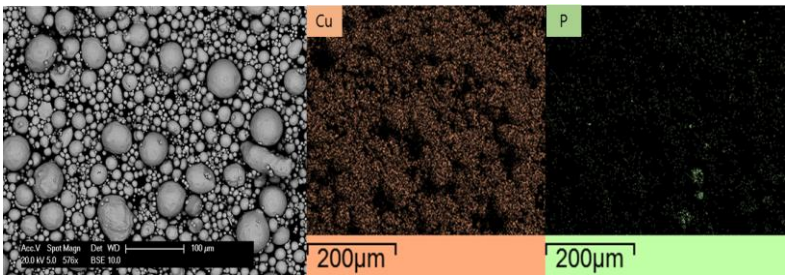

Figure 4-1: a) Particle Size Distribution of Cu powder and b) Elemental analysis using EDX show small traces of phosphorus

The feedstock powder was further analysed prior to absorptivity experiments. An XRD spectra was obtained to detect oxides present in fresh Cu powder. The powder was found to be oxide free as shown in Figure 4-2.

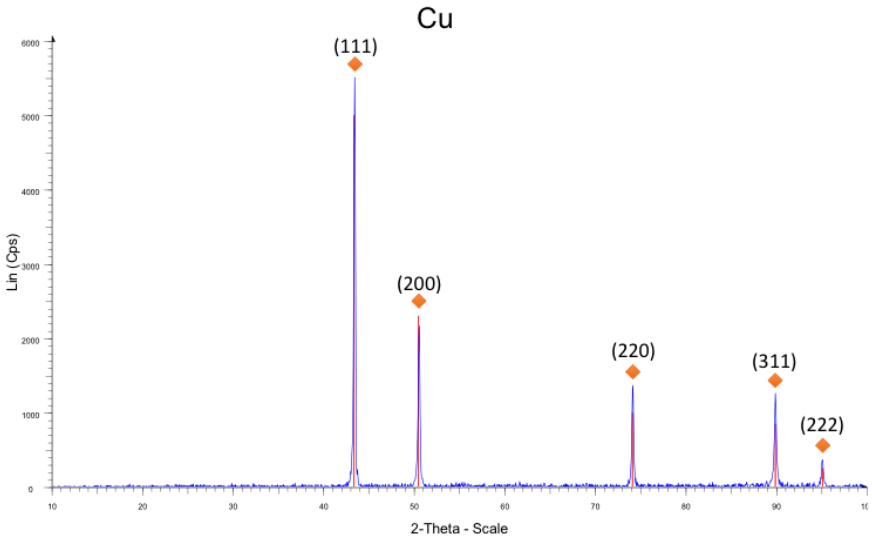

Figure 4-2: XRD spectra of Cu powder. No oxides were detected for fresh Cu powder measured at room temperature with step 0.05°, step time 2s and 2θ angle between [10°-100°].

4.3 Parameter Optimisation

4.3.1 Single scan tracks

For parameter optimisation, single tracks were investigated first to narrow down the process window. In order to determine the optimal laser scan-speed the range was set to the speeds previously reported in the literature between 50 and 275 mm/s. Laser scan speed with the Renishaw machines was defined as exposure time and a point distance and initially four-point distances were investigated (50,100,150,200 μm) as seen in Figure 4-3. Tracks were 18mm long with two tracks per parameter set in order to average out any variations in processing. Single tracks were created on a temporarily bonded (with ethyl-2cyanoacrylate) thin steel plate that could be removed and sectioned easily.

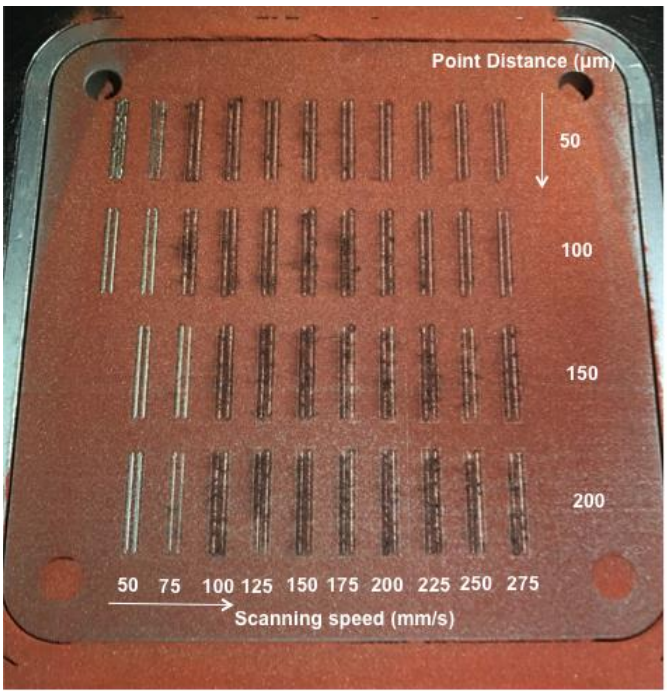

Figure 4-3: Single scan tracks of Cu powder with varying point distance and exposure time resulting in scanning speed between 50-275 mm/s.

Although the initial observations showed good quality melt tracks upon cross-sectioning and EDX elemental analysis, it was seen that a considerable amount of iron from the build plate had transported into the melt pool as shown in Figure 4-4(a). As such, whilst this platform aided in bonding to the substrate, it altered the melt characteristics and did not provide accurate information on the parameters needed for processing pure copper parts. No cracks or pores were observed in the SEM micrographs of the cross-sectioned melt pools) demonstrating that the laser energy density was sufficient to melt copper. However, the highly elliptical shape of the melt pool indicated that even though the processing parameters were optimised, the laser melting process remained in the conduction melting regime [178]. Higher laser power and slower scan speeds would

cause an increase in the energy density, thus, creating a deeper more stable melt pool through a transition towards the keyhole melting regime.

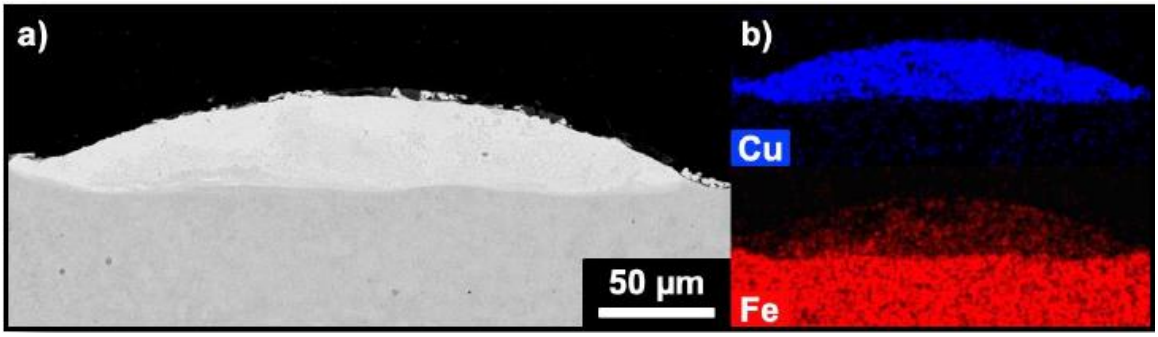

Figure 4-4: a) Cross section of single scan track and b) EDX analysis for copper and iron content

4.3.2 Thin Walls

After single scan tracks, thin walls were investigated as the next step of parameter optimisation. The same range of laser scan speeds and point distances were used to create thin walls which were 18mm long and 4mm tall. Two walls were created per parameter set in order to compare the same processing parameters with the laser scanning in opposite directions. This test set was repeated for three different layer thicknesses: 30, 45, 60µm. As with the single tracks there was a large amount of iron diffusion into the weld tracks at slower scan speeds. An extreme example can be seen in Figure 4-5 where a thin wall processed at 50mm/s has a large amount of iron diffused into the melt pool for the first 1.5mm. This transition from copper-iron to pure copper was characterised by a significant decrease in the wall thickness which was attributed to the higher thermal conductivity of copper and the much narrower heat affected zone.

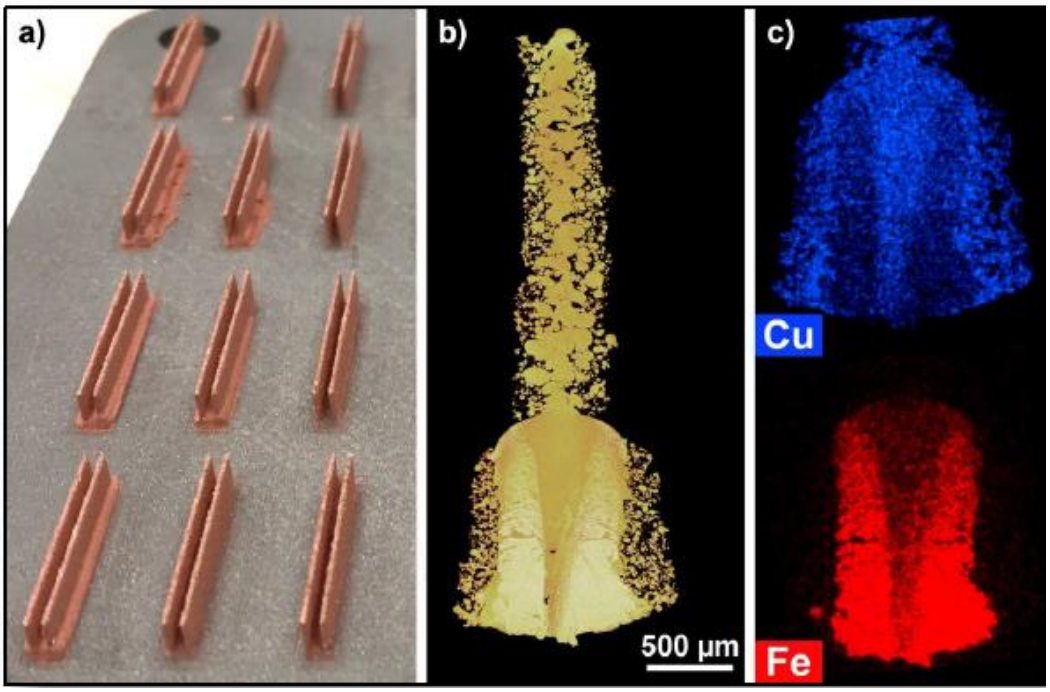

Figure 4-5: Thin walls fabricated with a high laser power and slow scan speeds showing the difference in wall thickness close to the substrate, EDX analysis revealing the interdiffusion between iron and copper.

When comparing the results for the three different layer thicknesses, 30µm layers resulted in some powder spreading issues which caused the first row of thin walls to have a raised section nearest to the powder re-coater, with random portions of the thin wall missing. The 60 µm thin walls had much less consistent weld tracks with greater amounts of sintering than melting. The 45 µm layers showed no signs of powder spreading issues and had much better melting behaviour than the thicker layer. For all remaining tests a 45 µm layer thickness was used.

Use of multiple scans for a single track was investigated as a way to try to improve the density by melting any particles that failed to form part of a continuous weld track. However, combinations of laser powers (100, 150, 200 W) in double and triple scans failed to improve the continuity of the thin walls. Instead, multiple high-power passes only resulted in increased balling of the thin walls. As a next step for parameter

optimisation, a wider range of point distances was selected (20 to 175 μm) to be tested at four laser scan speeds (150, 175, 200, 225 mm/s) at 200 W. By comparing these tests along with the first three sets of tests used with different layer thicknesses, it was determined experimentally that at many different speeds, a 50 μm point distance provided the most consistent thin wall and this was used for the remaining tests. Finally, a wider range of laser speeds was investigated from 200 to 1250 mm/s. It was expected that the highest laser scan speeds would not sufficiently melt the powder to form a thin wall, however, all parameters resulted in thin walls. Only the fastest scan speeds did result in very thin walls with minimal bonding and low strength but not in catastrophic failure. After comparing the continuity of weld tracks and thickness of the sintered particles the best resulted from a laser scan speed of 300 mm/s. In Figure 4-6 the thin walls processed with the various parameters are shown.

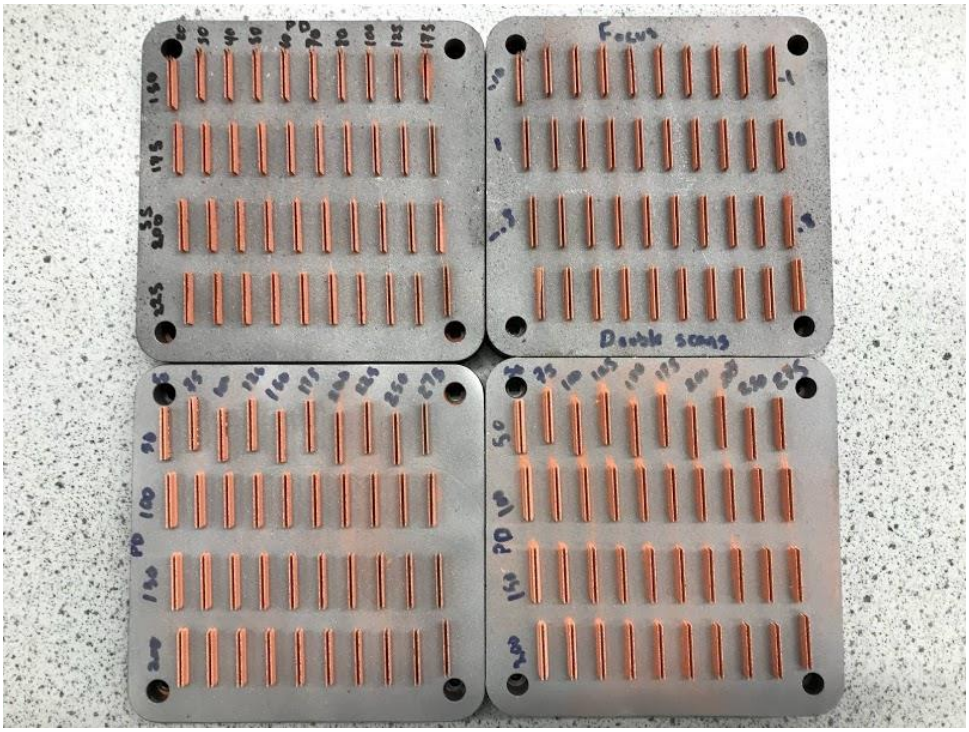

Figure 4-6: Parametric study of copper thin walls

4.3.3 Cube samples

Cubes with dimensions of 5 x 5 x 5 mm were created using a power of 200W, layer height of 45µm focus position of 0mm, point distance of 50 µm and exposure time of 167 µs, based on previous experiments on thin walls and single tracks. Hatch distances between 50 and 175 µm were investigated along with single and multiple scan strategies. Cubes were created first with a stripes scan pattern testing the hatch distance range with respect to cross-sectioned optical density measurements. An example of a copper cube fabricated with a striped scan strategy with no rotation is shown in Figure 4-7.

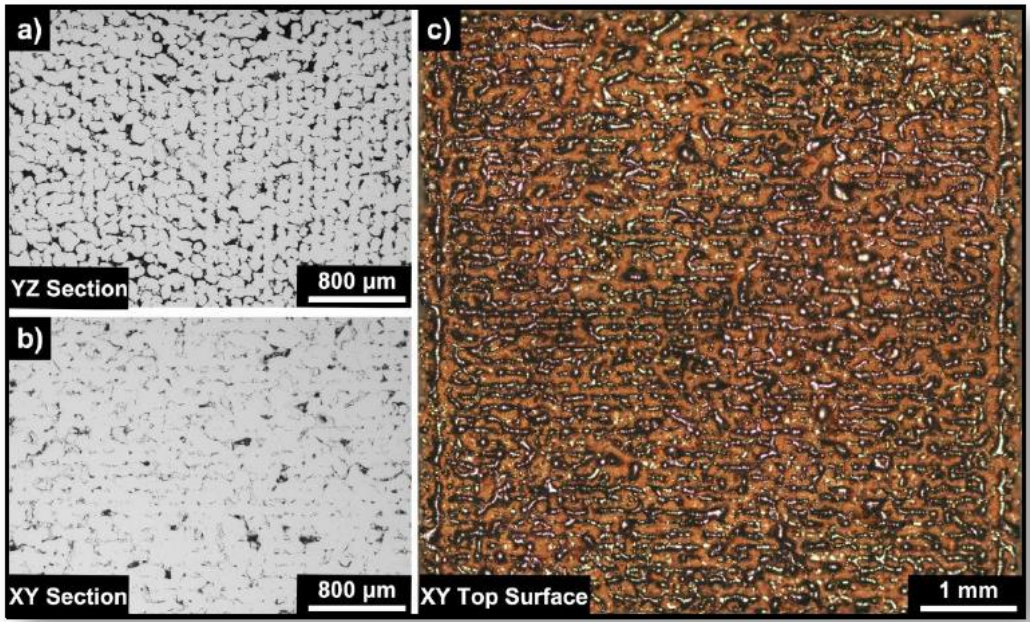

Figure 4-7: Cross-section of a cube sample processed with a)stripes and b)nested scan pattern with hatch distance of 100µm showing side plane, top plane and an optical image of the top as built surface.

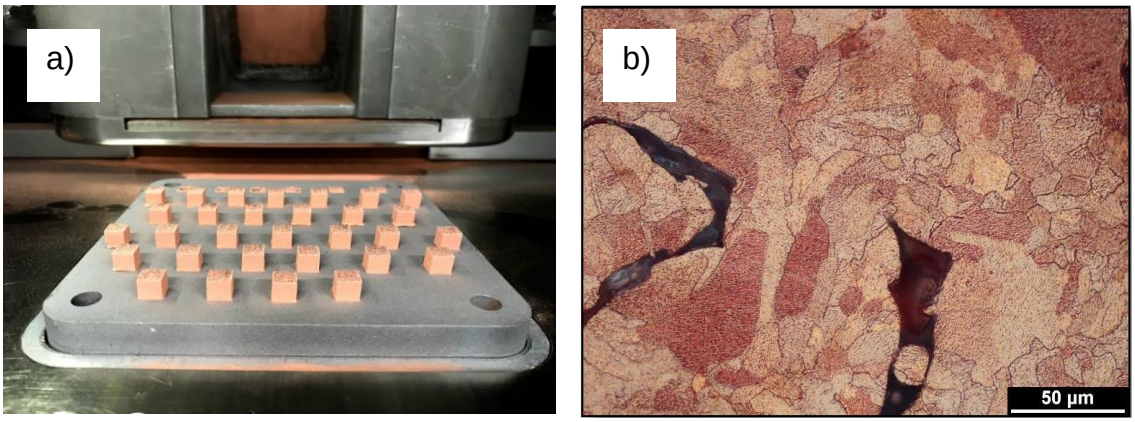

Figure 4-8: a) Cube samples still attached to the substrate and b) etched cross section of XY plane highlighting the grain structure of as-built pure copper.

The cube samples and the grain boundaries of a cross sectioned and etched cube sample are shown in Figure 4-8. The average grain size as shown in the etched specimen varies between 5 and 50 µm with a mean value of around 14 µm.

After analysing cube samples manufactured by the single scan strategies (stripes, islands, rotation and nested), it was found that there were non-melted areas of loosely sintered powder within and between scan tracks. In an attempt to melt and fuse these areas, multiple scans were applied within a single layer (pre-sintered with lower laser power, re-melt by repeating the scan, multiple scans and an offset scan between tracks). Despite the wide range of tested scan strategies, little change was seen in the apparent corresponding densities. It was found that the multiple scan strategies, whether the second was either directly on top of the previous scan or offset by half the hatch distance, resulted in 5-15% lower densities than the highest from the single scan strategies. This was due to a difference in absorptivity between powder and consolidated powder. The highest densities were found with a hatch distance of 100µm with several of the scan strategies. Rotation of the scan pattern by either 67^{o} or 90^{o} resulted in higher densities compared with non-rotated tests. All single scan patterns with the same scan parameters resulted in densities that were within 5% of each other. After comparing all scan

strategies, the final selected set of parameters used a 100 μm hatch distance with 90° rotation each layer.

4.3.4 Density

Relative densities were measured by both single cross-section optical density measurements using thresholding limits alongside helium pycnometry. The highest density using the optical method was 85.8%. The average density for all single scan patterns was 83.0% (Figure 4-9).

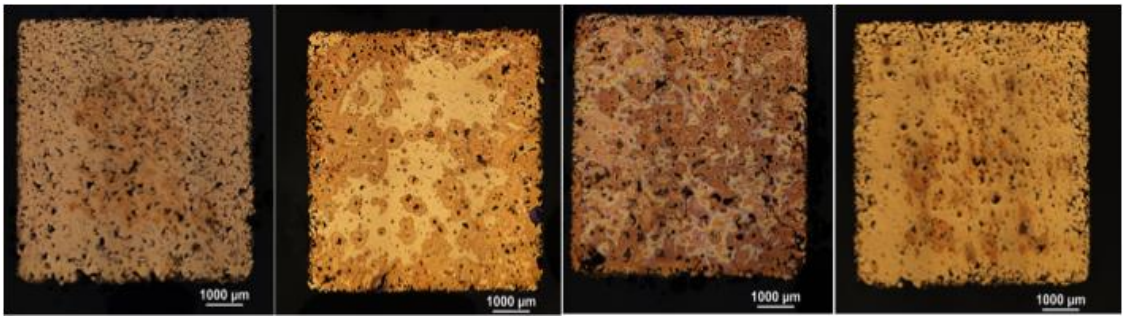

Figure 4-9: Cross-sectioned copper cube samples processed with various processing parameter sets reveal that the average density does not exceed 83%.

Density measurements using the gas pycnometer were obtained using cubes printed in both 90-degree alternating layer scan directions, as well as 67-degrees, as these two patterns were nearly identical in optical densities. The average for the 67-degree rotated cubes was 83.5% and the 90-degree cube was 84.2%. The optimised parameter set for copper resulting in the highest density is shown in Table 4-1.

Table 4-1: Optimised parameter set for Cu resulting in the highest density

Parameter	Value or Range
Laser power (W)	200 (maximum available)
Laser spot diameter (µm)	35 (minimum)
Powder bed temperature (°C)	170 (maximum allowable)
Laser scan speed (mm/s)	300
Layer thickness (µm)	30
Laser beam focus position (mm)	0
Hatch spacing (µm)	50
Scan strategies	Stripes with 67-90° rotation every layer

4.4 Electrical Resistivity

Despite much prior research into LPBF of copper and its alloys little work has been done to characterise the absorptivity, conductivity and electrical properties. Most prior research only specifies density, hardness and/or other mechanical properties. In prior published work on LPBF of Cu, electrical properties have been presented using indirect measurement techniques that assume isotropic material properties. However, due to the nature of the process AM parts are generally not isotropic and thus the accuracy of these indirect measurements needs to be questioned when applied to LPBF processed materials.

The test bars used for resistivity testing were manufactured using the cube parameters that resulted in the highest density. This parameter set was a scan strategy of stripes rotated 90° for each layer and included 3mm high supports in order to avoid iron contamination. They were printed in three orientations to determine sensitivity to orientation: a vertical orientation, horizontally as well as diagonally with a 45° incline. Some of the test bars were measured in the as-built condition while others were subjected

to a heat treatment at either 800 ºC or 1000 ºC with a ramp up temperature of 10 ºC per minute and a dwell time of either 30 minutes, 1 hour or 4 hours. The resistivity was

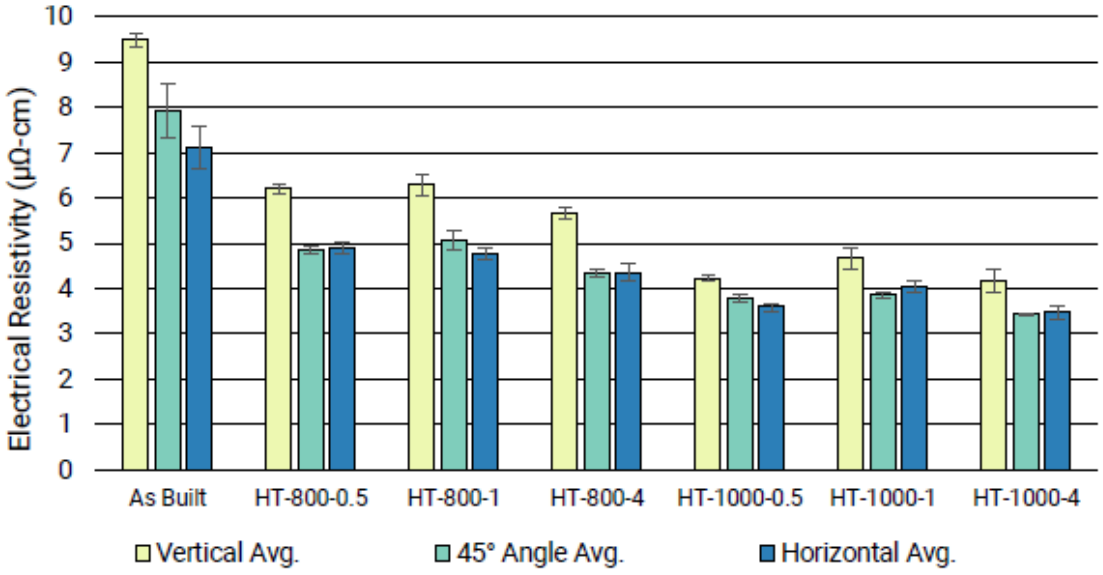

Figure 4-10: Averaged electrical resistivity under different tested conditions (as-built vs heat treated) for samples built with different orientations

measured using a DC four-wire Kelvin resistance measurement meter which directly measured the sample's resistance. By individually measuring the dimensions of the specimens after heat treatment and a light polishing of the surface the material resistivity was determined. The average standard deviation for the length of each specimen was 0.02 mm or 0.06% of the length and was 0.01 mm for width and height resulting in an average variance in cross-sectional area of 1.1%. The results of the resistivity measurements can be seen in Figure 4-10 along with the corresponding calculated standard deviations.

While the average resistivity of the as-built condition specimens was 8.18 μΩ-cm with heat treatment, the resistivity dropped to the lowest average of 3.69 μΩ-cm for the 1000 ºC heat treatment for four hours. The lowest average resistivity was found for the 45º orientation heat treated at 1000 ºC for 4 hours with a value of 3.43μΩ-cm which equates to 50.3% IACS. Out of each group of heat treatments, it can be seen that the vertical

orientation had on average 24% higher resistivity than the average of the other two orientations.

The electrical resistance of a solid pure metal is derived from the number of disruptions found in the periodic atomic lattice structure [179]. In alloys, this disruption comes from elements that are not the main element of the alloy. However, in pure elements, this disruption comes from imperfections in the crystal lattice. These imperfections are grain boundaries, vacancies or voids in the atomic lattice, and dislocations in the lattice structure. Larger grains result in lower resistivity due to the lower number of grain boundaries compared to small grain structures. But in the case where the material is not solid but porous, this porosity has the greatest influence on the resistance of the material.

In additively manufactured materials, porosity with respect to resistivity has been previously studied for a custom aluminium-magnesium alloy and shown to be linear [180]. This linear relationship has also been shown with porous metals manufactured with other powder metallurgy methods [181], where the resistivity for copper with a porosity of 15 per cent is approximately 2.5 μΩ-cm or 68.9% IACS. This is better than the best values with heat treatment found in this study and is perhaps due to the pressure which results in a reducing of pore size, typically used in conventional powder metallurgy (sintering) methods.

In all tested conditions, the specimens built in horizontal orientation had the lowest value of electrical resistivity in comparison to the other two orientations. This is reasoned by the cross-section of the top plane (XY) that shows more continuous tracks and fewer discontinuities than in the side plane (YZ) as previously shown in Figure 4-7 a) and b). The highest resistivity values were found in the vertically built specimens regardless of the applied heat treatments. This is perhaps due to an accumulation of partially-melted

tracks in the build direction (z-axis), in addition to the interlayer and intra-layer defects. These defects and lack of interlayer fusion minimised the amount of connected material along the direction of current flow in electrical testing which resulted in a higher electrical resistivity for the vertically built specimens.

When comparing the as-built condition to the longest heat treatment, the vertical specimen was fractured and analysed using SEM as seen in Figure 4-11 a) with as-built and b) heat treated at 1000 ºC for 4 hours on the right. As seen in the as-built condition, there is a number of un-melted powder particles in between the laser weld tracks. There are also noticeable defined edges between tracks. By comparing this to the heat-treated case, while there are still some attached powder particles, they appear to not be loose between the tracks but rather fused to them. The number of smaller un-melted powder particles is reduced after the heat treatment indicating sintering or partial melting. The weld tracks also appear to be fused together and do not show the same defined edges between them.

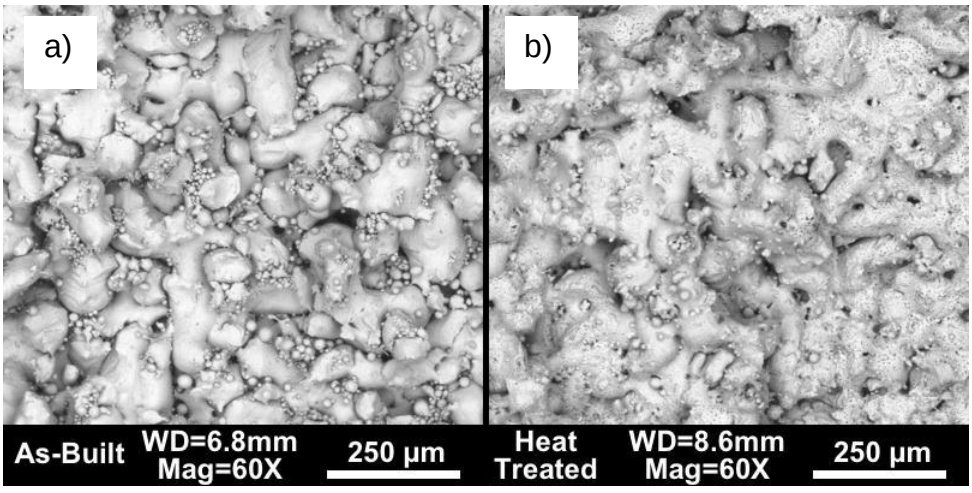

Figure 4-11: Comparison of a fractured section of a) as-built vertical test bar and b) heat treated at 1000°C for 4 hours vertical test bar.

This result shows that the heat treatment caused necking to occur for both the un-melted powders and for tracks that were adjacent to each other. This necking can be seen in 4-

12 where a number of fracture surfaces are identified. This necking and partial sintering decreased the number of discontinuities and gaps in the copper, minimising the effective path length electricity has to travel, and thus reducing the resistivity of the specimen.

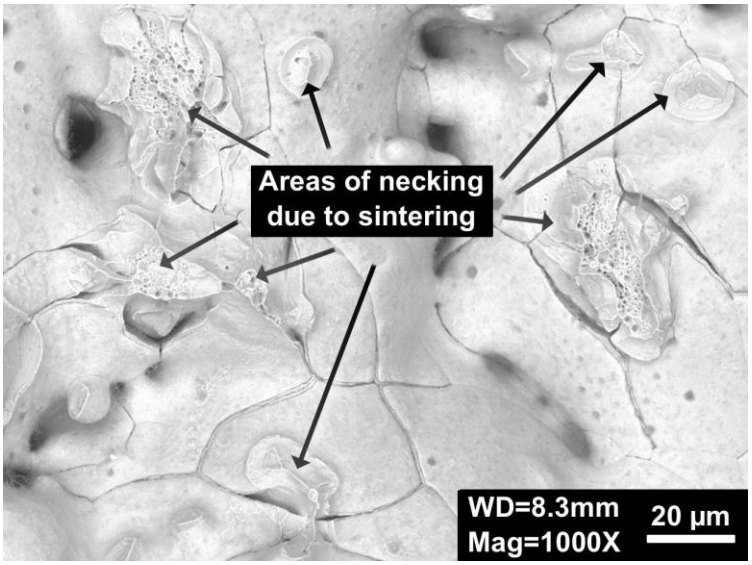

Figure 4-12: Areas on the fracture surface where localised necking of particles and weld tracks occurred but were broken off.

In order to minimise contact resistance in comparison to the actual material resistance, the ends of the test bars were soldered to the electrical tabs used for testing. However, this soldering could also have caused some of the variations seen in the measured resistivity values as, due to having a liquid phase metal on a porous surface, some wicking of the solder into the ends of the test bars can occur. While this can help reduce porosity, the resistivity of solder is much higher than copper at 15 µΩ-cm being composed of 50% tin and 50% lead. Additionally, some variations in resistivity can be attributed to small differences in porosity (2-4%) between specimens, due to the unstable build process. This is confirmed by using EDX on a sectioned specimen as seen in Figure 4-13. Multiple specimens were sectioned and the solder wicked an average of 0.6 mm.

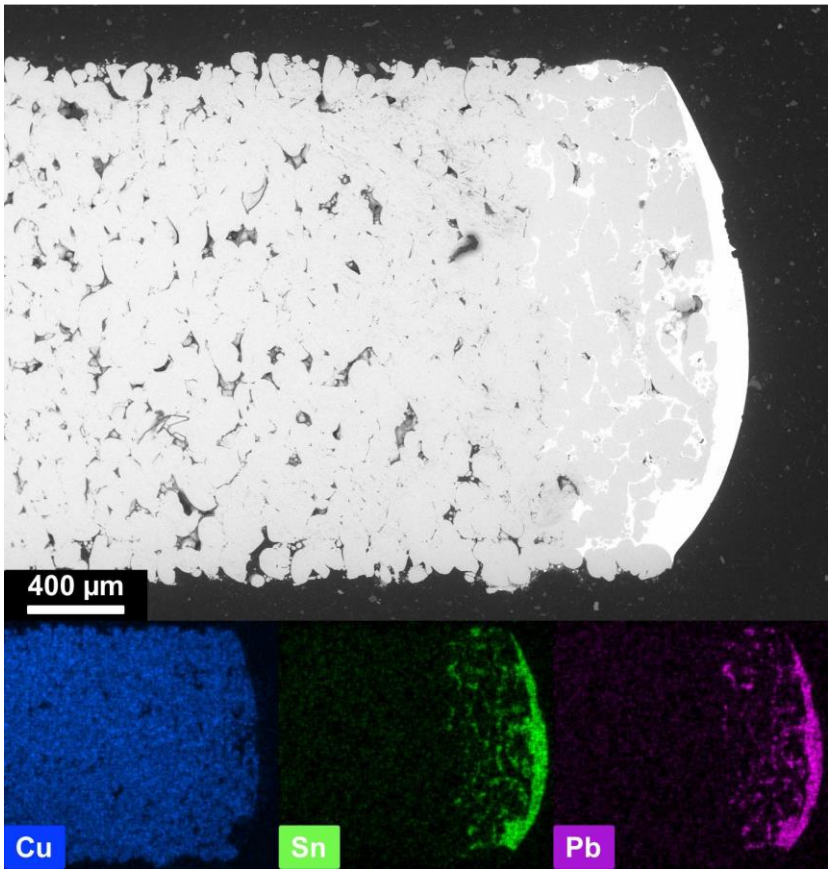

Figure 4-13: Sectioned SEM image of the soldered end of a copper test bar(a) along with EDX elemental analysis

4.5 LPBF of Cu Coil Windings

Electrical coils, shown in Figure 4-14 were created using the same processing parameters as the resistivity test bars and were subjected to a heat treatment at 1000 ^{o}C for half an hour. Resistance measurements were taken and were correlated to the CAD and as-built geometries. Due to the variation between CAD values and the actual external sintered dimensions of the coils, the exact geometry for calculating resistivity is more difficult to estimate. Based on an average of these values for these two coils, the expected resistivity in electromechanical applications is about 54% IACS and represents the best result from this study. It is worth pointing out that conventionally manufactured coils employed in EM usually feature 86-98% IACS. The design freedom of AM allows for structures that

cannot be created using traditional methods. These include varying the cross-sectional shape of a coil while maintaining the cross-sectional area in order to improve the cooling capability of end turn windings or to control local resistances within a coil. Hollow shapes can also be made for applications, which require additional cooling and running either air or a cooling liquid through the centre of the cross-section. It is necessary to improve the conductivity of copper processed via LPBF as it can greatly aid in the development of new electromechanical applications.

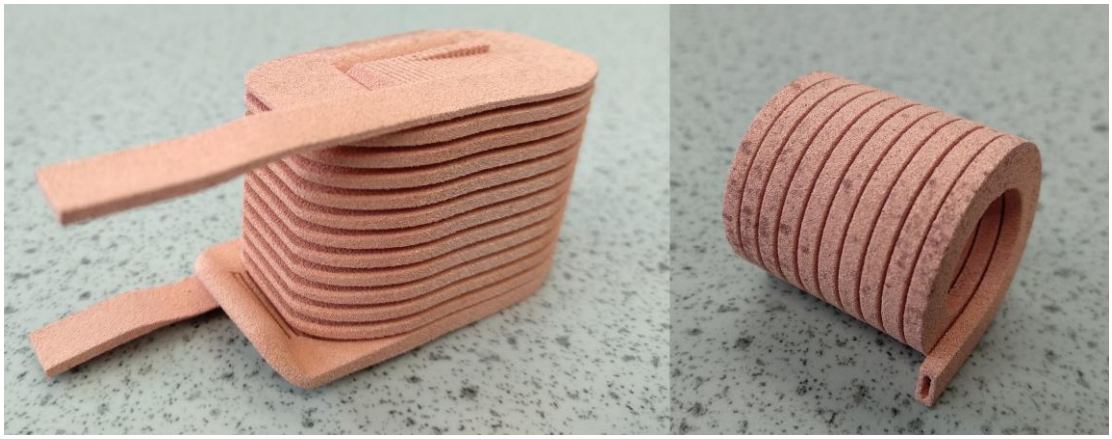

Figure 4-14: Examples of copper coils created with LPBF showing a variable cross-section and hollow core.

Based on the results from this study the resistivity of pure copper can be compared to the resistivity of other materials processed by LPBF. Despite having relatively high porosity, pure copper proves to be the best material choice in comparison to other metals and alloys processed with a 200W LPBF machine in terms of conductivity – though not sufficient to be truly useful for real electrical machines.

4.6 IR laser energy absorption of Cu

To enable efficient processing of copper at practical volumes it is essential to expand the parametric window of laser parameters within which copper can be fully melted to

produce fully dense parts. LPBF machines are commonly equipped with lasers featuring a maximum power up to 400 W [182]. However a new generation of LPBF machines with laser power between 500 and 700 W makes the determination of LPBF process parameters for copper manufacturing in this power range particularly important for industrial applications [183]. In this work, a systematic study is performed in which the key process parameters of scan speed and laser power are altered to fully evaluate the ability of copper to be processed using commercial equipment. In addition, substrate surface roughness was modified to represent typical processing scenarios, and the surface condition of the copper substrate was investigated via pre-process oven-based heat-treatment to induce a surface oxide layer. The cross-sectional features of the single tracks are analyzed to fully understand processing behavior in the context of conduction and keyhole melting regimes. High frame-rate video recording and optical metallography were also used to support the identification of conduction and keyhole welding regimes and offer new insights into the energy coupling of copper as a function of laser parameters.

4.6.1 Experimental method

Cu foils supplied from Goodfellow Ltd. UK, with thickness of 500 μm were EDM cut into 1 cm diameter plates for the absorptivity measurements. Two copper substrate preparations were used: bare substrate machined and 500-grit paper ground, and a substrate with a 100 μm recess where the powder was spread. Acetone was used for cleaning ground substrates prior to experiments. One substrate was placed into an oven at 200 ºC for 1 hour, to deliberately oxidise the near surface and assess the effect of this factor on copper absorptivity. After the laser-melting experiments and the excess powder was removed, the build plates were imaged using a reconstructed light microscope (VR-

3200 wide-area 3D Measurement System, Keyence Corporation, Japan). The substrates with the single tracks were cut perpendicular to the track length direction using a slow speed diamond saw (Model 65001, South Bay Technologies, USA) and mounted in epoxy resin for cross-sectional analysis. Metallographic preparation was performed down to a 1 μm diamond finish and samples were then etched using a 3:1 volume mixture of HCl and HNO3 to reveal the microstructure and melt pools. Imaging of melt pool depth and width was performed using an optical microscope (STM6 measuring microscope, Olympus Microscopes, UK) with submicron resolution.

The LPBF experiments for the absorptivity tests were performed by the author at Lawrence Livermore National Laboratory using an in-house built LPBF-AM machine equipped with a 600 W Yb, 1070 nm continuous wave fiber laser. The beam was focused using a 450 mm focal length lens to a nearly Gaussian shape with a $1/e^2$ diameter of 40±5 μm and scanned using x-y galvanometer scanning mirrors. The optical system was designed to simulate that of a typical commercial LPBF machine. The experiments were performed in a custom-built chamber [21] supplied with protective argon gas to ensure an inert atmosphere.

The same copper powder that was used earlier from ECKA Granules GmbH (Germany) was also employed for this study. Copper powder was manually spread using a razor blade as a 100 μm thick single layer on the circular pure copper discs. This layer thickness was chosen for the experiments as the small average powder particle size imposed a restriction in spreading a thinner homogenous layer on the substrates. Powder layer-height was controlled by the screwing of a threaded stage on which the substrate was mounted and was calibrated using a height gauge with a resolution of 0.01 mm and 0.02 mm accuracy (RS PRO Dial Indicator, UK). A series of 5 mm-long single tracks

was produced by varying laser power and scan speed. Processing parameters were narrowed down, by reaching the maximum power of the laser (400-540W), on bare copper substrate discs and discs coated with powder. Considering losses associated with the optics of the system, it was calculated that a 600 W nominal power translated to a 540 W actual power (10% difference). Laser powers of 400, 450, 500 and 540 W, and scan speeds from 25-1000 mm/s were used. These parameters were chosen after preliminary experimentation and represent practical parameters that are likely to be used for a range of highly reflective materials.

Two standard K-type thermocouple probes were spot welded on the rear side of the Cu substrate discs and used for temperature measurements with a standard error of 0.75%. This method allowed the measurement of only the part of the absorbed energy in the substrate while excluding the energy absorbed by metal vapor and energy that is removed by evaporation. The incident laser power varied from values of 100 W up to the maximum of 540 W. Scan speed was controlled by galvanometer mirrors. To avoid the inertial effects of the scanning mirror, the scanning distance was set to 10 mm and the laser was turned on after 5 mm of travelling distance and turned off at the end of the track. Temperature was recorded just before the laser irradiation for a duration of 120 s. A description of the extrapolation of absorptivity data in this system is also described in the work of J. Trapp et. al. [157] . An exponential decay function was fitted to temperature data of each thermocouple for $t > t_1$ and temperature was extrapolated to the time t_0 corresponding to the time the tracks were created, as shown in Figure 4-15.

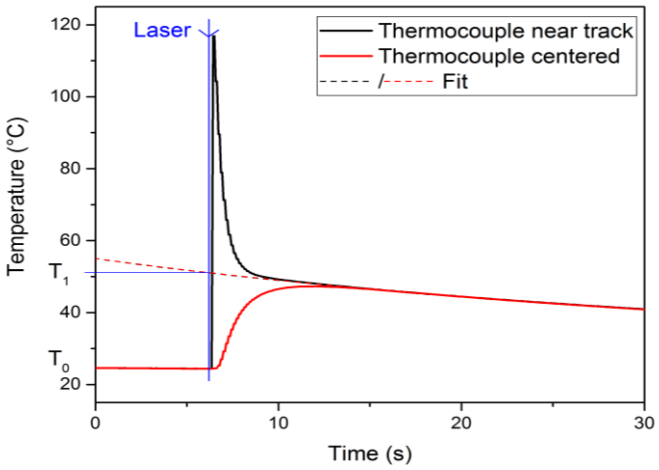

Figure 4-15: Typical temperature measurement curves for the evaluation of net energy absorption during laser scanning experiments

This procedure was chosen to compensate for temperature losses before temperature equilibration over the disc. These losses are primarily caused by convection as the heat lost through the thin thermocouple wires and the low conductivity sample holder is negligible. The total time of energy deposition was in the millisecond range, much shorter than the temperature equilibration time. With known disc temperature increase, the effective absorptivity can be calculated by dividing the energy necessary to uniformly heat the specimen from starting temperature T_0 to end temperature T_1 (EH) by the energy input due to the laser irradiation (EL):

$$Absorptivity = \frac{Energy\ Out}{Energy\ In} = \int_{T0}^{T1} \frac{mc_p(T)dT}{l/vP} \qquad (4.1)$$

$$T(t) = To + (T_1 - To)e^{-kt} \qquad (4.2)$$

where m is the mass of the disc including the powder layer (if applicable), P is the nominal laser power, *v* the scanning speed and l the total length of the laser track (5 mm for a single-track line). The temperature-dependent heat capacity over the temperature

range measured (25<T<150 C) is given by the function $C_p(T) = C_{p,0}(1 + ¸T)$ with $C_{p,0}$ and ¸ physical properties of copper are shown in Table 4-2.

Table 4-2: Physical properties of copper [6]

Property	Value and Units
Absorptivity, *A*	0.05
Density, *ρ*	8.94 g/cm^3
Specific heat capacity, c_p	386 J/(kg K)
Melting point, T_m	1084 ^{o}C
Thermal conductivity, *k*	399 W/(m K)
Latent Heat of Fusion	205 J/g
Latent Heat of Evaporation	4796 J/g
Thermal diffusivity, *D*	1.11 x 10^{-4} m^2/s

4.6.2 Cu single scan track morphology

Single tracks were produced using laser power of 400, 450, 500 and 540 W, with increasing scan speeds from 25-1000 mm/s. Tracks were produced on the two substrate types – 100 µm layer thickness powder, as well as 500 grit polished. Figure 4-16 shows confocal images and height maps for tracks produced at 400 and 500 W with increasing scan speeds, on substrates with 100 µm layer thickness copper powder. A clear difference in track quality and morphology between the two power parameters can be seen. Overall, the 500 W tracks are generally more homogenous and continuous indicating a more stable welding regime for higher laser power. For the 400 W tracks extensive balling and a start stop behavior in the melt pool was observed. In addition, width, height, and denudation zone of tracks at both 400 W and 500 W is reduced with the increasing speed. Moreover, in the case of the 500 W tracks, there is a clear change in melting behavior between 50 mm/s and 150 mm/s – whereby at 150 mm/s and above,

homogeneous tracks are produced. Morphological irregularities either in the form of balling or accumulation of material causing an increase in height of the tracks are represented as red spots on the height maps.

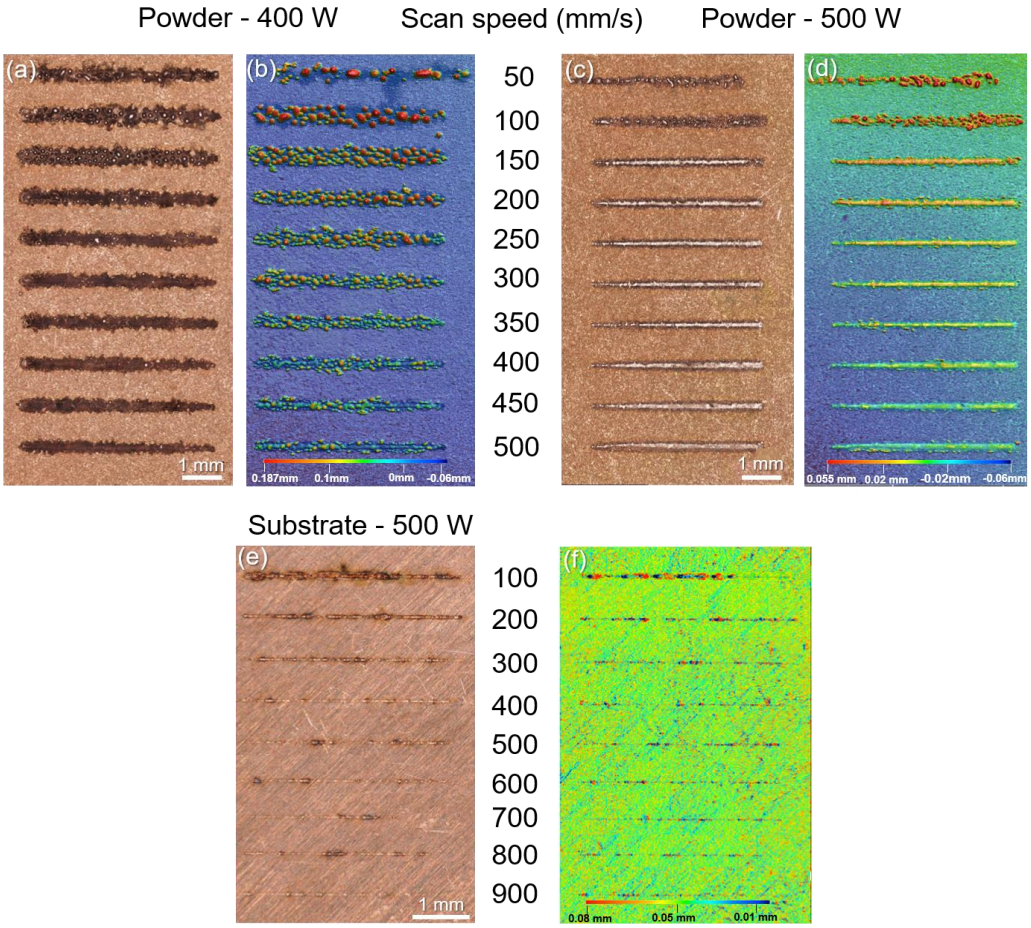

Figure 4-16: (a) and (c) optical micrographs and (b) and (d) height maps for single tracks of 100 µm layer thickness copper powder on copper substrates using 400 w and 500 w laser powers respectively, at increasing scan speeds. optical micrograph (e) and height map (f) for single tracks on bare copper substrate using 500w laser power at increasing scan speeds.

To further characterise and understand track morphology, track width and height measurements for 400 W and 500 W tracks for bare substrates and substrates with a 100 µm copper layer respectively are shown in Figure 4-17 The width and height of the tracks was measured for all tracks, taking an average of seven measurements along each track.

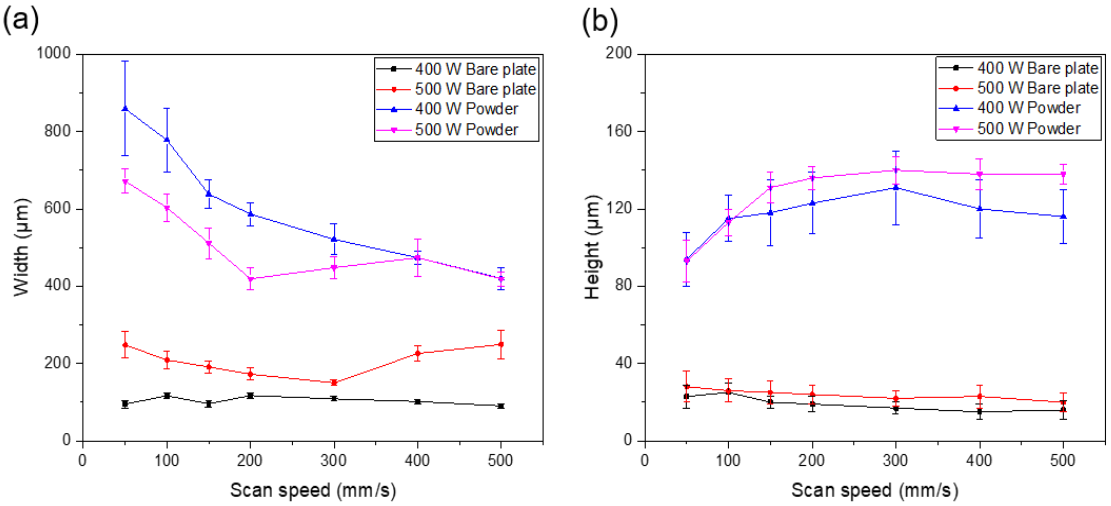

Figure 4-17: (a) widths and (b) heights of single tracks of copper powder on copper and bare copper substrates processed at increasing scan speeds, at 400 W and 500 W.

In the case of the substrates that have the copper powder layer, at 400 W and 500 W, there was a trend of decreasing width with increasing scan speed. This trend was particularly strong in the case of 400 W. For the bare plate, no significant trend of track width evolution with scan speed was observed. Under all scenarios, the track widths of the substrate with a powder layer were significantly larger than in the case of the bare substrate. Track heights in the case of the powder layer were as expected much higher than those of the bare substrates. As is the case for the widths, there was no trend of track heights for the bare substrates with increasing scan speed. However, for the powder layer, a trend of increasing track height from 50 mm/ s – 200 mm/s scan speeds was seen, after which track height remained relatively constant.

4.6.3 Cross sections of single scan tracks

To elucidate the melting behaviour further, cross-sections of tracks were analysed by SEM. Micrographs of key cross-sections at 400 and 500 W of tracks from copper powder layers are shown in Figure 4-18. The significant difference in melting behaviour between

400 W and 500 W powers in the case of the tracks on substrates including copper powder layers can be seen.

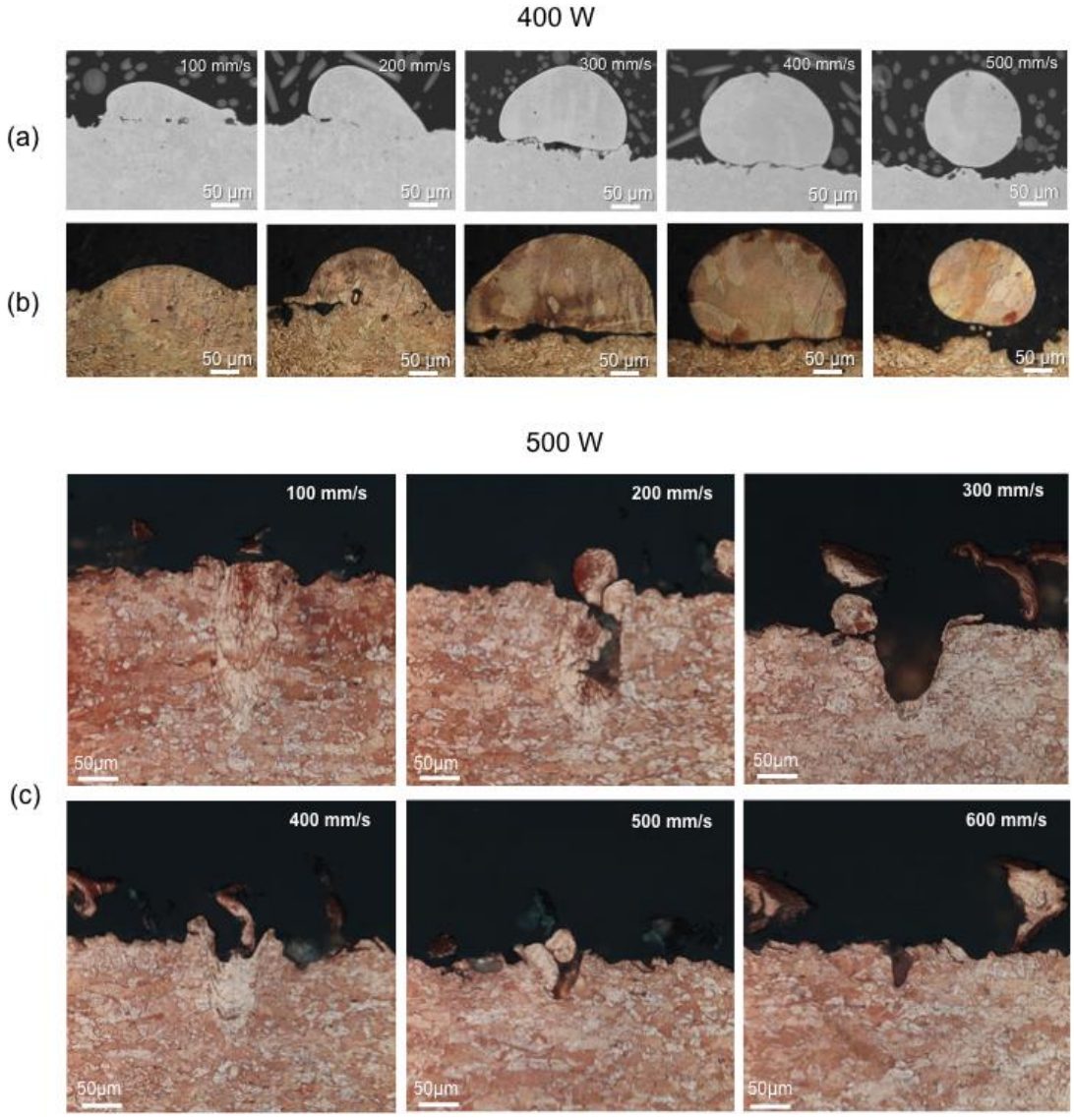

Figure 4-18: (a) SEM micrographs of polished and (b) etched cross sections of single scan tracks with increasing scanning speed and 400 W laser power. c) Keyhole deep melt pool is shown for tracks processed with 500 W laser power and slow scanning speed

At 400 W from Figure 4-18 (a), (b)), no penetrating melt pool could be seen irrespective of the scan speed, and at higher speeds, almost no bonding occurred. Moreover, at P=400 W the powder is partially melted, but the substrate is still intact. The melted powder evolves under the effect of the surface tension. A dense solid film forms on the surface

with good adhesion to the substrate. When the laser power is increased to 500 W, a transition to the keyhole regime was observed Figure 4-18 (c)). The formation of keyholes with depth being independent from scan speed is shown. High scan speed increases the probability of defects, both for 400 and 500 W. Lower scan speed means more time for voids to be closed. It is worth mentioning that the microstructure of melted Cu is similar to that of bulk virgin Cu. As a result, it is difficult to define details of the keyhole structure.

Figure 4-19 shows the melt pool evolution for maximum laser powers of 540 W and increasing scanning speed. Deep penetration key-holing was found with melt pools reaching a depth of 400 μm. Compared with the 500 W case no defects can be seen. The depth is independent of scan speed. Some variation in the shape of the melt pools can be explained by the instability of laser-matter interaction due to low absorption of the incoming laser energy. Overall, distinct profiles were observed determined by the melting regime: heating, melting and transition from conduction to keyhole. These melting regimes are critical for determining the overall stability and behaviour of the LPBF process.

Melt pool characteristics for 540 W at 100 mm/s are more consistent with a keyhole melting regime, given the higher aspect ratio melt pool, as opposed to the wider and shallower elliptical type melt pool seen at 500 mm/s. In the keyhole laser melting regime, the recoil pressure is higher than the surface tension and causes a deep and narrow melt pool depression to be formed.

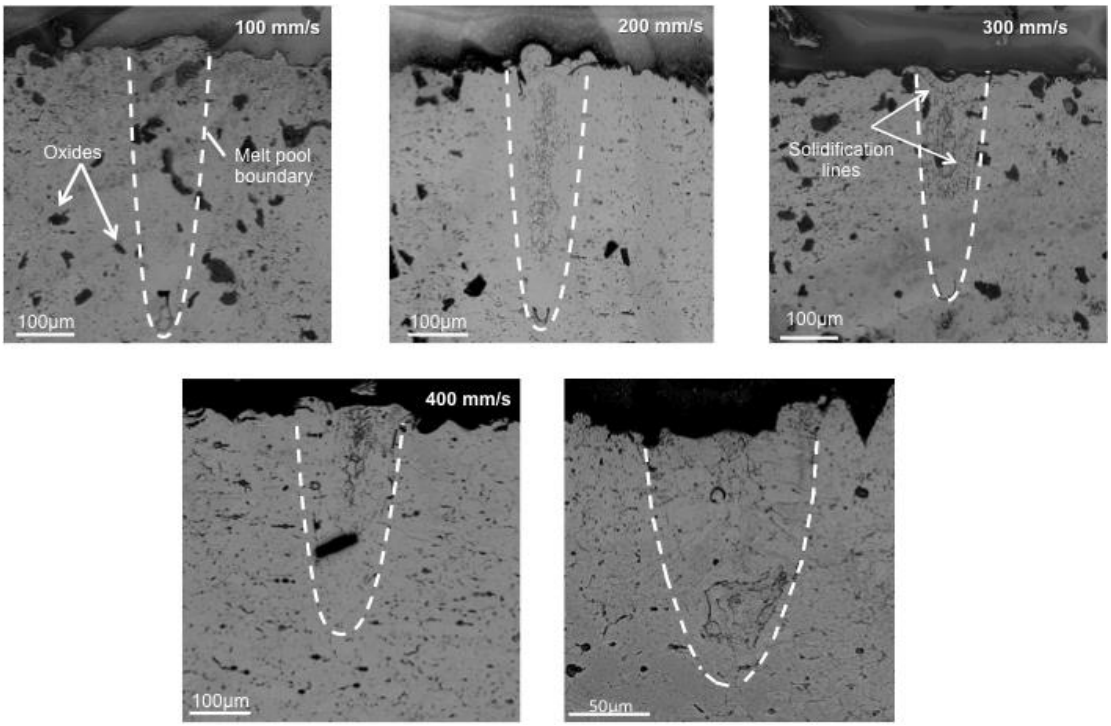

Figure 4-19: Evolution of a deep melt-pool in the keyhole regime with low scanning speed to a melt pool featuring a more elliptical shape for the transition melting regime. Conduction melting regime was observed for 540 W

4.6.4 In-situ absorptivity measurements

Figure 4-20 shows the effect of laser power at different scan speeds on absorptivity for bare plates and for powder. In the case of the bare substrate, absorptivity values start below 0.1 and remain at this value until the laser power reaches 350 W. Above this laser power, we generally observe a steep increase in absorptivity, indicating the transition from solid to liquid. It should be noted that scan velocity does not have a significant impact on the absorptivity of Cu. In general, materials featuring high thermal conductivity are prone to keyhole depression and they are much more dependent on temperature rather than scan velocity. For the powder layer, this same trend is followed, however the initial absorptivity is notably higher – between 0.165 and 0.2, which reaches 0.53 at maximum laser power of 540 W. It appears that for the fastest scanning speed (100 mm/s), in the case of the powder layer, the saturation value of absorptivity is

reached. The main reason is that for 100 mm/s the incident laser power of 540 W is sufficient to reach a keyhole-melting regime. This behaviour can be compared with the absorptivity of the bare plate at 100 mm/s, whereby saturation does appear to have been reached for the highest laser power.

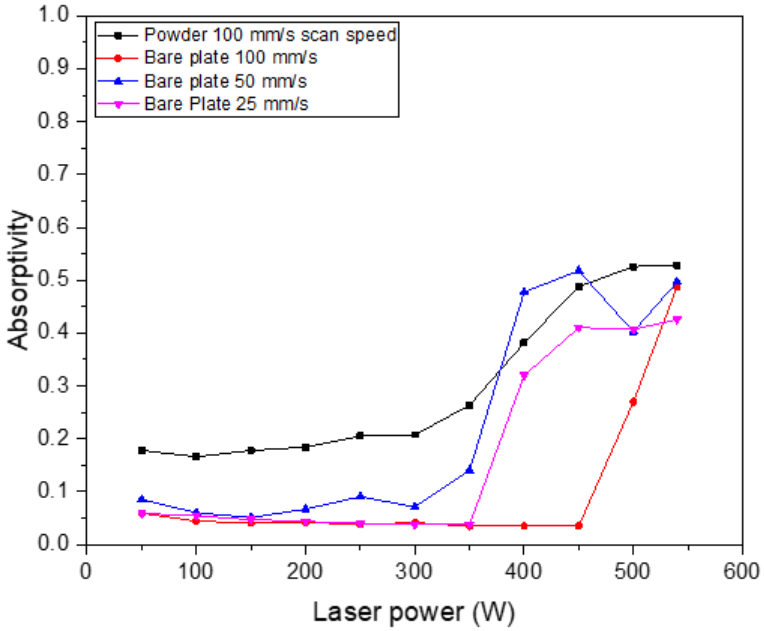

Figure 4-20: effect of laser power on absorptivity, for bare plate at 25, 50 and 100 mm/s scan speeds and for a copper powder layer at 100 mm/s scan speed (45 µm beam size).

4.6.5 Melting behaviour and absorptivity

This work has used in-situ absorptivity measurements of copper to understand its melting behaviour and dependence on typical processing parameters used in LPBF. With this information, practical implementation of LPBF of copper powder, and successful additive manufacturing, can therefore be achieved.

As can be seen from Figure 4-17, there is a clear trend, when using powder coated base plate, of decreasing track width with increasing scan speed. This is consistent with a higher energy density at lower scan speeds [184], and hence greater melt volume or melt efficiency. This behaviour is similar to other metals and alloys seen in LPBF [136]. At

400 W laser power, for both height and width metrics, the fluctuation of the data, represented here by the standard deviation, shows a steady decrease with increasing scan speed. This is indicative of a more unstable melting regime at lower scan speeds. It can also be noted that increased width for the 400 W power tracks may also be explained by a denudation phenomenon. This is where depletion of metal powder particles in the zone immediately surrounding the solidified track is observed, due to a competition between outward metal vapor flux directed away from the laser spot and entrainment of powder particles in a shear flow of gas driven by a metal vapor jet at the melt track [149]. However, at 500 W power, standard deviation of the height and width data, shows no trend with scan speed. This suggests that the transition between stable and unstable melting is between 400 and 500 W laser power. At both powers, the widths and heights of tracks, and their standard deviations, on the bare substrates show no trend with increasing scan speed. This indicates that the presence of a powder layer on the substrates dominates the melting behaviour.

The absorptivity results in Figure 4-20 support these findings. The presence of powder on the substrate increases the effective absorptivity at all processing parameters. Critically, there is a significant increase in measured absorptivity from 350 to 540 W in the case of the powder layer, up to a maximum of above 0.5. This is in contrast to the case of the bare substrate, whereby until 450 W, absorptivity remains low, and after which, rapidly increases. This behaviour is explained by multiple reflections and scattering of the laser beam in the presence of powder. For example, it has been shown previously that for high reflectivity materials, such as silver and gold, powder absorptivity can be increased by a factor of 4-7 in comparison to a flat surface, owing to the numerous reflections before effective absorption [185][186]. This is in contrast to low reflectivity materials, such as stainless steel and titanium, for which this factor is

only between 1.5-2. It can also be noted that in these results, there was no observed sharp decrease in absorptivity values at any particular point, which has been seen in the case of stainless steel powder for example [157]. This drop in absorptivity, followed by a rapid increase is expected in stainless steel powder when the powder initially forms a melt pool, and the measured absorptivity matches close to that of the bare substrate. This trend has been seen at both low (100 mm/s) and high (1500 mm/s) scan speeds in the case of stainless steel [157]. This is likely explained by divergence of energy to the solid-liquid phase transformation. This quite different trend for the copper powder seen here, where there was no drop in absorptivity, gives further evidence that the transition to a melting regime is not clear and sharp, supporting the argument that copper powder melting behaviour is not stable or predictable, under these processing conditions.

The instability of the melting regime for copper powder, and hence the requirement for fine-tuning of the process parameters, is explained by the inherent thermo-physical properties of the material. The rapid heat conduction of copper results in oscillations and turbulence in the melt pool resulting in melt ejections as well as defects in the tracks [136]. These phenomena can delay or obstruct the onset of effective penetrative melting, and the generation of a stable melting regime. The adopted melting mechanism, i.e. either conduction or keyhole, depends on the energy transfer efficiency during the process. Laser power and scan speed are the two main factors which affect the width and depth of the melt pool. When lower scan speeds are used, a higher temperature is reached within the melt pool, with lower viscosity, so the molten material moves outwards, improving bonding (wettability) [178]. The larger depth of the melt pool compared to its width indicates keyhole mode melting rather than conduction mode melting.

Track width scan speed dependence for the powdered sample may be related to slow melt motion due to the surface tension mentioned earlier and it is consistent with the width of tracks that greatly exceed the beam diameter, up to 15 times for low scanning speed. The beam diameter in these experiments is small, approximately the same size as the average powder particle. This in effect, results in fluctuations of absorptivity during the scan. When the laser beam hits a large copper particle the resulting absorptivity is low, close to the absorptivity of the bare copper substrate. But when the laser beam hits in-between powder particles, absorptivity increases abruptly due to reflections of the beam. The fluctuations of absorptivity during the scan can result in the fluctuation of the track structure. For a laser power of 500 W a transition to the key hole regime was observed. It is important to note that the transition is very sharp as there is no substrate melting at 400 W, in comparison to over 100 µm deep depressions at 500 W. This pattern is different from keyhole growth in other materials (e.g. Ti6Al4V, stainless steels and nickel superalloys) [154], where keyhole depth grows gradually (linearly) with laser power. This key difference in behaviour can be explained by the following and is illustrated in the schematic in Figure 4-21.

In the case of copper, the absorptivity of the laser light jumps rapidly by 1.5 times at the melting point, and thermal conductivity drops by 2.4 times. As a result, just after the laser melting of copper to a temperature above the melting point, there is a sharp temperature increase up to the boiling point, resulting in a sharp transition to the keyhole regime. Given the difficulties in LPBF of copper, it is critical to determine the process parameters that are practical for future implementation of copper in additive manufacturing. This work has shown that laser calorimetry is appropriate for determining the melting regime taking place during the melting of copper, and hence the

expected track and part quality. Despite this, it is clear that copper does not behave in a stable manner under all conditions.

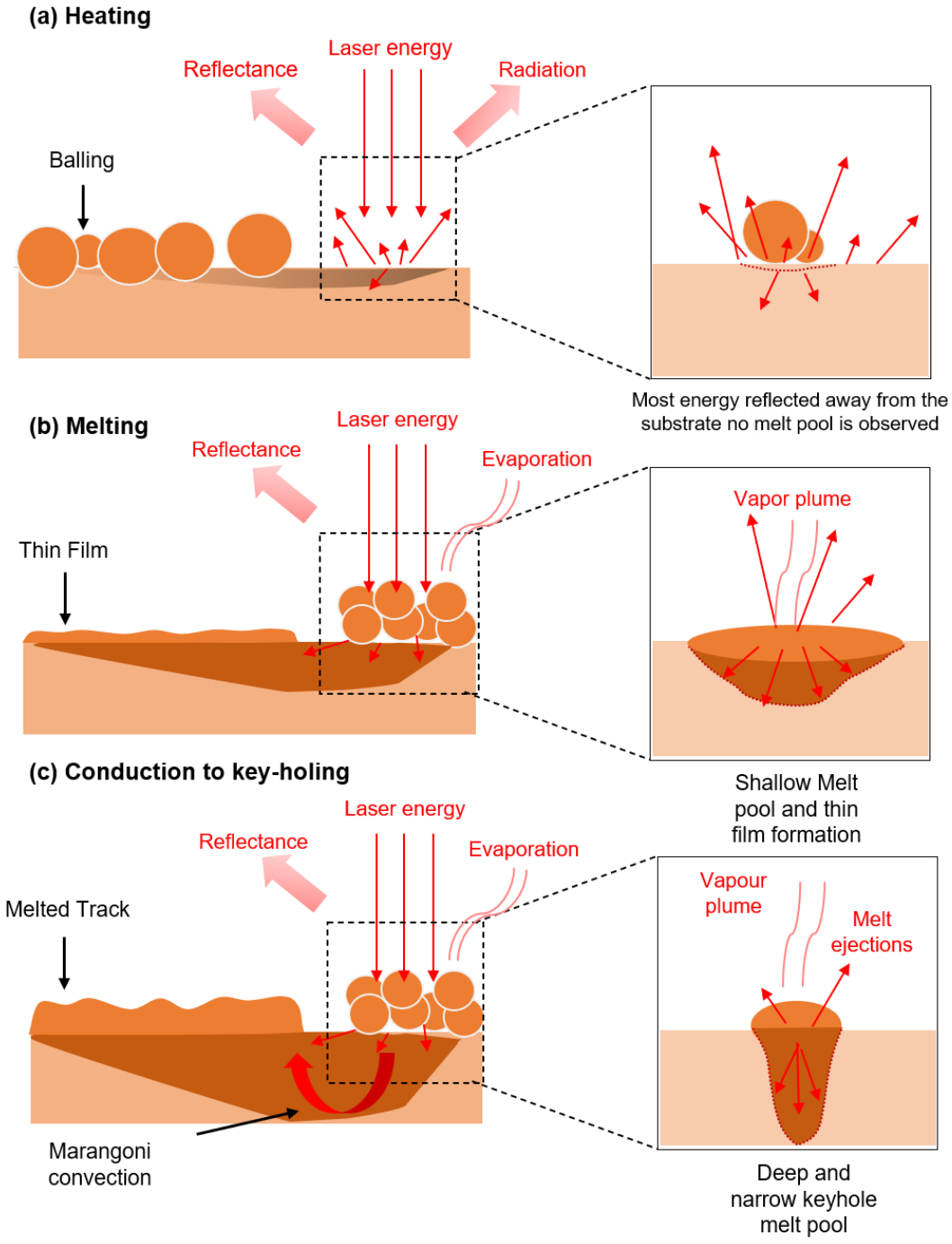

Figure 4-21: schematic showing melting regimes for copper powder on a copper substrate. (a) initial heating results in balling of material, (b) melting occurs resulting in a thin film of material and (c) a transition from conduction to key-holing takes place, resulting in a fully melted track.

4.6.6 Absorptivity Scaling behaviour

In order to obtain a comparative picture of the melt pool formation behaviour in copper, the bare plate absorptivity of a range of materials should be considered. In the study of Ye et al. [154], that focused on alloy systems with thermal diffusivities lower than copper (e.g. stainless steel, Ti-6Al-4 V and Inconel 625), it was found that the absorptivity is mainly dependent on two independent dimensionless parameters – namely normalised enthalpy β and normalised diffusion length L^*_{th}. These parameters take into account both material properties and laser processing parameters, and they can be calculated using equations (4.6) and (4.7) respectively:

$$\beta = \frac{A_m P}{\pi H_m \sqrt{D a^3 u}} \qquad (4.3)$$

$$L^*_{th} = \sqrt{\frac{D}{au}} \qquad (4.4)$$

For a given material with low thermal diffusivity, the transverse thermal diffusion is of minor importance as the increase of melt pool depth or depression depth is driven by vapour recoil pressure and Marangoni shear flow. In [187], Campanelli et al. found that the melt pool depth and absorptivity scale with βL^*_{th}, which leads to a simplified surface energy density dependence ($\propto Pu^{-1}$) [154]. Thus, for low thermal diffusion materials, the effect of thermal diffusivity will tend to cancel out through the counter-dependence of β and L^*_{th} on D. When this scaling is applied to copper, as shown in Figure 4-22 (a), the plots for different scan speeds become further separated. This is because the above scaling relationship is not applicable for high thermally conducting materials such as copper, where the melt pool depth is strongly influenced by thermal diffusion. For example, when comparing the thermal diffusion time, τ_{th}, for a 50 μm laser spot, copper

thermal diffusion times are in the order of μs while steel, inconel and titanium are in the order of 100′s of μs. This can be compared to an effective scan laser dwell time of ~100 μs for v = 500 mm/s. When the absorptivity is plotted against the original 'bare' form of normalised enthalpy β similar to the work of Hann et al. [188], which scales as $Pu^{-0.5}$, the plots follow a more unified behaviour, however, the threshold for the absorptivity jump is still broadly separated (see Figure 4-22 (b)). Instead, the scanning speed dependency is less significant due to high thermal diffusivity and short diffusion times. In fact, in deriving the normalised enthalpy from laser scan parameters, if one replaces the effective laser dwell time (a/u) with τ_{th}, the resulting form is $\beta' = AP = \beta/L^*_{th}$ which cancels out the effect of scanning speed ($\propto pu$). For a fixed material and laser spot size, this scaling is mainly dependent on power as shown Figures 4-20 and 4-22 (c). The increased overlapping of the plots proves that the laser absorptivity of copper is less dependent on scanning speed and is consistent with the observation that $L^*_{th} > 1$ for the temperature distribution around the melt pool. For the best t, the scaling exponent of absorptivity of copper bare plate vs scanning speed is found to be − 0.18 (Figure 4-22 (d)). Note that the powder case is still separated from the bare plate cases due to the effect of the lower thermal conductivity of the loosely packed powder layer.

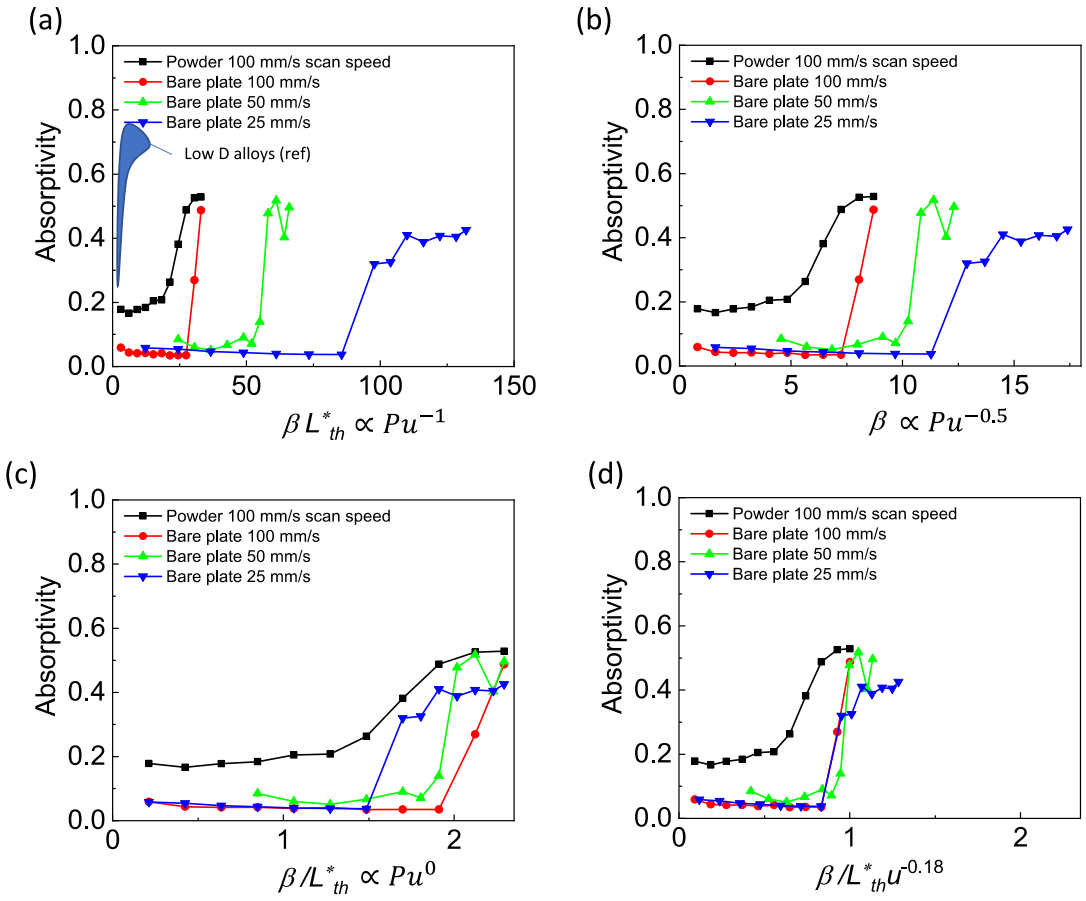

Figure 4-22: laser absorptivity as functions of the power of normalised enthalpy and normalised thermal diffusion length β/L*$_{th}$ (a), the normalised enthalpy β (b), the ratio of normalised enthalpy and normalised thermal diffusion length β/L*$_{th}$ (c), and β/L*$_{th}$u-0.18 (d).

4.7 Conclusions

Laser processing of copper is difficult due to its high laser reflectivity and thermal conductivity. The largest uncertainty in the evaluation of Cu laser processing is the effective absorptivity of the laser energy. Therefore, determining the correct parameters to produce predictable and stable processing conditions, is critically important. Even when processing parameters seem ideal, there is difficulty in qualifying the differences between different parameter sets. Direct calorimetry with in-situ absorptivity measurement is an emerging field of research that provides valuable insights to process behaviour.

Extensive parameter optimisation was carried out and results on the density of pure copper parts as well as results on the electrical resistivity and thermal conductivity were presented. In addition, the laser absorptivity of copper was measured with varying laser power and scanning speed. The absorptivity of Cu powder is approximately four times higher than for the bare material and the presence of copper powder reduces the critical laser power required to melt material. The powder layer can be melted at a laser power much lower than the melting threshold for the solid material. The melted layer is dense, not well bonded to the substrate but is expected to be adhered well enough for practical applications using LPBF. It was also demonstrated that melted layer quality and adhesion can be controlled by the manipulation of scan speed.

Laser calorimetry has been shown to be a useful method of characterising the melting behaviour of copper and advancing the understanding of material-process-property relationships otherwise difficult to identify. The main findings of this research can be summarised as the following:

- The absorptivity of copper powder is approximately four times higher than that for solid material, reaching a value of approximately 0.5.
- The difference in absorptivity of copper between solid (including powder) and liquid state increases between 6–8 %.
- The presence of copper powder reduces the critical energy density threshold required to sufficiently melt material during laser interaction when compared to bare substrate. The powder layer can be melted at a more stable and consistent manner when compared to the solid disc.
- It was demonstrated that melted layer quality and adhesion can be controlled by manipulation of scanning speed.

- The onset of increasing absorptivity is shifted to a higher power at increased scan speed.
- From an additive manufacturing perspective, higher laser power and use of the powder layer improves the process efficiency by increasing the effective absorptivity. This is attributed to the lower thermal conductivity of the loosely packed powder. However, even at the full power of the system at 540 W, the energy delivered was insufficient to create a stable keyhole melting regime for bare plate and powder. Explosive behavior with expulsion of material from the melt-pool and sudden changes in absorptivity, even when in the keyhole regime, were noticed.

In conclusion, these findings can be used as guidelines for parameter optimisation of copper and copper alloys in LPBF additive manufacturing. The work has also demonstrated that calorimetry can be used as practical method for performing monitoring of process behaviour during LPBF. The presented results regarding the various relationships between absorptivity and processing parameters may also be useful as a reference for LPBF of Copper, and of theoretical value for further research.

5. Chapter 5: Silicon steel alloys

5.1 Introduction

Silicon steel accounts for the majority of soft magnetic materials that are currently being used in electromagnetic applications. Low-percentage alloys, with a silicon content of between 1.5-3.5%, are used in the main in standard electric motors, generators and relays whereas higher percentage alloys, 3-6.5%, are used for high efficiency motors and power transformers. As discussed in Chapter 4, with the addition of silicon in iron, the permeability increases, hysteresis losses decrease, eddy-current loss decreases because of the higher resistivity and no deterioration is observed with time (aging). In this Chapter, some of the fundamental aspects of the Fe-Si binary alloy are presented and the effect of silicon content in the alloy is evaluated. In order to characterise Fe-Si alloys, metallic powder blends with high silicon content, between 3 to 6.9wt%, are processed via LPBF. Results are presented that shed light on the effect of processing parameters on microstructure and the resulting mechanical and magnetic properties. This will enable better understanding of the metallurgy of Fe-Si alloys processed via LPBF and determine the optimum silicon content for a 3D printed soft magnetic core based on the resulting mechanical, thermal and magnetic properties.

Silicon steel is highly susceptible to crack formation during LPBF, which cannot be avoided via process optimization solely. Therefore, a simple mixing method is introduced in this study in order to produce powder blends with varying silicon content. The various Fe-Si powder blends (3.5% 5%, 6%, 6.9%) were processed by LPBF. The aim of this study is to enhance the relative density of soft magnetic parts being processed with LPBF by changing the silicon content in order to fabricate defect-free samples.

Unlike other materials commonly used for structural applications such as Ti6Al4V, AlSi10Mg, Stainless steel etc., silicon steel had not been extensively researched and an optimised parameter set for a Renishaw-125 LPBF machine had not been previously published. The aim of this Chapter is to define the maximum silicon content that enables the successful fabrication of near fully dense silicon steel parts via LPBF. This research elucidates the effect of silicon content on the microstructure of high silicon steel with particular emphasis on mechanical and magnetostatic properties.

Silicon steel powder blends with 5wt%, 6wt% and 6.9wt% silicon content respectively, are processed by LPBF and analysed by performing microstructural investigation, micro-hardness measurements and tensile tests. In addition, magnetic tests with the use of a VSM were performed and the results are presented.

5.2 Feedstock Powder Characterisation

The chemical composition of the powders is shown in Table 5-1 based on suppliers' analysis. Figure 5-1 shows that the size distribution is positively skewed for pure Fe powder and the average size is 5 times smaller compared to the pre-alloyed Fe-Si powder, based on the results presented in Table 5-2. The powder-blend with 3.5% silicon content has two peaks due to the high amount of pure iron added to the blend in order to reduce the silicon content from the pre-alloyed powder. The left peak coincides with the peak of pure iron at 7 μm.

Table 5-1: Chemical composition in relative weight% of pre-alloyed Fe-Si and pure Fe powders

LPW					
Element	Si	Mn	C	P	O
Concentration (%wt)	6.9	0.05	0.01	0.009	0.0065

Sigma Aldrich					
Element	Cu	Mn	Ni	Pb	Zn
Concentration (%wt)	0.01	0.1	0.05	0.002	0.005

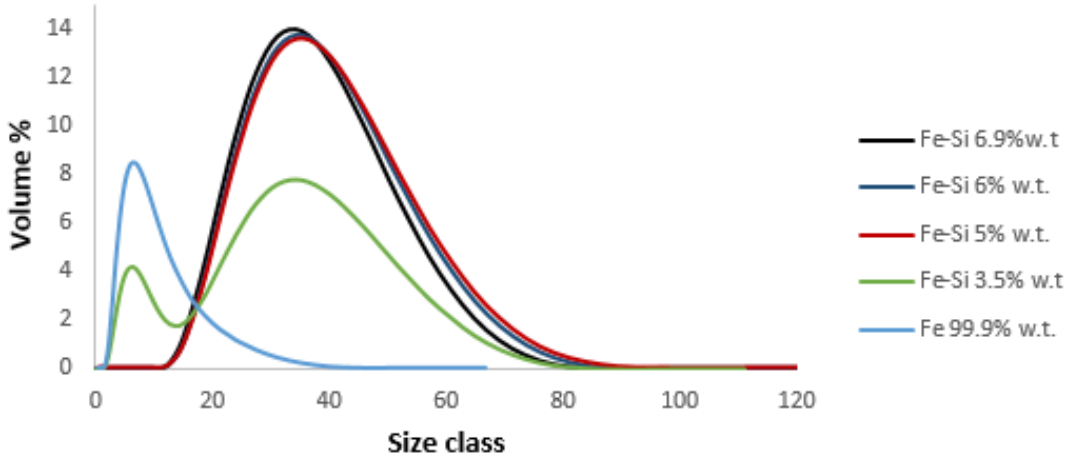

Figure 5-1: Particle size distribution analysis for the various powders and powder blends used in this study

Table 5-2 D-Values describing particle size distribution of the pre-alloyed Fe-Si powder and the resulting powder blends after mixing with pure Fe powder

	Silicon steel powders			
	6.9%	6.0%	5.0%	3.5%
D (10)	22.1	22.4	22.7	3.39
D (50)	36.2	36.1	36.7	7.1
D (90)	54	56.4	57.6	15.9

In Figure 5-2 (a) and (b) the particles of both powders are observed to be spherical, a morphology that favors both efficient packing and flowability. The cross-sectioned particles (see Figure 5-2 (d)) revealed inherent pores which suggest the presence of trapped gases that might contribute to porosity in the bulk samples fabricated. The

trapped gas inside the powder particles can be a side effect of the gas atomization process, which is employed for the fabrication of metallic powder suitable for LPBF.

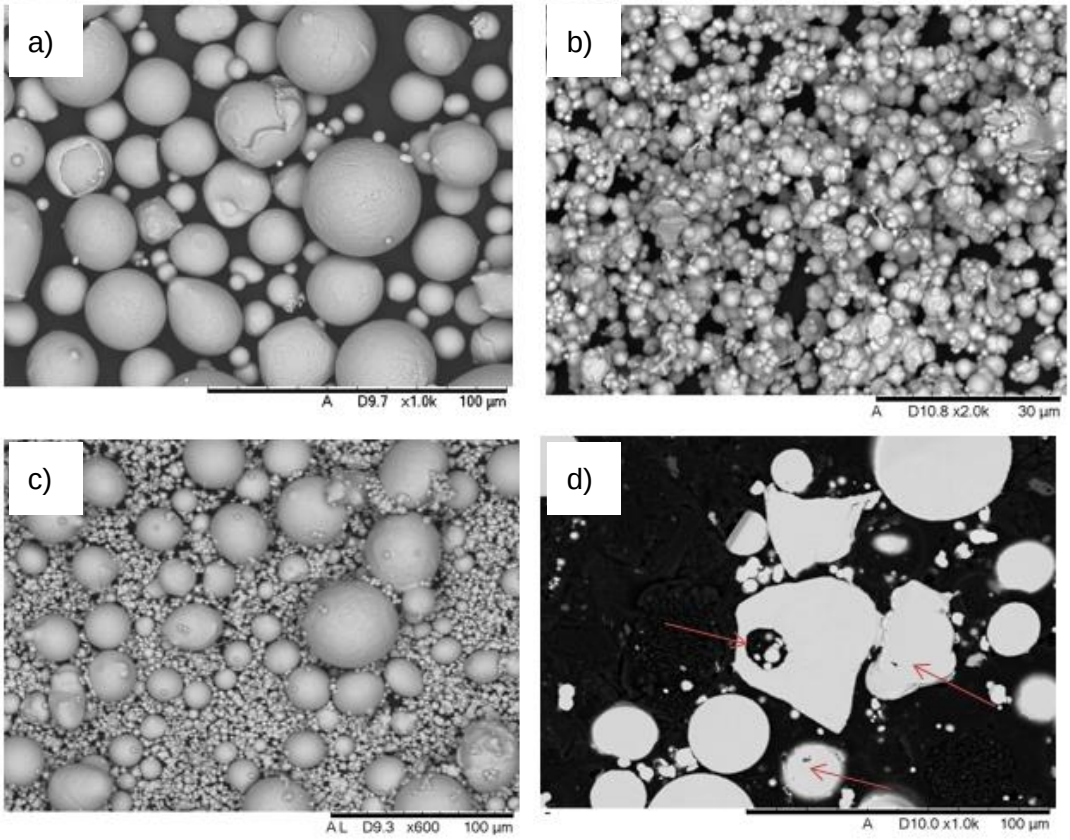

Figure 5-2: Feedstock material and resulting powder blends a) pre-alloyed Fe-6.9wt%Si, b) pure Fe, c) mixed powder blend Fe-5wt%Si and d) cross-sectioned particles of pre-alloyed Fe-Si with some inherent pores indicated by arrows

Table 5-3: Results of average density and flow rate for Fe-Si and pure Fe powders

Sample	Powder Type	Average Density	Standard Deviation (g/cm^3)	Flow Rate (s/50g)
#1	Pre-alloyed Fe-6.9% w.t. Si	7.4030 ± 0.007	0.0062	21.1
#2	Mixed Fe-6.0% w.t. Si	7.5058 ± 0.007	0.0176	21.7
#3	Mixed Fe-5.0% w.t. Si	7.6654 ± 0.007	0.0229	22.4
#4	Mixed Fe-3.5% w.t. Si	7.7371 ± 0.007	0.0199	23.5
#5	Pure Fe 99% w.t.	7.7552 ± 0.007	0.0075	28.3 (No flow)

Very fine powder, usually smaller than 10µm, is characterised by poor flowability, which agrees with the findings for pure iron in Table 5-3. Further, it is shown that the

higher the amount of pure iron added in the pre-alloyed Fe-Si powder, in order to achieve the desirable chemical composition, the more the flowability deteriorates. Thus, it is generally recommended to use pre-alloyed powders – however, this was not possible for this experimentation and thus mixed powders were used.

5.3 Parameter Optimisation

The aim of this set of experiments is to narrow down the processing parameters window and produce near fully dense soft magnetic parts by LPBF. In order to evaluate the effect of the silicon content of the powders as well as the effect of the building parameters on the formation of defects such as porosity and cracks, the study was divided into four phases listed below:

- Laser Power
- Scan Speed
- Hatch Distance
- Layer Thickness

The width of the tracks, the continuity and regularity as well as the response to changing laser power and scanning speed was determined. In numerous studies, the process parameter window was defined on the basis of geometric defects of 3D printed tracks and on the tracks dimensional accuracy. These authors presented the existence of stability and instability zones and demonstrated the dependence of the geometrical features of 316L stainless steel and 17-4PH steel single tracks on the energy density input. The stability zone is characterised by the formation of a stable molten pool and continuous vectors. On the other hand, instability zone features non-continuous scan vectors and drop formation (balling). Single scan tracks, thin walls and cubic specimens

were produced (Figure 5-3) to assess the effect of the processing parameters on the quality of the end parts. Scan strategies and their effect on density and crystallographic texture will be assessed separately later in this Chapter.

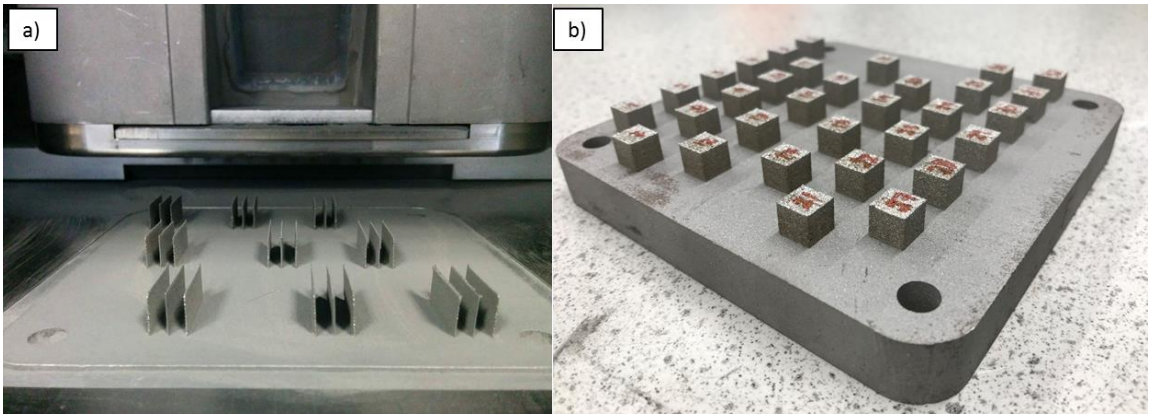

Figure 5-3: Silicon steel a) thin walls and b) cube samples fabricated with Renishaw AM-125 for parameter optimization and density analysis

5.3.1 Laser Power

Initially, the effect of the laser power on scan tracks was assessed and its impact on the relative density of coupons was studied. The laser power varied between 100 and 200 W with intervals of 20 W. The scanning speed (1000 mm/s), layer thickness (30 μm) and hatch distance (0.100 μm) were kept constant in order to evaluate only one process parameter at a time. The optical micrograph in Figure 5-4 shows that for the selected parameter set, a continuous track was obtained for maximum laser power of 200 W.

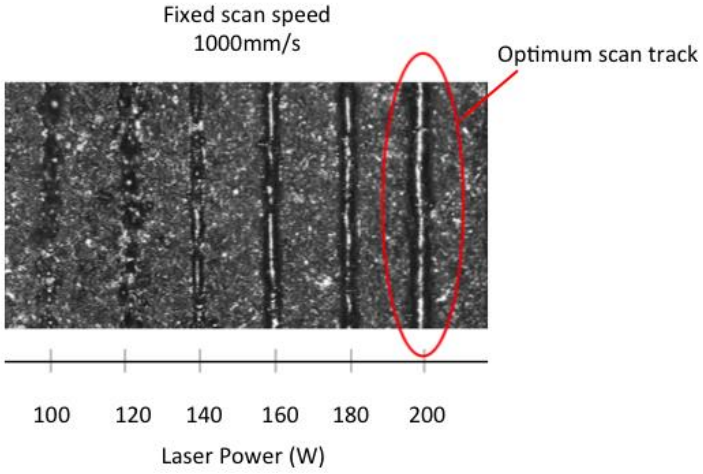

Figure 5-4: Single track morphology with increasing laser

5.3.2 Scan Speed

A further experiment was conducted to determine the optimum scan speed with the laser power fixed at 200 W. The layer thickness and hatch distance were kept constant at 30μm and 0.100 μm respectively. For the first set, scanning speed was varied between 300 and 500 mm/s with 50 mm/s intervals by changing the point distance and maintaining a fixed exposure time at 40 μs. For the second set, the point distance was kept constant at 20 μm and the exposure time varied between 15 and 60 μs resulting in a scanning speed between 500 and 1500 mm/s. To determine the scanning speed the point distance (PD) and exposure time (EX) settings were adjusted based on the following equation:

$$Scan\ speed = \frac{Point\ Distance}{Exposure\ Time} \qquad (5.1)$$

The scan speed that resulted in stable scan-tracks and maximum relative density in coupons was 1000 mm/s as shown in Figure 5-5.

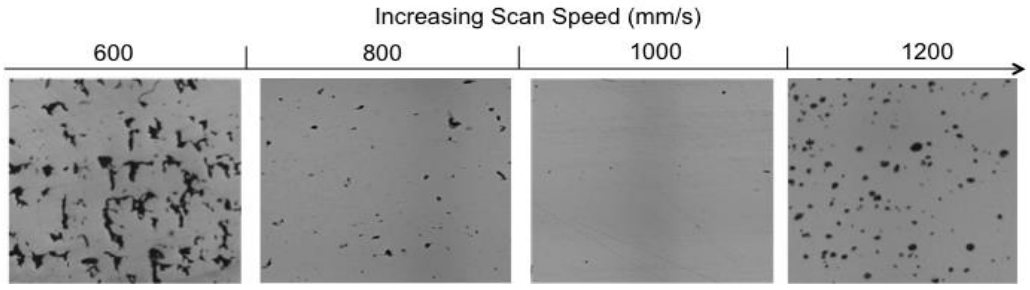

Figure 5-5: Evolution of density with scan speed, micrographs showing the XY (top) plane

5.3.3 Hatch Distance

A set of samples comprising of seven coupons was manufactured using hatch distance values between 60 and 120 μm with intervals of 10 μm. The other parameters were kept constant for the specimens in this study (Laser Power 200W, layer thickness 30μm and

scanning speed 1000 mm/s). The range of hatch distances (60-120 μm) evaluated in this study was relatively narrow and sufficient overlap between adjacent melt pools was achieved for 110 μm Significant difference in terms of porosity was observed for lower hatch distances Figure 5-6. In [14] the authors showed that heat accumulation in the melt pool occurs when using smaller hatch distances because it allows slow cooling of the layer, thereby giving a homogenous and continuous layer. Consequently, it is recommended to use the smaller hatch distance. In this case, the hatch distance of 110 μm was optimum and near fully dense parts were produced. This was considered the best compromise between speed of production and quality of the final parts.

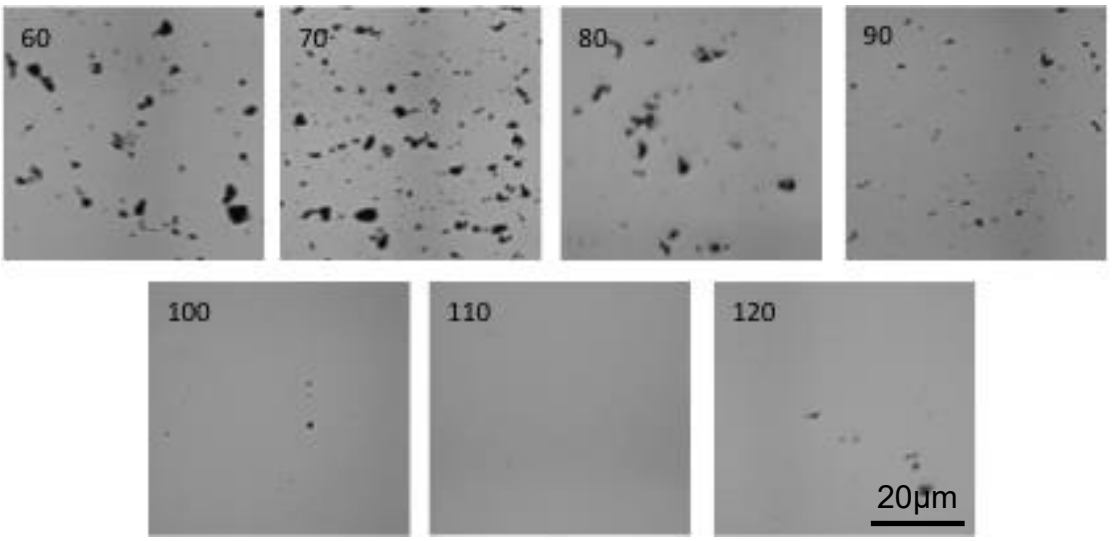

Figure 5-6: Effect of hatch distance in μm, on relative density of Fe-5%Si alloys

5.3.4 Layer Thickness

A number of papers [194,195] have presented results into how layer thickness influences the microstructure and properties of samples manufactured by LPBF technology. In this research we compare the average density of samples manufactured with a layer thickness of 30μm, 40μm and 50 μm for silicon steel alloys (Figure 5-7).

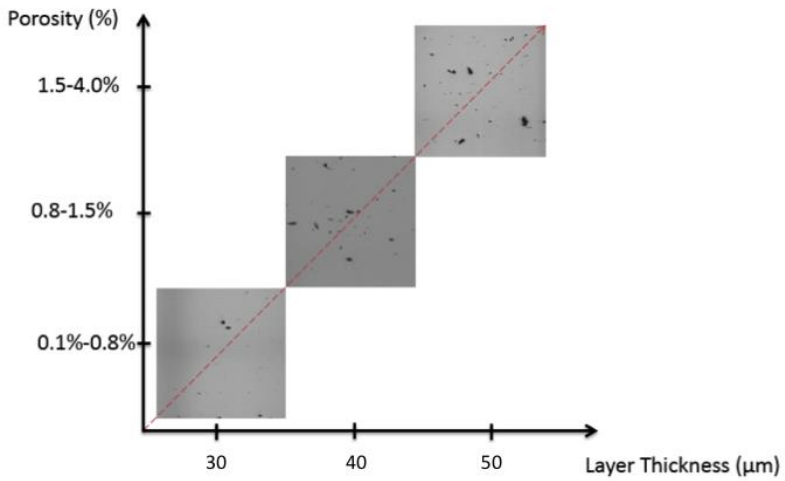

Figure 5-7: Increase in layer thickness results in lower density due to lack of fusion and formation of irregular pores

The powder layer thickness has a clear influence on relative density, mechanical properties, and on the size of the columnar dendritic cells forming during the LPBF process [196,197]. An increase in layer thickness will weaken the bonding between layers resulting in reduced tensile strength and hardness [198]. Layer thickness can also affect the heat input in the material and the intra-layer fusion between the new layer and the previous solidified layer [199]. A larger layer thickness can help reduce residual stresses and reduce build times and cost by reducing the total number of layers that are spread and melted. However, surface roughness is highly affected by the thickness of the powder layer because more powder is available to create spatter. Other studies have also highlighted that part density depends completely on layer thickness and if it is minimal, the melting between layers is improved, with a beneficial effect on part density [200,201]. For a layer thickness of 40 and 50 μm the energy density was not sufficient to fully melt the powder particles, giving rise to porosity. Therefore, it was concluded that optimum layer thickness (also minimum allowable layer thickness for the

Renishaw-125 LPBF machine) was 30 μm for this particular alloy. This was considered the best compromise between speed of production and quality of the final parts.

5.4 Porosity Investigation

Porosity is the most common defect typically observed in LPBF parts and laser power can greatly affect the number of pores and their morphology in the samples. When the laser power is increased, the density of the part is improved due to a higher degree of melted powder and reduced melt pool instabilities. However, if the laser power exceeds a specific limit, crack formation and propagation start taking place due to increased thermal gradients and stresses induced in the part.

There are two types of porosities observed in LBPF parts, metallurgical and keyhole pores, which correspond to the laser energy density and the resulting shape of the melt-pool. Metallurgical pores are irregular in shape and larger in size as shown in Figure 5-8(a) whereas keyhole pores are usually small in size with a spherical shape (Figure 5-8 (b). Metallurgical pores are created at low scanning speed and can be attributed to the high energy induced in the material which causes the entrapment of gases in the melt pool, while keyhole pores originate from keyhole instabilities in the melt pool [22][57]. It is possible to have two different samples with the same amount of porosity but different types of pores. One of the main sources of porosity is the presence of gas either between the powder particles when the packing density is low or in the form of gas bubbles trapped inside the powder particles during the gas atomization process. The gas dissolves in the melt pool and because of the high cooling rates the material solidifies instantly and the gas remains entrapped in the LPBF part.

Incomplete fusion holes, also known as lack-of-fusion (LOF) defects, are mainly caused due to the lack of energy input during LPBF. The formation of LOF defects occurs when powder particles are not fully melted to deposit a new layer on the previous layer with a sufficient overlap [24, 29]. There are two types of LOF defects: 1) poor bonding defects due to insufficient molten metal during a solidification process, as in Figure 5-8(c) and 2) defects with un-melted metal powders in Figure 5-8 (d). In the deposition process of a new layer, it can become difficult to fully re-melt these powders and, as a consequence, incomplete fusion holes are formed in the fabricated parts. Furthermore, if the laser energy input is too low to cause insufficient penetration depth in the melt-pool, LOF defects may be generated due to a poor interlayer bonding [24, 29, 37]. Therefore, LOF defects are usually distributed between the scan tracks and the deposited layers. Moreover, in a location where defects have been generated, the surface of the location becomes rough. The rough surface directly contributes to the poor flow of the molten metal to form interlayer defects. The interlayer defects may gradually extend and propagate upwards to form large multi-layer defects in a continuous deposition process [38]. For a easily oxidized alloy materials, such as aluminium AlSi10Mg, a layer of oxide film is usually produced at the surface of a part with residual oxygen in the LPBF process. As a consequence, wettability decreases and molten metal flow is blocked, leading to a poor bonding between the layers to form the incomplete fusion defects [25, 39].

For low laser power below between 100-160W, pores were observed in the cross-section micrographs of polished samples. The pores were uniformly dispersed, they were irregular in shape and interconnected. Moreover, they featured large cavities filled with un-melted powder particles.

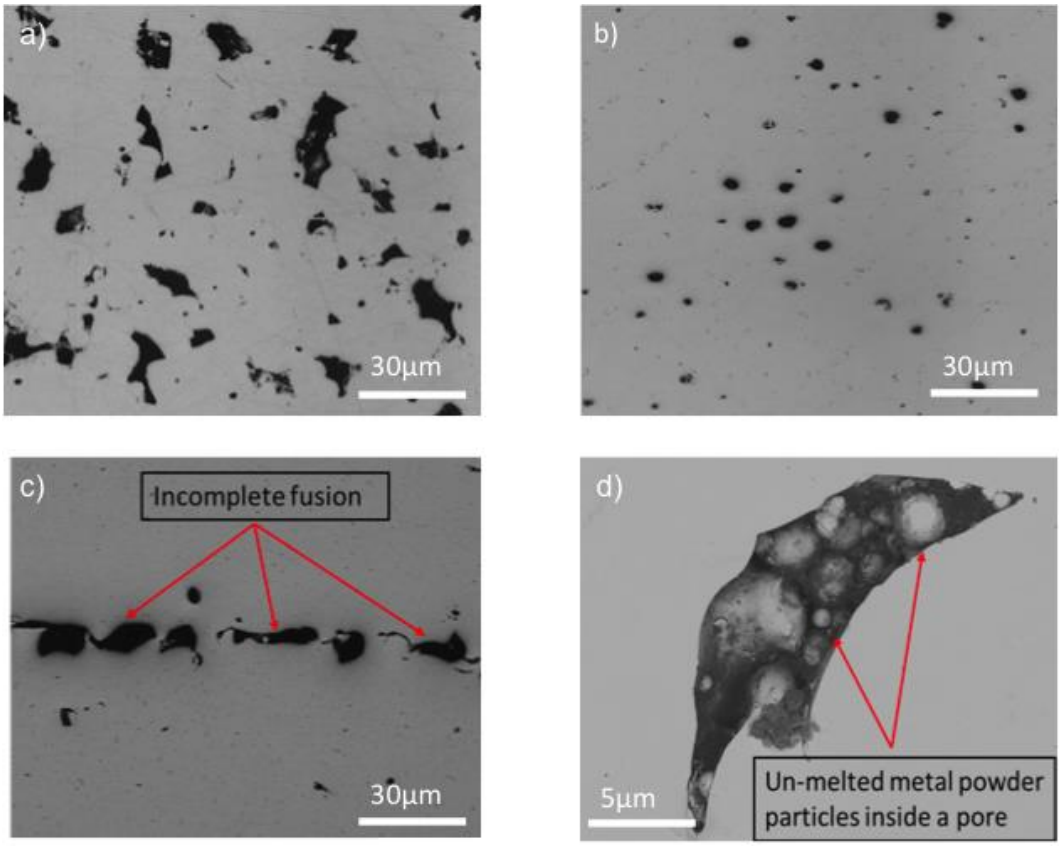

Figure 5-8: Two types of porosity (a) Irregular Keyhole pores, (b) Spherical Metallurgical Pores, Porosity due to incomplete fusion and d) Un-melted powder particles trapped inside a pore.

At low laser power the size of the melt pool is small and powder particles are not adequately molten to ensure sufficient bonding between the layers due to lower penetration depth of laser. At higher laser power the pores are mostly spherical in shape. With higher laser power low melting elements might evaporate and become entrapped leaving behind gas voids and solidification shrinkage. Similar results were obtained for all the compositions of silicon steel alloys that were tested in this study.

5.5 Cracks Analysis

Cracks have a detrimental impact on mechanical and magnetic performance of parts. A high-power laser beam irradiates metal powders during the LPBF process, which causes

rapid melting and solidification with high cooling rates in the melt pool. Effectively, high temperature gradients are created within the part and large residual stresses are induced. The combination of the two during the layer by layer process causes crack initiation and propagation as mentioned in [202–205]. Similar to stainless steels and nickel-based super-alloys, silicon steel has a low thermal conductivity and high thermal expansion coefficient, thus it is highly susceptible to cracking [206,207].

The morphology and size of the cracks was determined by optical and scanning electron microscope. Figure 5-9 shows that cracks in silicon steel are more prone to initiate either from a pore or from the edge of the part where residual stresses are usually larger. There is an increase in the crack formation with a slight increase in the energy density due to the large thermal stresses induced in the as built parts. An increase in the number of cracks per sample is also observed with the increase of silicon content.

Substrate pre-heating proved to be only partially effective to reduce the total number of cracks and their size. On-going work is being done to evaluate the residual stresses of high-silicon parts with different scan strategies that might open the path to processing silicon steel with higher silicon content. Preheating the substrate to temperatures higher than 200 ^{o}C can reduce the thermal gradients and correspondingly the cracks in the laser processed parts [208].

Cracks were found in all the samples that were fabricated with the pre-alloyed 6.9%w.t. (Figure 5-10) For the powder blends with silicon content lower than 6.0%w.t only a few

cracks were formed at the edge of the samples. All Fe-3.5%Si and Fe-5.0%Si samples were crack free.

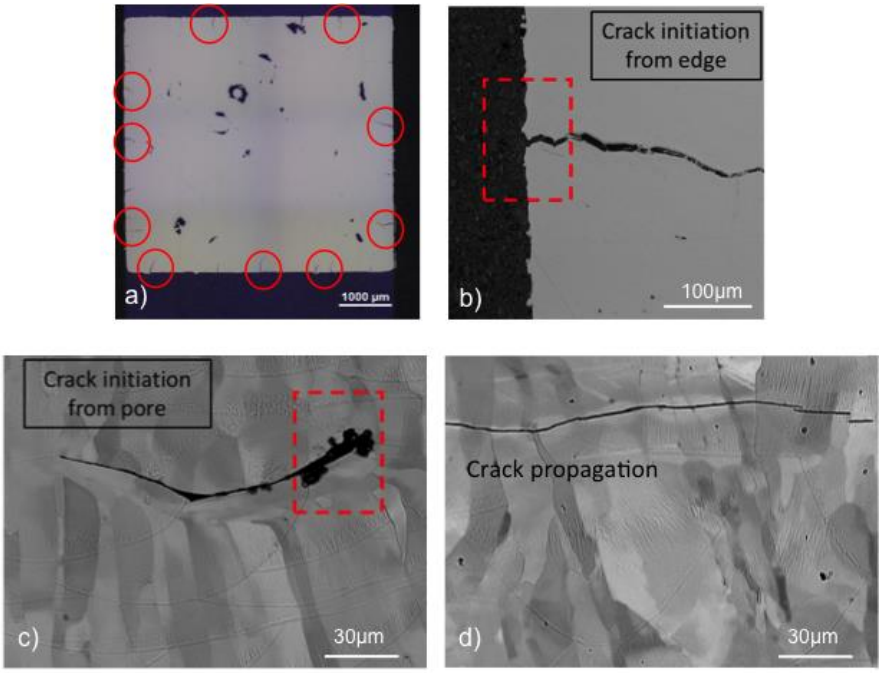

Figure 5-9: (a) Optical micrograph showing the initiation of a crack from the edge, (b) SEM micrograph with pore as the starting point of the crack, (c) Micro-cracks due to higher silicon content and embrittlement of the sample, (d) Crack propagating perpendicular to the build direction.

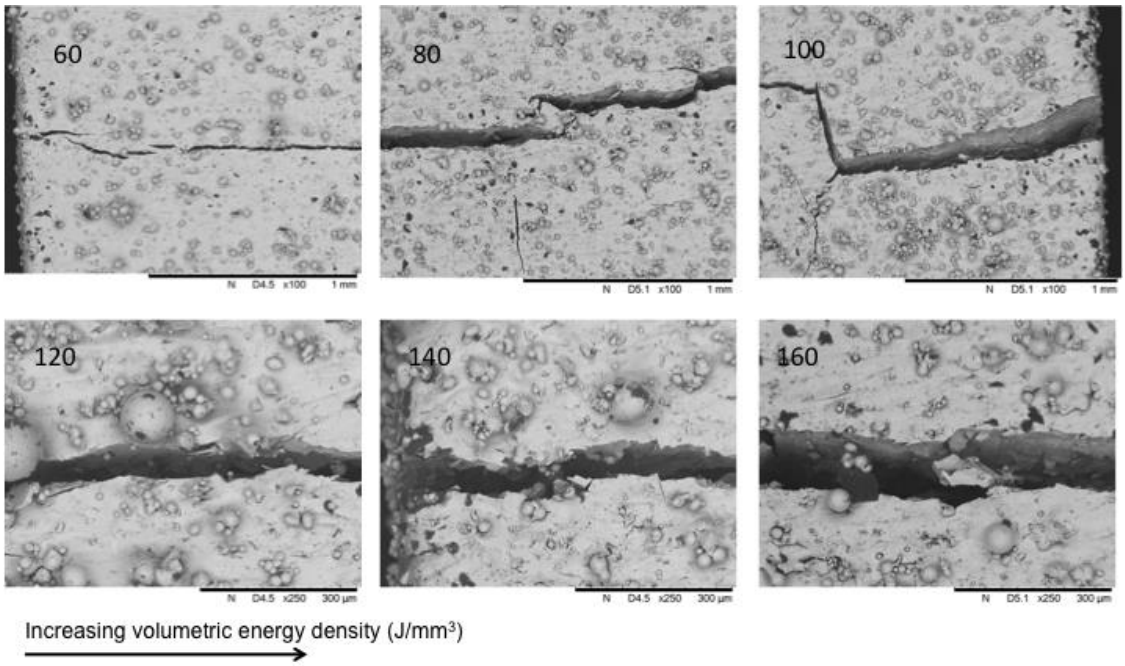

Figure 5-10: Low and high magnification SEM micrographs of cracks formed in Fe-6.9wt% Si with increasing volumetric energy density.

5.6 Microstructure

The optical and SEM micrographs in Figure 5-11 show the grain structure of the samples in the as-built condition (a, b, c) as well as after annealing (d, e, f). Grain size is within the 20-50 μm range for the as-built microstructure (Figure 5-11 a), b) and c)) irrespectively of silicon content.

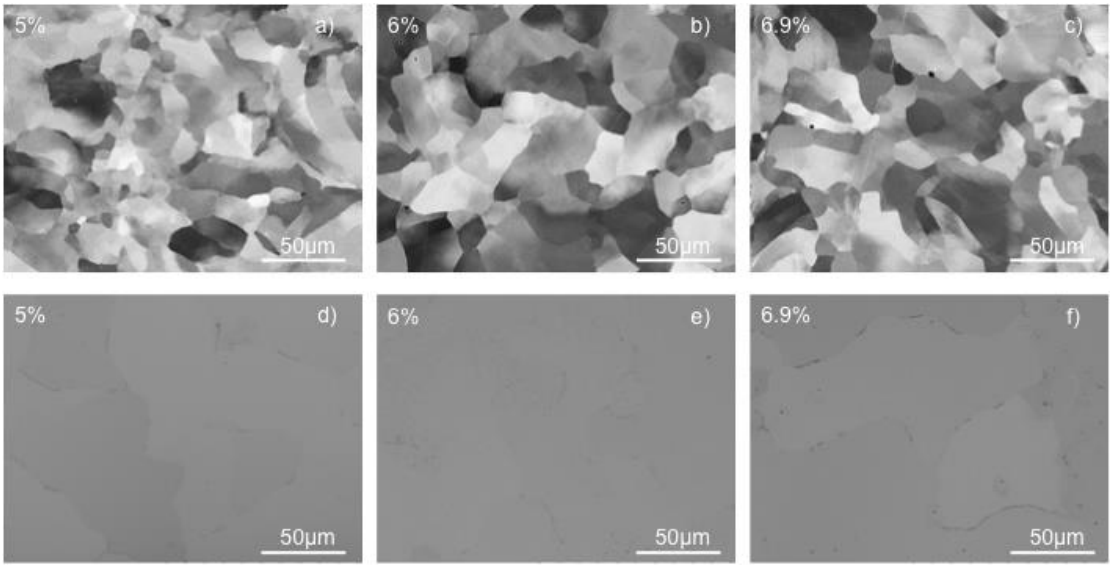

Figure 5-11: Comparison of Fe-Si samples with increasing silicon content in the as-built a), b), c) and annealed condition d), e), f) respectively. SEM micrographs in the XY plane

The microstructure in the as built state is characterised by continuous melt pools and ferritic grains that grow epitaxially over several built layers (Figure 5-12 a)). In higher magnification images (Figure 5-12 c) it is possible to observe the cellular-dendrites, which are slightly larger closer to the melt pool boundaries where the material remains the longest time at the hottest temperature. During solidification the growth of the grains starts at the melt pool boundary and continues towards its centre and mainly follows the build direction aligning to the z axis (Figure 5-12 b)). Such epitaxial growth has been also reported in [8] for Fe-6.9wt%. The melt pool boundary appears thick as the material contains a high amount of Si that segregates in these regions. While the x-y plane shows a clear anisotropy in the form of grains elongated in z direction, the grain orientation is

completely inhomogeneous on the x-y plane (Figure 5-11) for all three compositions of the soft magnetic alloy.

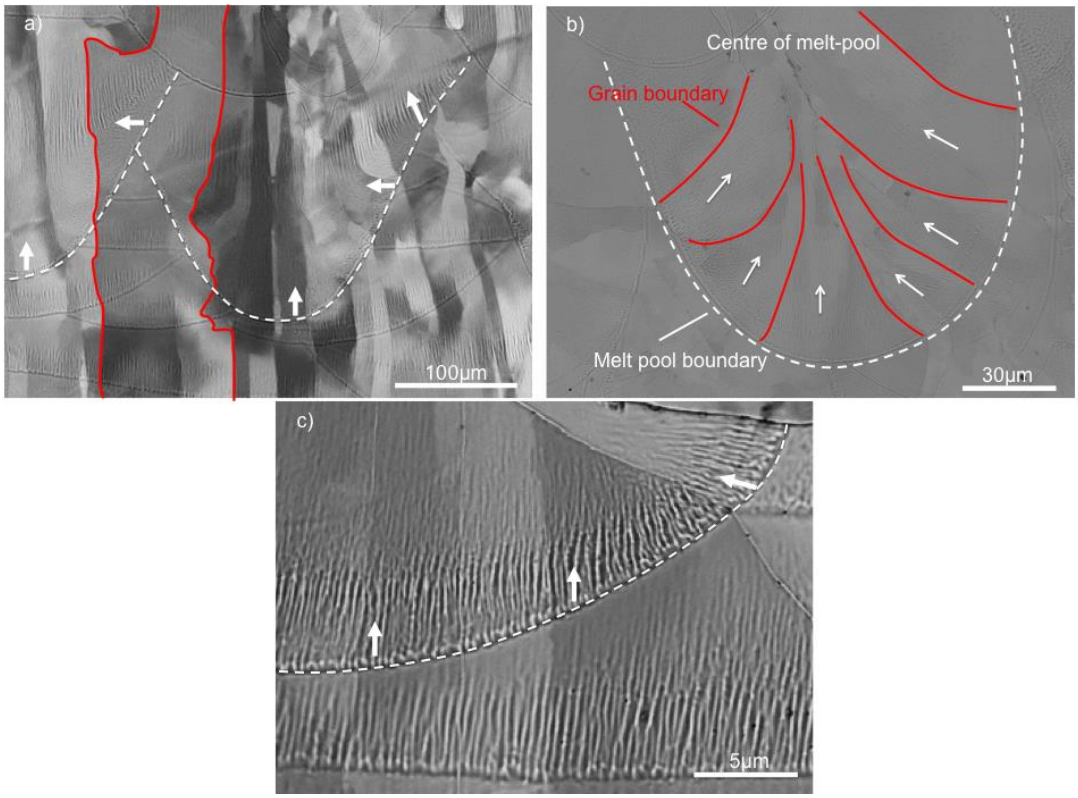

Figure 5-12: a) Epitaxial growth of grains over several layers, b) grain growth in melt-pool, c) cellular-dendrites

The samples were subjected to annealing in an argon atmosphere at 1150 ^{o}C for 90 min hour followed by furnace cooling. After annealing the microstructure appears to be coarse-grained, and fully homogenised. The melt pool boundary lines have completely disappeared (Figure 5-11) and this is attributed to the dissolution of Si in the solid. The high annealing temperature resulted in a complete dissolution of the melt pool structure and small traces of segregation were observed. In higher magnification SEM micrographs (Figure 5-13 a), b) and c)) residual cementite can be seen. In [209] J. Lemke et. al. observed the formation of residual cementite even though they used an ultra-low carbon steel with carbon content down to 0.002 wt. %, which is lower than the Fe-Si alloys in this study. In the annealed condition the epitaxial structure disappeared and the

material became more isotropic as the grain structure becomes more homogenous. The segregations that were originally found at melt pool boundaries went into solid solution, the material was completely homogenised and residual traces of the silicon-rich zones were not observed. During the slow furnace cooling, the silicon segregated again resulting in a structure that overlaid the ferritic grains. Therefore quenching should be used as the final step during heat treatment [60].

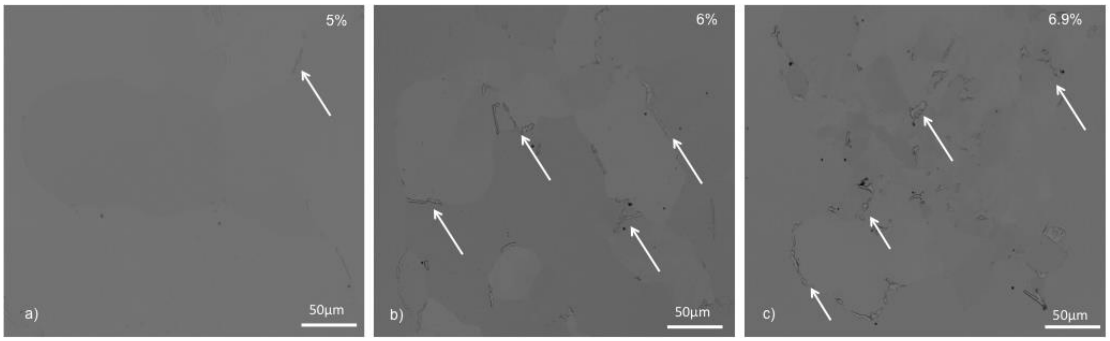

Figure 5-13: Micrographs for a) 5%, b) 6% and c) 6.9% with arrows showing residual cementite in the grain boundaries after annealing

5.7 Effect of Scan Strategies on density and crystallographic texture

Up to this point the effect of scan strategies on the manufacturing of silicon steel samples has not been tested and evaluated. The objective of this further study was to determine whether a specific scan strategy could improve the density and alter the crystallographic texture. The scan strategies that were used to process Fe-6wt%Si and the resulting relative densities are shown in Table 5-4.

Table 5-4: Scan strategies used for assessment of density microstructure and texture of Fe-6wt%Si processed via LPBF

Scan Strategy	No. of scans per layer	Uni/bi-directional	Rotation angle	Island size (mm)	Laser Power 1st Scan (W)	Laser Power 2nd Scan (W)	Relative Density (%)
Meander 1	1	Unidirectional	90°	-	200	-	99.845
Meander 2	1	Unidirectional	67°	-	200	-	99.986
Stripes 1	1	Unidirectional	90°	-	200	-	99.347
Stripes 2	1	Unidirectional	67°	-	200	-	99.763
Checkerboard 1	1	Unidirectional	90°	5	200	-	99.579
Checkerboard 2	1	Bidirectional	67°	5	200	-	99.723
Checkerboard 3	1	Bidirectional	90°	2.5	200	-	97.629
Checkerboard 4	1	Bidirectional	67°	2.5	200	-	99.410
Pre-melt 1	2	Unidirectional	67°	-	100	200	99.875
Pre-melt 2	2	Unidirectional	67°	-	100	150	99.313

Meander bidirectional scan strategy with a rotation angle of 67 and 90 degrees between layers was employed and resulted in the highest relative density. The checkerboard scan strategy resulted in samples with slightly lower density. The 'Pre-melt' scan strategy applies two scans in each layer with a layer scanned at first with half the power followed by a second scan with full power. Although the 'Pre-melt' scan strategy resulted in a smooth surface finish of the test samples the density values were actually inferior when compared to 'Meander 2'. In Figure 5-14 a sample fabricated with 2.5 x 2.5 mm islands is illustrated. With respect to the checkerboard scan strategies, when the overlap between islands was set to zero it resulted in small gaps between adjacent islands at the intersections of the corners (90o). This finding is highly pertinent as it can be applied for printing parts where eddy current reduction is relevant, where the "air-gaps" will effectively reduce the eddy current loops in the part and, consequently, the losses related to eddy currents.

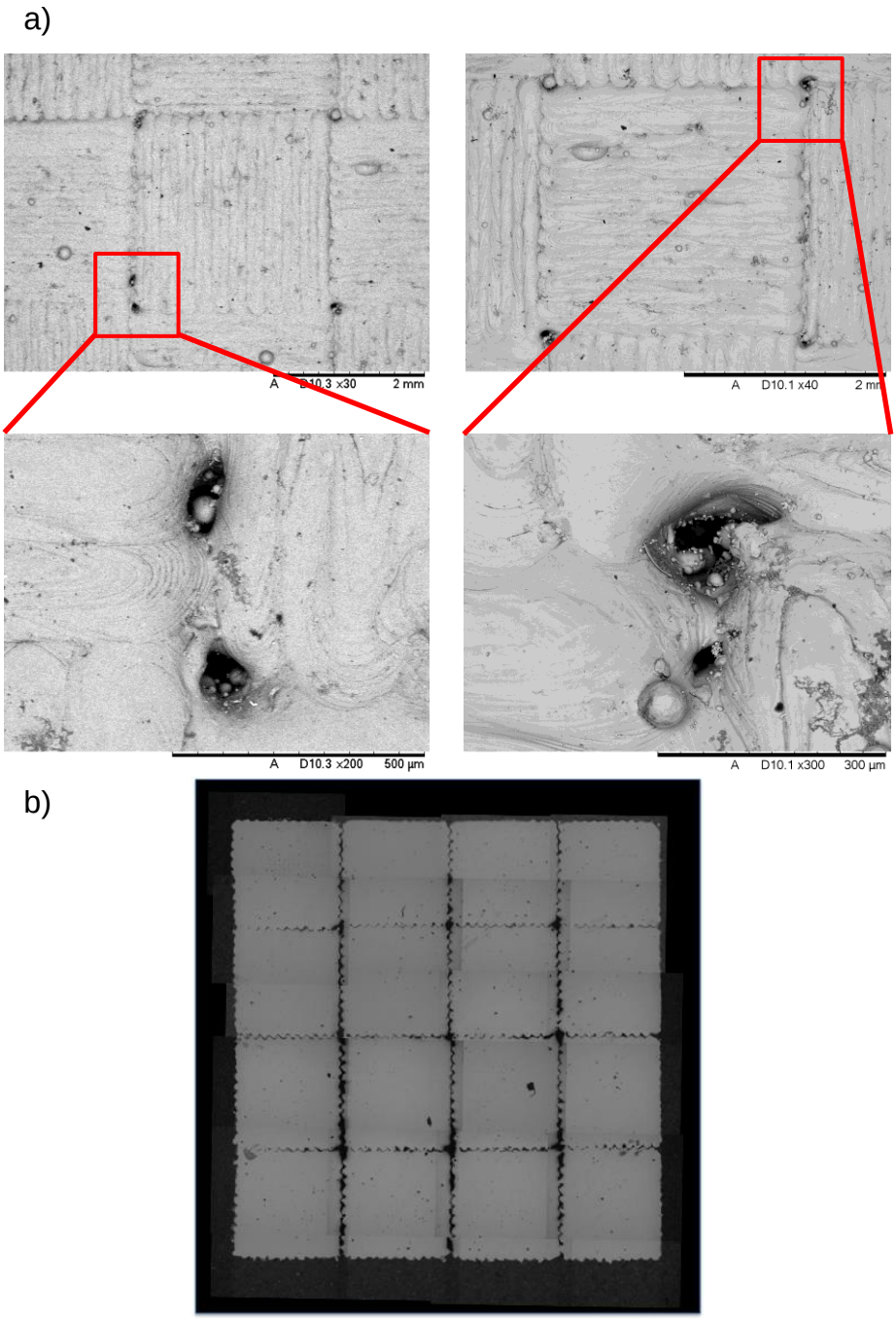

Figure 5-14: a) SEM micrographs showing lack of fusion in between islands boundaries for the checkerboard 1 & 3 scan strategies in low and high magnification of the top surface. b) Optical micrograph (stitched images) of prototype cube 10x10x10 mm fabricated with checkerboard 3 scan strategy and zero overlap between islands.

For the analysis of the crystallographic texture, EBSD maps were collected for each sample covering an area of 2.3 mm^2 at a step size of 10 µm. All the samples exhibited texture, but the type and strength of the textures varied considerably. The majority of

samples were characterised by a <111> fibre texture parallel to the growth direction, usually dominated by one or two orientations around the fibre axis. Of these, meander 1 and checkerboard 4 had relatively strong <111> fibre textures, while for meander 2, stripes 1, checkerboard 1 and checkerboard 2 the strength was moderate, and for pre-melt 1 it was weak.

Furthermore, most of the samples had concentrations of {100} pole density around the growth direction, though in most cases this was relatively weak. The exceptions are checkerboard 3, which showed a cube texture, and pre-melt 2, which showed a <100> fibre texture parallel to the growth direction, both of moderate strength. Pre-melt 1 had a roughly equal mixture of the <100> and <111> fibre textures. Pole Figure images for 3 scan strategies are presented in Figure 5.16. All pole Figures can be found in APENDIX 2.

In [211] the texture strength index of Fe-6.9wt% Si alloy for various annealing conditions was presented. It was shown that high temperature annealing can be performed without weakening the beneficial crystallographic texture induced by LPBF [212]. However, in this study when the energy density was increased the 3D printed parts suffered from extensive cracking. Therefore, a trade-off between part quality and texture intensity was made.

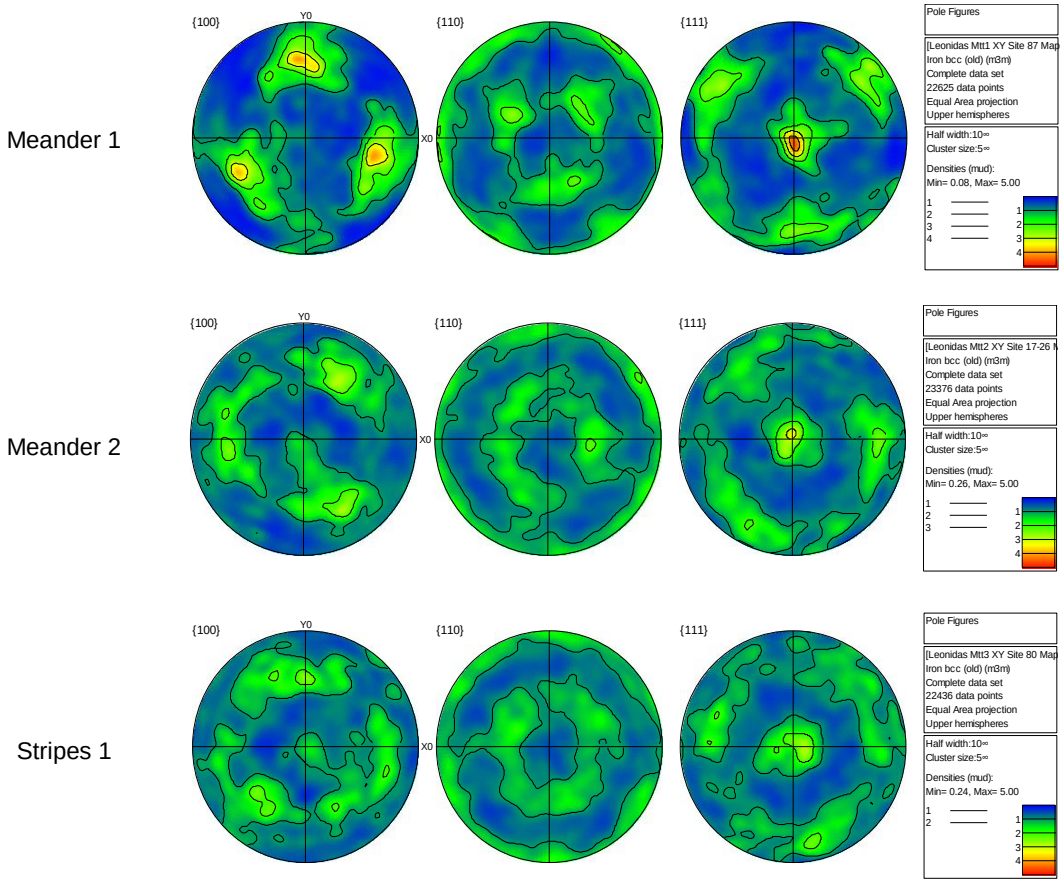

Figure 5-15: Pole figures showing the type and intensity of texture for the 10 scan strategies employed

The EBSD maps in Figure 5-15 show the crystallographic texture of the grains along the build direction, and the transverse direction for meander 1 and meander 2 scanning strategies. The EBSD analysis indicates that the scanning strategies employed in this study do not alter significantly the <001> fibre texture induced by LPBF along the build direction. However, there was clear evidence of grain orientation differences due to scan direction effects. As seen, for meander 1 scan strategy (Figure 5-17), a square pattern (mosaic) is apparent in the XY plane because of the specific scan paths used for fabricating the sample. The same effect was found for stripes 1 scan strategy. The size of each square is approximately 100-120µm which is similar to the hatch distance of 110µm. The same effect was also observed for the stripes scan strategy with 90^{o} rotation between layers. A schematic of the formation mechanism was first presented in [210]

and is also illustrated in Figure 5-16 below; during LPBF, the thermal gradients and growth rates differ along the melt pool due to the movement of the laser beam. Similar to the findings in [108] the highest thermal gradients were located in the central regions of the melting track and decreased towards the borders [27]. The previously melted tracks were subjected to over-heating; they were heavily re-melted and crossed on the subsequent laser tracks. In the XZ plane the grains were found to orientate along the build direction, which is attributed to the epitaxial mode of grain growth and to the symmetry of the BCC crystallographic cell. For meander 2 and stripes 2 (67°) the grains are not so well defined in the XY and XZ planes.

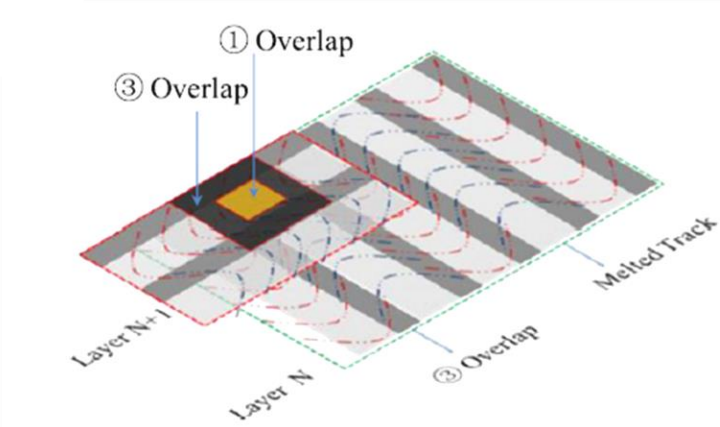

Figure 5-16: Schematic illustration of formation of square pattern in top view XY for meander with 90° rotation between layers [210]

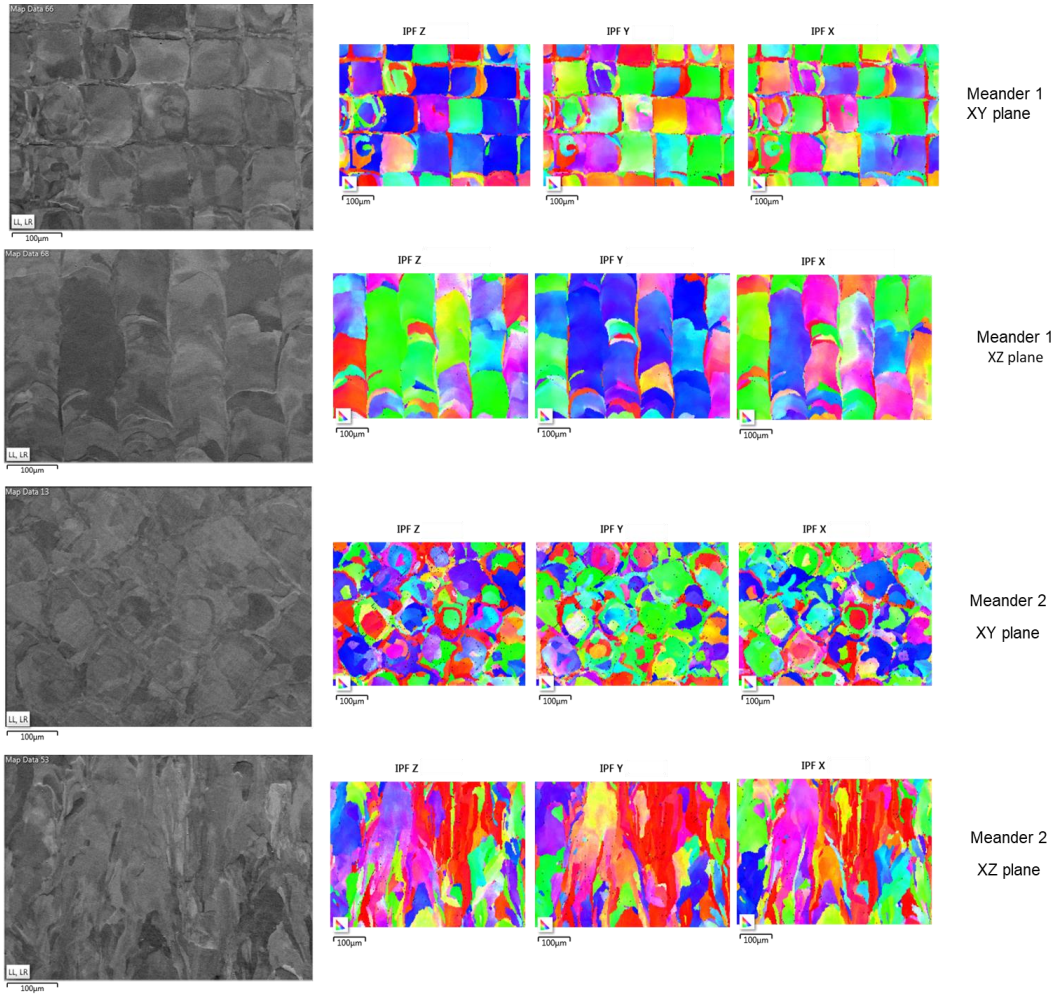

Figure 5-17: SEM micrographs and EBSD maps for meander 1 (90º) and meander 2 (67º) with epitaxial growth along the build direction and mosaic pattern formed in the XY plane for meander 1.

5.8 XRD Results

XRD samples for Fe-Si alloys with a silicon content between 5-6.9%w.t. were measured with an XRD Bruker D8 Advanced Diffractometer (Figure 5-18). Samples of the feedstock material in powder form, cubes processed via LPBF in the as built condition and annealed cubes were compared. The XRD results elucidate the effect of the LPBF process and high temperature annealing on the appearance of DO3/B2 ordered phases. A comparison between the three Fe-Si alloys (5%, 6%, 6.9%) used in this study is presented. It is shown that the microstructures of all samples are characterised by a

single bcc-phase because the high silicon content suppresses the formation of γ phase. However, it is evident that diffraction peaks associated with type B2-DO3 phase ordering appear following LPBF processing for 6% and 6.9%, where it is assumed that LPBF cooling rates cannot fully suppress the ordering phase transformation.

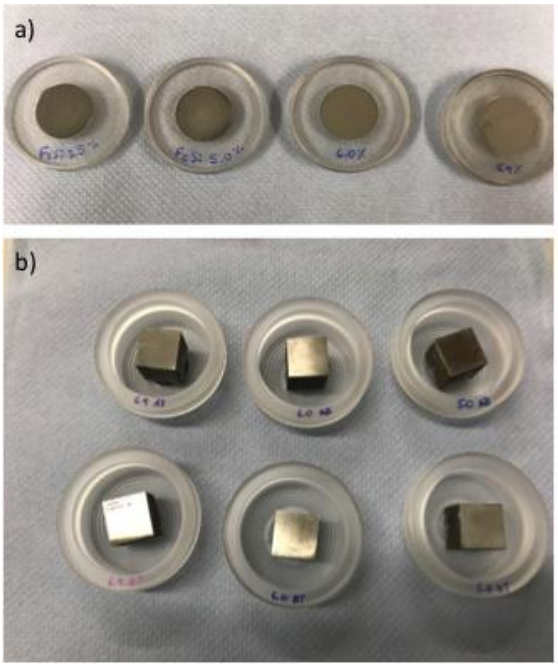

Figure 5-18: Fe-Si samples with varying silicon content between 3.5-6.9%w.t. in a) metal powder samples and b) as built and heat-treated cubic samples processed by LPBF.

After annealing at 1150 C for 90 min, the intensity of peaks is increased suggesting that the slow cooling rate (furnace cooling) is not sufficient to prevent ordering. However, if quenching follows after annealing, the cooling rates are fast enough to keep the Si in solid solution and prevent the ordering reaction, thus quenching of samples processed via LPBF is recommended. It must be noted that the ramp up and ramp down temperature must be kept to a minimum to avoid cracking of the samples during post processing. The XRD results are presented in Figure 5-19.

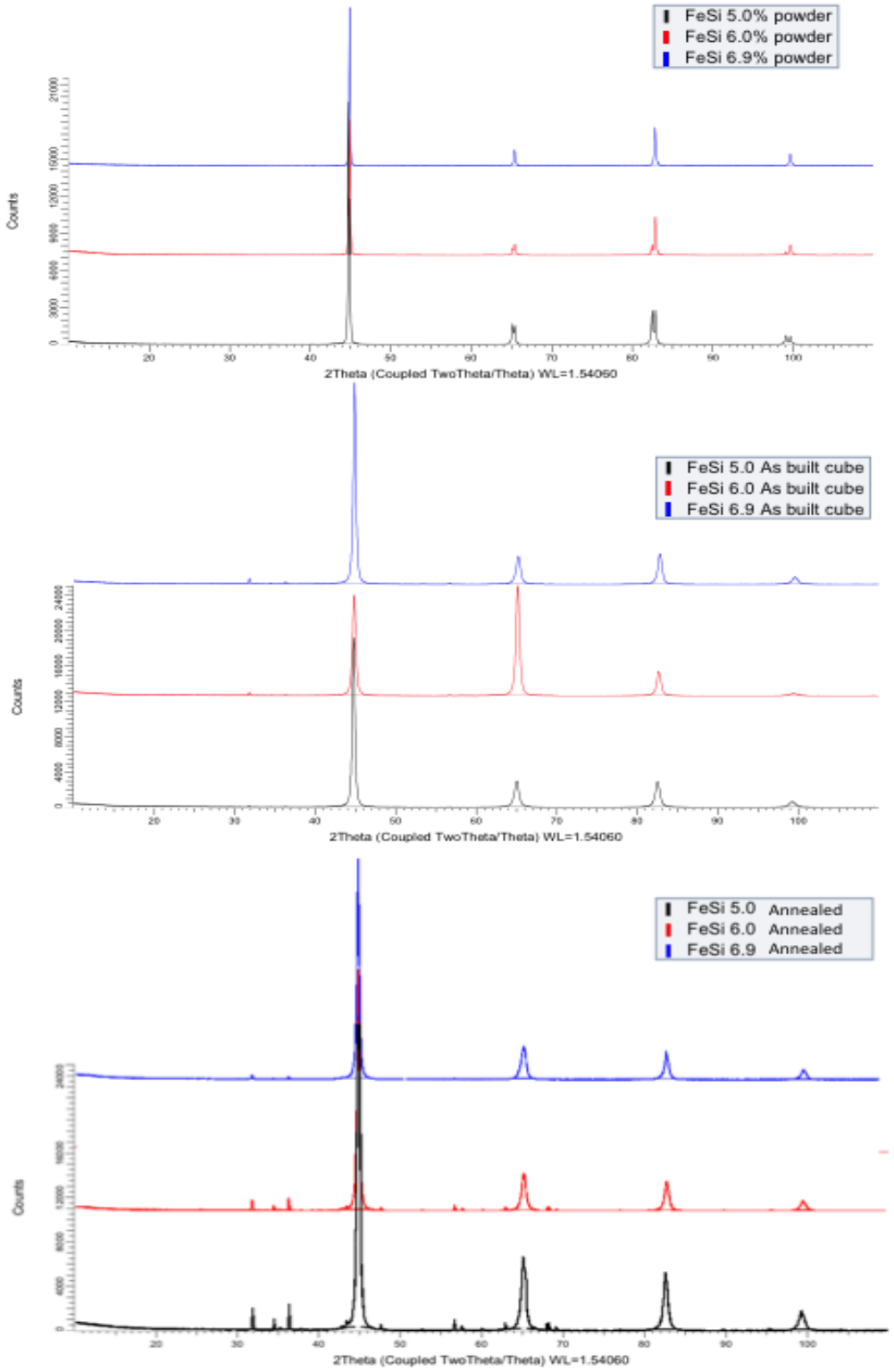

Figure 5-19: Comparison of XRD spectra for Fe-Si alloys with 5%, 6% and 6.9%w.t Si for powder, as built cubes and annealed cubes at 1150 C for 90 min.

5.9 Lattice Peak Parameter

The lattice parameter of the Fe-Si system decreases linearly with increasing Si content [35]. The slope of the function describing the linear relationship changes abruptly at 5%Si, owing to the onset of atom ordering. As previously shown in [108] the lattice parameter for high-silicon steel samples has a lower value when compared to the value for pure bcc-Fe and is well above that for cast Fe-6.9%Si, where superstructure lines in the XRD spectrum are known to appear due to ordering initiation [35]. The value for the unprocessed powder blends was found to be lower than as built and annealed samples (Figure 5-20).

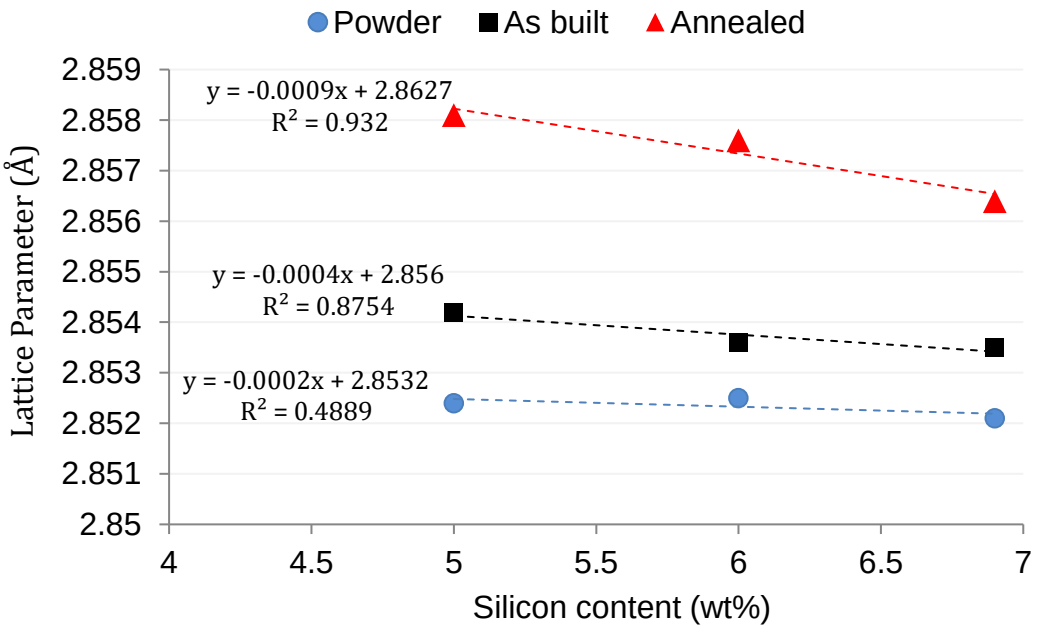

Figure 5-20: Evolution of lattice parameter for silicon steel with increasing silicon content for metallic powder, as built and annealed samples

Moreover, the lattice parameter decreases with increasing silicon content which is in agreement with the findings in [108] and [211]. The decrease of the lattice parameter can be explained as the result of diffusion of the silicon with smaller atomic size into the

iron matrix, which is characterised by a larger atomic size. Thus, a substitutional solid solution is formed during the crystallization process.

5.10 Conclusions

The experimental approach to optimise the process parameters for silicon steels has been described in this Chapter. The effects of the main LPBF process parameters on the quality of the soft magnetic alloys and a microstructural analysis have been presented. It has been shown that within the optimal window of laser energy density, some process parameters can be adjusted for increased density without undermining the properties of the material. However, it must be noted that for Fe-Si powders with high silicon content, some defects, such as pores and cracks, were observed in the samples even when processed with the optimum parameter set. The impact of scan strategies on the crystallographic texture was also presented with the use of pole Figures and EBSD maps. Finally, XRD was used to investigate the ordering-disordering transformations for the Fe-Si alloys in various conditions (powder, as built and annealed).

In summary, the laser melting of Fe–Si alloys with a silicon content of 5.0%w.t., 6.0%w.t. and 6.9%w.t. was systematically investigated in this work. The main findings of this research can be summarised in the following points:

1. Various scan strategies were tested in order to measure and minimise the residual stresses and consequently improve the processing ability of Fe-Si binary alloys with LPBF. The effects of the scan strategies on the microstructure and texture were also assessed
2. Fe-5wt%Si samples processed with the optimum set of parameters featured the highest relative density of 99.98%. With higher silicon content, the relative

density of samples decreased with density values of 99.8% and 98.5% for Fe-6wt%Si and Fe-6.9wt%Si respectively.

3. The microstructure of all the LPBF samples consisted of α' columnar grains oriented towards the build direction (z-axis).
4. Two main defects were observed in the solid specimens, porosity and cracks. The formation of un-melted powder defects was mainly attributed to inappropriate overlap rates and unstable scanning tracks, which can be eliminated by adjusting the processing parameters.
5. XRD measurements indicated that there is a difference between the phase of high silicon steel powders and parts processed by LPBF. Ordering phases were observed for the Fe-Si alloy compositions that were investigated.
6. Metallurgical and keyhole pores were eliminated with the optimization process. However micro-cracks were highly dependent on the silicon content. High silicon content and its interaction with high thermal gradients and residual stresses induced during the LPBF manufacturing process cause embrittlement and crack propagation in components with silicon content higher that 6%w.t.

6. Chapter 6: Fe-Si alloys material properties

6.1 Introduction

The material properties of silicon steel alloys processed using LPBF are presented in this Chapter, which aims to shed light on the mechanical and magnetic properties of the alloys, in order to lay the foundation for the application of this class of materials for the production of electric motors. The effect of silicon content and condition (as built, annealed) on the properties of the binary soft magnetic alloy is investigated.

6.2 Micro-hardness (Vickers Hardness)

In this study, silicon steel cube samples with silicon content between 3%-6.9%w.t. were processed by LPBF with an optimum parameter set. In order to assess the effect of the silicon content on the mechanical properties, micro-hardness was measured with the use of a Vickers indenter. Indentation results are expressed as mean ± standard error and are shown in Figure 6-1.

The theoretical values shown in Figure 6-1 were calculated for a high and low silicon content based on empirical equations 2.1 and 2.2 It can be observed that for the low silicon content area (silicon content below 5%w.t.) the experimental value for Fe-3.5%w.t. Si is significantly higher (219.36 HV) in comparison to the theoretical value (approximately 145HV). However, for the higher silicon content area (above 5%w.t.), it is shown that LPBF as built Fe-Si samples have lower values than the theoretically calculated. This indicates that high silicon steel soft magnetic alloys processed by LPBF are more ductile in comparison to the theoretical values calculated and have been previously validated in the literature.

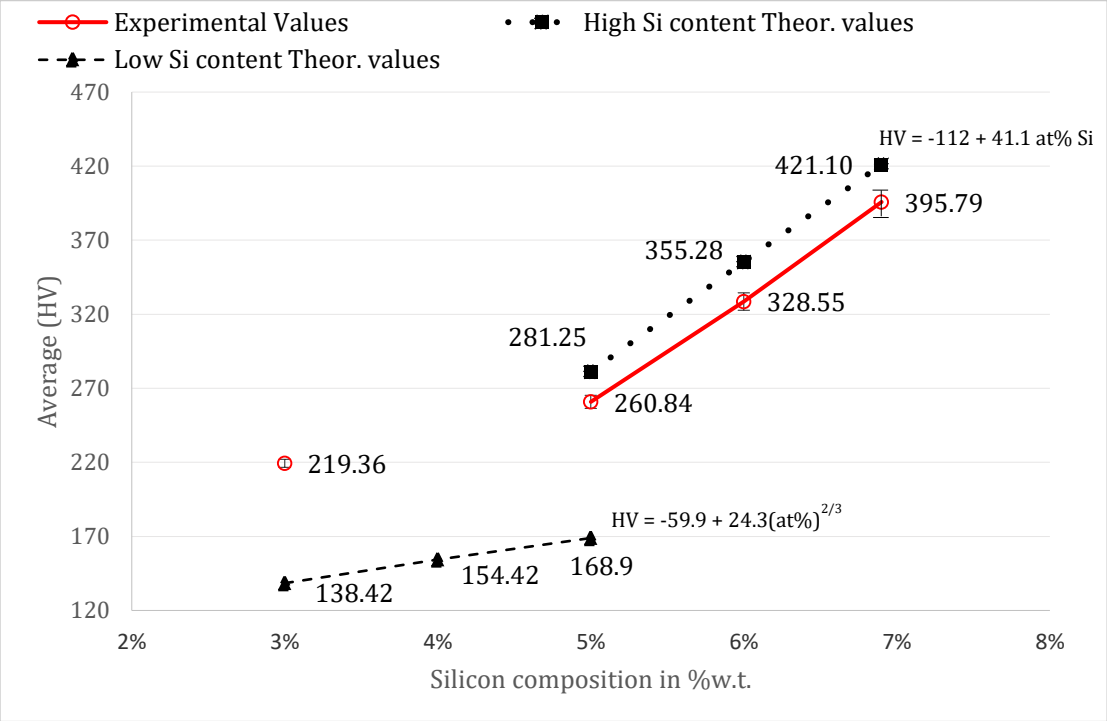

Figure 6-1: Effect of silicon content on the average Vickers Hardness, experimental results are shown with red line and dashed line shows the theoretical values calculated based on equations (6.1) and (6.2) for high and low silicon content.

The micro-hardness was also measured for samples that were heat treated at 1150 ºC for 90min and the results were compared to the as-built samples. The hardness increases with increasing silicon content both for the as built and the annealed samples (Figure 6-2). Annealing causes an overall increase in the micro-hardness of Fe-Si processed via LPBF. The evolution of hardness following the heat treatment is more evident for silicon over 5%w.t. The increase in hardness values is attributed to the formation of ordered phases for the high silicon steel alloys. The XRD spectra presented in Figure 5-19 verifies the presence of ordered phases that is known to increase the HV. This explanation is also supported by the small increase in the HV of 3.5%Fe-Si where ordered phases were absent in the XRD spectra.

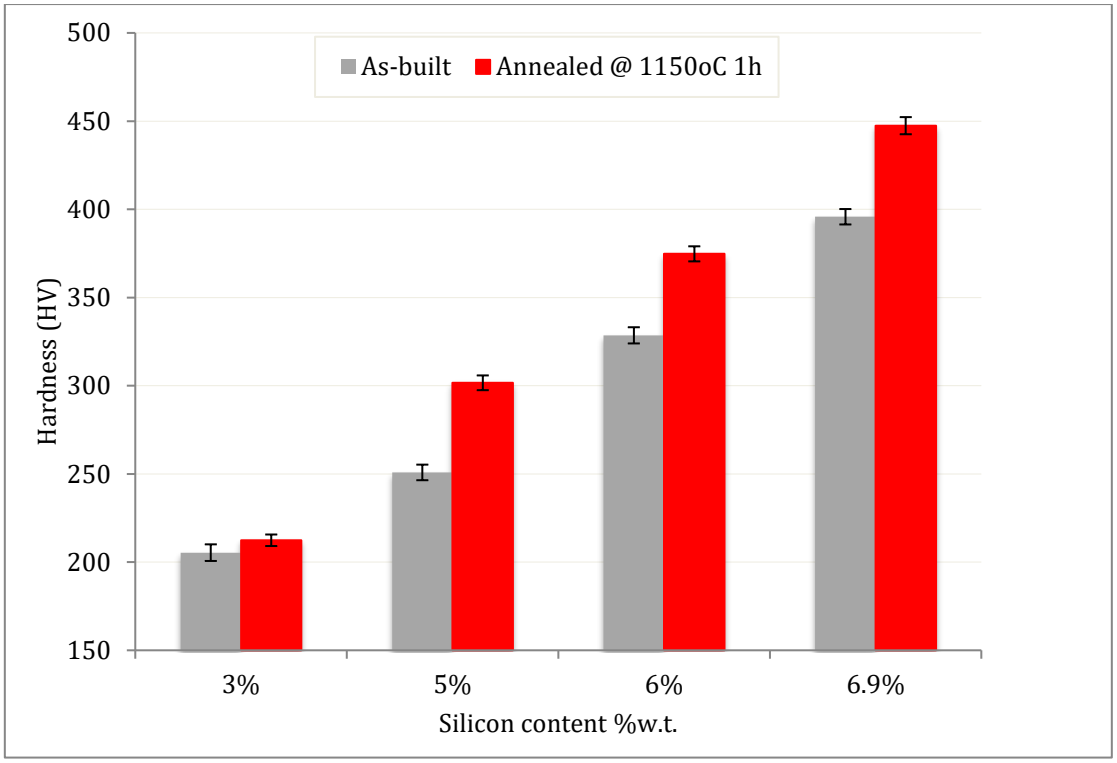

Figure 6-2: Comparison of Vickers Hardness for as-built vs annealed samples with varying silicon content

The results so far indicate that hardening takes place during stress relief [81] and high temperature annealing of Fe-Si alloys that have been manufactured by LPBF. Vickers Hardness is dependent mainly on Si-content only for near fully dense samples, regardless of the heat treatment conditions. For the range of Fe-Si alloys investigated in this study, part of the material under the indenter was pushed out on the surface forming a small pile up around the sides of the imprint (Figure 6-3). This was observed for both as-built and annealed samples.

An additional set of Fe-6%w.t. Si samples was used to evaluate the effect of porosity on micro-hardness. The samples were processed with the maximum laser power of 200 W and increasing scan speeds between 800-1500 mm/s with intervals of 100 mm/s. The samples featured an increasing value of porosity with increasing scan speed and the maximum density was achieved for 1000mm/s.

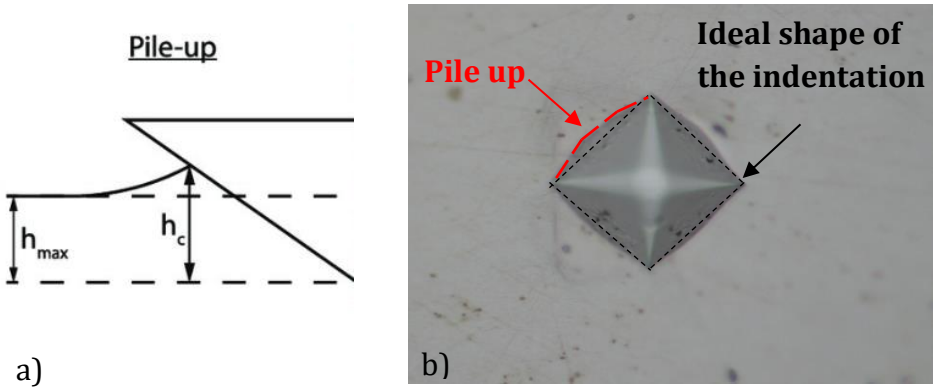

Figure 6-3: a) Schematic of indentation pile up shape and b) optical micrograph of a typical indentation of a Fe-5%Si sample.

Figure 6-4 shows that the relationship is linear and the micro-hardness decreases linearly with a decrease in energy density and effectively an increase in porosity values. It is also important to note that the micro-hardness values presented so far were for indentations on the plane parallel to the build direction in the as built and heat-treated samples. The plane perpendicular to the build direction showed an average micro-hardness of 5% lower. As reported previously, anisotropy in the mechanical properties of LPBF parts is attributed to the layer-by-layer manufacturing approach and the grain structure and texture developed as a result of the thermal gradient. Anisotropy was not observed in the

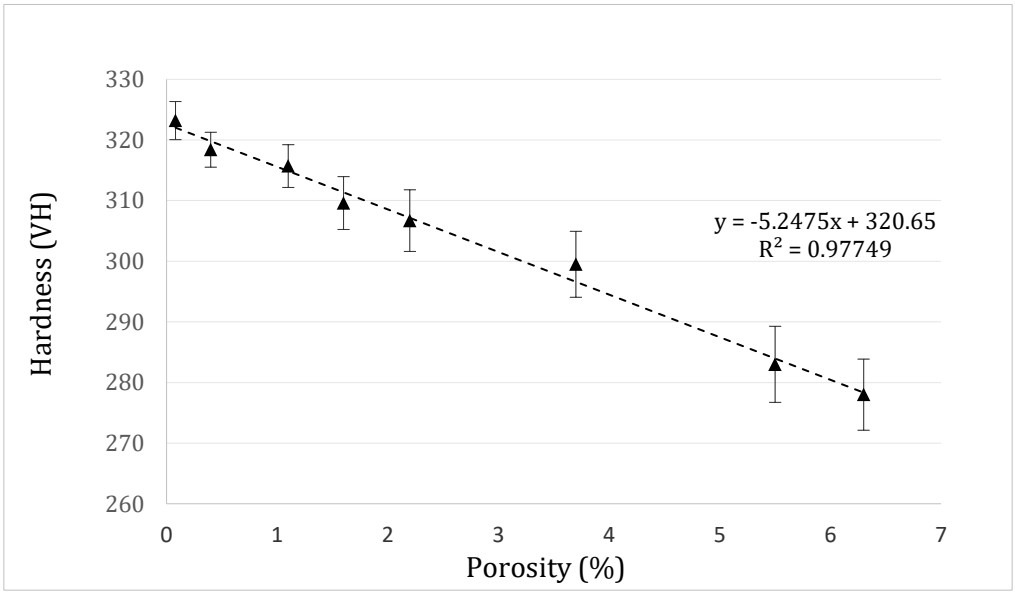

Figure 6-4: Effect of porosity on Vickers Hardness for Fe-6%w.t. Si processed with 200 W and increasing scan speed between 800-1500 mm/s resulting in increased porosity

material after heat treatment and the hardness in both planes was similar to the as-built samples. This can be explained on the basis that the microstructure and texture are homogenized after annealing at 1150 ºC for 90 min as shown in section 5.5.

6.3 Tensile Test Results

Two geometries were used for fabricating tensile specimens as shown in Figure 6-5. The first type of samples, were found to be unsuitable for testing. Cracks were observed in the thin gauge section of the samples after removal from the substrate. This was caused likely by the brittle nature of Fe-Si and the thermal stress induced by the manufacturing process. Next, geometry 2 was selected and manufactured with a thicker gauge section. Ten samples were produced in total, three dog-bones per each condition (as built, stress relieved, annealed) to ensure repeatability in the measurements and a spare sample for backup.

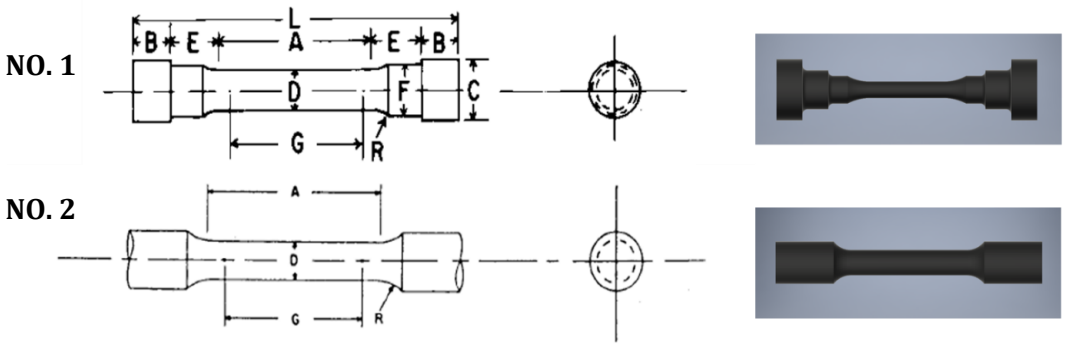

Dimensions, mm [in.]
For Test Specimens with Gauge Length Four times the Diameter [E8]

	Standard Specimen	Small-Size Specimens Proportional to Standard			
	Specimen 1	Specimen 2	Specimen 3	Specimen 4	Specimen 5
G—Gauge length	50.0 ± 0.1 [2.000 ± 0.005]	36.0 ± 0.1 [1.400 ± 0.005]	24.0 ± 0.1 [1.000 ± 0.005]	16.0 ± 0.1 [0.640 ± 0.005]	10.0 ±0.1 [0.450 ± 0.005]
D—Diameter (Note 1)	12.5 ± 0.2 [0.500 ± 0.010]	9.0 ±0.1 [0.350 ± 0.007]	6.0 ± 0.1 [0.250 ± 0.005]	4.0 ± 0.1 [0.160 ± 0.003]	2.5 ± 0.1 [0.113 ± 0.002]
R—Radius of fillet, min	10 [0.375]	8 [0.25]	6 [0.188]	4 [0.156]	2 [0.094]
A—Length of reduced section, min (Note 2)	56 [2.25]	45 [1.75]	30 [1.25]	20 [0.75]	16 [0.625]

Figure 6-5: Geometries No.1 and No.2 used for manufacturing tensile specimens. Drawings and CAD models are shown based on the dimensions of specimen 4 according to ASTME8/E8M standard

All tensile specimens were built horizontally with respect to the build direction (Z-axis) because of limitations in the build height (Figure 6-6). The selected build orientation allowed the minimisation of build-time but it added workload in terms of post-processing and support removal. For all the samples, support structures were built to anchor the parts to the build platform. This allowed for an easier removal (no EDM required) and contributed in the reduction of residual stresses in the built parts while minimising cracks and delamination. After removal from the substrate the samples were post machined to achieve dimensional accuracy according to the CAD files.

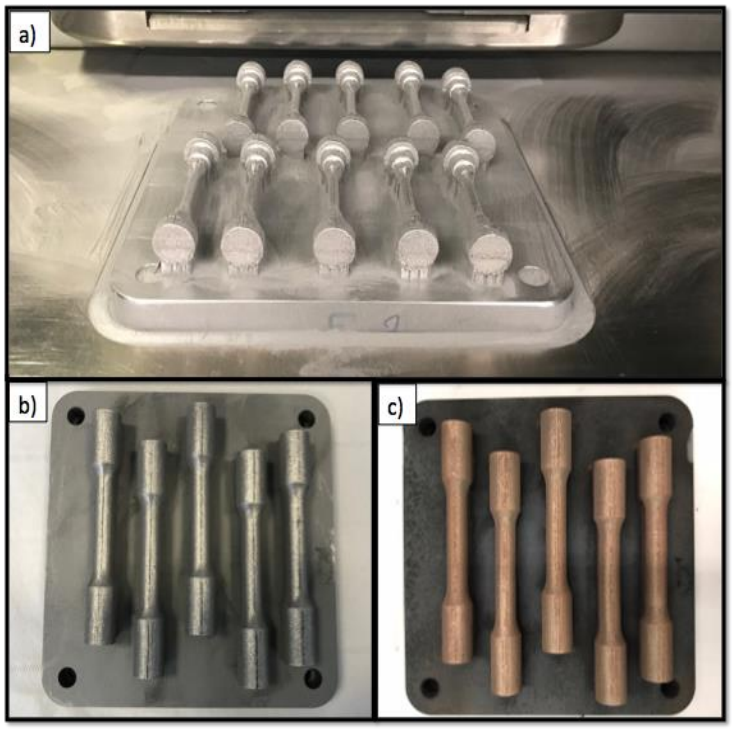

Figure 6-6: a) Tensile samples of geometry 1, b) tensile samples of geometry 2 in the as-built condition and c) after annealing

Yield and tensile strengths increase up to 4.5% in silicon content, but they suddenly start deteriorating at higher Si contents. Importantly, ductility quickly goes to 0 in the vicinity of 5% Si. Because of the brittle nature of high-Si steels, processing this material (e.g., by rolling and punching) becomes extremely difficult. Therefore, practically all-

commercial Fe-Si cores contain around 3.5%w.t. Si. Before fabricating soft magnetic cores from high silicon steel, the mechanical strength of the printed material must be measured to ensure structural robustness during operation. Mechanical integrity of the printed objects becomes particularly relevant for rotors employed in high-speed electrical machines, as even relatively small structural inconsistencies are likely to lead to propagation of cracks in the rotor and fatigue failure in its integrity. In this study, tensile tests only for Fe-6.0%w.t. Si alloy were performed for as-built, stress relieved (700 ^{o}C for 1h) and annealed (1150 ^{o}C for 90 min) samples.

Monotonic uniaxial tension tests were conducted using an Instron 5581 universal testing machine with a load cell that has a maximum capacity of 50 kN. The tests were carried out in accordance with the ASTM standard E8/E8M [176]. The crosshead speed was 1mm/min employing a 0.5%strain rate. A random spatter pattern was applied to the surface of the tensile samples using white and black spray paint to collect strain data using a video gauge as shown in Figure 6-7. The fracture surfaces of the tensile samples were imaged with the use of SEM. The engineering stress-strain curves in Figure 6-8 show that all the samples behave in a brittle fashion under tensile loading. Brittle fracture generally occurs in materials that exhibit low levels of yielding and elasticity.

When the material is under excessive stress levels sudden catastrophic crack propagation can initiate from a micro-scale defect such as a void, inclusion or discontinuity. Due to brittle failure all samples exhibited a flat fracture with cleavage failure surface. No plastic deformation was observed during the tests. As-built samples are found to be marginally stronger than the samples subjected to annealing.

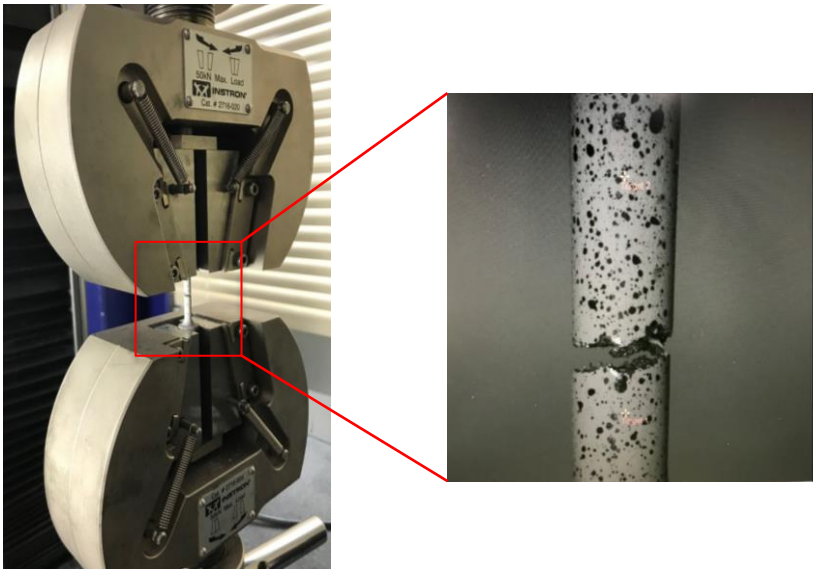

Figure 6-7: a) Fe-6%w.t. Si tensile sample during test and b) image captured by video gauge after rupture has occurred.

Stress relief post heat treatment of the samples at 700 ^{o}C for 1hr followed by furnace cooling reduced further the material's strain hardening capacity and fracture occurred for a tensile strain below 0.3%. With regard to the annealed samples, the ductility is slightly decreased without a drastic loss in tensile strength. This supports earlier findings where the micro-hardness of the as-built material was found to be lower in comparison to the annealed specimens.

Although the material behaviour is clearly brittle, in order to reveal the failure mode, the macroscopic features of the fracture surfaces of the tensile samples were investigated. The brittle failure mechanism is categorised based on two types of fracture mode, namely transgranular and interganular. Transgranular fracture is characterised by fracture cracks that pass-through grains and the fracture surface features faceted texture because of the different orientation of cleavage planes in grains. On the other hand, intergranular fracture is characterised by fracture crack propagation along grain boundaries. High magnification SEM micrographs were obtained and revealed that

failure always originated from a defect such as a pore or crack and intergranular fracture was observed. As shown in Figure 6-9 (a), cracks propagate along the plane perpendicular to the loading direction until catastrophic failure. Shallow dimples were not observed in any of the tested samples. Macroscopically, the fracture surface was relatively flat with no signs of shear lips.

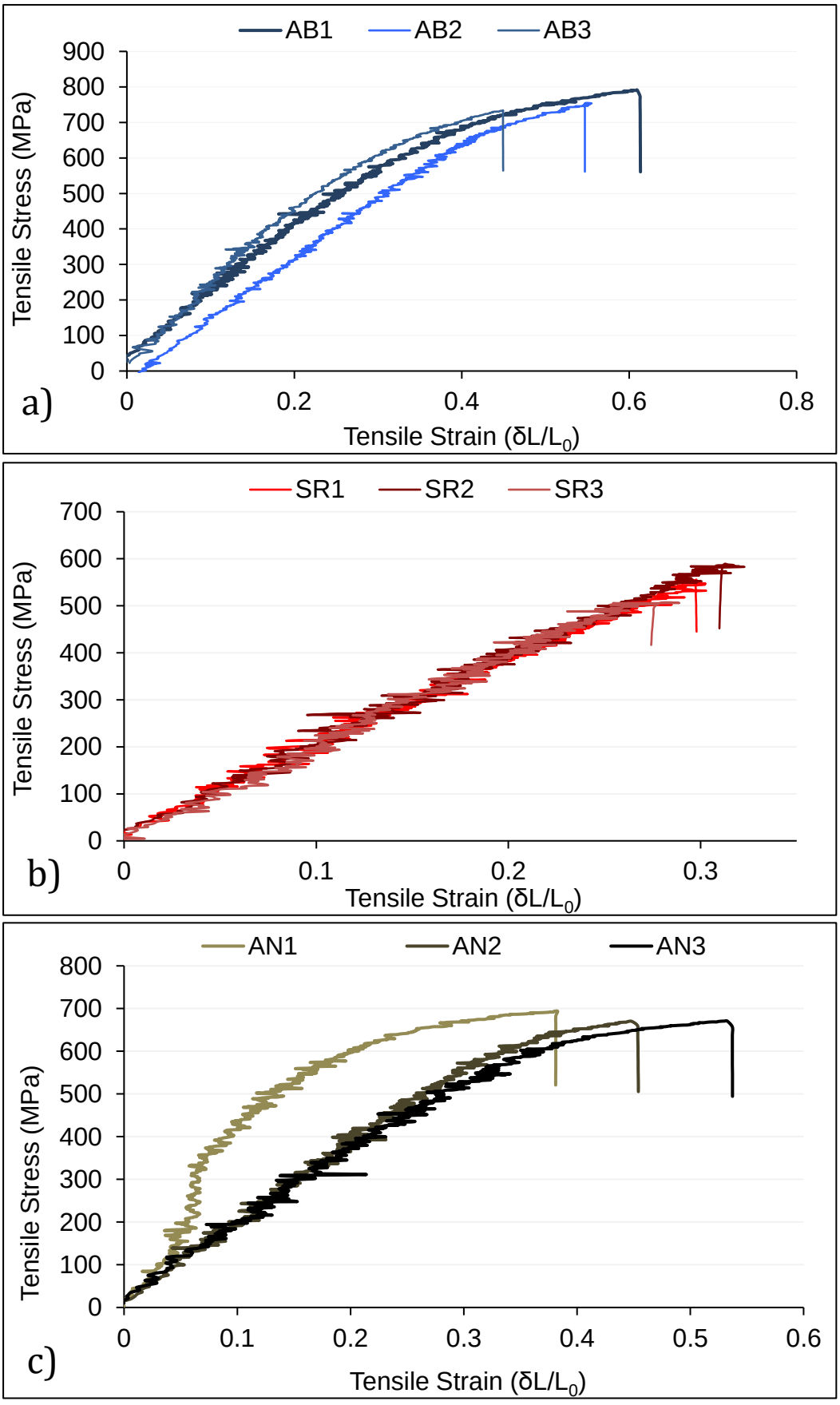

Figure 6-8: Series of tensile Stress-Strain curves comparing the mechanical behavior of Fe-6wt% samples in a) as-built, b) stress relief heat treatment (700 ºC) and c) annealing (1150 ºC).

Low to no ductility was also evident by the lack of necking in the tested samples (Figure 6-9 (b)). The fracture surface of the tensile samples features distinguishable tear ridges (Figure 6-9 c)), micro-voids (Figure 6-9 d)) and secondary cracks (Figure 6-9e)). This suggests that the crack propagates along the grain boundaries between melt pools that are weakened or embrittled and failure occurs through de-cohesion between layers (Figure 6-9 d)).

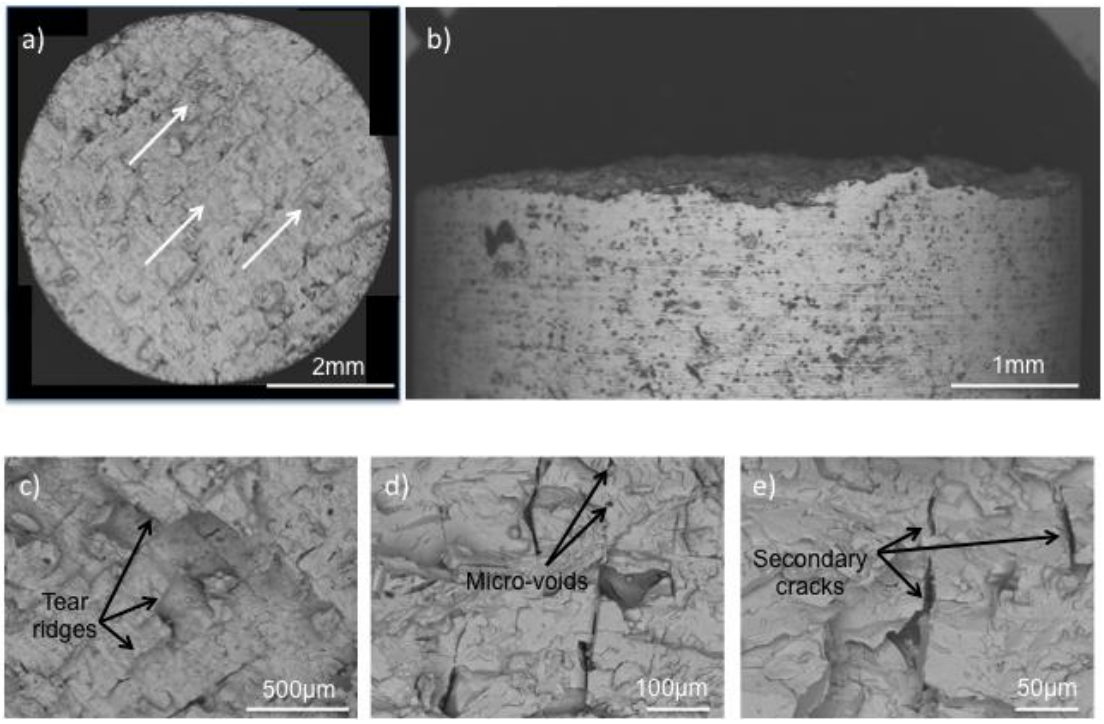

Figure 6-9: SEM micrographs of the fracture surfaces of horizontally built Fe-6wt% Si, a) Overall morphology of failure with cleavage fracture features aligned as indicated by the arrows, b) Relatively flat fracture with no indication of "necking", c) Tear ridges d) Micro-voids of varying size, e) Secondary cracks aligned with cleavage features

In [213] Lemke also observed a similar step-like failure morphology for horizontally built stainless steel 316L samples and it was speculated that cracks are more prone to propagate across layer boundaries. Hence, horizontal specimens appeared as more damage tolerant when subjected to tensile loads. This is further supported by the numerous short and long secondary cracks that appear over the whole fracture surface.

The effect of secondary cracks is also evident in the tensile strain curve as small deviations (noise) during the measurements.

The overall tensile properties of the samples for all three conditions can be found in Table 6-1. The decrease in the material's ultimate tensile strength, yield strength, and modulus of elasticity after low and high temperature heat treatments is attributed to the microstructural coarsening, as determined by the microscopic investigation, meaning reduction in the amount of grain boundaries that hinder the motion of dislocations during deformation. Stress relief reduced the ultimate tensile strength by approximately 28%, whilst decreasing the ductility by a factor of 1.8. The tensile results presented for high-silicon steel processed via LPBF, are an addition to the literature on tensile behavior of LPBF Fe-6wt% Si.

Table 6-1: Comparison of tensile properties of Fe-6wt% developed via LPBF in this study for the as built condition and with low and high temperature post heat treatment

Sample	Tensile Yield Strength (0.2% offset) MPa	Tensile modulus (GPa)	Ultimate Tensile Strength (MPa)	Elongation at failure (%)
As built	657.612 ± 42	195 ± 27	760 ± 29	5.3 ± 0.8
Stress Relieved	474.134 ± 32	185 ± 7	550 ± 41	3 ± 0.2
Annealed	631.227 ± 24	190 ± 19	685 ± 13	5.2 ±0. 6

In comparison to horizontally built stainless steel samples (316L) via LPBF [213], Fe-Si shows the same UTS value of 685MPa in the annealed condition and a superior UTS value of 760MPa for the as-built samples. Further research on the effect of build orientation on the tensile strength of Fe-Si alloys is required because the layer-by-layer manufacturing process during LPBF can have an impact on the mechanical behavior of parts built in different orientations. The authors in [214] presented that pores or melting

defects, segregation, oxidation and inclusions increase stress in parts and deteriorate the mechanical performance. These become more frequent at the interface between layer boundaries normal to the build direction. In vertical samples, boundary surfaces between adjacent layers are perpendicular to the loading direction, whereas in horizontal samples, these surfaces are aligned to the loading direction. Hence, the position of layer boundaries with respect to the loading direction could cause premature yielding and lower strength and elongation to failure in vertical samples.

A comparison between the fracture surfaces of samples in all three conditions is shown in Figure 6-10. The SEM micrographs reveal a similar fracture surface, however, a decrease in the number of micro-voids and partially melted powder particles can be seen for the stress relief and annealed condition. In comparison to the as-built condition, annealed samples feature a smoother surface.

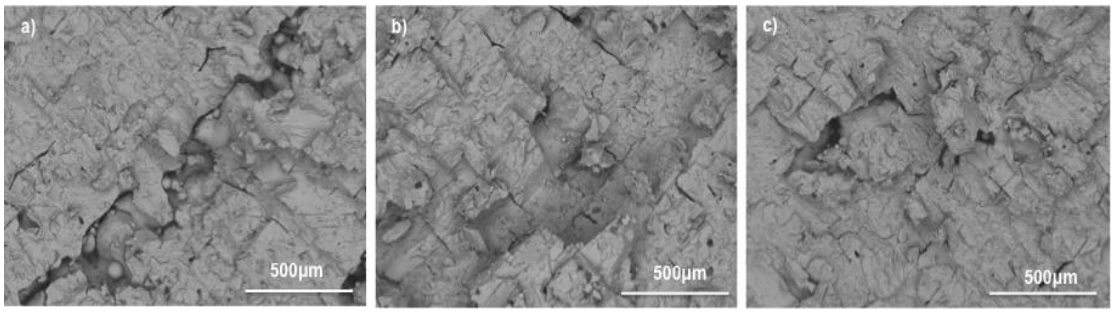

Figure 6-10: Fractured surface of Fe-6%wt Si samples a) as-built, b) stress relieved and c) annealed. Micro-cracks can be observed in all three conditions.

In order to improve the mechanical properties of Fe-Si alloys, a further increase in the ductility of high silicon steel is required. To overcome this problem, two methods can be applied. The first method includes the investigation of heat treatments and cooling rates that could retard or completely inhibit the appearance of disordered phases. Tensile tests presented in [215] on annealed Fe-6.5%w.t. Si steel produced by melt spinning, suggested that the appearance of D03 super-lattice structure is responsible for the loss

of ductility. The authors also showed that the ductile as-quenched samples could be converted into brittle materials by air cooling or annealing, and brittle ribbons can be converted back into ductile ribbons by annealing above the B2-D03 temperature followed by quenching; this further supports the argument that D03 ordering renders the Fe-6.5wt% Si steel brittle.

With regards to the second method, various alloying additions have also been explored in the literature such as Al, Ni, Nb and Mn that were found to slightly increase the plasticity of high silicon steel [216][217][218]. However, careful consideration is required when alloying silicon steel with additional elements because they can have a detrimental effect on the magnetic properties [217]. Hence, alloying additions must be restricted to a limited amount.

6.4 Magnetic Properties

In this study Fe-Si alloys with silicon content 5%, 6% and 6.9% respectively, are investigated to assess the effect of silicon content on the magnetic properties. The effect of the build orientation (horizontal and vertical) and post heat treatment annealing are evaluated and correlated to the magnetic performance of the binary soft magnetic alloys. All samples were processed with the optimum parameter set to eliminate any macro-structural and crystallographic effect originating from variance in energy density. The magnetization (M-H) curves of all three Fe-Si alloys in the as built condition are shown in Figure 6-11 and the results for annealed samples in Figure 6-12. They feature well-defined hysteresis loops both in the as-built and annealed condition and exhibit a typical soft ferromagnetic behaviour.

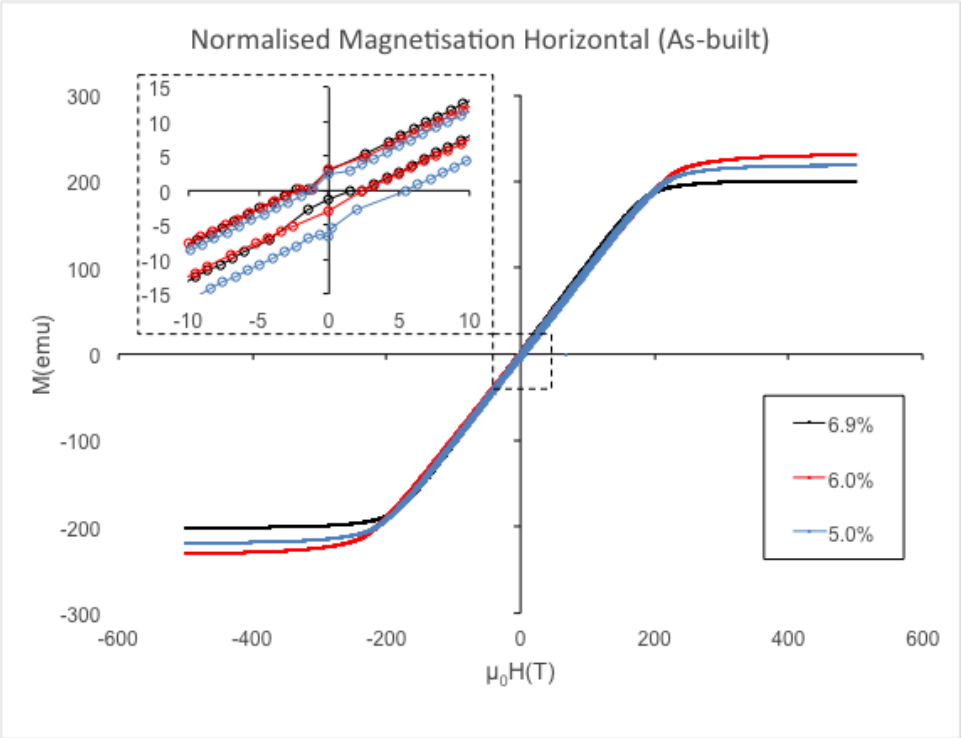

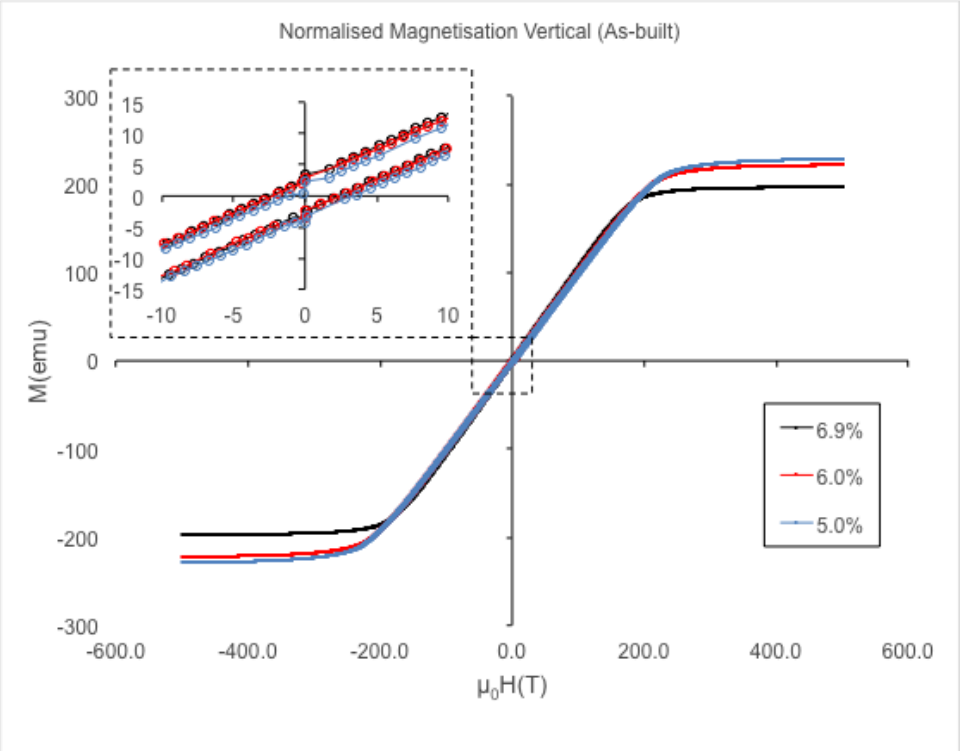

Figure 6-11: Normalised magnetisation curves (hysteresis loops) for horizontally and vertically built Fe-Si alloys in the as built condition

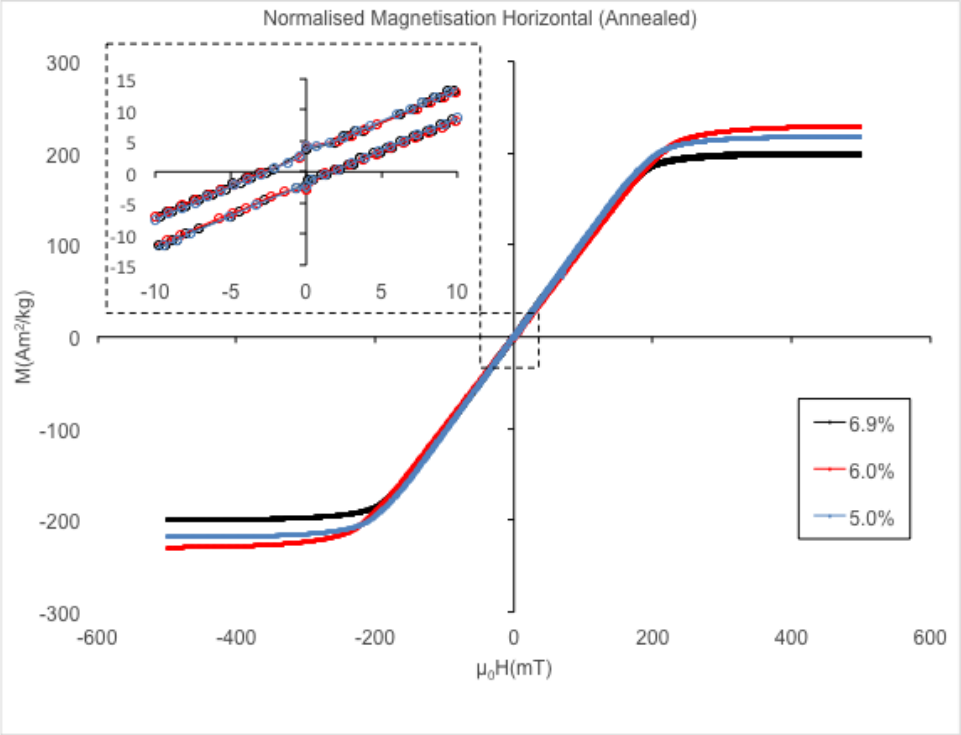

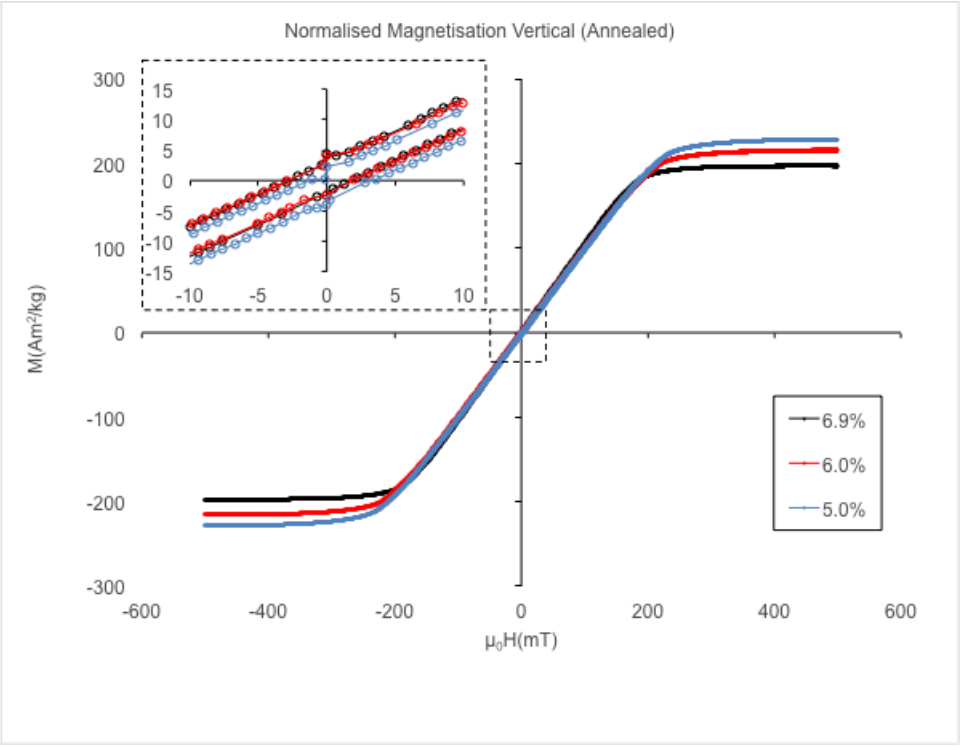

Figure 6-12: Normalised magnetisation curves (hysteresis loops) for annealed horizontal and vertical Fe-Si alloys with insets zoomed in on the data around zero field.

The saturation magnetization (Ms) and maximum permeability values for the Fe-6.9wt% Si samples in the as built condition are 204 emu/g and 2170 respectively. After annealing the saturation magnetisation remained the same but the maximum permeability increased significantly to 26450. Grain growth after annealing justifies this increase, and the results are in good agreement with the findings in [81] where the same alloy composition was used. However, the addition of silicon beyond 5% did not improve the magnetic permeability significantly although permeability is highly dependent on the composition. This could be attributed to the increase in cracks and pores for the higher silicon content samples. The remanence ratio was also calculated and a decreasing trend was observed with an increase in the silicon content of the silicon steel, which was more pronounced for the annealed samples. The average values of magnetisation saturation (Ms) residual magnetization (Mr), maximum permeability (μ_{max}) and the remanence ratio (Mr/Ms) are summarised in Table 6-2.

Table 6-2: Magnetic properties of high silicon steel alloys in the as built and annealed condition for samples built in two directions (horizontal 0° and vertical)

Fe-Si Alloy		5%		6%		6.9%	
		Horizontal	Vertical	Horizontal	Vertical	Horizontal	Vertical
As-built	Mass (g)	1.03	1.05	0.95	0.97	1.01	1.06
	M_s (emu/g)	222.5±5	225±4	223±7	218±3	204±5	203±7
	M_r (emu/g)	4.65±0.13	4.32±0.07	2.96±0.09	3.39±0.06	3.40±0.03	3.56±0.12
	μ_{max}	1973	1768	1824	1925	2170	2867
	M_r/M_s (%)	2.08	1.92	1.32	1.55	1.66	1.70
Annealed	Mass (g)	1.04	1.02	1	0.94	1.02	1.06
	M_s (emu/g)	222±6	223±4	222±7	212±3	204±4	202±6
	M_r (emu/g)	4.27±0.09	4.29±0.09	3.86±0.13	3.32±0.03	2.36±0.05	2.37±0.06
	μ_{max}	23676	23580	22890	21490	26450	26640
	M_r/M_s (%)	1.92	1.92	1.73	1.56	1.15	1.17

Unfortunately, no coercivity values can be provided for the samples under investigation. Normally to calculate coercivity values, one just estimates where the magnetization crosses the y (m) = zero axis as the field increases (this would be a positive field h+) and where it crosses the y axis (m=0) as the field decreases (this would be a negative field h-) and then calculate $H_c = \frac{(h^+ - h^-)}{2}$. In every case as the field increases the magnetization crosses m = 0 at some negative value of h and as the magnetic field is decreasing m crosses 0 at some positive field. So, this is unphysical as shown Figure 6-13). Basically, the coercive field of the samples are lower than the trapped field in the superconducting solenoid magnet. The trapped field in the solenoid will be negative (between -10 and -30 mT) as the magnetic field is decreasing and around (+10 to +30 mT) when the magnetic field is increasing. In other words, the data just reflects the trapped field in the magnet. Hence, the coercive fields in these samples are lower than 10 mT (the trapped field in the magnet). Due to the very soft magnetic nature of the samples, they may have a coercive field of 0 to 10 mT, which cannot provide sufficient and credible data for the calculation of H_c.

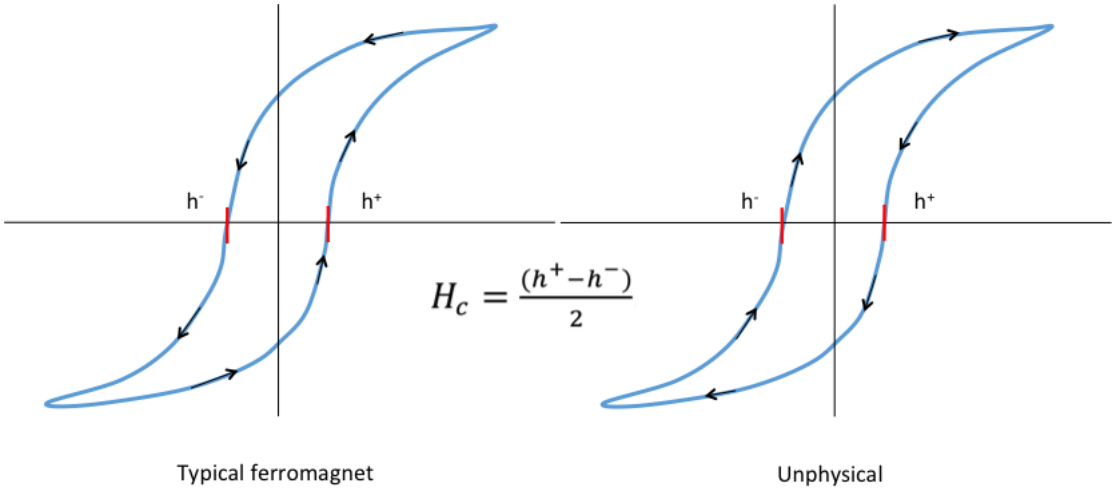

Figure 6-13: Inability to provide coercivity values due to the unphysical behavior during tests

A representative permeability curve for Fe-6wt% Si is shown in Figure 6-14. The permeability was calculated from the 5th quadrant of the M-H curve when a magnetisation cycle is complete. The experimental technique of ac susceptibility can be used as a probe of magnetic dynamics in a wide variety of systems. Its use is restricted to the low-frequency regime and thus is sensitive to relatively slow processes. Rather than measuring the dynamics of single spins, ac susceptibility can be used to probe the dynamics of collective objects, such as domain walls in ferromagnets.

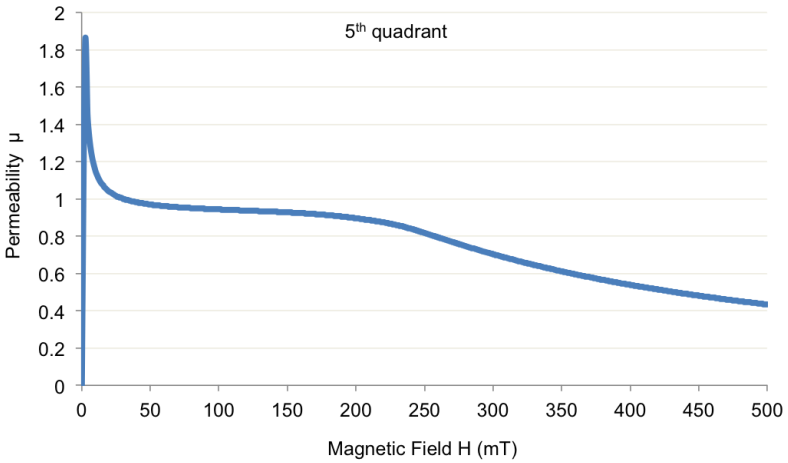

Figure 6-14: Representative permeability curve for Fe-6wt%Si soft magnetic alloy

The AC susceptibility results in Figure 6-15 show the magnetic response of Fe-6wt%Si where χ is plotted against the applied ac field H. Measurements of χ versus ac field H were taken at six fixed frequencies f (11, 31, 113, 311, 1031 and 3343 Hz) in an ac driving field of 1Oe. The frequencies are roughly log spaced and are all prime numbers. The dc field was swept from 0 to 5 kOe with increments of 200 Oe for each run. Furthermore, measurements for χ AC versus frequency f at fixed field H in an ac driving field of 1 Oe were conducted. Fields were 0, 1, 2 3, 4 and 5 kOe and frequencies were 10 to 7000 Hz with 50 steps on a log scale (sometimes the run ended before 7 kHz as the signal was too large and the signal saturated).

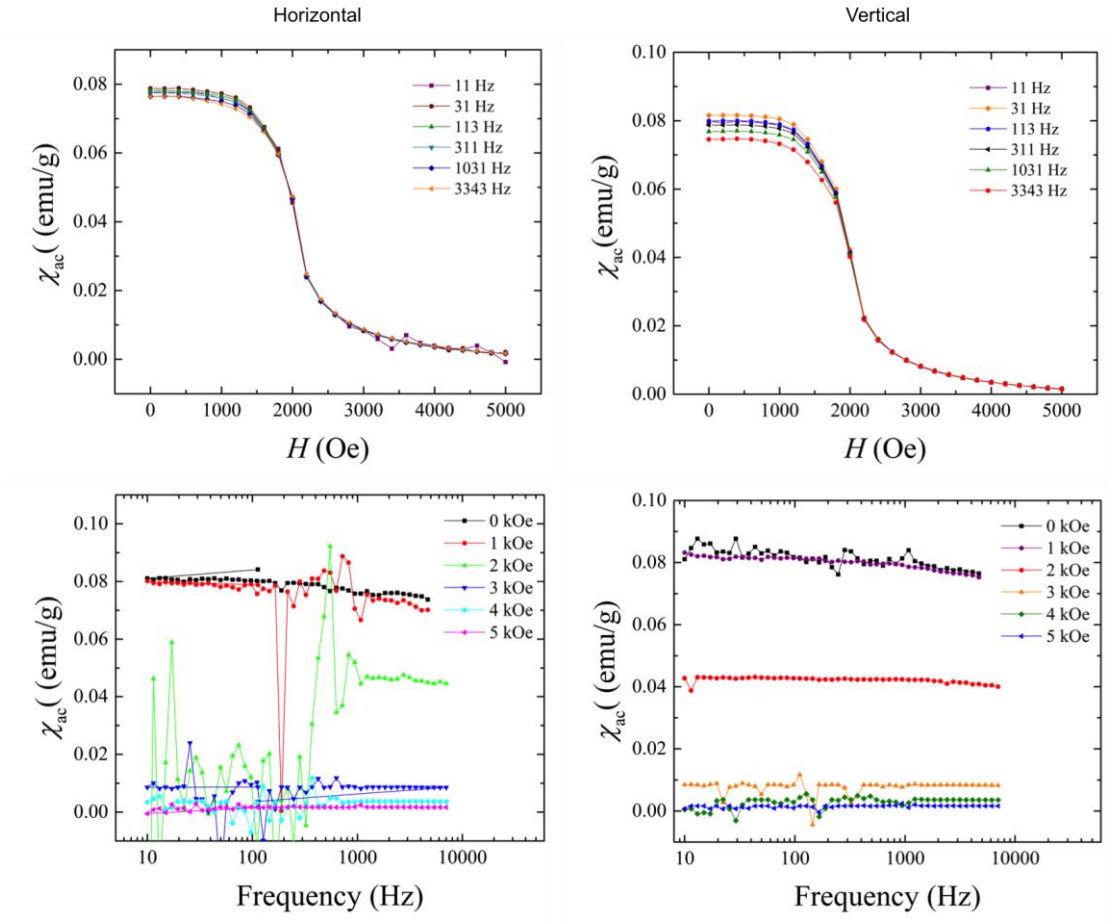

Figure 6-15: AC susceptibility χ of Fe-6wt% Si soft magnetic alloy for samples built horizontally and vertically in the as built condition. χ is plotted against applied field H and against frequency

It can be seen that the AC susceptibility is essentially frequency independent. From this data set, there is little evidence that the AC response varies with frequency, but this is quite a small frequency range (11 Hz to 3343 Hz). Furthermore, the AC susceptibility becomes smaller (tends to zero) in higher field as the magnetization of the samples saturates. The ability to process high silicon steel in near-net shape form in 3D geometries via LPBF with good magnetic properties is a step towards the fabrication of complex geometries for novel components used in electromagnetic applications.

6.5 Electrical Resistivity

In this study, the electrical resistivity of silicon steel samples, only in the as-built condition, with varying silicon content was measured. The results are summarised in Figure 6-16 for three build orientations. The resistivity was measured using a DC four-point Kelvin resistance measurement meter that measured the specimen's resistance directly. The rectangular test bars were 50mm long with a cross sectional area of 25 mm^2 fabricated with the optimised parameter set.

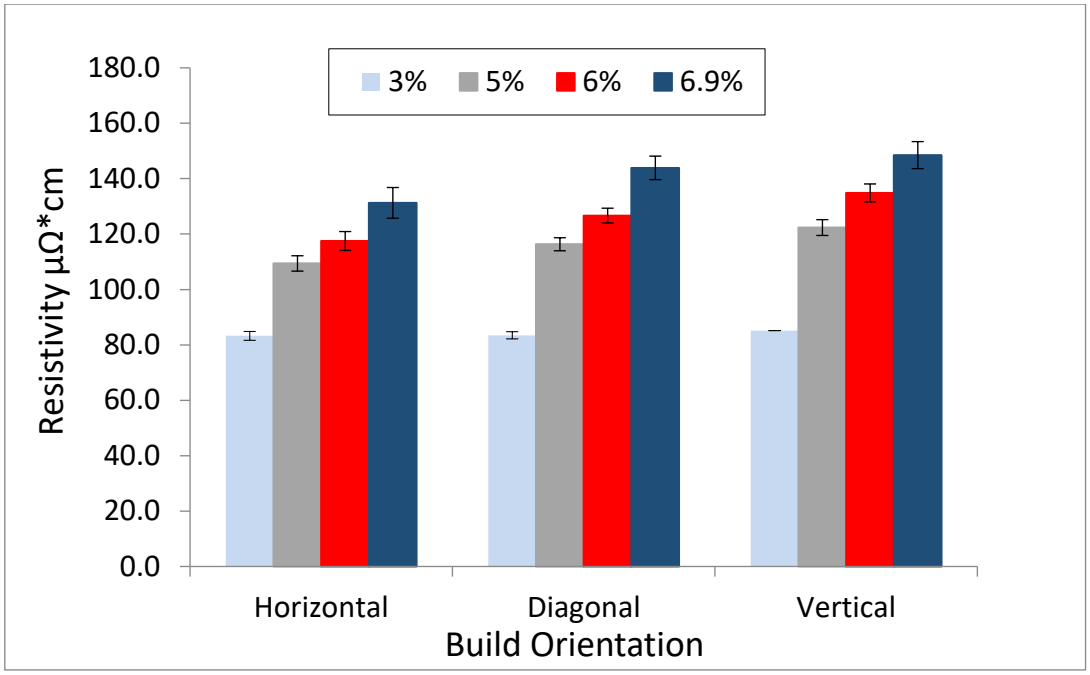

Figure 6-16: Electrical resistivity of Fe-Si samples in the as-built condition with varying silicon content and build orientation

It is evident from the results that the resistivity increased with an increase in silicon content, as one would expect. The lowest resistivity was found for Fe-3%w.t.Si with an average value of 85.2 µΩ-cm and featured isotropic electrical resistivity irrespectively of the build orientation. Hence, it is suggested that for the lower silicon content, silicon steel does not experience anisotropic crystal structure during LPBF with the optimum set of parameters. However, when the alloy contains a higher percentage of silicon, anisotropic behavior can be observed. It can also be observed that the anisotropy increases with an increase in silicon content. For all the Fe-Si alloys investigated in this study, the highest resistivity values were found in the vertically built specimens showing a dependence of sample resistivity in relation to the build orientation.

According to the literature, the resistivity for commercial 3% and 6.5% Si content silicon steel are approximately 47 and 85 µΩ-cm, respectively [14]. Based on the results from this investigation, the resistivity values of Fe-Si processed by LPBF is approximately

two times higher when compared to Fe-Si fabricated with traditional manufacturing methods. The highest resistivity value was 152.6 μΩ-cm for Fe-6.5wt% Si test bars, as one would expect. All cracks propagated perpendicular to the build direction of the samples, which is an indication of high thermal gradients and residual stresses which resulted in higher resistivity for diagonally and vertically built samples in comparison to horizontally built samples.

Silbernagel et. al. found that the electrical properties of AlSi10Mg processed by LPBF were anisotropic, which was attributed to the melted microstructure of the printed samples [161]. The lowest resistivity was measured in the build direction, because needle-like shapes of aluminium solidified in the build direction. The anisotropic behaviour was eliminated after heat-treatment of the samples, which resulted in a homogenous internal structure. Anisotropic behavior was observed in this study for high silicon steel in the as built condition. Further research in the electrical resistivity of 3D printed silicon steel is required for the annealed condition. The results are expected to be in agreement with the findings in [161] because a homogenised microstructure was found for all three compositions of Fe-Si alloys that were subjected to annealing.

6.6 Conclusions

LPBF is a promising manufacturing technology for the fabrication of complex net-shape electromagnetic components from soft magnetic alloys and this Chapter has shown how varying Si content and the use of a post process anneal can be used to optimise the process to minimise defects and achieve a balance between mechanical and magnetic properties. However, it still remains a challenging process due to various material properties and multiple processing parameters.

- Micro-hardness of the samples is mainly affected by the content of silicon and not by the processing parameters. However, it must be noted that increased porosity leads to decreased material hardness. Material hardness reached a maximum for the pre-alloyed powder with 6.9%wt Si.
- Electrical resistivity measurements for the binary alloys under investigation were superior to traditionally fabricated silicon steel. More specifically, 6.5%wt Si featured a resistivity approximately two times higher than this of hot-cold rolled silicon steel with a value reaching 152.6 μΩ-cm.
- Tensile tests for Fe-6.0%wt Si in three conditions (as built, stress relieved and annealed) were performed and the tensile yield strength, UTS, tensile modulus and elongation at failure were presented. It was shown that stress relief heat treatment reduced the ultimate tensile strength by approximately 28%, whilst decreasing the ductility by a factor of 1.8. The best mechanical performance was obtained for the as-built parts.

7. Chapter 7: 3D-printed Rotor for Switched Reluctance Motor

7.1 Introduction

This Chapter investigates the readiness of metal additive manufacturing applied to electrical machines and contributes to bridging the gap of how to use this technology in power and energy applications. A soft magnetic material featuring high silicon content (Fe-5.0%w.t. Si) has been developed for laser powder bed fusion and a rotor has been 3D printed for a switched reluctance machine. The printed rotor was assembled into a conventionally laminated stator and the performance of the whole machine was evaluated. Its performance was compared to an identical machine equipped with a laminated rotor of the same dimensions made of conventional non-oriented silicon steel. A comparative study was carried out through both finite element simulations and experimental tests. The efficiency of the two machines were assessed, together with the principal electrical and mechanical quantities, under several operating conditions. Considering the AM rotor, the findings show increased power losses at high frequency operations, due to the greater amount of eddy currents losses in the solid piece rotor. However, in terms of output power and efficiency up to 600rpm (i.e., rated speed) the overall behavior of both SRMs is comparable.

7.2 Benchmark SRM

The SRM is a singly excited, doubly salient EM, where the energy conversion occurs in discrete cycles exploiting the tendency of the rotor to align spontaneously with the stator according to the principle of minimum magnetic reluctance path [22]. In recent years, the SRMs gained renewed attention in both the academic and the industrial world, because of their rugged and robust structure, as well as independence from permanent

magnets [23, 24]. Further, SRMs can cover wide constant power speed ranges and operate efficiently in harsh environments [22]. Although the SRM's control relies on more advanced and complex strategies, the mentioned benefits led the SRM in being considered a valuable alternative to permanent magnet and induction machines in many applications such as aerospace, automotive, industrial and energy storage.

In this work, an off-the-shelf, three-phase SRM was chosen as the benchmark EM, because of the rotor simplicity and availability. The selected SRM has 12 slots and 8 poles, and its rated values are listed in Table 7-1 along with the main geometrical dimensions. In particular, the outer diameter of stator and rotor and the axial length were 150 mm, 79.2 mm and 104 mm, respectively.

Table 7-1: Parameters of the benchmark SRM

Parameter	Value
Rated Speed	600 rpm
Rated Torque	17.2 Nm
Rated Voltage	360 V_{pk}
Number of Slot	12
Number of Pole	8
Axial Length	104 mm
Stator Outer Diameter	150 mm
Rotor Outer Diameter	79.2 mm
Number of Turns	220x4

Both stator and rotor cores were laminated structures featuring 0.35 mm lamination thickness made of non-oriented silicon steel M800 (Fe-3.5%w.t. Si). The cross-sectional view of the machine and its winding layout are illustrated in Figure 7-1. Each phase has a total of 4 series-connected coils with 220 turns each. The measured DC phase resistance at 20 C was 10Ω.

A standard, commercial converter implementing a soft-switching strategy was used for controlling the machine. The controller receives the rotor position feedback from a simple optical position sensor based on three photodiodes and three light emitting devices. Based on the rotor position, the control algorithm generated and sent the control signals to the switching devices. A digital hysteresis control algorithm was used for maintaining a flat-topped current when the SRM operated at low speed (i.e., the phase voltage was chopped for maintaining the current within the hysteresis band). The turn-on and turn-off angles of each phase were automatically selected, according to the instantaneous torque request, for minimising the required current (i.e., maximum torque per ampere algorithm).

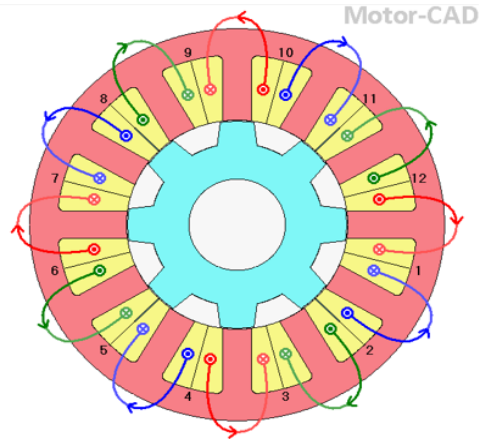

Figure 7-1: Cross-sectional view and winding layout of the case study SRM.

7.3 3D printing of the SRM rotor

In the presented work, a step-by-step approach was preferred to evaluate the viability of the AM technologies applied to the EMs. For this reason, it was decided to 3D print only one out of the two SRM's ferromagnetic cores, namely the rotor core. Indeed, the extra core losses arising from the choice of also having an AM stator might be source of concerns in terms of thermal management, due to the undersize of the benchmark SRM's cooling system. Therefore, the 8 poles rotor was additively manufactured and its

dimensions mirrored those of the benchmark SRM's rotor. As for the samples previously 3D printed, the LPBF process was employed, since it produces near net shape parts with densities comparable to the bulk material. Based on the data contained inside the CAD file of the benchmark SRM's rotor, a high-power laser beam was applied to the metallic powder layer and its energy fully melts the powder layer-by-layer. The subsequent rapid cooling of the layer effectively creates a near net shape metal part (Figure 7-2).

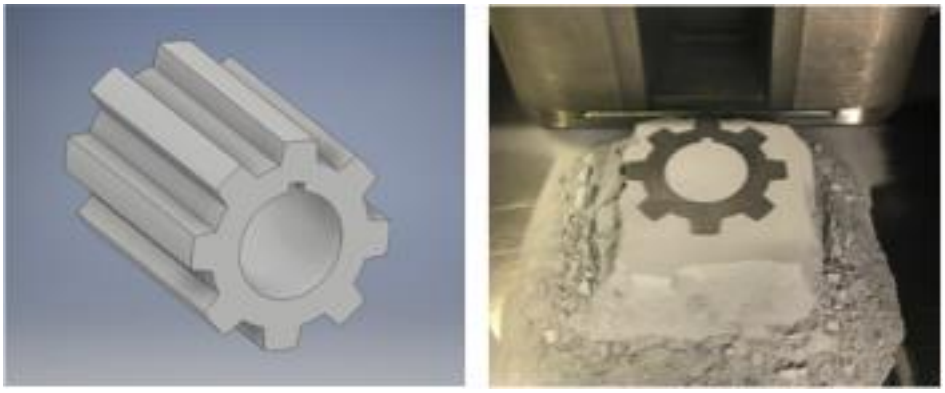

Figure 7-2: CAD design and 3D printed prototype inside the build chamber

Due to build height restrictions in the LPBF machine, the AM rotor made of Fe-5.0%w.t. Si was fabricated in three segments for an overall axial length of 104 mm, as depicted in Figure 7-3. Due to technical difficulties with the LPBF machine, the rotor height was prohibitive for one build. Therefore, the rotor was divided into three segments. In particular, the first segment featured an axial length of 54 mm, while the other two were 25 mm long. The final AM rotor was composed of the three segments, and the ensuing eddy current paths along the axial direction were thus shorter compared to a single piece solution. Thus, a positive impact on the containment of the eddy current losses was expected on the 3D-Printed rotor.

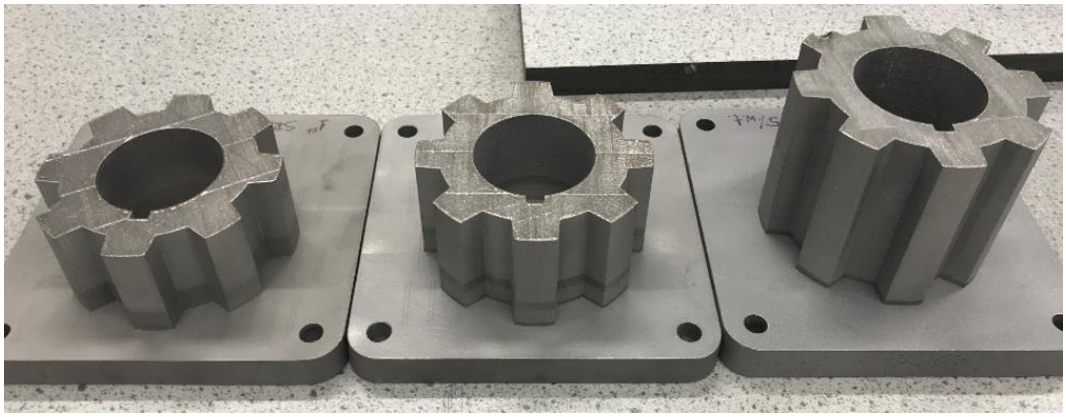

Figure 7-3: Fe5%Si 3D-printed segments on 125x125mm mild steel substrates; two 25mm long and one 54mm long segment constitute the 3D-Printed rotor.

For Fe-6.0%w.t. Si processed via LPBF, despite the various scanning strategies employed to reduce residual stress, all SRM rotors were found to be delaminated as shown in Figure 7-4. Catastrophic delamination and warping near the edges of the rotor's teeth occurred in most cases during manufacturing. In some cases, delamination and crack propagation was observed during cool down of the substrate whilst in the build chamber of the LPBF machine. Overall, for parts with dimensions bigger than 10x10x10 it was very hard to obtain crack free parts when the silicon content exceeded 6%w.t.

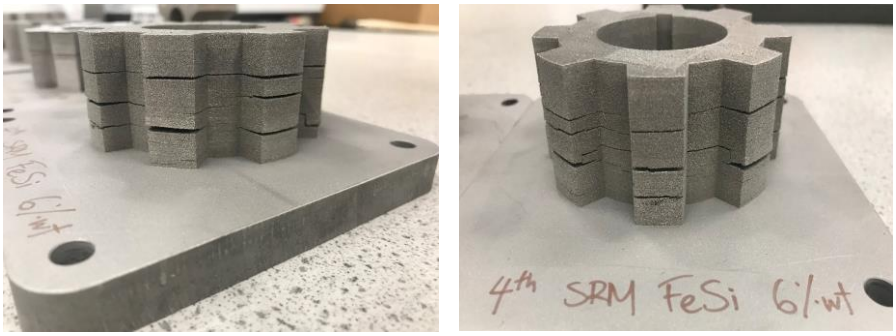

Figure 7-4: Delamination and cracks were observed for all 3D Printed SRM rotors made of Fe-6%Si.

After machining, to ensure the right tolerances, the three segments were assembled as a single piece on a mild steel key-locked shaft, with the same dimensions as the benchmark machine. The AM rotor was mechanically balanced up to a speed of 3500 rpm, by

removing the exceeding material from the mild steel lock rings. In Figure 7-5, the fully assembled 3D printed rotor is shown and compared to the laminated one of the benchmark SRM. In turn, both rotors of Figure 7-5 have been integrated into the benchmark SRM's stator and tested. Knowing the magnetic properties of the high silicon content material (Fe-5%w.t. Si), a comparative analysis was performed on both SRMs through FE simulations, before moving to the experimental tests campaign.

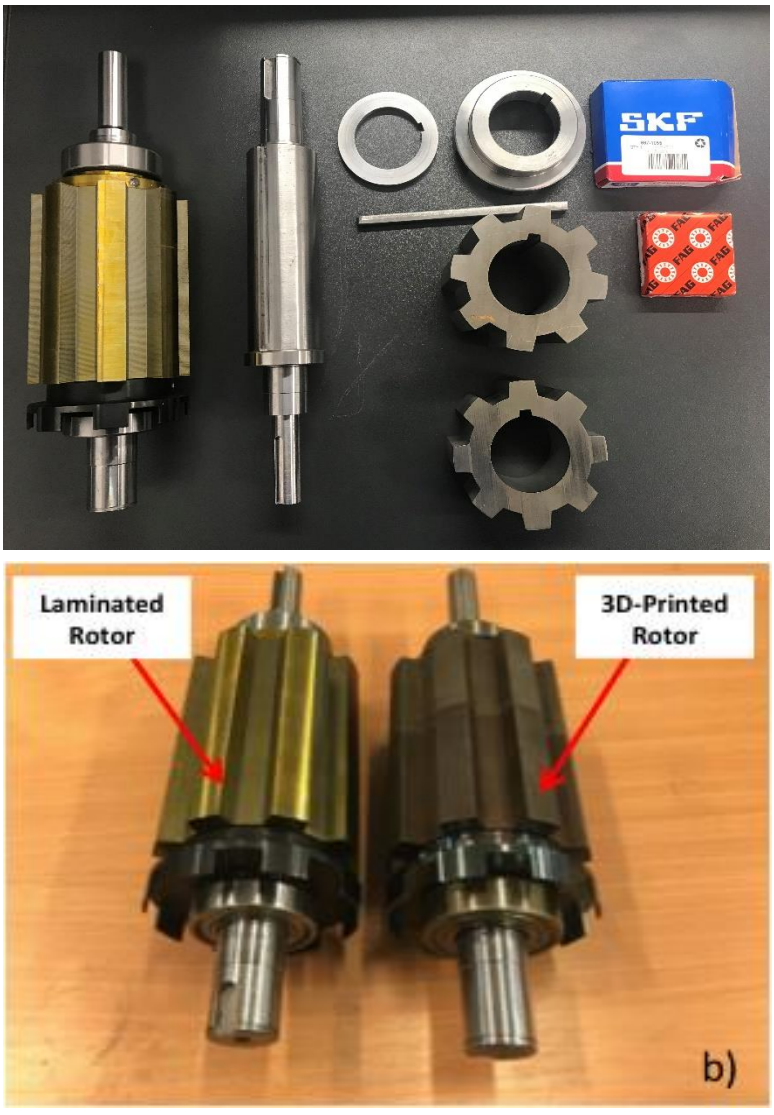

Figure 7-5: Conventional laminated 8-pole SRM rotor (left-hand side) and identical 3D printed rotor (right-hand side) a) before and b) after assembly.

7.4 SRMs FE Analysis

The fastest way to gain in depth insight over the SRM, mounted with the additively manufactured rotor, consists in implementing its 2D FE model and simulating the related electromagnetic behaviour (see Figure 7-6). The FE simulations have been carried out with the use of MotorCad considering two cases: 1) both stator and rotor ferromagnetic cores are made of M800 laminated silicon steel (i.e., benchmark SRM) and 2) the stator core material remained unchanged, while the rotor core, adopted the 3-piece high silicon content material (i.e., AM SRM).

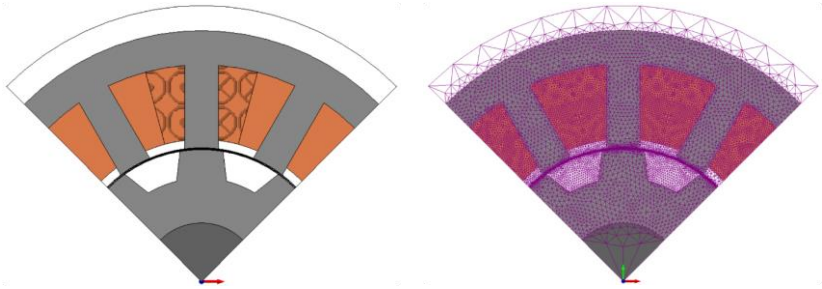

(a) (b)

Figure 7-7: FEA model: (a), solid components, (b) 2D mesh.

The machine performance was evaluated in terms of generated electromagnetic torque, magnetic saturation level and losses. By determining the iron loss distribution, we can calculate the iron losses of the rotor so that experimental results can be better analysed. In order to quantify the rotor loss variation equation (1) was used where P_{rot} were the rotor losses, P_{el} was the electrical input power, P_{Joule} were the winding Joule losses, P_{stat} were the stator iron losses, T was the shaft torque and ω_m was the mechanical speed.

$$P_{rot} \approx P_{el} - P_{Joule} - P_{stat} - T \cdot \omega_m \qquad (7.1)$$

Windage losses are not included due to the relatively low operational speed.

Figure 7-7 shows the flux map and magnetic field lines of the benchmark and 3D printed SRM while operating at base speed and delivering the rated (average) torque of 18.7 Nm. From this plot it was possible to verify that the magnetic core of the 3D printed SRM was slightly more saturated as opposed to the benchmark machine. Such an effect was more accentuated within the stator poles, meaning that the 3D printed machine must be fed with a larger current (and ensuing larger magnetic flux density) for developing the rated torque. Despite the visible loss concentration in the rotor teeth tips (Figure 7-8), the rotor losses share over the total iron losses is less than 20%, as reported in Table 7-2, where the loss results obtained from the FE simulation are summarised. These include also the Joule losses, which are one order of magnitude higher than iron losses.

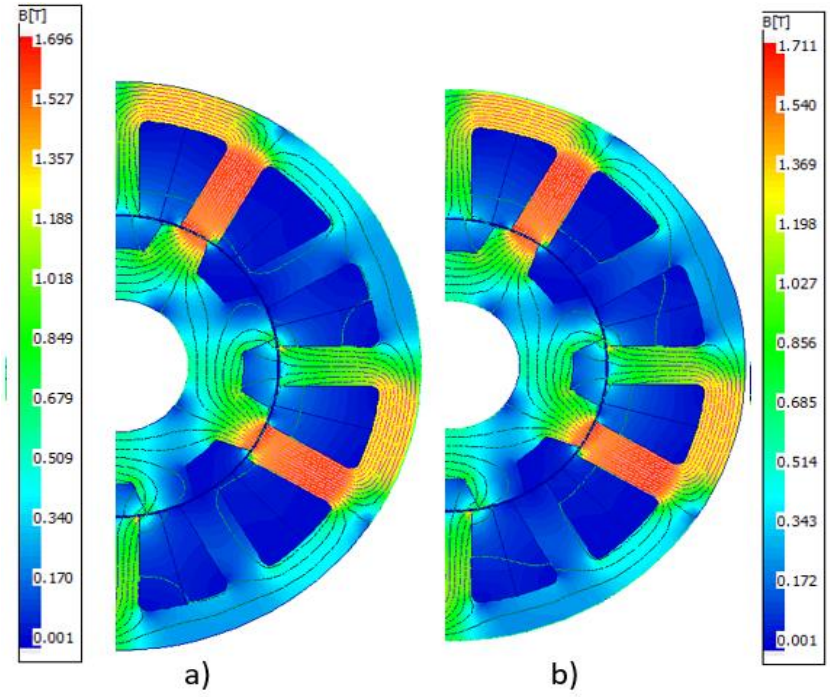

Figure 7-8: Flux density and magnetic field lines at rated operating condition for a) benchmark SRM and b) 3D printed SRM.

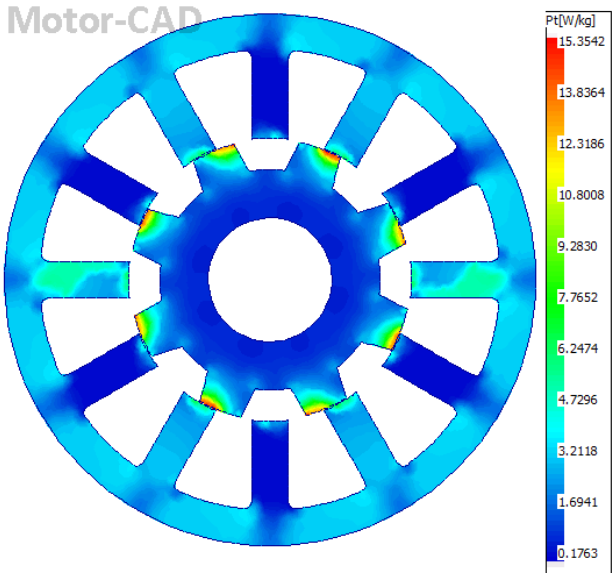

Figure 7-9: Iron loss distribution for the benchmark SRM operating at rated condition.

Moreover, a speed-sweep analysis was carried out for determining if there was any particular operating speed range in which the SRM developed excessive torque ripple. As a result, it was found that within the range 800 – 1200 rpm an anomalous ripple was detected. This is visible in Figure. 7-9, where the instantaneous torque developed at 1000 rpm is plotted. Its torque ripple is higher than 120%. Therefore, experimental tests with the machine operating within the aforementioned speed range was avoided.

Table 7-2: Loss distribution for the benchmark SRM (rated condition)

Loss component	**Magnitude**
Stator iron	11.3 W
Rotor (total)	2.7 W
Joule losses	615 W

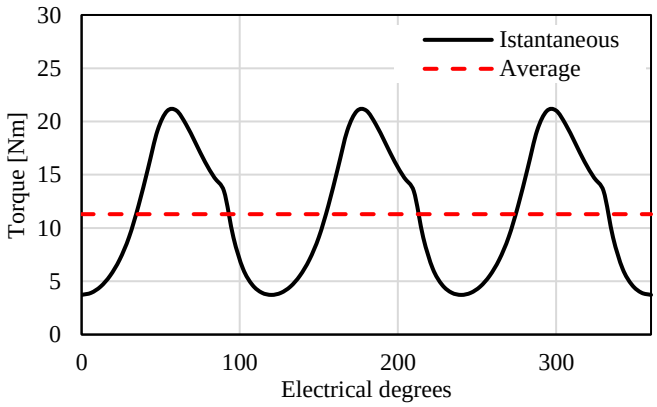

Figure 7-10: Shaft torque for the benchmark SRM operating at 1000 rpm obtained through FE analysis.

7.5 SRMs Experimental Tests and Test-bed description

This Section describes the experimental test procedure and reports the main results for both the benchmark and the 3D printed SRMs. In order to test the electromechanical performances of the manufactured 3D printed SRM and to compare them with the benchmark machine, the testbed shown in Figure 7-10 was used. The description of each component/instrument is reported in Table 7-3.

The SRM was flange-mounted to an "L" plate. Its shaft was mechanically coupled through a Magtrol® torque meter to a 70 kW, variable-speed Oswald® induction motor. The load induction machine was torque controlled via an Emerson Unidrive® three-phase inverter. Phase current and voltage were measured through a hall-effect current clamp and a differential probe respectively. These were connected to a Lecroy® Wavetouch oscilloscope for instantaneous time-domain analysis and logging. In addition, the instantaneous electric power analysis was carried out using a Rode & Shwarz power analyzer, which records and processes the phase and current voltage.

Table 7-3: Test-bed Components / Instruments

ID	Description
1	3D printed SRM
2	Magtrol torquemeter
3	Oswald induction machine (load)
4	Lecroy Wavetouch® oscilloscope
5	Rode & Shwarz power analyzer
6	Magtrol torque / speed datalogger
7	Pico current and voltage probes
8	Benchmark/Laminated SRM drive (converter)
9	Induction machine drive cabinet

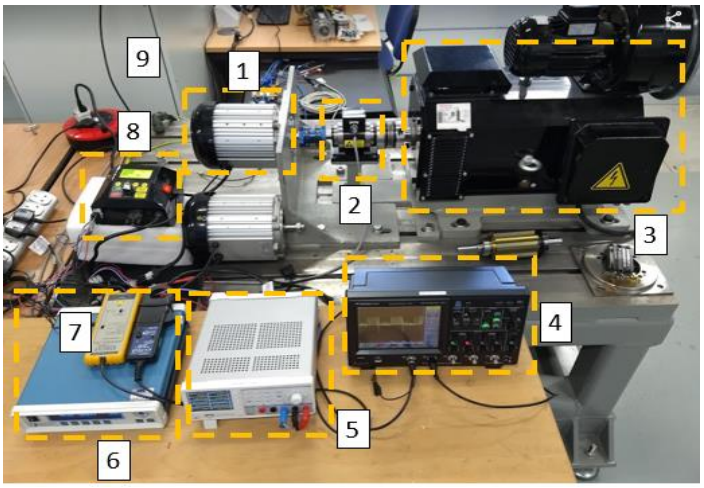

Figure 7-11: Experimental test-bed (analytical description provided in Table 7-3).

7.6 Test Results

Both machines (i.e., benchmark SRM and the one with 3D printed rotor) were tested at various operating conditions, with the purpose of covering the entire torque / speed envelope. In particular, both machines were tested at more than 50 different operating

points. For brevity the measured torque speed envelope, and efficiency maps are summarised in Figure 7-11 and 7-12 for the benchmark and 3D printed machines respectively. At rated speed (i.e., 600 rpm), the SRM with the 3D printed rotor produced 13% less torque compared to the benchmark SRM. This was more clearly identifiable from the data reported in Table 7-4, where the measured electrical and mechanical quantities at rated speed are tabulated. When the operating speed was increased, the 3D SRM's performance tended to improve, both in terms of both maximum mechanical power and efficiency, as observed in Table 7-5, where the electric and mechanical power quantities, measured at 1500 rpm and maximum torque, are listed.

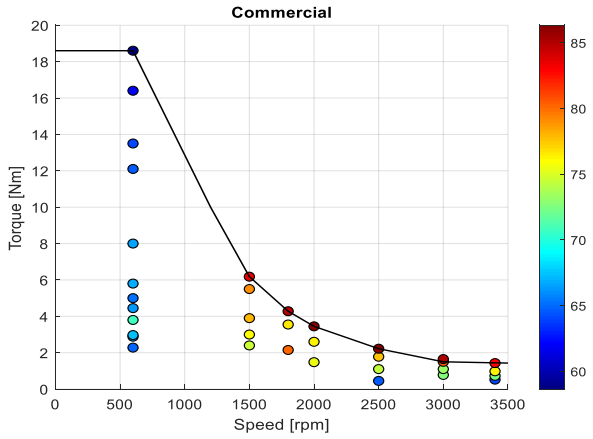

Figure 7-13: Measured efficiency map and torque/speed envelope for the benchmark SRM.

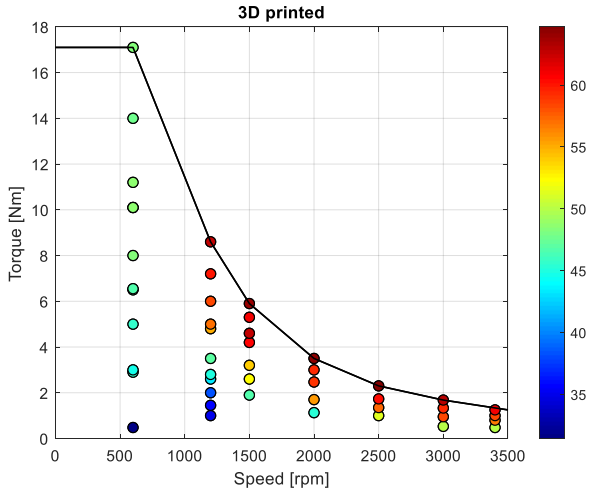

Figure 7-12: Measured efficiency map and torque/speed envelope for the 3D printed SRM.

Table 7-4: Measured Quantities at Base Speed

Measured quantities	Benchmark SRM	3D Printed Rotor
Mechanical Power	1170 W	1020 W
Electric Power	1995 W	2130 W
Average phase current	3.27 A	3.31 W
RMS phase current	4.11 A	4.17 A

Table 7-5: Measured Quantities at 2.5 times the Base Speed

Measured quantities	Benchmark SRM	3D Printed Rotor
Mechanical Power	960 W	925 W
Electric Power	1149 W	1420 W
Average phase current	1.74 A	1.77 W
RMS phase current	2.13 A	2.44 A

7.7 Time domain analysis and discussion

Reporting the time domain electric quantities for both machines provides a more insightful analysis on the obtained experimental results. In particular, in Figure 7-13 and Figure 7-14 the instantaneous electric quantities for the benchmark SRM running at base speed are plotted. Similarly, Figures 7-15 and 7-16 report the measured electric quantities for the SRM with the 3D printed rotor operating at 600 rpm.

For the benchmark EM (i.e., Figure 7-13), it was possible to observe the soft-chopping action, necessary to maintain the current within the hysteresis band. On the contrary, a flat-topped voltage waveform was recorded for the 3D printed rotor SRM (i.e., Figure 7-15). This indicates that the power electronics converter has reached its current limit. Such an observation was also confirmed by the time-period of current / voltage

waveforms. Indeed, for the benchmark EM, two electrical periods last 25ms, whilst they last c.a. 27ms for the 3D printed rotor SRM. Accordingly, by calculating the mechanical speed as in (2), where f_{el} was the electrical frequency, it was possible to verify that the 3D SRM was actually slowing down by c.a. 45 rpm.

$$\omega_m[rpm] = \frac{60 \cdot f_{el}}{Rotor\ Poles} \qquad (2)$$

Further considerations can be made relying on the instantaneous power waveforms (Figure 7.14 and 7.16). First of all, by calculating the ratio between active and apparent power, it was possible to obtain the power factor. At base speed the latter, was equal to 0.52 for both machines. This interesting result indicates that, in principle, the volt-ampere rating of the power converter for a 3D printed rotor SRM can be identical to a standard laminated one (with the same rated power).

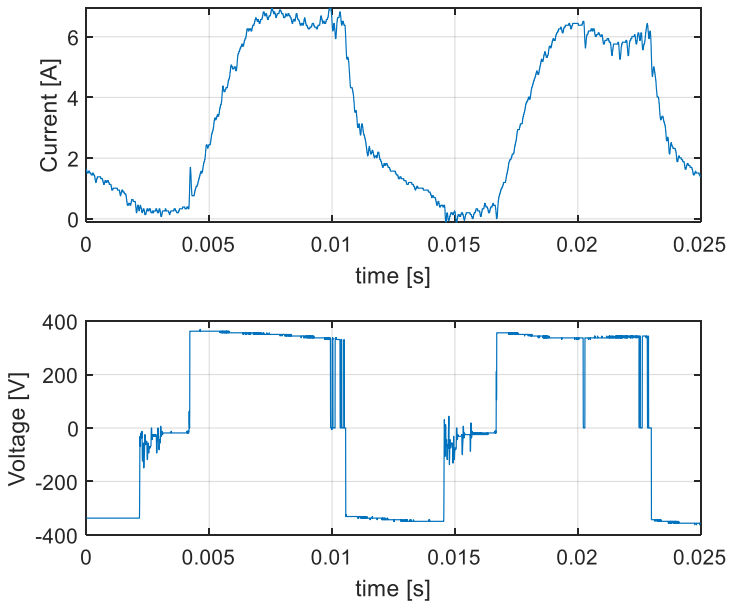

Figure 7-14: Voltage and current for the benchmark SRM at base speed and rated torque.

However, for the SRM at hand, because of the increased rotor losses caused by the solid rotor structure, the power converter results slightly underrated. In fact, the RMS input power for the benchmark SRM was 3.83 kVA, whilst it was equal to 4.24 kVA for the

3D printed rotor SRM. The larger demanded apparent power was needed for partially compensating the efficiency reduction, which can be calculated as the ratio between average mechanical power and average electric power. In particular, the efficiency reduction (at base speed) was c.a. 22 %. As the operating speed was increased, the efficiency of both machines rises accordingly; peaking at c.a. 83 % for the benchmark SRM and 65 % for the 3D printed one. Such behaviour was mainly ascribable to the progressively decreasing RMS phase current with increasing speed (for constant and decreasing power operating conditions). Accordingly, the stator Joule losses tend to decrease at high speed, leading to a higher overall efficiency for both machines.

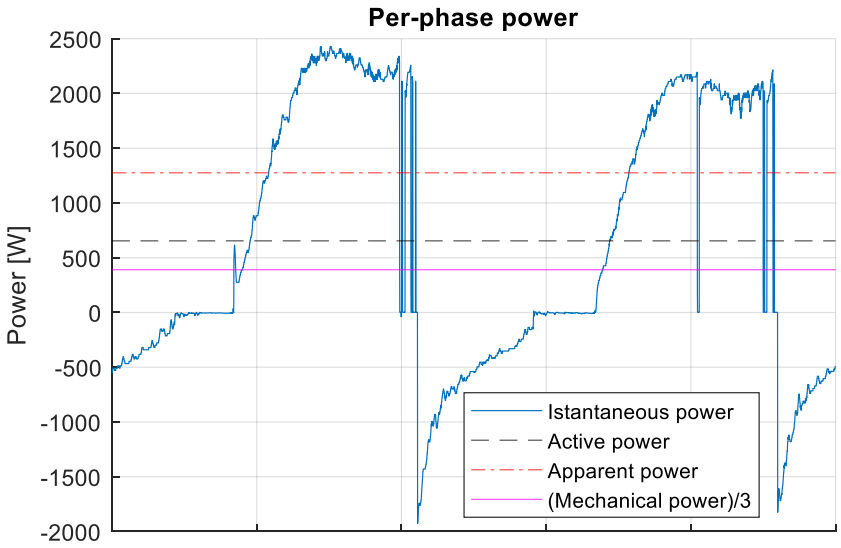

Figure 7-15: Instantaneous power for the benchmark SRM at base speed and rated torque

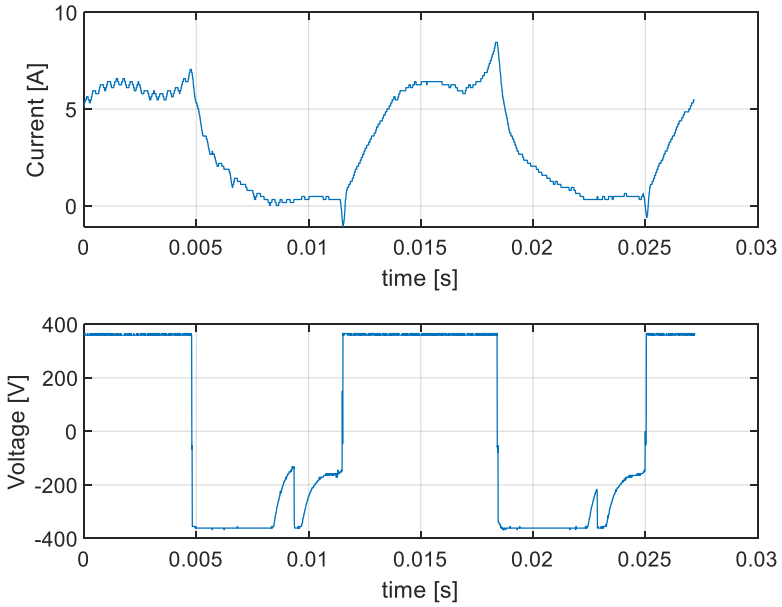

Figure 7-16: Voltage and current for the 3D printed SRM at base speed and rated torque.

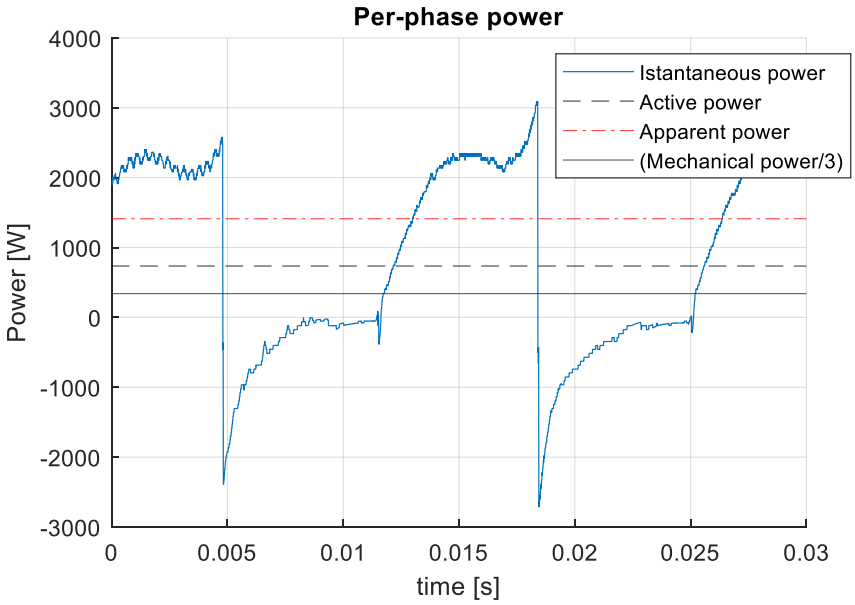

Figure 7-17: Instantaneous power for the 3D printed SRM at base speed and rated torque.

7.8 Conclusions

Additive manufacturing can be one of the main enablers for future, high performance electrical machines. This work demonstrates the high technology readiness level of 3D printing and more specifically LPBF, as a manufacturing method for soft magnetic materials employed in electrical machines.

Although there is a wide on-going research effort on the topic, few are the examples of operational 3D printed active parts for electrical machines. The main objective of this work is to prove the concept that additive manufacturing for electric motors is actually viable and feasible from a manufacturing and technological point of view. Starting from the raw material (i.e., soft magnetic powder), a complete, test-ready rotor has been manufactured through LPBF and coupled to an existing commercial switched reluctance stator. Comprehensive experimental tests have been carried out, covering the whole torque / speed envelope. The obtained results have been compared to those experimentally recorded on an identical, benchmark machine, featuring a conventional, laminated rotor.

Clearly, because the rotor was a relatively simple solid block with no laminations, its losses were considerably higher with respect to the benchmark machine due to higher eddy current losses. However, thanks to the strengths of additive manufacturing, a more geometrically complex and magnetically optimized rotor could be easily built, for improved overall machine efficiency. Nonetheless, the main objective of this work was achieved. Namely, to prove that additive manufacturing for electric motors is viable and feasible from a manufacturing and technological point of view.

Future work will investigate a multi-objective, 3D finite element optimization and how the magnetic structure can be modified / improved in order to mitigate the effect of eddy

current losses. The outcomes of this Chapter highlight comparable behaviors within the low-speed region, while improvements to contain the core losses are required at higher speed.

8. Chapter 8: Conclusions and recommendations for future work

8.1 Conclusions

In this thesis, a systematic approach was followed to manufacture a 3D printed electric motor via LPBF. Due to the inherent physical properties of Fe-Si and Cu, which were the materials of interest in this study, extensive parameter optimisation and material characterisation was carried out before trying to manufacture motor components (rotor, stator, windings etc.). This Chapter is divided into three parts based on the results. New information on the two materials investigated in this study will be shown and the results from the 3D-printed SRM rotor will be presented. The first part presents the main findings on pure copper processed via LPBF, the second part presents the findings on Fe-Si steels and the third part presents the main conclusions that were drawn based on the experimental tests of the 3D-printed SRM.

8.2 Copper Findings

Laser processing of copper is difficult due to its inherent properties such as high thermal conductivity and high reflectivity. In this work, in-situ absorptivity measurements for copper were used, to understand its melting behaviour and dependence on typical processing parameters used in LPBF.

- AM has the potential to create windings with higher fill factors than traditional manufacturing methods suitable for electric motors.
- Cu cannot be processed to near fully dense parts with a 200W IR laser.
- The use of several scan strategies did not have a significant impact on the density of copper samples (pre-melting, re-melting etc.)

- As-built specimens by LPBF featured anisotropic resistivity that was justified by the lack of both intra-layer and inter-layer fusion.
- Horizontal samples had a lower resistivity than vertical ones.
- Post-heat treatments aided in sintering together material and slightly increased the density of samples resulting in a lower resistivity.
- Anisotropic resistivity was also observed for the heat-treated samples.
- For both as built and heat-treated samples, resistivity remained higher for the vertical samples.
- In-situ absorptivity measurements were conducted (laser calorimetry) to shed light on the interaction of pure copper with an IR laser up to 600W and understand better its melting behaviour.

8.3 Fe-Si Findings

One of the main challenges in laser powder bed fusion of high silicon steel alloys is the formation of high degrees of cracking in the fabricated parts. In this study, the composition of a soft magnetic alloy was modified in order to improve ductility and reduce the in-process formation of cracks. Higher silicon content in the alloy, leads to embrittlement, therefore a first step was to gradually reduce the %w.t of Si. A pre-alloyed Fe-6.9%Si powder was mixed with high purity Fe-powder. The resulting powder blends were used to produce near fully dense samples that were characterised in terms of mechanical, thermal and electromagnetic properties. The novelty and results of this work on Fe-Si can be summarised in the following:

- Through compositional adjustments of the soft magnetic powder blends it has been shown that robust rotor cores can be manufactured via LPBF.

- An optimum parameter set was identified for the production of near fully dense (99.98%), crack-free, Fe-5%w.t. Si parts via LPBF. It was observed that the higher silicon content resulted in less dense parts and increased porosity. In addition, embrittlement leading to multiple cracks initiating either from pores or from the edges of samples was seen for Fe-6.9%w.t. Si alloy independent of geometry and size.
- Higher substrate temperatures resulted in a reduction of in-process crack formation and reduced residual stresses.
- Extensive cracks and delaminations were observed in several cases for silicon steel powders with silicon content higher than 6%w.t.
- For increased volumetric laser density in LPBF of Fe-Si alloys the samples feature a cube texture along the build direction which can be favorable for electromagnetic applications. However, increased laser density causes a higher degree of porosity and/or cracks leading to parts with inferior mechanical, thermal and magnetic properties.

8.4 3D-Printed SRM Findings

One of this work's aims was to provide an initial proof of concept for a 3DP electric motor. For the purpose, a switched reluctance machine was chosen as a case study. Its rotor core was additively manufactured through laser powder bed fusion. Its performance was compared to that of an identical commercial motor featuring a laminated rotor core, via in-depth experimental tests. The main conclusions are presented:

- It has been demonstrated that successful manufacturing of a soft magnetic core via LPBF is possible. The functional 3D-printed SRM rotor was tested at rated

speed and two times the rated speed and the performance was directly compared to a laminated rotor core.

- The 3D printed soft magnetic rotor core was able to develop the rated power, however an efficiency reduction was noticed when compared to the conventional motor.
- Losses were found to be considerably higher for the 3DP rotor with respect to the conventional laminated rotor. That is attributed to the fact that the 3DP rotor was a relatively simple block of material consisting of 3 segments. It is well known that a laminated construction reduces losses, so this is not unexpected and the 3DP rotor performs well considering it is not of a laminated construction.
- In terms of output power and efficiency up to 600rpm (rated speed) the overall behaviour of both SRMs is comparable. This allows us to conclude that LPBF has the potential to pave the way towards the widespread adoption of AM in the production of components for lightweight and highly efficient electrical motors.

8.5 Benefits of the study

The findings from this study, can be beneficial for many industrial sectors interested in selective laser melting of soft magnetic alloys and highly conductive metals and alloys such as pure copper for electromagnetic applications. Automotive, aerospace and energy are some of the sectors where the successful implementation of AM for the fabrication to fabricate components can revolutionise the way electrical machines are manufactured. A trade-off between the material's ability to be processed by LPBF and its magnetic performance was made in order to successfully fabricate near fully dense parts. A significant increase in porosity and cracks was observed for the Fe-Si with silicon content above 6%wt.t. Therefore, it was determined experimentally that a good

composition for silicon steel LPBF was Fe-5%w.t.Si, which can be used as a baseline for further research. Moreover, the availability of a wide range of Fe-Si alloys, together with their main physical properties, is also expected to help machine designers in industry and academia to decide on the appropriate composition with application dependent criteria.

8.6 Recommendations for future work

The development of new soft magnetic alloys and the expansion of the list of materials suitable for the LPBF process is necessary. For example, adding Al to high silicon steel alloys to enhance their process-ability and determine the processing windows for soft magnetic alloys with commercial LPBF systems. As an alternative to silicon content reduction, elements that increase the ductility of the alloy could be added specifically to silicon steel with silicon content 6%w.t or higher. A good candidate would be aluminium, which is often added to Fe-Si alloys to improve their ductility and increase resistivity. However, aluminium addition in Fe-Si could decrease permeability and saturation magnetisation, therefore, in depth investigation of dynamic losses is required. One of the current limitations with commercial LPBF systems is the substrate temperature reaching a maximum of 200^{o}C. It would be beneficial both for soft magnetic alloys such as Fe-Si and highly reflective metals and alloys such as copper to be processed at higher temperatures. In the case of Fe-Si, this would allow successful processing of high silicon steel alloys and for copper it could expand the process parameter window.

The heat treatment applied in this study on Fe-Si was a simple annealing at 1150^{o}C for 1½ h based on standard heat-treating practices for silicon steel sheets. There is a lack of information in the existing literature regarding the influence of annealing temperature,

time duration and cooling rate on the microstructure of LPBF processed Fe-Si. Further investigation in fine-tuning of heat treatments is necessary in order to better understand its effects on the resulting microstructure and effectively on mechanical and magnetic properties. It is expected that improvements in heat treatment procedures may result in corresponding improvements in the soft-magnetic properties. Heat treatments should be correlated to the frequency and the operating temperature of the 3D-printed components.

Although several research groups have claimed that they have successfully produced a fully 3D printed electric motor there is still no evidence of a functional motor with all its components fabricated through AM. LPBF currently features the highest technology readiness level for such an endeavour.

It has already been demonstrated that soft magnetic materials can be manufactured through LPBF for stators and rotors. Furthermore, coils and windings can be made of aluminium or copper by various AM technologies. The next stage would be to design a motor that incorporates all the components that could be manufactured entirely via AM. AM has several advantages to offer, and a next logical step would be the production and testing of a fully 3D printed electric motor as a proof-of- concept. More radical design solutions are required to enhance the performance of a 3DP-SRM. Some design ideas are presented below for future research:

- Reduce eddy currents generated in the soft magnetic rotor core through the introduction of slits in the microstructure or in the end design of the rotor.
- Lattice structure integrated into the casing for weight reduction and improved cooling performance.
- Waved coils with a non-uniform cross section to increase fill factor and heat dissipation

- Skewed rotor for low torque ripple
- Curved air gap for enhanced magnetic flux
- Integrated cooling channels (windings and/or casing)

More design iterations for the SRM motor are required to further improve its efficiency by reducing its weight and improve its efficiency by minimising eddy current losses formed in the bulk material.

APPENDIX 1 – Grinding & Polishing Steps

Fe-Si	Wheel/Cloth	Lubricant	Force (N)	Wheel-Speed (rpm)	Time (min)
Plane Grinding	SiC 220 mesh	Methylated Spirit	30	300	3
	SiC 800 mesh	Methylated Spirit	30	300	3
Fine Grinding	SiC 1200 mesh	Methylated Spirit	30	300	3
Polishing	MD-Largo	9μm diamond suspension	10	150	3
	MD-Dac	3μm diamond suspension	10	150	10
	MD-Floc	1μm diamond suspension	10	150	15
	MD-Chem	0.04μm silica suspension	10	150	30

Cu	Wheel/Cloth	Lubricant	Force (N)	Wheel Speed (rpm)	Time (min)
Plane Grinding	SiC 400 mesh	Water	25	300	As needed
	SiC 800 mesh	Water	25	300	1
Fine Grinding	SiC 1200 mesh	Water	25	300	1
	SiC 4000 mesh	Water	25	300	1
Polishing	MD-Mol	DiaPro Mol R3	25	150	4
	MD-Chem	Iron (III) Nitrate	15	150	1

APPENDIX 2 – Pole Figures for various scan strategies

Stripes 2

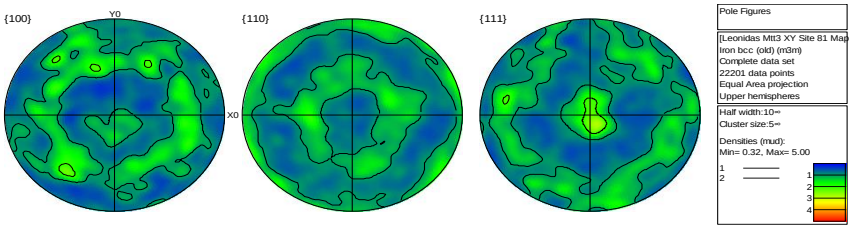

Checkerboard 1

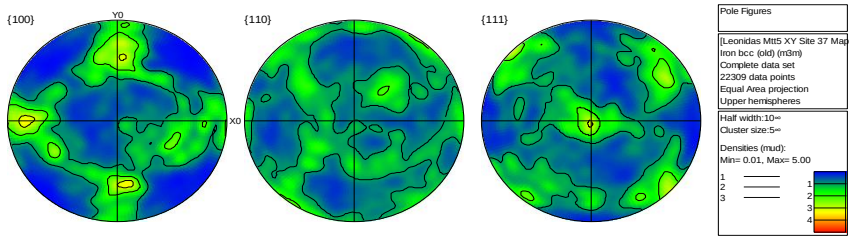

Checkerboard 2

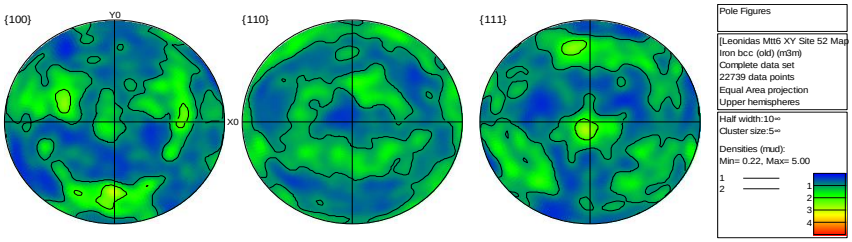

Checkerboard 3

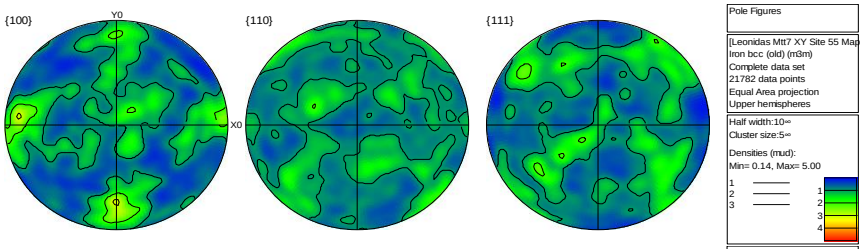

Checkerboard 4

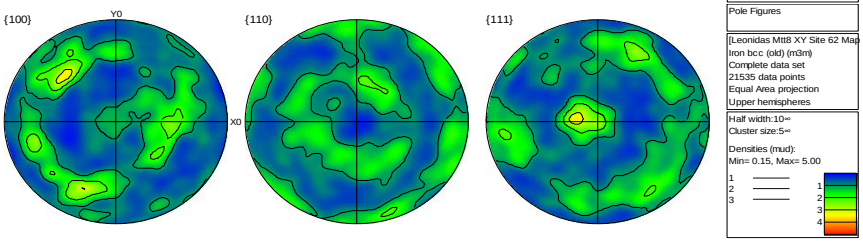

Pre-melt 1

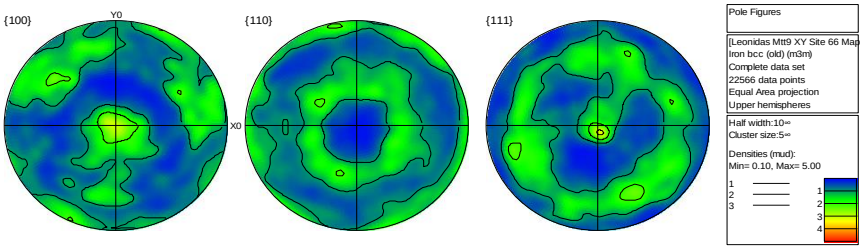

Pre-melt 2

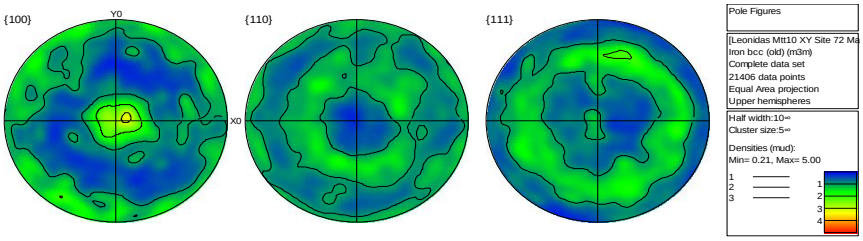

References

[1] P.M. Hopkinson, N., Hague, R.J.M., Dickens, Rapid Manufacturing, John Wiley & Sons, Ltd, Chichester, UK, UK, 2005. doi:10.1002/0470033991.

[2] R. Hague, I. Campbell, P. Dickens, Implications on design of additive manufacturing, Science. 217 (2003) 25–30.

[3] R. Hague, S. Mansour, N. Saleh, Material and design considerations for Rapid Manufacturing, International Journal of Production Research. 42 (2004) 4691–4708. doi:10.1080/00207840410001733940.

[4] B. M., Economic aspects of additive manufacturing: benefits costs and energy consumption, Doctoral Thesis. (2012). https://dspace.lboro.ac.uk/2134/10768.

[5] D. Thomas, Costs, benefits, and adoption of additive manufacturing: a supply chain perspective, International Journal of Advanced Manufacturing Technology. 85 (2016) 1857–1876. doi:10.1007/s00170-015-7973-6.

[6] D. Alberts, D. Schwarze, G. Witt, In Situ Melt Pool Monitoring and the Correlation To Part Density of Inconel 718 for quality assurance in selective laser melting, Solid Freeform Fabrication Symposium. (2017).

[7] W. Zouhri, J.Y. Dantan, B. Häfner, N. Eschner, L. Homri, G. Lanza, O. Theile, M. Schäfer, Optical process monitoring for Laser-Powder Bed Fusion (L-PBF), CIRP Journal of Manufacturing Science and Technology. 31 (2020) 607–617. doi:10.1016/j.cirpj.2020.09.001.

[8] M. Garibaldi, C. Gerada, I. Ashcroft, R. Hague, H. Morvan, The Impact of Additive Manufacturing on the Development of Electrical Machines for MEA Applications : A Feasibility Study, 3rd International Conference More Electric Aircraft (MEA 2015). (2015) 2–5. https://hal.archives-ouvertes.fr/hal-01178353%5Cnwww.see.asso.fr/node/12121.

[9] J. Kruth, M. Badrossamay, E. Yasa, J. Deckers, L. Thijs, J. Van Humbeeck, Part and material properties in selective laser melting of metals, 16th International Symposium on Electromachining. (2010) 1–12.

[10] D.D. Gu, W. Meiners, K. Wissenbach, & R. Poprawe, R. Poprawe, Laser additive manufacturing of metallic components: materials, processes and mechanisms, International Materials Reviews. 6608 (2017). doi:10.1179/1743280411Y.0000000014.

[11] T. Laumer, M. Karg, M. Schmidt, Laser Beam Melting of Multi-Material Components, Physics Procedia. 39 (2012) 518–525. doi:10.1016/j.phpro.2012.10.068.

[12] Z. Hu, B. Nagarajan, X. Song, R. Huang, W. Zhai, J. Wei, Formation of SS316L Single Tracks in Micro Selective Laser Melting: Surface, Geometry, and Defects, Advances in Materials Science and Engineering. 2019 (2019). doi:10.1155/2019/9451406.

[13] B. Nagarajan, Z. Hu, X. Song, W. Zhai, J. Wei, Development of Micro Selective Laser Melting: The State of the Art and Future Perspectives, Engineering. (2019). doi:10.1016/j.eng.2019.07.002.

[14] Y. Pupo, J. Delgado, L. Serenó, J. Ciurana, Scanning space analysis in Selective Laser Melting for CoCrMo powder, Procedia Engineering. 63 (2013) 370–378. doi:10.1016/j.proeng.2013.08.228.

[15] M. Shiomi, K. Osakada, K. Nakamura, T. Yamashita, F. Abe, Residual Stress within Metallic Model Made by Selective Laser Melting Process, CIRP Annals - Manufacturing Technology. 53 (2004) 195–198. doi:10.1016/S0007-8506(07)60677-5.

[16] B. Cheng, S. Shrestha, K. Chou, Stress and deformation evaluations of scanning strategy effect in selective laser melting, Additive Manufacturing. 12 (2016) 240–251. doi:10.1016/j.addma.2016.05.007.

[17] L. Parry, I.A. Ashcroft, R.D. Wildman, Understanding the effect of laser scan strategy on residual stress in selective laser melting through thermo-mechanical simulation, Additive Manufacturing. 12 (2016) 1–15. doi:10.1016/j.addma.2016.05.014.

[18] J. Jhabvala, T. Antignac, E. Boillat, R. Glardon, Study and simulation of different scanning strategies in SLM, Innovative Developments in Design and Manufacturing. (2009). doi:10.1201/9780203859476.ch57.

[19] B. Qian, Y.S. Shi, Q.S. Wei, H.B. Wang, The helix scan strategy applied to the selective laser melting, International Journal of Advanced Manufacturing Technology. 63 (2012) 631–640. doi:10.1007/s00170-012-3922-9.

[20] S. Catchpole-smith, N. Aboulkhair, L. Parry, C. Tuck, I.A. Ashcroft, A. Clare, Fractal Scan Strategies for Selective Laser Melting of ' Unweldable ' Nickel Superalloys : selective laser melting , Nickel alloys , scan strategies , Additive Manufacture ., (n.d.).

[21] L. Thijs, K. Kempen, J.-P. Kruth, J. Van Humbeeck, Fine-structured aluminium products with controllable texture by selective laser melting of pre-alloyed AlSi10Mg powder, Acta Materialia. 61 (2013) 1809–1819.

[22] L. Thijs, F. Verhaeghe, T. Craeghs, J. Van Humbeeck, J.-P. Kruth, A study of the microstructural evolution during selective laser melting of Ti–6Al–4V, Acta Materialia. 58 (2010) 3303–3312.

[23] S.H. Sun, K. Hagihara, T. Nakano, Effect of scanning strategy on texture formation in Ni-25 at.%Mo alloys fabricated by selective laser melting, Materials and Design. 140 (2018) 307–316. doi:10.1016/j.matdes.2017.11.060.

[24] N.T. Aboulkhair, N.M. Everitt, I. Ashcroft, C. Tuck, Reducing porosity in AlSi10Mg parts processed by selective laser melting, Additive Manufacturing. 1 (2014) 77–86. doi:10.1016/j.addma.2014.08.001.

[25] J.P. Kruth, L. Froyen, J. Van Vaerenbergh, P. Mercelis, M. Rombouts, B. Lauwers, Selective laser melting of iron-based powder, Journal of Materials Processing Technology. 149 (2004) 616–622. doi:10.1016/j.jmatprotec.2003.11.051.

[26] A. Hughes., Electric motors and drives fundamentals, types and applications, 2006. doi:10.1016/B978-0-08-098332-5.00001-2.

[27] T. Finken, M. Felden, K. Hameyer, Comparison and design of different electrical machine types regarding their applicability in hybrid electrical vehicles, Proceedings of the 2008 International Conference on Electrical Machines, ICEM'08. (2008). doi:10.1109/ICELMACH.2008.4800044.

[28] W. Cao, B.C. Mecrow, G.J. Atkinson, J.W. Bennett, D.J. Atkinson, Overview of electric motor technologies used for more electric aircraft (MEA), IEEE Transactions on Industrial

Electronics. 59 (2012) 3523–3531. doi:10.1109/TIE.2011.2165453.

[29] S. Li, S. Member, S. Zhang, S. Member, T.G. Habetler, Modeling , Design Optimization and Applications of Switched Reluctance Machines – A Review, 9994 (2019) 1–22. doi:10.1109/TIA.2019.2897965.

[30] J. Hopkinson, Magnetic Properties of Alloys of Nickel and Iron, in: Proceedings of the Royal Society of London, 1890: pp. 1–13. http://rspl.royalsocietypublishing.org/.

[31] R.A. Hadfield, On alloys of iron and silicon., Journal of the Iron and Steel Institute. (1889) 222–255.

[32] M.F. Littmann, Iron and Silicon-Iron Alloys, IEEE Transactions on Magnetics. 7 (1971) 48–60. doi:10.1109/TMAG.1971.1066998.

[33] G. Herzer, Modern soft magnets: Amorphous and nanocrystalline materials, Acta Materialia. 61 (2013) 718–734.

[34] A. Schoppa, P. Delabre, A. Schatz, Optimal use of soft magnetic powder composites (SMC) in electrical machines, in: International Conference on Powder Metallurgy & Particulate Materials, 2013.

[35] R.M. Bozorth, Ferromagnetism, Ferromagnetism, by Richard M. Bozorth, Pp. 992. ISBN 0-7803-1032-2. Wiley-VCH, August 1993. (1993) 992.

[36] R.C. O'Handley, Modern Magnetic Materials:Principles and Applications, 1999.

[37] B.D. Cullity, C.D. Graham, Introduction to magnetic materials, John Wiley & Sons, 2011.

[38] H. Kronmuller, S. Parkin, Handbook of Magnetism and Advanced Magnetic Materials Vol.4 - Novel Materials, NJ, 2007.

[39] F. Fiorillo, C. Appino, M. Pasquale, Soft magnetic materials, 2016. doi:10.1088/0305-4624/6/6/409.

[40] A.J. Moses, Energy efficient electrical steels: Magnetic performance prediction and optimization, Scripta Materialia. 67 (2012) 560–565. doi:10.1016/j.scriptamat.2012.02.027.

[41] ASTM International, A677-16 Standard Specification for Nonoriented Electrical Steel , Fully Processed Types, (2005) 1–5. doi:10.1520/A0677-16.2.

[42] ASTM International, A726-18 Standard Specification for Cold-Rolled Magnetic Lamination Quality Steel , Semiprocessed Type, ASTM International. A726 − 05 (2010) 1–5. doi:10.1520/A0726-05R10.2.

[43] S. Tumanski, Handbook of Magnetic Measurements, 2011.

[44] V. Stoyka, O. Stupakov, I. Petryshynets, Texture evolution in Fe – 3 % Si steel treated under unconventional annealing conditions, Materials Characterization. 1 (2010) 1066–1073. doi:10.1016/j.matchar.2010.06.020.

[45] D. Dorner, S. Zaefferer, L. Lahn, D. Raabe, Overview of Microstructure and Microtexture Development in Grain-oriented Silicon Steel, Journal of Magnetism and Magnetic Materials. 304 (2006) 183–186. doi:10.1016/j.jmmm.2006.02.116.

[46] M. NAMIKAWA, H. NINOMIYA, T. YAMAJI, High silicon steel sheets realizing excellent high frequency reactor performance, JFE Steel Corporation, …. 6 (2005). http://www.jfe-steel.co.jp/en/research/report/006/pdf/006-04.pdf.

[47] J.M. Miller, Oak Ridge National Laboratory Annual Progress Report for the Power Electronics and Electric Motors Program, 2013.

[48] H. Haiji, K. Okada, T. Hiratani, A. Abe, M. Ninomiya, Magnetic properties and workability of 6.5% Si steel sheet, Journal of Magnetism and Magnetic Materials. 160 (1996) 109–114. doi:10.1016/0304-8853(96)00128-X.

[49] International Electrotechnical Commision, IEC 60404-8-8:2017 Magnetic Materials - Part 8: Specifications for individual materials - Section 8: Specification for thin magnetic steel strip for use at medium frequencies, (n.d.).

[50] A. International, Standard Specification for Thin-Gauge Nonoriented Electrical Steel Fully Processed Type, ASTM International. A1086 − 13 (2013) 1–6. doi:10.1520/A1086.

[51] P.R. Swann, L. Granas, B. Lehtinen, The B2 and DO3 Oredering Reactions in Iron-Silicon Alloys in the vicinity of the Curie Temperature, Metal Science. 9 (1975) 90–96.

[52] O. Kubaschewski, Iron-binary Phase Diagrams, Berlin, Germany, 1982.

[53] F. González, Y. Houbaert, A review of ordering phenomena in iron-silicon alloys, Revista de Metalurgia. 49 (2013) 178–199. doi:10.3989/revmetalm.1223.

[54] W.J. Yuan, R. Li, Q. Shen, L.M. Zhang, Characterization of the evaluation of the solid solubility of Si in sintered Fe–Si alloys using DSC technique, Materials Characterization. 58 (2007) 376–379. doi:10.1016/j.matchar.2006.06.003.

[55] J.S. Shin, J.S. Bae, H.J. Kim, H.M. Lee, T.D. Lee, E.J. Lavernia, Z.H. Lee, Ordering-disordering phenomena and micro-hardness characteristics of B2 phase in Fe-(5-6.5%)Si alloys, Materials Science and Engineering A. 407 (2005) 282–290. doi:10.1016/j.msea.2005.07.012.

[56] R.D. Cava, W.J. Botta, C.S. Kiminami, M. Olzon-Dionysio, S.D. Souza, A.M. Jorge, C. Bolfarini, Ordered phases and texture in spray-formed Fe–5wt%Si, Journal of Alloys and Compounds. 509S (2011) S260–S264. doi:10.1016/j.jallcom.2010.11.184.

[57] Y. Ustinovshikov, I. Sapegina, Morphology of ordering Fe-Si alloys, Journal of Materials Science. 39 (2004) 1007–1016. doi:10.1023/B:JMSC.0000012934.96045.a3.

[58] T. Ros-Yanez, D. Ruiz, J. Barros, Y. Houbaert, R. Colás, Study of deformation and aging behaviour of iron-silicon alloys, Materials Science and Engineering A. 447 (2007) 27–34. doi:10.1016/j.msea.2006.10.075.

[59] D. Ruiz, T.R. Yañez, G.J. Cuello, R.E. Vandenberghe, Y. Houbaert, Order in Fe-Si alloys: A neutron diffraction study, Physica B: Condensed Matter. 385-386 I (2006) 578–580. doi:10.1016/j.physb.2006.05.364.

[60] J.N. Lemke, M. Simonelli, M. Garibaldi, I. Ashcroft, Calorimetric study and microstructure analysis of the order-disorder phase transformation in silicon steel built by SLM, Journal of Alloys and Compounds. 722 (2017) 121–125.

[61] H.D. Fu, Q. Yang, Z.H. Zhang, J.X. Xie, Effects of precipitated phase and order degree

on bending properties of an Fe-6.5 wt%Si alloy with columnar grains, Journal Of Materials Research. 26 (2011) 1711–1718. doi:10.1557/jmr.2011.136.

[62] K. Narita, M. Enokizono, Effect of Ordering on Magnetic Properties of 6.5-Percent Silicon-iron Alloy, IEEE Transactions on Magnetics. 15 (1979) 911–915. doi:10.1109/TMAG.1979.1060174.

[63] H. Ninomiya, Y. Tanaka, A. Hiura, Y. Takada, Magnetostriction and applications of 6.5% Si steel sheet, Journal of Applied Physics. 69 (1991) 5358–5360. doi:10.1063/1.348028.

[64] H. Seifert, M. Jurisch, J. Tobisch, G. Oertel, Mechanical properties of Fe-4.5-6w.t.%Si double roller ribbons, Materials Science and Engineering A. 133 (1991) 292–296.

[65] M. Garibaldi, I. Ashcroft, N. Hillier, S.A.C. Harmon, R. Hague, Relationship between laser energy input, microstructures and magnetic properties of selective laser melted Fe-6.9%wt Si soft magnets, Materials Characterization. (2018). doi:10.1016/j.matchar.2018.01.016.

[66] F. Faudot, J.F. Rialland, J. Bigot, Study of order-disorder effect on magnetic properties of rapidly quenched Fe-6.5 wt% Si alloys, Physica Scripta. 39 (1989) 263–267. doi:10.1088/0031-8949/39/2/013.

[67] P. Arato, I. Boc, T. Grof, Effect of composition on the loss of non-oriented medium silicon electric steels, Journal of Magnetism and Magnetic Materials. 41 (1984) 53–55.

[68] C.-K. Hou, Effect of silicon content on the loss separation and permeability of laminated steels, Journal of Magnetism and Magnetic Materials. 162 (1996) 280–290. doi:10.1016/S0304-8853(97)00651-3.

[69] F.W. Glaser, Electrical resistivity measurements on iron-silicon compacts prepared by the powder metallurgy procedure., Transactions. A.I.M.E. 185 (1949) 475–480.

[70] F.W. Glaser, W. Ivanick, Study of the Fe-Si order-disorder transformation, Trans. AIME J. Met. 206 (1956) 1290–1295.

[71] K.I. Numakura, A. Tsugawa, M. Sugano, Y. Sato, Magnetic and electric properties of iron-silicon alloys, 1972.

[72] T.D. Yensen, Magnetic and other properties of Iron-Silicon Alloys melted in Vacuo, 1915.

[73] P.W. Bridgman, Effects of pressure on binary alloys V: fifteen alloys of metals of moderately high melting point, in: Proc. Am. Acad. Arts Sci., 1957: pp. 131–177.

[74] D. Ruiz, T. Ros-Yáñez, L. Vandenbossche, L. Dupré, R.E. Vandenberghe, Y. Houbaert, Influence of atomic order on magnetic properties of Fe-Si alloys, Journal of Magnetism and Magnetic Materials. 290-291 PA (2005) 1423–1426. doi:10.1016/j.jmmm.2004.11.496.

[75] J.M. Makar, B.K. Tanner, Effect of plastic deformation and residual stress on the permeability and magnetostriction of steels, Journal of Magnetism and Magnetic Materials. 222 (2000) 291–304. doi:10.1016/S0304-8853(00)00558-8.

[76] R. Li, Q. Shen, L. Zhang, T. Zhang, Magnetic properties of high silicon iron sheet fabricated by direct powder rolling, Journal of Magnetism and Magnetic Materials. 281 (2004) 135–139.

[77] Y.F. Liang, F. Ye, J.P. Lin, Y.L. Wang, G.L. Chen, Effect of annealing temperature on magnetic properties of cold rolled high silicon steel thin sheet, Journal of Alloys and Compounds. 491 (2010) 268–270. doi:10.1016/j.jallcom.2009.10.118.

[78] J.H. Yu, J.S. Shin, J.S. Bae, Z. Lee, T.D. Lee, H.M. Lee, E.J. Lavernia, The effect of heat treatments and Si contents on B2 ordering reaction in high-silicon steels, Materials Science and Engineering A. 307 (2001) 29–34.

[79] J.S. Shin, Z.H. Lee, T.D. Lee, E.J. Lavernia, The effect of casting method and heat treating condition on cold workability of high-Si electrical steel, Scripta Materialia. 45 (2001) 725–731. doi:10.1016/S1359-6462(01)01086-7.

[80] R.K. Roy, A.K. Panda, M. Ghosh, A. Mitra, R.N. Ghosh, Effect of annealing treatment on soft magnetic properties of Fe-6.5 wt% Si wide ribbons, Journal of Magnetism and Magnetic Materials. 321 (2009) 2865–2870. doi:10.1016/j.jmmm.2009.04.052.

[81] M. Garibaldi, I. Ashcroft, J.N. Lemke, M. Simonelli, R. Hague, Effect of annealing on the microstructure and magnetic properties of soft magnetic Fe-Si produced via laser additive manufacturing, Scripta Materialia. 142 (2018) 121–125.

[82] P.Beckley, Electrical steels for Rotating Machines, (2000) 43–80.

[83] F.J.G. Landgraf, T. Yonamine, R. Takanohashi, F.Q. Silva, J.P. V Tosetti, F.B. Neto, E. Albertin, V.N.G. Mazzarella, I.G.S. Falleiros, M. Emura, Magnetic properties of silicon steel with as-cast columnar structure, Journal of Magnetism and Magnetic Materials. 254–255 (2003) 364–366. doi:10.1016/S0304-8853(02)00869-7.

[84] S. Nakashima, K. Takashima, J. Harase, Effect of silicon content and carbon addition on primary recrystallisation of Fe-3pct Si, Metallurgical and Materials Transactions A. 28 (1997) 681–687.

[85] Z. Zhang, W. Wang, H. Fu, J. Xie, Effect of quench cooling rate on residual stress, microstructure and mechanical property of an Fe-6.5Si alloy, Materials Science and Engineering A. 530 (2011) 519–524. doi:10.1016/j.msea.2011.10.013.

[86] S.C. Paolinelli, A. da C. Marco, Effect of stress relief annealing temperature and atmosphere on the magnetic properties of silicon steel, Journal of Magnetism and Magnetic Materials. 304 (2006) 599–601. doi:10.1016/j.jmmm.2006.02.187.

[87] C. Bolfarini, M.C.A. Silva, A.M. Jorge, C.S. Kiminami, W.J. Botta, Magnetic properties of spray-formed Fe–6.5%Si and Fe–6.5%Si–1.0%Al after rolling and heat treatment, Journal of Magnetism and Magnetic Materials. 320 (2008) e653–e656. doi:10.1016/j.jmmm.2008.04.104.

[88] M.F. De Campos, J.C. Teixeira, F.J.G. Landgraf, The optimum grain size for minimizing energy losses in iron, Journal of Magnetism and Magnetic Materials. 301 (2006) 94–99. doi:10.1016/j.jmmm.2005.06.014.

[89] J. Qin, P. Yang, W. Mao, F. Ye, Effect of texture and grain size on the magnetic flux density and core loss of cold-rolled high silicon steel sheets, Journal of Magnetism and Magnetic Materials. 393 (2015) 537–543. doi:10.1016/j.jmmm.2015.06.032.

[90] K. Raviprasad, K. Aoki, K. Chattopadhyay, The nature of dislocations and effect of order in rapidly solidified Fe-(5.5-7.5)wt.%Si alloys, Materials Science & Engineering A. 172

(1993) 125–135.

[91] B. Viala, J. Degauque, M. Fagot, M. Baricco, E. Ferrara, F. Fiorillo, Study of the brittle behaviour of annealed Fe-6.5 wt%Si ribbons produced by planar flow casting, Materials Science and Engineering A. 212 (1996) 62–68. doi:10.1016/0921-5093(96)10188-X.

[92] X. Wang, H. Liu, H. Li, Z. Liu, Effect of Cooling Rate on Order Degree of 6.5 wt.% Si Electrical Steel After Annealing Treatment, IEEE Transactions on Magnetics. 51 (2015) 1–4. doi:10.1109/TMAG.2015.2444012.

[93] C. P. Steinmetz, On the Law of Hysteresis," Trans. Am. Inst. Electr. Eng., vol. IX, no. 1, pp. 1–64, Jan. 1892., Trans. Am. Inst. Electr. Eng. IX (1982) 1–64.

[94] C.E. Webb, The power losses in magnetic sheet material at high flux densities, Electr. Eng. J. Inst. 64 (1926) 409–427.

[95] R.H. Pry, C.P. Bean, Calculation of the energy loss in magnetic sheet materials using a domain model, Journal of Applied Physics. 29 (1958) 532–533.

[96] G. Bertotti, General properties of power losses in soft ferromagnetic materials, IEEE Transactions on Magnetics. 24 (1988) 621–630.

[97] G. Bertotti, Physical interpretation of eddy current losses in ferromagnetic materials. II. Analysis of experimental results, Journal of Applied Physics. 57 (1985) 2118.

[98] D.M. Ionel, M. Popescu, S.J. Dellinger, T.J.E. Miller, R.J. Heideman, M. I. McGilp, On the variation with flux and frequency of the core loss coefficients in electrical machines, 42 (2006) 658–667.

[99] S. Takajo, T. Hiratani, T. Okubo, Y. Oda, Effect of silicon content on iron loss and magnetic domain structure of grain-oriented electrical steel sheet, IEEE Transactions on Magnetics. 54 (2018) 1–6. doi:10.1109/TMAG.2017.2759103.

[100] D. Goll, D. Schuller, G. Martinek, T. Kunert, J. Schurr, C. Sinz, T. Schubert, T. Bernthaler, H. Riegel, G. Schneider, Additive manufacturing of soft magnetic materials and components, Additive Manufacturing. (2019). doi:10.1016/j.addma.2019.02.021.

[101] A. Plotkowski, J. Pries, F. List, P. Nandwana, B. Stump, K. Carver, R.R. Dehoff, Influence of scan pattern and geometry on the microstructure and soft-magnetic performance of additively manufactured Fe-Si, Additive Manufacturing. 29 (2019) 100781. doi:10.1016/j.addma.2019.100781.

[102] B. Zhang, N.E. Fenineche, L. Zhu, H. Liao, C. Coddet, Studies of magnetic properties of permalloy (Fe30%Ni) prepared by SLM technology, Journal of Magnetism and Magnetic Materials. 324 (2012) 495–500. doi:10.1016/j.jmmm.2011.08.030.

[103] B. Zhang, N.-E.E. Fenineche, H. Liao, C. Coddet, Magnetic properties of in-situ synthesized FeNi3 by selective laser melting Fe-80% Ni powders, Journal of Magnetism and Magnetic Materials. 336 (2013) 49–54. doi:10.1016/j.jmmm.2013.02.014.

[104] C. V. Mikler, V. Chaudhary, T. Borkar, V. Soni, D. Choudhuri, R. V. Ramanujan, R. Banerjee, Laser additive processing of Ni-Fe-V and Ni-Fe-Mo Permalloys: Microstructure and magnetic properties, Materials Letters. 192 (2017) 9–11. doi:10.1016/j.matlet.2017.01.059.

[105] C. V. Mikler, V. Chaudhary, V. Soni, B. Gwalani, R. V. Ramanujan, R. Banerjee, Tuning

the phase stability and magnetic properties of laser additively processed Fe-30at%Ni soft magnetic alloys, Materials Letters. 199 (2017) 88–92. doi:10.1016/j.matlet.2017.04.054.

[106] J. Pippuri, S. Metsä-Kortelainen, T. Lindroos, M. Savolainen, A. Jokinen, A. Revuelta, A. Pasanen, K. Ruusuvuori, 3D Printing of Soft Magnetic Cores For Electrical Machines, in: Proceedings of the 1st Annual SMACC Research Seminar 2016, Department of Mechanical Engineering and Industrial Systems, Tampere, Finland, 2016: pp. 48–51. http://smacc.fi/wp-content/uploads/2016/10/Proceedings-of-the-1st-Annual-SMACC-reserch-Seminar-2016-v4.pdf.

[107] T. Riipinen, S. Metsä-Kortelainen, T. Lindroos, J.S. Keränen, A. Manninen, J. Pippuri-Mäkeläinen, Properties of soft magnetic Fe-Co-V alloy produced by laser powder bed fusion, Rapid Prototyping Journal. 25 (2019) 699–707. doi:10.1108/RPJ-06-2018-0136.

[108] T. Lindroos, T. Riipinen, S. Metsä-Kortelainen, J. Pippuri, J. Lagerbom, A. Revuelta, J. Metsäjoki, Soft magnetic alloys for selective laser melting, Proceedings Euro PM 2017: International Powder Metallurgy Congress and Exhibition. (2017).

[109] A.B. Kustas, D.F. Susan, K.L. Johnson, S.R. Whetten, M.A. Rodriguez, D.J. Dagel, J.R. Michael, D.M. Keicher, N. Argibay, Characterization of the Fe-Co-1.5V soft ferromagnetic alloy processed by Laser Engineered Net Shaping (LENS), Additive Manufacturing. 21 (2018) 41–52. doi:10.1016/j.addma.2018.02.006.

[110] M. Garibaldi, I. Ashcroft, M. Simonelli, R. Hague, Metallurgy of high-silicon steel parts produced using Selective Laser Melting, Acta Materialia. 110 (2016) 207–216. doi:10.1016/j.actamat.2016.03.037.

[111] N. Kang, M. El Mansori, F. Guittonneau, H. Liao, Y. Fu, E. Aubry, Controllable mesostructure, magnetic properties of soft magnetic Fe-Ni-Si by using selective laser melting from nickel coated high silicon steel powder, Applied Surface Science. 455 (2018) 736–741. doi:10.1016/j.apsusc.2018.06.045.

[112] B. Khatri, K. Lappe, D. Noetzel, K. Pursche, T. Hanemann, A 3D-printable polymer-metal soft-magnetic functional composite-development and characterization, Materials. 11 (2018). doi:10.3390/ma11020189.

[113] L.M. Bollig, P.J. Hilpisch, G.S. Mowry, B.B. Nelson-Cheeseman, 3D printed magnetic polymer composite transformers, Journal of Magnetism and Magnetic Materials. 442 (2017) 97–101. doi:10.1016/j.jmmm.2017.06.070.

[114] M. Garibaldi, C. Gerada, I. Ashcroft, R. Hague, Free-Form Design of Electrical Machine Rotor Cores for Production Using Additive Manufacturing, Journal of Mechanical Design, Transactions of the ASME. 141 (2019). doi:10.1115/1.4042621.

[115]. .. Pippuri J. Metsä-Kortelainen S., Lindroos T., Savolainen M., Jokinen A., Revuelta A., Pasanen A., Manufacturing of topology optimized soft magnetic core through 3D printing, NAFEMS Exploring the Design Freedom of Additive Manufacturing through Simulation. (2016).

[116] S. Lammers, G. Adam, H.J. Schmid, R. Mrozek, R. Oberacker, M.J. Hoffmann, Additive Manufacturing of a Lightweight Rotor for a Permanent Magnet Synchronous Machine, 13 (2016).

[117] M. Garibaldi, C. Gerada, I. Ashcroft, R. Hague, Free-Form Design of Electrical Machine

Rotor Cores for Production Using Additive Manufacturing, Journal of Mechanical Design. 141 (2019). doi:10.1115/1.4042621.

[118] S.M. Kortelainen, T. Lindroos, M. Savolainen, A. Jokinen, A. Revuelta, A. Pasanen, K. Ruusuvuori, J. Pippuri, Manufacturing of topology optimised magnetic core through 3D printing, in: NAFEMS Nordic Seminar, 2016.

[119] A. Manninen, J. Keranen, J. P.Makelainen, S.M. Kortelainen, T. Riipinen, T. Lindroos, Topology Optimisation of 3D Printed Switched Reluctance Motor, in: NAFEMS Nordic Seminar, 2018.

[120] G. Tseng, K.Ļ. Jyun, P. Huang, W. Lee, Application of Additive Manufacturing for Low Torque Ripple of 6 / 4 Switched Reluctance Motor, Proceedings of the 19th International Conference on Electrical Machines and Systems (ICEMS). (2016) 3–6. doi:10.1016/j.cognition.2010.08.013.

[121] J.R. Davis, ASM Specialty Handbook: Copper and Copper Alloys, ASM International, 2001.

[122] D.L. Ellis, GRCop-84 : A High-Temperature Copper Alloy for High-Heat-Flux Applications, (2019). https://ntrs.nasa.gov/search.jsp?R=20050123582.

[123] S.R. Pogson, P. Fox, C.J. Sutcliffe, W. O'Neill, The production of copper parts using DMLR, Rapid Prototyping Journal. 9 (2003) 334–343. doi:10.1108/13552540310502239.

[124] P. Frigola, O.A. Harrysson, T.J. Horn, H.A. West, R.L. Aman, J.M. Rigsbee, D.A. Ramirez, L.E. Murr, F. Medina, R.B. Wicker, E. Rodriguez, Fabricating copper components with electron beam melting, Advanced Materials and Processes. 172 (2014) 20–24.

[125] S.J. Raab, R. Guschlbauer, M.A. Lodes, C. Körner, Thermal and Electrical Conductivity of 99.9% Pure Copper Processed via Selective Electron Beam Melting, Advanced Engineering Materials. 18 (2016) 1661–1666. doi:10.1002/adem.201600078.

[126] P.A. Lykov, E.V. Safonov, A.M. Akhmedianov, Selective Laser Melting of Copper, Materials Science Forum. 843 (2016) 284–288. doi:10.4028/www.scientific.net/MSF.843.284.

[127] F. Trevisan, F. Calignano, M. Lorusso, M. Lombardi, D. Manfredi, P. Fino, Selective laser melting of chemical pure copper, 2017.

[128] D. Becker, W. Meiners, K. Wissenbach, Additive manufacturing of copper alloys by selective laser melting, in: WLT – German Scientific Laser Societey (Ed.), Proceedings of the 5th International WLT-Conference on Lasers in Manufacturing (LiM2009), Munich, Germany, 2009: pp. 195–200.

[129] J.-P. Kruth, X. Wang, T. Laoui, L. Froyen, Lasers and materials in selective laser sintering, Assembly Automation. 23 (2003) 357–371. doi:10.1108/01445150310698652.

[130] S.R.R. Pogson, P. Fox, C.J.J. Sutcliffe, W. O'Neill, The production of copper parts using DMLR, Rapid Prototyping Journal. 9 (2003) 334–343. doi:10.1108/13552540310502239.

[131] T.-T. Ikeshoji, K. Nakamura, M. Yonehara, K. Imai, H. Kyogoku, Selective Laser Melting of Pure Copper, Jom. (2017). doi:10.1007/s11837-017-2695-x.

[132] N.K. Tolochko, T. Laoui, Y. V Khlopkov, S.E. Mozzharov, V.I. Titov, M.B. Ignatiev, Absorptance of powder materials suitable for laser sintering, Rapid Prototyping Journal. 6

(2000) 155–160. doi:10.1108/13552540010337029.

[133] R.W. McVey, R.M. Melnychuk, J.A. Todd, R.P. Martukanitz, Absorption of laser irradiation in a porous powder layer, Journal of Laser Applications. 19 (2007) 214–224. doi:10.2351/1.2756854.

[134] S.B. Boyden, Y. Zhang, Temperature and wavelength-dependent spectral absorptivities of metallic materials in the infrared, Journal of Thermophysics and Heat Transfer. 20 (2006) 9–15. doi:10.2514/1.15518.

[135] J. Wang, C. Weng, J. Chang, C. Hwang, I. Introduction, The influence of temperature and surface conditions on surface absorptivity in laser surface treatment, 87 (2000).

[136] S. Liebl, R. Wiedenmann, A. Ganser, P. Schmitz, M.F. Zaeh, Laser Welding of Copper using Multi Mode Fiber Lasers at near infrared Wavelength, Physics Procedia. 56 (2014) 591–600. doi:10.1016/j.phpro.2014.08.047.

[137] A. Hess, R. Schuster, A. Heider, R. Weber, T. Graf, Continuous wave laser welding of copper with combined beams at wavelengths of 1030 nm and of 515 nm, Physics Procedia. 12 (2011) 88–94. doi:10.1016/j.phpro.2011.03.012.

[138] A. Heider, A. Hess, R. Weber, T. Graf, Stabilized copper welding by using power modulated green and ir laser beams, 30th International Congress on Applications of Lasers and Electro-Optics, ICALEO 2011. 395 (2011) 395–402. doi:10.2351/1.5062263.

[139] S. Engler, R. Ramsayer, R. Poprawe, Process Studies on Laser Welding of Copper with Brilliant Green and Infrared Lasers, Physics Procedia. 12 (2011) 339–346. doi:10.1016/j.phpro.2011.03.142.

[140] M. Haubold, A. Ganser, T. Eder, M.F. Zäh, Laser welding of copper using a high power disc laser at green wavelength, Procedia CIRP. 74 (2018) 446–449. doi:10.1016/j.procir.2018.08.161.

[141] E. Kaiser, E. Dold, A. Killi, S. Zaske, Application benefits of welding copper with a 1 kW , 515 nm continuous wave laser, (2018) 1–6.

[142] S. Masuno, M. Tsukamoto, K. Tojo, A. Keita, Y. Funada, S. Yu, Metal powder bed fusion additive manufacturing with 100 W blue diode laser, in: 36th International Congress Appllication Lasers Electro-Optics, 2017: pp. 4–5.

[143] A. Hess, A. Heider, R. Schuster, R. Weber, T. Graf, Benefits from combining laser beams with different wavelengths (green and IR) for copper welding, ICALEO. 540 (2010). doi:10.2351/1.5062078.

[144] D.Q. Zhang, Z.H. Liu, C.K. Chua, Investigation on forming process of copper alloys via Selective Laser Melting, in: High Value Manufacturing: Advanced Research in Virtual and Rapid Prototyping, 2013. doi:10.1201/b15961-53.

[145] M. Colopi, L. Caprio, A.G. Demir, B. Previtali, Selective laser melting of pure Cu with a 1 kW single mode fiber laser, Procedia CIRP. 74 (2018) 59–63. doi:10.1016/j.procir.2018.08.030.

[146] M. Colopi, A.G. Demir, L. Caprio, B. Previtali, Limits and solutions in processing pure Cu via selective laser melting using a high-power single-mode fiber laser, International Journal of Advanced Manufacturing Technology. (2019). doi:10.1007/s00170-019-04015-3.

[147] D. Petring, V.N. Goneghany, Parameter Dependencies of Copper Welding with Multi-kW Lasers at 1 Micron Wavelength, 12 (2011) 95–104. doi:10.1016/j.phpro.2011.03.013.

[148] Jadhav, Dadbakhsh, Vleugels, Hofkens, Puyvelde, Yang, Kruth, Humbeeck, Vanmeensel, Influence of Carbon Nanoparticle Addition (and Impurities) on Selective Laser Melting of Pure Copper, Materials. 12 (2019) 2469. doi:10.3390/ma12152469.

[149] P.R. Gradl, C. Protz, S.E. Greene, D. Ellis, B. Lerch, I. Locci, Development and Hot-fire Testing of Additively Manufactured Copper Combustion Chambers for Liquid Rocket Engine Applications, in: 53rd AIAA/SAE/ASEE Joint Propulsion Conference, American Institute of Aeronautics and Astronautics, Reston, Virginia, 2017. doi:10.2514/6.2017-4670.

[150] D.L. Ellis, D.J. Keller, Thermophysical Properties of GrCop-84, NASA/CR-2000-210055. 4 (2000) 1–45. doi:10.1002/0471777471.ch1.

[151] I. Yadroitsev, A. Gusarov, I. Yadroitsava, I. Smurov, Single track formation in selective laser melting of metal powders, Journal of Materials Processing Technology. 210 (2010) 1624–1631. doi:10.1016/j.jmatprotec.2010.05.010.

[152] I. Yadroitsev, P. Krakhmalev, I. Yadroitsava, S. Johansson, I. Smurov, Energy input effect on morphology and microstructure of selective laser melting single track from metallic powder, Journal of Materials Processing Technology. 213 (2013) 606–613. doi:10.1016/j.jmatprotec.2012.11.014.

[153] M.J. Matthews, G. Guss, S.A. Khairallah, A.M. Rubenchik, P.J. Depond, W.E. King, Denudation of metal powder layers in laser powder-bed fusion processes, Additive Manufacturing Handbook: Product Development for the Defense Industry. 114 (2017) 677–693. doi:10.1201/9781315119106.

[154] J. Ye, S.A. Khairallah, A.M. Rubenchik, M.F. Crumb, G. Guss, J. Belak, M.J. Matthews, Energy Coupling Mechanisms and Scaling Behavior Associated with Laser Powder Bed Fusion Additive Manufacturing, Advanced Engineering Materials. 21 (2019) 1900185. doi:10.1002/adem.201900185.

[155] S. Ly, A.M. Rubenchik, S.A. Khairallah, G. Guss, M.J. Matthews, Metal vapor micro-jet controls material redistribution in laser powder bed fusion additive manufacturing, Scientific Reports. 7 (2017) 1–12. doi:10.1038/s41598-017-04237-z.

[156] R.P. Martukanitz, R.M. Melnychuk, M.S. Stefanski, S.M. Copley, Dynamic absorption of a powder layer, ICALEO 2004 - 23rd International Congress on Applications of Laser and Electro-Optics, Congress Proceedings. 1404 (2004) 2–8. doi:10.2351/1.5060217.

[157] J. Trapp, A.M. Rubenchik, G. Guss, M.J. Matthews, In situ absorptivity measurements of metallic powders during laser powder-bed fusion additive manufacturing, Applied Materials Today. 9 (2017) 341–349. doi:10.1016/j.apmt.2017.08.006.

[158] M. Matthews, J. Ye, L. Gargalis, G. Guss, S. Khairallah, A. Rubenchik, Absorptivity and energy scaling associated with laser powder bed fusion additive manufacturing, Optics InfoBase Conference Papers. Part F127- (2019) 5–6. doi:10.1364/CLEO_AT.2019.AW3I.5.

[159] A.M. Rubenchik, W.E. King, S.S. Wu, Scaling laws for the additive manufacturing, Journal of Materials Processing Technology. 257 (2018) 234–243. doi:10.1016/j.jmatprotec.2018.02.034.

[160] F. Lorenz, J. Rudolph, R. Wemer, Design of 3D Printed High Performance Windings for Switched Reluctance Machines, Proceedings - 2018 23rd International Conference on Electrical Machines, ICEM 2018. (2018) 2451–2457. doi:10.1109/ICELMACH.2018.8506845.

[161] C. Silbernagel, I. Ashcroft, P. Dickens, M. Galea, Electrical resistivity of additively manufactured AlSi10Mg for use in electric motors, Additive Manufacturing. 21 (2018) 395–403. doi:10.1016/j.addma.2018.03.027.

[162] C. Silbernagel, L. Gargalis, I. Ashcroft, R. Hague, M. Galea, P. Dickens, Electrical resistivity of pure copper processed by medium-powered laser powder bed fusion additive manufacturing for use in electromagnetic applications, Additive Manufacturing. 29 (2019) 100831. doi:10.1016/j.addma.2019.100831.

[163] A.P. Ventura, C.J. Marvel, G. Pawlikowski, M. Bayes, M. Watanabe, R.P. Vinci, W.Z. Misiolek, The Effect of Aging on the Microstructure of Selective Laser Melted Cu-Ni-Si, Metallurgical and Materials Transactions A. (2017). doi:10.1007/s11661-017-4363-8.

[164] N. Simpson, P.H. Mellor, Additive manufacturing of shaped profile windings for minimal AC loss in gapped inductors, 2017 IEEE International Electric Machines and Drives Conference, IEMDC 2017. (2017) 1–7. doi:10.1109/IEMDC.2017.8002337.

[165] C. Wallis, B. Buchmayr, Effect of heat treatments on microstructure and properties of CuCrZr produced by laser-powder bed fusion, Materials Science and Engineering A. 744 (2019) 215–223. doi:10.1016/j.msea.2018.12.017.

[166] G. Jacob, A. Donmez, J. Slotwinski, S. Moylan, Measurement of powder bed density in powder bed fusion additive manufacturing processes, Measurement Science and Technology. 27 (2016) 115601.

[167] R.M. German, Powder metallurgy science, Metal Powder Industries Federation, 105 College Rd. E, Princeton, N. J. 08540, U. S. A, 1984. 279. (1984).

[168] R.M. German, Powder metallurgy of iron and steel, Wiley New York, 1998.

[169] A.B. Spierings, M. Voegtlin, T. Bauer, K. Wegener, Powder flowability characterisation methodology for powder-bed-based metal additive manufacturing, Progress in Additive Manufacturing. 1 (2016) 9–20.

[170] E.O. Olakanmi, Effect of mixing time on the bed density, and microstructure of selective laser sintered (sls) aluminium powders, Materials Research. 15 (2012) 167–176.

[171] Malvern Mastersizer-3000, (n.d.). http://www.malvern.com/en/products/product-range/mastersizer-range/mastersizer-3000/[(accessed February 12, 2018).

[172] ASTM B 213-17, Standard test methods for flow rate of metal powders using the hall flowmeter, ASTM International. (2017) 49–52. doi:10.1520/B0213-17.2.

[173] R.L. Carr, Evaluating flow properties of solids, Chem. Eng. 18 (1965) 163–168.

[174] B. Liu, B.Q. Li, Z. Li, Selective laser remelting of an additive layer manufacturing process on AlSi10Mg, Results in Physics. 12 (2019) 982–988. doi:10.1016/j.rinp.2018.12.018.

[175] J. Vaithilingam, R.D. Goodridge, R.J.M. Hague, S.D.R. Christie, S. Edmondson, The effect of laser remelting on the surface chemistry of Ti6al4V components fabricated by selective laser melting, Journal of Materials Processing Technology. 232 (2016) 1–8.

doi:10.1016/j.jmatprotec.2016.01.022.

[176] E8/E8M-13a Standard Test Method for tension testing of metallic materials, ASTM International. (2013). doi:10.1520/E0008.

[177] M. Fazio, E. Gutman, C. Hsia, G. Jones, Standard test method for resistivity of electrical conductor materials, Astm: B193-89. 02 (1990) 1–5. doi:10.1520/B0193-02R08.2.

[178] S.A. Khairallah, A.T. Anderson, A. Rubenchik, W.E. King, Laser powder bed fusion additive manufacturing: Physics of complex melt flow and formation mechanisms of pores spatter and denudation zones, Acta Materialia. 108 (2016) 36–45.

[179] G.T. Dyos, The Handbook of Electrical Resistivity: New materials and pressure effects, The Institution of Engineering and Technology, London, 2012. doi:10.1049/PBED013E.

[180] Y. Shi, P. Rometsch, K. Yang, F. Palm, X. Wu, Characterisation of a novel Sc and Zr modified Al–Mg alloy fabricated by selective laser melting, Materials Letters. 196 (2017) 347–350. doi:10.1016/j.matlet.2017.03.089.

[181] P. Grootenhuis, R.W. Powell, R.P. Tye, Thermal and Electrical Conductivity of Porous Metals made by Powder Metallurgy Methods, Proceedings of the Physical Society. Section B. 65 (1952) 502.

[182] P.F. Francesco Trevisan, Flaviana Calignano, Diego Manfredi, Selective laser melting of chemical pure copper powders, Euro PM2017. (2017) 1–6. doi:ISBN: 978-1-899072-49-1.

[183] P. Lykov, R. Baytimerov, S. Vaulin, E. Safonov, D. Zherebtsov, Selective Laser Melting of Copper by 200 W CO2 Laser, in: SAE Technical Paper Series, 2016: pp. 215–227. doi:10.4271/2016-01-0333.

[184] U. Scipioni Bertoli, A.J. Wolfer, M.J. Matthews, J.P.R. Delplanque, J.M. Schoenung, On the limitations of Volumetric Energy Density as a design parameter for Selective Laser Melting, Materials and Design. 113 (2017) 331–340. doi:10.1016/j.matdes.2016.10.037.

[185] A. Rubenchik, S. Wu, S. Mitchell, I. Golosker, M. LeBlanc, N. Peterson, Direct measurements of temperature-dependent laser absorptivity of metal powders, Applied Optics. 54 (2015) 7230. doi:10.1364/AO.54.007230.

[186] C.D. Boley, S.A. Khairallah, A.M. Rubenchik, Calculation of laser absorption by metal powders in additive manufacturing, Additive Manufacturing Handbook: Product Development for the Defense Industry. 54 (2017) 507–517. doi:10.1201/9781315119106.

[187] S.L. Campanelli, G. Casalino, N. Contuzzi, A. Angelastro, A.D. Ludovico, Analysis of the molten/solidified zone in selective laser melted parts, in: F. Dorsch (Ed.), Proceedings of SPIE - The International Society for Optical Engineering, 2014: p. 8963:896311. doi:10.1117/12.2042170.

[188] D.B. Hann, J. Iammi, J. Folkes, A simple methodology for predicting laser-weld properties from material and laser parameters , 44 (44) (2011), p. 445401, J. Phys. D. Appl. Phys. 44 (2011) 44–54.

[189] I. Yadroitsev, I. Smurov, Selective laser melting technology: From the single laser melted track stability to 3D parts of complex shape, Physics Procedia. 5 (2010) 551–560. doi:10.1016/j.phpro.2010.08.083.

[190] I. Yadroitsev, P. Bertrand, I. Smurov, Parametric analysis of the selective laser melting process, Applied Surface Science. 253 (2007) 8064–8069. doi:10.1016/j.apsusc.2007.02.088.

[191] M. Averyanova, E. Cicala, P. Bertrand, D. Grevey, Experimental design approach to optimize selective laser melting of martensitic 17-4 PH powder: part I–single laser tracks and first layer, Rapid Prototyping Journal. 18 (2012) 28–37.

[192] N.W. Makoana, H. Moller, H. Burger, M. Tlotleng, I. Yadroitsev, Evaluation of single tracks of 17-4PH steel manufactured at different power densities and scanning speeds by selective laser melting, South African Journal of Industrial Engineering. 27 (2016) 210–218.

[193] I. Yadroitsev, I. Yadroitsava, P. Bertrand, I. Smurov, Factor analysis of selective laser melting process parameters and geometrical characteristics of synthesized single tracks, Rapid Prototyping Journal. 18 (2012) 201–208.

[194] V.S. Sufiiarov, A.A. Popovich, E. V. Borisov, I.A. Polozov, D. V. Masaylo, A. V. Orlov, The Effect of Layer Thickness at Selective Laser Melting, Procedia Engineering. 174 (2017) 126–134. doi:10.1016/j.proeng.2017.01.179.

[195] Q.B. Nguyen, D.N. Luu, S.M.L. Nai, Z. Zhu, Z. Chen, J. Wei, The role of powder layer thickness on the quality of SLM printed parts, Archives of Civil and Mechanical Engineering. 18 (2018) 948–955. doi:10.1016/j.acme.2018.01.015.

[196] M.M. Savalani, J.M. Pizarro, Effect of preheat and layer thickness on selective laser melting (SLM) of magnesium, Rapid Prototyping Journal. 22 (2016) 115–122. doi:10.1108/RPJ-07-2013-0076.

[197] M. Ma, Z. Wang, M. Gao, X. Zeng, Layer thickness dependence of performance in high-power selective laser melting of 1Cr18Ni9Ti stainless steel, Journal of Materials Processing Technology. 215 (2015) 142–150.

[198] K.K.B. Hon, Digital Additive Manufacturing: From Rapid Prototyping to Rapid Manufacturing BT - Proceedings of the 35th International MATADOR Conference, in: S. Hinduja, K.-C. Fan (Eds.), Springer London, London, 2007: pp. 337–340.

[199] G.R. Buican, G. Oancea, C. Lancea, M.A. Pop, Influence of Layer Thickness on Internal Structure of Parts Manufactured from 316-L Steel Using SLM Technology, Applied Mechanics and Materials. 809–810 (2015) 369–374. doi:10.4028/www.scientific.net/AMM.809-810.369.

[200] S. Dingal, T.R. Pradhan, J.K.S. Sundar, A.R. Choudhury, S.K. Roy, The application of Taguchi's method in the experimental investigation of the laser sintering process, The International Journal of Advanced Manufacturing Technology. 38 (2008) 904–914.

[201] M.M. Savalani, L. Hao, P.M. Dickens, Y. Zhang, K.E. Tanner, R.A. Harris, The effects and interactions of fabrication parameters on the properties of selective laser sintered hydroxyapatite polyamide composite biomaterials, Rapid Prototyping Journal. 18 (2012) 16–27. doi:10.1108/13552541211193467.

[202] P. Mercelis, J. Kruth, Residual stresses in selective laser sintering and selective laser melting, Rapid Prototyping Journal. 12 (2006) 254–265. doi:10.1108/13552540610707013.

[203] J.-P. Kruth, G. Levy, F. Klocke, T.H.C. Childs, Consolidation phenomena in laser and powder-bed based layered manufacturing, CIRP Annals. 56 (2007) 730–759.

[204] S. ZHANG, R.Z. GUI, Q.S. WEI, Cracking behavior and formation mechanism of TC4

alloy formed by selective laser melting, Journal of Mechanical Engineering. 49 (2013) 21–27.

[205] D. Gu, Y.C. Hagedorn, W. Meiners, G. Meng, R.J.S. Batista, K. Wissenbach, R. Poprawe, Densification behavior, microstructure evolution, and wear performance of selective laser melting processed commercially pure titanium, Acta Materialia. 60 (2012) 3849–3860. doi:10.1016/j.actamat.2012.04.006.

[206] C. Jing, L. Xin, W. Tao, Y. Haiou, H. Weidong, The hot cracking mechanism of 316L stainless steel cladding in rapid laser forming process, Rare Metal Materials and Engineering. 32 (2003) 183–186.

[207] L.N. Carter, K. Essa, M.M. Attallah, Optimisation of selective laser melting for a high temperature Ni-superalloy, Rapid Prototyping Journal. 21 (2015) 423–432.

[208] K. Kempen, B. Vrancken, S. Buls, L. Thijs, J. Van Humbeeck, J.-P. Kruth, Selective Laser Melting of Crack-Free High Density M2 High Speed Steel Parts by Baseplate Preheating, Journal of Manufacturing Science and Engineering. 136 (2014) 061026. doi:10.1115/1.4028513.

[209] K. Shibata, K. Asakura, Transformation behavior and microstructures in Ultra-Low Carbon Steels, ISIJ International. 35 (1995) 982–991.

[210] Y. Lu, S. Wu, Y. Gan, J. Li, C. Zhao, D. Zhuo, J. Lin, Investigation on the microstructure, mechanical property and corrosion behavior of the selective laser melted CoCrW alloy for dental application, Materials Science and Engineering C. 49 (2015) 517–525. doi:10.1016/j.msec.2015.01.023.

[211] F. Huyan, R. Larker, P. Rubin, P. Hedström, Effect of solute silicon on the lattice parameter of ferrite in ductile irons, ISIJ International. 54 (2014) 248–250. doi:10.2355/isijinternational.54.248.

[212] M. Garibaldi, Laser Additive Manufacturing of Soft Magnetic Cores for Rotating Electrical Machinery:Materials Development and Part Design, University of Nottingham, 2017.

[213] J. Lemke, DEVELOPMENT OF IRON-BASED ALLOYS FOR INNOVATIVE POWDER METALLURGY PROCESSES T, 2016.

[214] A. Mertens, S. Reginster, H. Paydas, Q. Contrepois, T. Dormal, O. Lemaire, L.-B. J., Mechanical properties of alloy Ti–6Al–4V and of stainless steel 316L processed by selective laser melting: influence of out-of-equilibrium microstructures, Powder Metallurgy. 57 (2014) 184–189.

[215] G. Ouyang, B. Jensen, W. Tang, K. Dennis, C. Macziewski, S. Thimmaiah, Y. Liang, J. Cui, Effect of wheel speed on magnetic and mechanical properties of melt spun Fe-6.5 wt.% Si high silicon steel, AIP Advances. 8 (2018). doi:10.1063/1.5006481.

[216] V. Pricop, E. Helerea, M. Daniel Calin, Influence of alloy elements on magnetic properties of electrical steels, 2016 International Conference on Applied and Theoretical Electricity, ICATE 2016 - Proceedings. (2016). doi:10.1109/ICATE.2016.7754607.

[217] J. Barros, T. Ros-Yañez, L. Vandenbossche, L. Dupré, J. Melkebeek, Y. Houbaert, The effect of Si and Al concentration gradients on the mechanical and magnetic properties of electrical steel, Journal of Magnetism and Magnetic Materials. 290-291 PA (2005) 1457–1460.

doi:10.1016/j.jmmm.2004.11.547.

[218] T. Nakayama, N. Honjou, T. Minaga, H. Yashiki, Effects of manganese and sulfur contents and slab reheating temperatures on the magnetic properties of non-oriented semi-processed electrical steel sheet, Journal of Magnetism and Magnetic Materials. 234 (2001) 55–61. doi:10.1016/S0304-8853(01)00208-6.

[219] X. Zhou, K. Li, D. Zhang, X. Liu, J. Ma, W. Liu, Z. Shen, Textures formed in a CoCrMo alloy by selective laser melting, Journal of Alloys and Compounds. 631 (2015) 153–164. doi:10.1016/j.jallcom.2015.01.096.

[220] M. Yilmaz, Limitations/capabilities of electric machine technologies and modeling approaches for electric motor design and analysis in plug-in electric vehicle applications, Renewable and Sustainable Energy Reviews. 52 (2015) 80–99. doi:10.1016/j.rser.2015.07.033.

[221] W. Tong, Mechanical design of electric motors, 2014. doi:10.1201/b16863.

[222] A. Krings, A. Boglietti, A. Cavagnino, S. Sprague, Soft Magnetic Material Status and Trends in Electric Machines, IEEE Transactions on Industrial Electronics. 0046 (2016) 1. doi:10.1109/TIE.2016.2613844.

[223] The Hysteresis Loop and Magnetic Properties, (n.d.). https://www.nde-ed.org/EducationResources/CommunityCollege/MagParticle/Physics/HysteresisLoop.htm (accessed October 22, 2019).

[224] G. Ouyang, X. Chen, Y. Liang, C. Macziewski, J. Cui, Review of Fe-6.5wt%Si high silicon steel—a promising soft magnetic material for sub-kHz application, Journal of Magnetism and Magnetic Materials. (2019). doi:10.1016/j.jmmm.2019.02.089.

[225] J. Schneider, A. Schoppa, K. Peters, Magnetic application choice among among different nonoriented electrical steels, Physics. 8 (1998) 755–762.

[226] R. Secco, Thermal conductivity and Seebeck coefficient of Fe and Fe-Si alloys: Implications for variable Lorenz number, Physics of the Earth and Planetary Interiors. 265 (2017) 23–34. doi:10.1016/j.pepi.2017.01.005.

[227] S. Urbanek, B. Ponick, A. Taube, K.P. Hoyer, M. Schaper, S. Lammers, T. Lieneke, D. Zimmer, Additive Manufacturing of a Soft Magnetic Rotor Active Part and Shaft for a Permanent Magnet Synchronous Machine, 2018 IEEE Transportation and Electrification Conference and Expo, ITEC 2018. (2018) 217–219. doi:10.1109/ITEC.2018.8450250.

[228] Copper Development Association, High Conductivity Coppers for Electrical Engineering, CDA Publication. (1998) 80.